Bacterial protein import mediated by an iron transporter

By

Paul White

St. Cross College

A thesis presented for the degree of Doctor of Philosophy at the University of Oxford

Michaelmas Term 2017

Supervised by

Professor Colin Kleanthous

Declaration

I hereby confirm that the work presented in this thesis, submitted for the degree of Doctor of Philosophy, is my own original work. Work that is not my own is duly referenced. This thesis has not been previously submitted at this or any other university.

Paul White

September 2017

Acknowledgements

I am deeply thankful to many people for their support, advice and friendship throughout what has been a truly rewarding and enjoyable endeavour. First and foremost, I would like to thank my supervisor Professor Colin Kleanthous for the opportunity to undertake a DPhil in his laboratory, for his continued guidance and mentorship, and for allowing me the freedom to develop the project from the outset. I owe many thanks to Dr Nicholas Housden for his help and advice in all aspects of the project, for laying the foundations of the project, for training me in a wide array of lab techniques, and for his patience when I inevitably had questions to ask. I thank Dr Amar Joshi and Dr Ed Lowe for sharing their crystallography expertise, and I thank Dr Patrice Rassam for his assistance with fluorescence microscopy. Many thanks to Dr Renata Kaminska for her assistance with molecular biology techniques and for helping with the production of several protein constructs essential to this project. Thanks to Connor Sharp for all his help with bioinformatics, as well as being healthy competition in the thesis submission race. I would like to say thank you to all the members of the Kleanthous lab for helpful discussions either work-related or otherwise, and for being wonderful colleagues and friends. I would like to thank Professor Shabaz Mohammed and Dr Svenja Hester for the mass spectrometry analysis of my many crosslinking samples, and for their assistance with the data analysis. I thank Dr David Staunton for help with biophysical techniques. Many thanks to our collaborators Professor Daniel Walker and Dr Laura McCaughey for providing *Pseudomonas* strains and the original pyocin S2 clone, and thank you to Professor Iain Lamont for providing the *tonB* mutant strains. Thank you to my fellow 'Wellfies' of the WT programme 2013 cohort, Harriet-Lane Serff, Verity Jackson and Helen Ginn, for sharing this experience with me and for their friendship, which I hope continues long after we leave Oxford. Finally, I would like to thank my family for getting me where I am today and for their support throughout my academic career. I would like to thank my girlfriend Lizzi Underwood for always being there for me, for her support, and most importantly, for helping me secure my next challenge, a Postdoctoral Research Fellowship.

I am extremely grateful to the Wellcome Trust for funding this work.

Abstract

Multidrug resistant bacteria (MDR) have the potential to push back society to the pre-antibiotic era. Although discovered before penicillin, the inexorable rise in antibiotic resistance has revitalised interest in bacteriocins as treatments for bacterial infections. Bacteriocins are protein antibiotics principal to competition amongst pathogens and commensals, but the mechanisms by which they translocate across the Gram-negative cell envelope are poorly understood. The work presented in this thesis demonstrates how the endonuclease bacteriocin pyocin S2 (pyoS2) exploits the iron transporter FpvAI to translocate across the outer membrane (OM) of *Pseudomonas aeruginosa*. FpvAI is a 22-strand β-barrel and virulence factor in *P. aeruginosa* that transports iron into the cell in the form of a small siderophore, ferripyoverdine (Fe-Pvd). Uptake of Fe-Pvd requires the proton motive force (PMF), which is transduced to the ligand-bound receptor by TonB1 and its partner proteins ExbB-ExbD in the inner membrane (IM). The crystal structure of the high affinity complex (K_d = 240 pM) formed between the N-terminal domain of pyoS2 (pyoS2^{NTD}) and FpvAI is presented, which shows pyoS2^{NTD} mimics Fe-Pvd, and induces the same conformational changes in the receptor. Fluorescently-labelled pyoS2^{NTD} was actively imported into *P. aeruginosa* PAO1 cells and this import was dependent on the PMF, TonB1 and a TonB1-box motif at the N-terminus of pyoS2^{NTD}. Finally, photo-activated crosslinking of stalled translocation intermediates demonstrated pyoS2^{NTD} translocates through the FpvAI β-barrel lumen by a process analogous to that of Fe-Pvd. Following binding to FpvAI, translocation begins by the unfolding of a force-labile portion of the plug domain, opening a narrow channel through FpvAI. This enables pyoS2 to deliver its own TonB1-box to the periplasm where contact with TonB1 activates its import through the same channel, most likely as an unfolded polypeptide. Hence, this study demonstrates that bacteria possess a rudimentary protein import system that exploits energised nutrient transporters in the OM.

Table of Contents

List of Figures

List of Tables

Abbreviations List

ABC	ATP-binding cassette
ADP	Adenosine diphosphate
AF488	Alexa Fluor 488
AFM	Atomic force microscopy
Amp	Ampicillin
AMP	Adenosine monophosphate
APS	Ammonium persulphate
ATP	Adenosine triphosphate
ATPase	Adenosine triphosphatase
BAM	β-barrel assembly machinery
Cm	Chloramphenicol
CCCP	Carbonyl cyanide m-chlorophenyl hydrazone
CD	Circular dichroism
CDI	Contact dependent inhibition
CPA	Common polysaccharide antigen
Cryo-EM	Electron cryo-microscopy
CTD	C-terminal domain
DEAE	Diethylaminoethane
DMF	Dimethylformamide
DMSO	Dimethylsulphoxide
DNA	Deoxyribonucleic acid
DNase	Deoxyribonuclease
DTT	Dithiothreitol
E. coli	*Escherichia coli*
ECF	Extra-cytoplasmic function
EDTA	Ethylenediaminetetraacetic acid
ER	Endoplasmic reticulum
ERAD	ER-associated degradation
ESI-MS	Electrospray ionisation mass spectrometry
ESRF	European synchrotron radiation facility
Fe-Ent	Ferric enterobactin
Fe-Pvd	Ferripyoverdine
FptA	Ferripyochelin receptor
FpvAI	Type I ferripyoverdine receptor
FRAP	Fluorescence recovery after photobleaching
Fur	Ferric utilisation regulator
GFP	Green fluorescent protein
GTPase	Guanosine triphosphatase
IM	Inner membrane
IMP	Inner-membrane peptidase
ImS2	Immunity protein S2
ImS5	Immunity protein S5
IPTG	Isopropyl β-D-1-thiogalactopyranoside
ITC	Isothermal titration calorimetry
IUTD	Intrinsically unstructured translocation domain
K_a	Bimolecular association equilibrium constant
Kan	Kanamycin

K_d	Bimolecular dissociation equilibrium constant
k_{off}	Bimolecular dissociation rate constant
k_{on}	Bimolecular association rate constant
LB	Lysogeny broth
LC-MS/MS	Liquid chromatography coupled to tandem mass spectrometry
LIS	Lithium diiodosalicyclic acid
LPS	Lipopolysaccharide
MDR	Multidrug resistant
MPP	Mitochondrial processing peptide
MWCO	Molecular weight cut-off
NADH	Nicotinamide adenine dinucleotide
NADPH	Nicotinamide adenine dinucleotide phosphate
NAG	N-acetylglucosamine
NAM	N-acetylmuramic acid
NCS	Non-crystallographic symmetry
NEB	New England Biolabs
n-OPOE	n-Octylpolyoxyethylene
NTD	N-terminal domain
OBS	OmpF-binding site
OM	Outer membrane
OMPs	Outer membrane proteins
P. aeruginosa	*Pseudomonas aeruginosa*
PAM	Pre-sequence translocase-associated motor
***p*Bpa**	*Para*-Benzoylphenylalanine
Pch	Pyochelin
PCR	Polymerase chain reaction
PDB	Protein Data Bank
PEG	Polyethylene glycol
PG	Peptidoglycan
PMF	Proton motive force
PMSF	Phenylmethylsulphonyl fluoride
POTRA	Polypeptide transport-associated
PRR	Proline rich region
Pvd	Pyoverdine
PyoS2	Pyocin S2
PyoS5	Pyocin S5
PyoS2-E2	Pyocin S2-colicin E2 chimera
PyoS2^{NTD}-Ia	Pyocin S2 N-terminal domain colicin Ia chimera
PyoS2^{NTD}-S5	Pyocin S2 N-terminal domain pyocin S5 chimera
RMSD	Root-mean-square deviation
RNA	Ribonucleic acid
RNase	Ribonuclease
SAM	Sorting and assembly machinery
SAXS	Small angle X-ray scattering
SDS	Sodium dodecyl sulphate
SDS-PAGE	Sodium dodecyl sulphate polyacrylamide gel electrophoresis
SEC	Size exclusion chromatography
SM	Succinate medium
SPP	Stromal processing peptide
SRP	Signal recognition particle

TEA	Triethanolamine
T1SS	Type I secretion system
T2SS	Type II secretion system
T3SS	Type III secretion system
T4SS	Type IV secretion system
T5SS	Type V secretion system
T6SS	Type VI secretion system
Tat	Twin arginine translocase
TBDT	TonB-dependent transporter
TBE	Tris-borate-EDTA
TCEP	Tris(2-carboxyethyl)phosphine
TEMED	Tetramethylethylenediamine
TEV	Tobacco etch virus
TIC	Translocon at inner membrane of chloroplast
TIM	Translocase of the inner membrane
TM	Transmembrane
T_m	Melting temperature
TOC	Translocon at outer membrane of chloroplast
TOM	Translocase of the outer membrane
tRNA	Transfer ribonucleic acid
UV	Ultraviolet
β-OG	n-Octyl-β-D-glucopyranoside

Chapter 1. General Introduction

Bacteria are ubiquitous microorganisms which constitute a large proportion of the prokaryotic domain, and are among the most primitive life forms on the planet. Despite being only a few micrometres in length, their collective mass exceeds that of all plants and animals. Although many species of bacteria are harmless or even beneficial to our health, those with a capacity to cause disease are a constant threat to modern medicine. In our relentless battle against bacterial pathogenicity, antibacterials continue to be the most succesful group of medicines in history, yet worryingly, their future is becoming ever more uncertain with emerging antibiotic-resistant strains threatening to put us back into the pre-antibiotic era. In a modern society dependent on antibiotics for survival, longevity, quality of life and productivity, and a bleak outlook on the continued effectiveness of these drugs, it is clear that new therapies will soon be required (WHO., 2014).

1.1. Multidrug resistant (MDR) *Pseudomonas aeruginosa*

The widespread use of antibiotics has introduced resistance patterns driven by a strong evolutionary selection pressure, sparking the need for more rational approaches as the efficacy of antibiotics derived from natural products diminishes. The decline in antibacterial research, fuelled partly by the pharmaceutical industry finding it harder to get a return on investment, is further cause for concern. This has culminated in a ~30 year 'discovery void' where there have been no new antibiotics, and continued resistance has made some existing drugs obselete (Ventola, 2015, Brown, 2015).

The opportunistic pathogen *P. aeruginosa* is a major problem in hospitals, particularly in immunocompromised patients where infections of the blood, pneumonia and infections

following surgery can often be fatal (Micek *et al.*, 2015). Moreover, *P. aeruginosa* colonises the lungs of cystic fibrosis patients resulting in higher rates of mortality than the disease itself (Murray *et al.*, 2007). The threat level of *P. aeruginosa* is currently classified as serious by the Centres for Disease Control and Prevention, with over 50,000 cases leading to around 400 deaths in the United States each year (Frieden, 2013). Some strains of *P. aeruginosa* are resistant to all or nearly all of the available antibiotics, not only due to its capacity to acquire resistance factors, but also through intrinsic resistance mechanisms. This intrinsic resistance is mediated by the low permeability of the outer membrane, and the high surface expression levels of multidrug efflux pumps including the MexAB-OprM and MexCD-OprJ systems (Lambert, 2002). Furthermore, the transition from acute to chronic infections is associated with phenotypic changes including mucoidy and biofilm formation which serve to protect bacterial communities from external agents (Harmer *et al.*, 2013, Whiteley *et al.*, 2001). *P. aeruginosa* is able to establish a chronic infection by acquisition of iron from iron-scarce environments such as the airway (Konings *et al.*, 2013).

1.2. The Gram-negative bacterial cell envelope

In the 19th century, the Danish bacteriologist Hans Christian Gram classified nearly all bacteria into two groups based on whether they retained a purple-coloured stain, which became known as the Gram stain (Gram, 1884). The bacteria which were dyed purple were named Gram-positive whilst those which resisted staining were named Gram-negative. Structural differences in the cell envelope underpin the differences in staining susceptibility between Gram-positive and Gram-negative bacteria. The cell envelope of Gram-positive bacteria, including organisms like *Staphylococcus aureus* and *Bacillus subtilis*, consists of a single cytoplasmic membrane and a thick peptidoglycan (PG) cell

wall containing teichoic and lipoteichoic acids. In contrast, the Gram-negative cell envelope of organisms such as *Escherichia coli* and *P. aeruginosa*, is composed of an inner membrane (IM), an asymmetric outer membrane (OM) and an intervening periplasmic space containing the PG cell wall (Figure 1-1) (Silhavy *et al.*, 2010).

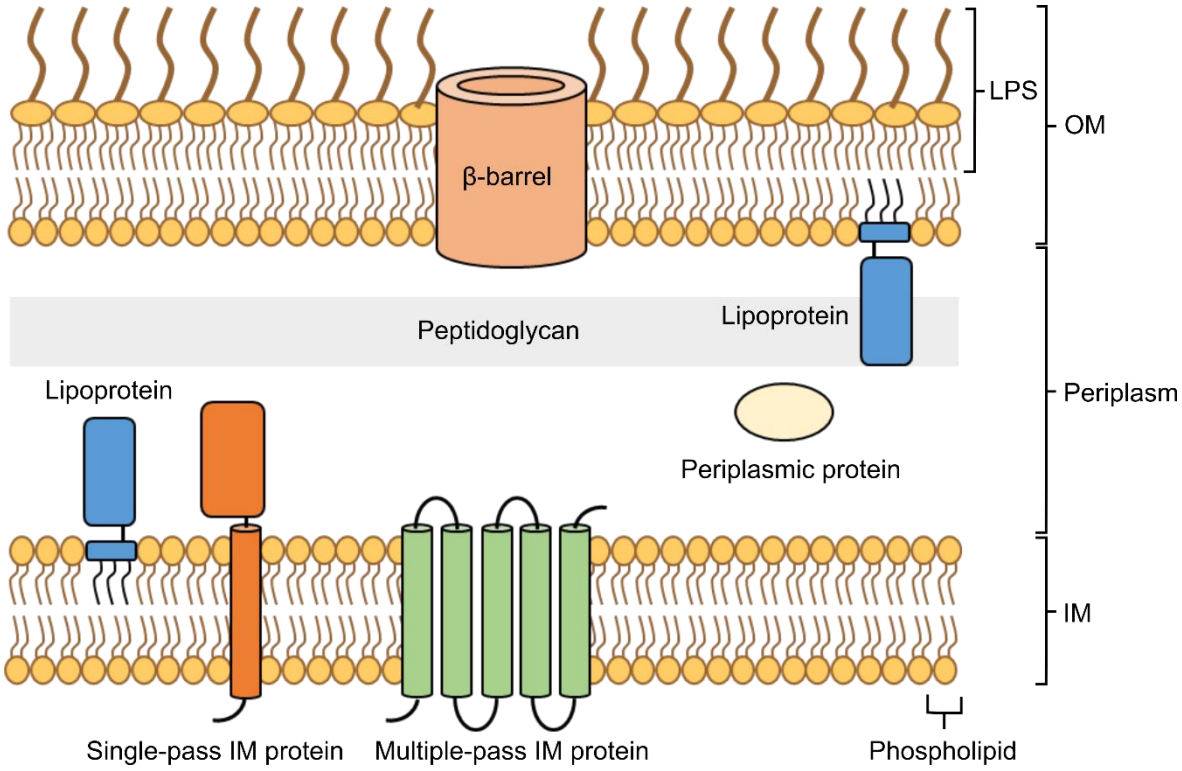

Figure 1-1. The Gram-negative cell envelope.
In *E. coli*, the entire cell envelope spans ~30 nm. The width of the periplasm ranges between ~13 and ~21 nm and the PG is around ~6 nm in width (Vollmer and Seligman, 2010).

1.2.1. The outer membrane (OM)

A biological membrane typically comprises two symmetric layers of phospholipid where the hydrophobic acyl chains are shielded by hydrophilic phosphate-containing head groups. Conversely, the OM of Gram-negative bacteria is asymmetric with phospholipids such as phosphatidylethanolamine, phosphatidylglycerol and cardiolipin making up the inner leaflet, and a glycolipid outer leaflet primarily composed of lipopolysaccharide

(LPS). LPS is composed of a hexa- or hepta-acylated glucosamine disaccharide, known as lipid A, with a polysaccharide core and variable polysaccharide chains known as the O-antigen. The O-antigen plays a prominent role in Gram-negative pathogenicity and is often responsible for endotoxic shock in cases of septicemia (Raetz and Whitfield, 2002).

The OM forms the cell boundary with the external environment and functions as a permeability barrier, regulating the transport of substances including nutrients and toxins. Key to this regulation are proteins, the majority of which are lipoproteins or β-barrel OM proteins. Lipoproteins are mostly anchored to the inner leaflet through an acyl chain attached to an N-terminal cysteine residue (Sankaran and Wu, 1994). Integral membrane proteins of the OM nearly always adopt a β-barrel structure whereby antiparallel β-strands, usually between 8-24 strands, fold into cylinders. These proteins, commonly referred to as OMPs, function as porins, ligand-gated transporters, enzymes or virulence factors. Porins are monomeric or trimeric and allow non-specific passive diffusion of small molecules such as sugars or amino acids through their lumen. Ligand-gated transporters actively transport large ligands such as iron-siderophore complexes or vitamins. They are distinguished from porins by a greater number of strands in their β-barrels (typically 20-24), a lower copy number per cell and the presence of an N-terminal globular 'plug' which occludes the barrel pore, enabling more specific transport (Nikaido, 2003). Enzymatic β-barrels function to process proteins (proteases), phospholipid (phospholipases) and LPS in the OM. Some β-barrels form large multidrug-efflux complexes to effectively excrete anti-microbial drugs, greatly reducing their efficacy (Delmar *et al.*, 2014). The β-barrel assembly machinery (BAM) facilitates the correct folding and insertion of OMPs into the OM (Iadanza *et al.*, 2016).

1.2.2. The inner membrane (IM)

The IM of Gram-negative bacteria is a symmetrical bilayer of glycerophospholipids, with the same composition as the inner leaflet of the OM (Raetz, 1978, Raetz and Dowhan, 1990). Essential functions, including the generation of energy, lipid biosynthesis, secretion and transport, all take place on the IM because, unlike eukaryotes, bacteria lack specialised intracellular organelles (Silhavy *et al.*, 2010). The proteins which carry out these diverse functions are α-helical, with single or multiple-pass α-helices, or are anchored in the periplasmic-facing leaflet by an N-terminal acyl chain (Dalbey *et al.*, 2011).

1.2.3. The periplasm

Separating the IM and the OM is a protein-rich, aqueous environment known as the periplasm. The periplasm, ranging between 11 and 21 nm in width (Bayer, 1991, Vollmer and Seligman, 2010), is spanned by trans-periplasmic complexes such as the flagellar motor, bacterial secretion systems and the AcrAB-TolC system (Diepold and Armitage, 2015, Yamaguchi *et al.*, 2015). Compartmentalisation in the periplasm is also able to sequester harmful degradative enzymes including alkaline phosphatase and RNaseA, and may therefore be an evolutionary precursor of the eukaryotic lysosome (Silhavy *et al.*, 2010).

1.2.4. The peptidoglycan (PG) cell wall

Within the periplasm lies the PG layer, a polymer consisting of repeating units of N-acetyl glucosamine-N-acetyl muramic acid (NAG-NAM) disaccharide densely crosslinked into a mesh-like structure by pentapeptide linkages (Vollmer, 2008). Its strength and rigidity governs the shape of the bacterial cell and is the reason why cells resist lysis when placed into a hypertonic solution. The PG is tightly associated with the OM by covalent attachment mediated through Braun's lipoprotein, Lpp (Braun, 1975), but also through

non-covalent interactions with OMPs and other lipoproteins (Park *et al.*, 2012). Cells can remain metabolically active after the PG has been removed in a process known as spheroplasting, but are not viable, lose their shape and are highly susceptible to lysis (Silhavy *et al.*, 2010). The enzymes underpinning PG synthesis are frequently targeted in the development of antibiotics. In 1928, the most famous of all antibiotics, penicillin, was discovered by Alexander Fleming and was later developed by Howard Florey and Ernst Chain. Penicillin is a β-lactam antibiotic which strongly inhibits the transpeptidation reaction required to form peptide crosslinks between glycan chains by inactivating penicillin-binding proteins. It has been widely accepted that whilst β-lactam antibiotics inhibit PG synthesis, PG hydrolases known as autolysins continue to function compromising the integrity of the structure until osmotic pressure eventually causes the cell to lyse (Vollmer *et al.*, 2008). However, recently it has been shown that β-lactam antibiotics kill bacteria by disruption of the cell wall synthesis machinery, leading to an endless cycle of PG turnover that ultimately depletes cellular resources (Cho *et al.*, 2014).

1.2.5. Cell envelope biogenesis

The cell envelope is composed of a diverse range of macromolecules including integral membrane proteins, soluble proteins, lipoproteins, phospholipids, PG and LPS. All of these components are synthesised in the cytoplasm or the inner leaflet of the IM, and therefore must be transported throughout the cell envelope and assembled into their final functional state.

Lipoproteins are anchored to the periplasmic leaflet of the IM or the OM by N-terminal acyl chains. Lipoproteins are first synthesised in the cytoplasm with an N-terminal signal sequence which is recognised by the Sec system (described in section 1.3.1) for translocation into the periplasm. A diacylglyceride moiety is then tethered via a thioester bond to a conserved cysteine residue following the signal sequence, which is

subsequently cleaved by signal peptidase II. A third acyl chain is conjugated to the cysteine N-terminus, and the mature lipoprotein is inserted into the IM (Silhavy *et al.*, 2010). The presence of an aspartate residue immediately following the acylated cysteine acts as an IM retention signal, keeping the lipoprotein at the IM whilst the majority of lipoproteins are targeted to the OM (Yamaguchi *et al.*, 1988). OM localisation is mediated by the Lol system, consisting of an ATP-binding cassette (ABC) transporter (LolCDE), a periplasmic protein (LolA) and a lipoprotein (LolB). The ABC transporter LolCDE releases the lipoprotein from the IM and passes it to LolA at the expense of ATP hydrolysis. LolA shuttles the protein across the periplasm, ultimately passing it on to LolB for insertion into the OM (Silhavy *et al.*, 2010). Despite this, a recent study has revealed that LolA and LolB are not required for lipoprotein trafficking, but instead function to prevent toxic accumulation of OM lipoproteins in the IM (Grabowicz and Silhavy, 2017).

Phospholipids are initially synthesised on the inner leaflet of the IM from precursors of glycerol-3-phosphate and fatty acyl-ACP (Raetz and Dowhan, 1990). Next, the newly synthesised lipids are trafficked to the outer leaflet of the IM, a kinetically unfavourable process catalysed by the ABC transporter MsbA (Doerrler *et al.*, 2004). How lipids are subsequently transported across the periplasm to the OM is still not fully understood, but lipid transport appears to be bidirectional (Jones and Osborn, 1977, Donohue-Rolfe and Schaechter, 1980).

LPS is composed of lipid A, a core oligosaccharide and a highly extended O-antigen, all of which are synthesised on the inner leaflet of the IM (Raetz and Whitfield, 2002). However, the K-12 strain of *E. coli*, commonly used in the laboratory, does not produce an extended O-antigen due to mutations in the *rfb* gene cluster (Stevenson *et al.*, 1994). The lipid A-core oligosaccharide is translocated to the periplasmic leaflet of the IM by

MsbA (Greenfield and Whitfield, 2012), whilst the O-antigen, carried on undecaprenyl-pyrophosphate, is translocated by a flippase encoded by the *wzx* gene (Liu *et al.*, 1996). The O-antigen is then conjugated to the lipid A-core by WaaL, producing mature LPS (Raetz and Whitfield, 2002). LPS must then cross the periplasm and translocate across the OM, a process mediated by the seven proteins of the Lpt system. LptF and LptG are predicted to be ATPases that, along with LptB and LptC shuttle LPS from the IM to LptA (Ruiz *et al.*, 2008). LptA spans the periplasm as part of the 'Lpt bridge' shielding the hydrophobic acyl chains during transport to the OM (Okuda *et al.*, 2016). Once at the OM, the β-barrel LptD and the lipoprotein LptE facilitate LPS incorporation into the outer leaflet through the opening of a lateral gate in LptD (Botos *et al.*, 2016, Silhavy *et al.*, 2010).

1.3. Protein translocation systems in bacteria

The three-layered architecture of the Gram-negative cell envelope presents a formidable barrier for the transport of substances into the cell. The transport of larger molecules, such as proteins, is an even bigger challenge, requiring dedicated systems for transportation between cellular compartments, the environment and other bacteria or eukaryotic cells. All of these functions are essential for cell viability and pathogenicity. Protein secretion pathways have been well studied but the mechanisms by which proteins are imported into bacteria are still poorly understood.

1.3.1. The Sec and Tat secretory systems

With the exception of some peptides, all bacterial proteins are synthesised on ribosomes in the cytoplasm, yet the abundance of proteins in the cell envelope requires translocation across the IM. Proteins destined for the periplasm or the OM are synthesised with an N-

terminal signal peptide for recognition as substrates for a heterotrimeric IM complex known as SecYEG (Driessen and Nouwen, 2008). Because the Sec complex is unable to transport folded proteins, substrates are stabilised in a translocation-competent unfolded state by the cytoplasmic chaperone SecB, before they are shuttled toward the SecYEG translocase. The proton motive force (PMF) along with the ATPase SecA provide the energy for translocation across the IM and into the periplasm. In addition to post-translational translocation, secreted proteins can also be co-translationally translocated in process assisted by the signal recognition particle (SRP). In this scenario, once the signal peptide has emerged from the ribosome, it is bound by the SRP which associates with FtsY localising the entire translation apparatus onto SecYEG. The nascent polypeptide chain, whilst still being synthesised, is then passed directly into the translocase. Once in the periplasm, the signal peptide is then cleaved and for periplasmic proteins, this is where the journey ends. The fate of precursor OMPs is described in the subsequent section.

Where the Sec secretory machinery accepts unfolded substrates, the Twin arginine translocation (Tat) system is capable of translocating fully folded proteins across the IM. Substrates recognised for Tat-mediated transport have an N-terminal signal sequence containing a pair of adjacent arginine residues, from where the system takes its name. TatBC recognises substrates and oligomerisation of TatA facilitates translocation across the membrane (Berks *et al.*, 2000).

1.3.2. The β-barrel assembly machinery (BAM)

After Sec-mediated translocation into the periplasm, precursor OMPs must be efficiency folded and inserted into the OM. This process is catalysed by the 203 kDa β-barrel assembly machinery (BAM) complex consisting of five proteins (BamA-E). The core component, BamA, is a β-barrel of the Omp85 family with five polypeptide transport-associated (POTRA) domains at its N-terminus. Associated with BamA are the

lipoproteins BamB-E anchored in the membrane through their N-terminal acyl chains (Wu *et al.*, 2005). Although only BamA and BamD are essential in *E. coli*, all components are required for maximal OMP folding (Mahoney *et al.*, 2016). Chaperones including SurA, Skp and DegP bind OMP precursors to protect against proteolytic degradation and keep them in a folding-competent state (Schiffrin *et al.*, 2016, Sklar *et al.*, 2007). The molecular mechanism of BAM-catalysed folding and insertion is still an area of active research but recent advances have revealed that BAM exists in an ensemble of conformations. Crystal structures have captured BamA in a state where the β-barrel is open to the periplasm probably to allow substrate OMPs to enter (Gu *et al.*, 2016). More recently, studies using X-ray crystallography and electron cryo-microscopy (cryo-EM) have captured BamA in a 'lateral open' conformation where the first and last β-strands are separated to allow the OMP substrate to access the outer leaflet of the OM (Bakelar *et al.*, 2016, Iadanza *et al.*, 2016). These states are believed to be part of a complex reaction cycle involving the concerted actions of all five Bam proteins and the POTRA domains.

1.3.3. Secretion systems

Gram-negative bacteria utilise a number of systems to invade tissues and evade the host immune response during infection. One such example, the secretion of virulence proteins, is central to their pathogenicity. Most proteins secreted by the Sec and Tat systems are destined for the periplasm, the IM or the OM, whilst some are secreted outside the cell by another specialised transporter. Secretion systems that are Sec/Tat-independent span the entire cell envelope, transporting substrates directly outside the cell. In some cases, virulence proteins are secreted directly into the cytoplasm of another cell. There are six secretions systems in Gram-negative bacteria named type I to type VI, each transporting a different subset of protein substrates (Green and Mecsas, 2016). The type

I secretion system (T1SS) consists of an IM ABC transporter and a membrane fusion protein that spans the periplasm to a pore-forming OMP. The T1SS secretes unfolded substrates with diverse functions including enzymes, adhesins and heme-binding proteins (Delepelaire, 2004). Type II secretion systems (T2SS) transport proteins from within the periplasm and therefore only consist of an OM pore. T2SS substrates are secreted in a folded state with mainly enzymatic roles (Korotkov *et al.*, 2012). Type III secretion systems (T3SS) are one of the largest trans-envelope complexes in Gram-negative bacteria and are evolutionally related to the flagellum (Diepold and Armitage, 2015). They consist of a basal body spanning the entire cell envelope, an extracellular needle through which unfolded substrates pass, and a translocon complex which inserts into the membrane of a target cell (Radics *et al.*, 2014). The roles of T3SS effector proteins are not fully understood and largely differ between species, yet their functions probably involve the remodelling of cellular processes within the target cell (Green and Mecsas, 2016). The type IV secretion system (T4SS) is involved in the exchange of protein, DNA and protein-DNA complexes between bacterial cells and is evolutionally related to primitive DNA conjugation systems (Cascales and Christie, 2003). The type V secretion system (T5SS), like the T2SS, is Sec-dependent though substrates are secreted in an unfolded state. T5SS substrates are autotransporters, with predominantly virulence-related roles such as proteases, adhesins and mediators of immune evasion (Green and Mecsas, 2016). Type VI secretion systems (T6SS) are trans-envelope injectosomes that translocate cytotoxic effector proteins into target bacteria and some eukaryotes (Alteri and Mobley, 2016, Ruhe *et al.*, 2013). The injection spike exhibits homology to phage tails leading to the hypothesis that the T6SS evolved from a reversed phage tail, delivering effector proteins to the outside of the cell (Pukatzki *et al.*, 2007). Effector activities

include nucleases, lipases, peptidoglycan hydrolases and the crosslinking of actin (Alteri and Mobley, 2016).

1.3.4. Mitochondrial and plastid protein import

All the translocation systems introduced thus far involve the secretion of proteins to the exterior of the cell. Conversely, bacteria have no recognised protein import systems, yet import of proteins into bacteria is central to inter-bacterial competition (Kirkup and Riley, 2004). Their descendants, mitochondria and plastids, have nonetheless evolved dedicated protein import machinery. Endosymbiotic theory suggests mitochondria and plastids evolved from primitive α-proteobacteria and cyanobacteria, respectively, which became engulfed by a eukaryotic cell (Zimorski *et al.*, 2014, Gould *et al.*, 2015). Like their ancient ancestors, they possess an OM and an IM, and a DNA genome encoding many, but not all, proteins essential for function. The majority of the mitochondrial and plastid proteome is encoded by the nuclear genome and is synthesised in the cytosol, and must therefore be imported (Wiedemann and Pfanner, 2017).

Protein precursors destined for mitochondria are synthesised with an N-terminal pre-sequence that is recognised by the translocase of the outer membrane (TOM) complex. The complex consists of a 19-strand β-barrel (Tom40) forming the main channel, along with additional subunits Tom22, Tom7, Tom6 and Tom5. The pre-sequence, forming an amphipathic α-helix with hydrophobic and positively-charged faces (Roise *et al.*, 1986), is recognised by associated Tom20 and Tom70 subunits (Dolezal *et al.*, 2006). Tom40 of the voltage-dependent anion channel superfamily, has hydrophilic and hydrophobic surfaces suitable for importing a diverse range of protein precursors, including both soluble matrix proteins and membrane proteins. Precursors of β-barrels are inserted into the OM by the sorting and assembly machinery (SAM), which is a member of the Omp85 family. After crossing the OM, proteins are shuttled to the pre-sequence translocase of

the inner membrane (TIM23) complex, which directs precursors into the IM or to the matrix. TIM23 is composed of multiple subunits; Tim50 recognises the pre-sequence as it emerges from TOM, Tim23 forms the channel across the IM, and both Tim21 and Tim17 function as regulatory subunits. For the most part, import is driven by membrane potential where the positively charged pre-sequence is drawn towards the negatively charged matrix. However, complete translocation into the matrix requires the ATP-driven pre-sequence translocase-associated motor (PAM). The N-terminal pre-sequence is eventually cleaved by mitochondrial processing peptidase (MPP) and sometimes also by inner-membrane peptidase (IMP) (Wiedemann and Pfanner, 2017).

Like mitochondria, the majority of plastid proteins are encoded by the nuclear genome, requiring multicomponent translocases for their import. The mechanisms by which protein precursors are imported into chloroplasts are indeed remarkably similar to those of mitochondria. Precursors are synthesised with an N-terminal pre-sequence which, in chloroplasts, is recognised by the translocon at outer membrane of chloroplast (TOC) complex. Toc159 and Toc34 are receptors with GTPase activity which recognise the precursor protein pre-sequence, and Toc75 forms the translocation channel. Toc64 forms a non-essential forth subunit. Translocation into the stroma is facilitated by the translocon at inner membrane of chloroplast (TIC) complex, which is composed of multiple subunits and associated chaperones. The pre-sequence is ultimately cleaved by stromal processing peptidase (SPP) (Shi and Theg, 2013). Unlike, mitochondrial protein import which uses the membrane potential and ATP, the energy source for protein import into chloroplasts is provided exclusively by ATP hydrolysis in the stroma (Theg *et al.*, 1989).

1.4. Energy transduction in Gram-negative bacteria

1.4.1. The proton motive force (PMF)

The PMF is the major electrochemical gradient across the IM involved in energy production. The cytoplasmic side of the IM is relatively alkaline compared to the periplasmic side, and it is this difference which drives the flow of protons required for ATP synthesis, secondary active transport, motility and secretion. Under aerobic conditions, the PMF is maintained by the electron transport chain involving IM protein complexes, iron-sulphur clusters, quinones and cytochromes, which participate in a series of oxidation-reduction reactions. The initial electron donor, in most cases nicotinamide adenine dinucleotide (NADH), transfers electrons to ubiquinone by NADH dehydrogenase. Next, ubiquinol transfers electrons to the terminal ubiquinol oxidase complex containing *b*- and *d*-type, or *b*- and *o*-type cytochromes, where molecular oxygen is ultimately reduced to water. Some bacteria use a cytochrome oxidase as the terminal acceptor complex and therefore require an additional step involving the transfer of electrons from ubiquinol to the cytochrome bc_1 complex. During electron transfer, protons are accumulated on the periplasmic side of the IM, creating the diffusion gradient termed the PMF (Anraku, 1988). Depletion of the PMF by chemical agents such as carbonyl cyanide m-chlorophenyl hydrazone *(*CCCP*)* or nigericin is always lethal. CCCP shuttles protons across the IM in the direction of the diffusion gradient, whilst nigericin is a proton-K^+ antiporter (Orlov *et al.*, 1994).

1.4.2. The Ton and Tol systems

The PMF can be used by the F_0-F_1 ATP synthase to drive ATP synthesis, or by secondary active transporters. The periplasm is devoid of ATP and no electrochemical gradients exist across the OM, making transport of substances across the OM more challenging. Gram-negative bacteria have therefore evolved trans-envelope systems to transduce the

energy from the PMF to the OM. Principal to this are the Ton and Tol systems (Figure 1-2). The Ton system comprises an IM complex of three proteins, ExbB, ExbD and TonB, with the latter spanning the length of the periplasm to contact TonB-dependent transporters (TBDTs) at the OM. Energy from the PMF is propagated to TBDTs through TonB (Noinaj *et al.*, 2010), driving the uptake of specific nutrients. Analogous to the Ton system is the Tol system, an IM complex of TolQ, TolR and TolA, the soluble periplasmic protein, TolB, and the OM-anchored lipoprotein, Pal. TolB has been shown to bind TolA and Pal, as well as Lpp and OmpA, mediating trans-periplasmic communication (Clavel *et al.*, 1998). The role of the Tol system for stabilisation of the OM was apparent after mutations in *tol* genes lead to hypersensitivity to detergents and antibiotics, OM blebbing and defects in O-antigen synthesis (Bernstein *et al.*, 1972, Paterson *et al.*, 2009). The Tol system is also hijacked by certain bacteriophages (Jakob *et al.*, 2012) and bacteriocins (Gokce *et al.*, 2000, Bouveret *et al.*, 1998) to gain entry to the cell. Both TonB and TolA undergo conformational changes in response to the PMF (Germon *et al.*, 2001).

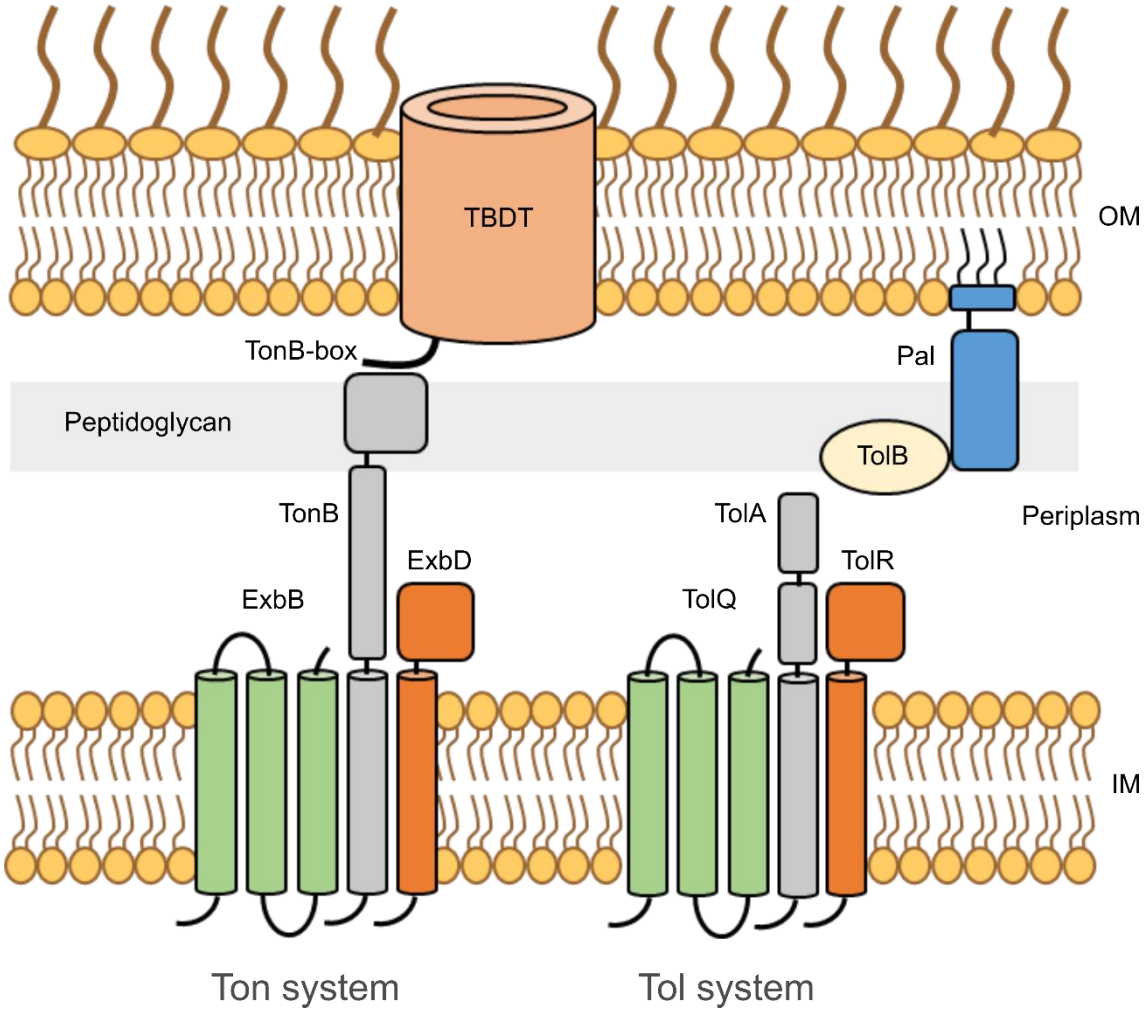

Figure 1-2. Schematic of the Ton and Tol systems.
The Ton system consists of ExbB, trans-periplasmic TonB bound to the TonB box of a TBDT, and ExbD. The Tol system consists of TolQ, TolR and TolA, along with periplasmic TolB bound to the OM lipoprotein Pal.

How the PMF is harnessed by the Ton system is still unclear, but a recent study on the structure of the *E. coli* Ton complex revealed ExbB exists as a pentameric pore that may act as proton conducting channel (Figure 1-3) (Celia *et al.*, 2016). The study also showed ExbD forms dimer and there is at least one copy of TonB present in the complex. The central ExbB pore is lined with a hydrophobic surface, followed by basic and acidic layers within the cytoplasm. The hydrophobic region of the ExbB pore is occupied by the transmembrane (TM) helix of ExbD, and the authors proposed a second copy of ExbD is located outside the pore embedded in the IM. This work led to a model where

translational or rotational motion of ExbD within the pore, driven by electrostatic interactions, acts on TonB (Braun and Herrmann, 2004, Celia *et al.*, 2016). Energy-dependent motion of TonB has been seen previously; TonB fused to green fluorescent protein (GFP) displayed decreased anisotropy in energy depleted cells (Jordan *et al.*, 2013).

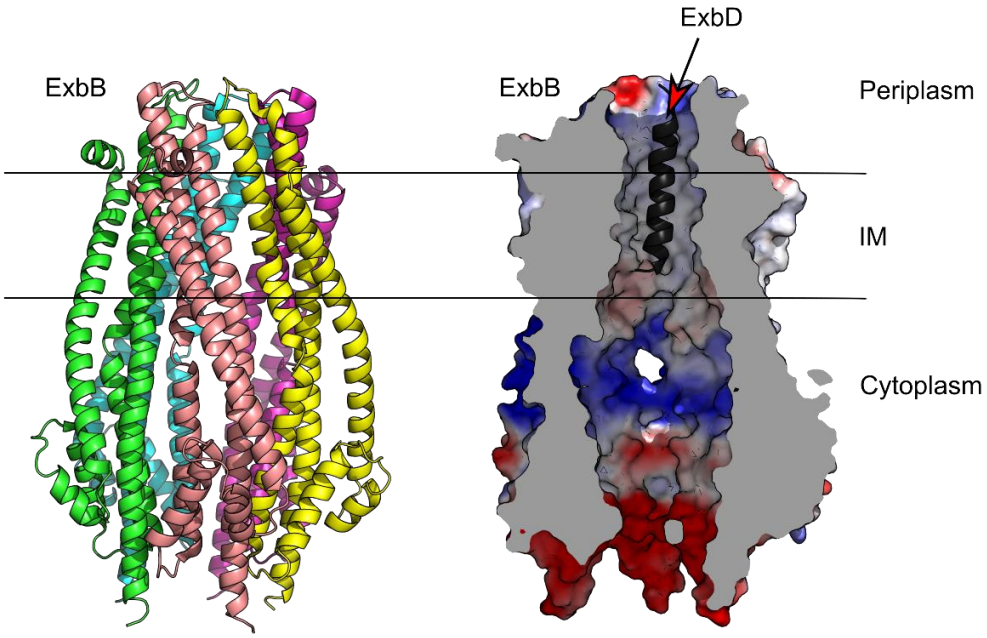

Figure 1-3. Structure of the ExbB pentamer.
Crystal structure of the ExbB pentamer at pH 4.5. ExbB forms a pore with internal hydrophobic, basic and acidic surfaces. The ExbD TM helix (*black*) binds inside the ExbB pore (PDB ID 5SV1 (Celia *et al.*, 2016)).

Although the precise mechanism is unknown, ExbB and ExbD harness the PMF and deliver the resulting energy-dependent conformational changes to TonB, which then acts on TBDTs. The TonB N-terminal TM helix is followed by a periplasmic spanning domain, and a C-terminal βαββ domain (CTD). The physiological oligomeric state of the CTD is disputed with arguments both for monomeric (Sauter *et al.*, 2003) and dimeric forms (Freed *et al.*, 2013), and monomer-dimer transitions (Gresock *et al.*, 2015).

Dimeric forms involve the exchange of β-strands between subunits and are normally seen with the CTD in isolation. Propensity to bind β-strands is implicated in the function of the CTD, which interacts with TBDTs through a short conserved motif in the N-terminus of the transporter (the TonB-box) to form a fourth β-strand on the β-sheet (Figure 1-4) (Pawelek *et al.*, 2006, Shultis *et al.*, 2006). Energised TonB induces conformational changes in the transporter which are coupled to ligand transport.

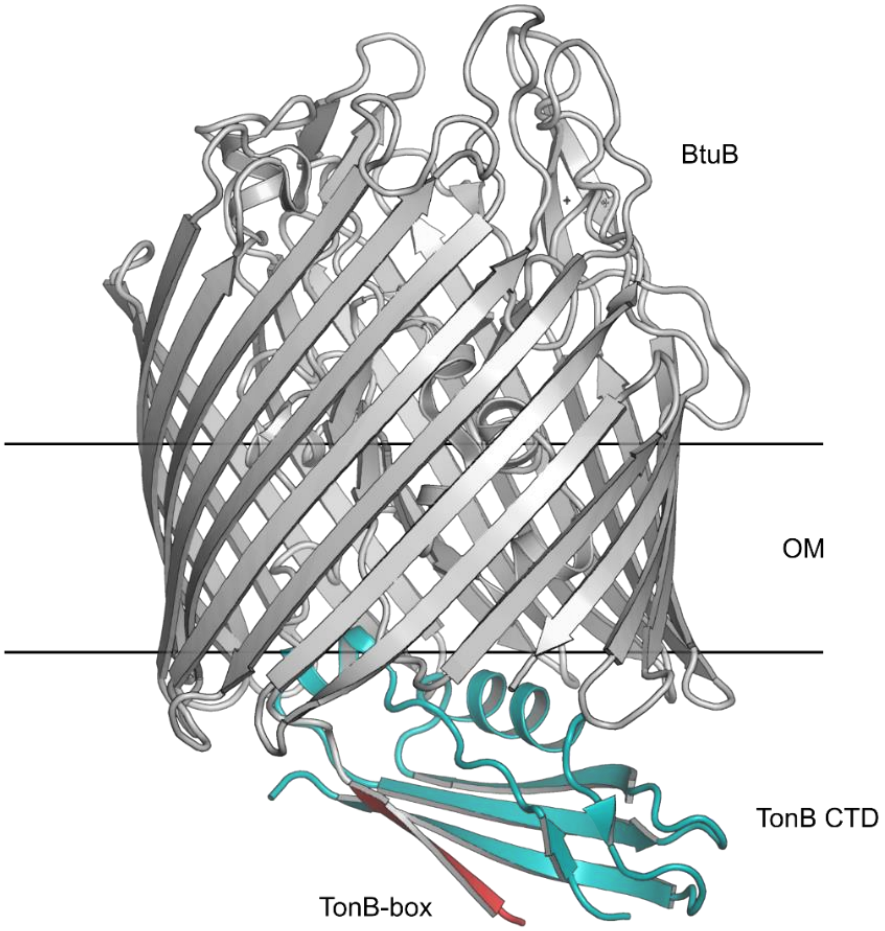

Figure 1-4. Structure of BtuB in complex with TonB.
Crystal structure of the TonB CTD *(cyan)* bound to BtuB (*grey*) highlighting the TonB-box (*red*) which forms a fourth β-strand on TonB (PDB ID 2GSK, (Shultis *et al.*, 2006)).

1.5. Iron acquisition and metabolism

The OM of Gram-negative bacteria serves to protect the cell from harmful external agents, whilst permitting the transport of essential metabolites. Porins allow passive diffusion of small solutes, but many essential nutrients exist in such low concentrations that they must be actively transported. For example, iron is an essential nutrient for microbial growth and virulence, but is scarce, often sequestered by the iron-binding proteins lactoferrin and transferrin. Iron must first be captured from the environment, and then be actively transported across the cell envelope. In *P. aeruginosa,* iron acquisition pathways are regarded as virulence factors because they are essential for establishing chronic infections. *P. aeruginosa* is able to effectively acquire iron from its host by producing cyclic peptide siderophores which readily outcompete iron-binding proteins (Konings *et al.*, 2013). The primary iron acquisition pathway in the PAO1 strain of *P. aeruginosa* involves the fluorescent siderophore pyoverdine (Pvd) and its OM receptor the type I ferripyoverdine receptor, FpvAI. FpvAI is the best characterised Pvd transporter in *P. aeruginosa*, though related transporters exist including FpvAII, FpvAIII and FpvB (de Chial *et al.*, 2003, Ghysels *et al.*, 2004). In addition to Pvd transporters are several other OM siderophore transporters including FptA, PfeA, FoxA, FiuA and HasR, which transport ferripyochelin, ferric enterobactin, ferrioxamine B, ferrichrome, and heme, respectively (Cobessi *et al.*, 2005, Llamas *et al.*, 2006, Dean and Poole, 1993, Ochsner *et al.*, 2000).

1.5.1. FpvAI

FpvAI is a 90 kDa 22-strand β-barrel and TBDT found in the OM of *P. aeruginosa* PAO1 (Poole *et al.*, 1993), which actively transports Pvd in complex with ferric (Fe^{3+}) iron. Pvd is a 1.2 kDa mixed hydroxamate-catecholate siderophore with a conserved dihydroxyquinoline chromophore bonded to a variable cyclic peptide (Visca *et al.*, 2007)

that readily chelates Fe^{3+} with a K_a of 10^{32} M^{-1} (Albrecht-Gary *et al.*, 1994). Its fluorescence significantly contributes to the fluorescent appearance of some *Pseudomonas spp.*, although fluorescence is quenched when complexed with iron (Albrecht-Gary *et al.*, 1994). Fe-Pvd complexes bind to FpvAI with a K_d of 0.5-1.5 nM and are then transported into the cell through the action of TonB1, one of the three TonB proteins in *P. aeruginosa* (Clément *et al.*, 2004, Hoegy *et al.*, 2005, Schalk *et al.*, 2001). As with iron, FpvAI is a virulence factor in *P. aeruginosa.* The structures of unliganded FpvAI, FpvAI bound to Fe-Pvd and FpvAI bound to non-cognate Pvds have been solved previously (Figure 1-5) (Greenwald *et al.*, 2009, Cobessi *et al.*, 2005, Brillet *et al.*, 2007). Fe-Pvd is buried within the extracellular loops of FpvAI and mostly contacts the plug domain, a globular domain occluding the barrel lumen. It has been suggested that conformation changes within the plug, triggered by Fe-Pvd binding, activate the receptor for transport by exposing the TonB1-box (Greenwald *et al.*, 2009). The TonB1-box is subsequently bound by TonB1 providing a trans-periplasmic link, coupling energy from the PMF to the receptor (Adams *et al.*, 2006, Brillet *et al.*, 2007). The precise mechanism of transport has not been fully elucidated. Once Fe-Pvd complexes reach the periplasm, ferric iron is reduced to ferrous iron (Fe^{2+}) where it readily dissociates from Pvd (Greenwald *et al.*, 2007). Ferrous iron is then chelated by a periplasmic binding protein and shuttled to an IM ABC-transporter, whilst Pvd is recycled by the PvdRT-OpmQ system in an unmodified state (Imperi *et al.*, 2009).

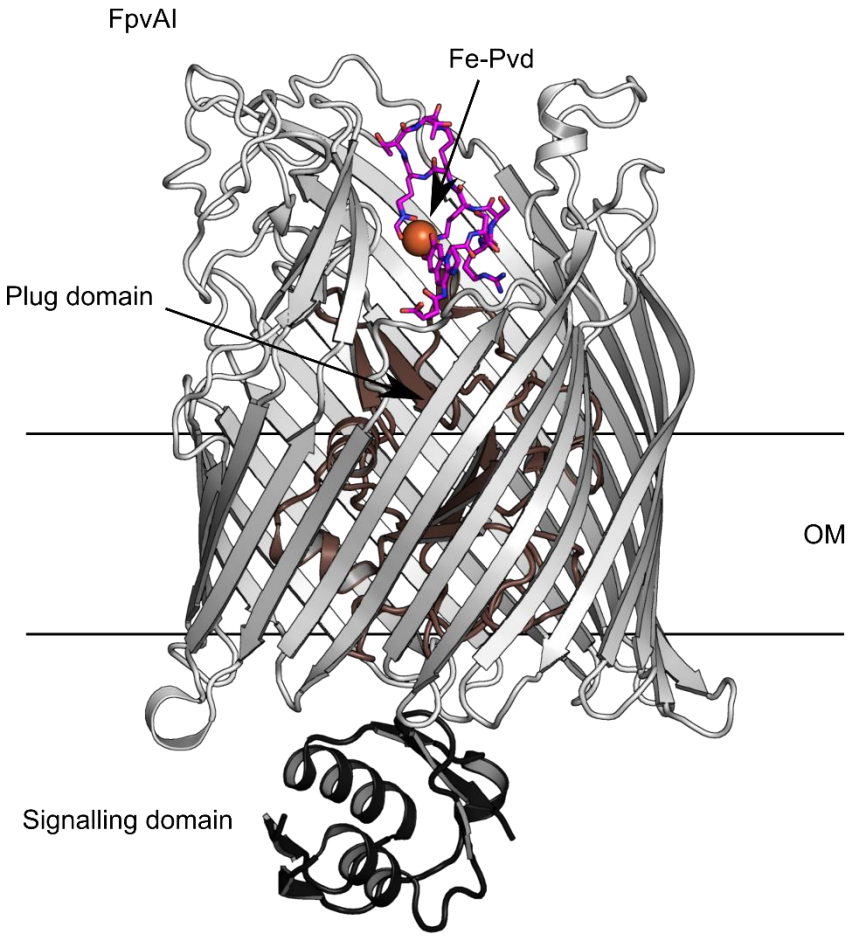

Figure 1-5. Crystal structure of FpvAI bound to Fe-Pvd.
Crystal structure of FpvAI (*grey*) bound to Fe-Pvd (*magenta*). The plug domain (*brown*) occluding the pore and the signalling domain (*black*) are highlighted. The TonB-box, located in a linker region between the signalling and plug domains, is absent from this structure (PDB ID 2W16 (Greenwald *et al.*, 2009)).

As well as iron transport, FpvAI also regulates iron uptake and metabolism through an N-terminal extension referred to as the signalling domain (Shen *et al.*, 2002). Uptake of iron must be tightly regulated because although iron is essential, excessive iron can be toxic. Pvd production and FpvAI expression increases in response to iron limitation and is down-regulated in iron-rich environments in a process mediated by a homologue of the *E. coli* ferric utilisation regulator (Fur) (Braun, 2003, Poole and McKay, 2003). In the absence of Fe-Pvd, the extra-cytoplasmic function (ECF) sigma factors FpvI and PvdS

are inhibited by the anti-sigma factor FpvR in the IM. In iron-limiting conditions, when Fe-Pvd complexes are being transported, the FpvAI signalling domain contacts FpvR resulting in TonB-dependent proteolysis of FpvR. This releases FpvI and PvdS to activate expression of FpvAI and the Pvd biosynthesis gene locus, respectively (Redly and Poole, 2005). Other virulence factors including exotoxin A and PrpL are also up-regulated by Pvd signalling (Ochsner et al, 1996, Wilderman et al, 2001).

1.6. Inter-bacterial warfare

1.6.1. Contact-dependent inhibition (CDI)

Instead of existing in isolation, bacteria form multicellular communities which must compete with each other to establish their ecological niche. Inter-bacterial warfare involves the killing or growth-inhibition of neighbouring cells by direct contact, including CDI and T6SS effectors, and by diffusible cytotoxic agents such as microcins and bacteriocins. CDI is found in many bacteria. In *E. coli* it involves two proteins, the CDI exporter CdiB, and a large hemagglutinin-repeat protein carrying the growth-inhibition activity, CdiA. CdiA passes through the CdiB β-barrel in the OM to contact its target cell receptor, BamA. Upon contact, the C-terminal effector domain of CdiA is cleaved and imported into the cell by an unknown mechanism. CDI toxins lead to growth inhibition in a number of ways, including pore-forming, nuclease, adenosine deaminase, ADP-ribosyl cyclase and metallopeptidase activities (Ruhe *et al.*, 2013). Beck *et al* (2014) have shown that a CDI toxin enters cells independent of BamA, Tol and Ton, by binding to the F-pilus which is subsequently internalised.

1.6.2. Bacteriocins

Almost 100 years ago Gratia observed 'a remarkable antagonism between two strains of *Escherichia coli*', identifying a toxic substance produced by *E. coli* V which killed *E. coli* Φ (Gratia, 1925). This marked the beginning of bacteriocin biology. Colicin-producing strains of *E. coli*, termed colicinogenic, express colicins from pCol plasmids via the SOS pathway in response to stress (Papadakos *et al.*, 2012). Co-expression with a lysis protein allows release of the colicin into the extracellular medium where they kill related strains of *E. coli* thus reducing competition for resources (Cascales *et al.*, 2007). On encountering a target cell, the colicin is localised on the OM by high-affinity binding to a specific receptor, usually a porin or a TBDT. The colicin then hijacks components of the cell envelope, including the Tol and Ton systems and the PMF, to translocate across the OM (Webster, 1991, Postle and Kadner, 2003). Killing is achieved in one of two mechanisms; the enzymatic colicins cleave bacterial nucleic acids or PG whereas the pore-forming colicins depolarise the IM (Papadakos *et al.*, 2012). Colicins range in size from 40 kDa to 80 kDa with multiple domains involved in the processes of translocation, receptor-binding and cytotoxicity. For nuclease colicins, which must also cross the IM, the ATP-dependent protease, FtsH, cleaves the cytotoxic domain and mediates translocation into the cytoplasm (Walker *et al.*, 2007, Kim *et al.*, 2014). To prevent cell suicide, the enzymatic colicins are produced with a cognate immunity protein which binds with very high affinity to the cytotoxic domain neutralising its activity (Kleanthous and Walker, 2001). Further details on the mechanisms of receptor-binding and translocation across the OM will be introduced in Chapters 4 and 5, respectively.

In contrast to colicins, very little is known about the bacteriocins specific for *P. aeruginosa*, the pyocins. Insoluble R and F-type pyocins elicit killing by depolarisation of the IM whereas the soluble S-type pyocins are protease sensitive and possess DNase,

RNase or pore-forming activity (Michel-Briand and Baysse, 2002). It has been shown that pyocin L1 of the more recently discovered lectin-like class of pyocins recognises the common polysaccharide antigen (CPA) of *P. aeruginosa* LPS but the mechanism of killing is unknown (McCaughey *et al.*, 2014). Like colicins, S-type pyocins are multi-domain proteins with the domains having specific roles in receptor-binding, translocation and cytotoxicity. The first S-type pyocins characterised were pyocins S1 to S5, and AP41 (Michel-Briand and Baysse, 2002). More recently, pyocin S6, isolated from a cystic fibrosis patient, was shown to possess RNase activity similar to that of colicin E3, and possess receptor-binding and translocation domains like those of pyocin S1 (Dingemans *et al.*, 2016). A comprehensive bioinformatics study later found several more pyocins including pyocins S7-S13 and S3C. These appear to have also recombined domains from other bacteriocins; for example, pyocins S13 and S3C carry the cytotoxic domains from colicin D and colicin E3, respectively (Sharp *et al.*, 2017). In addition to the three functional domains, another domain of unknown function has been identified in pyocins S2 (pyoS2) and AP41, known as domain II (Sano *et al.*, 1993). The receptor-binding domain tends to be present at the N-terminus, unlike colicins which have central receptor-binding domains (Sano *et al.*, 1993). A number of studies have sought to identify the receptors of S-type pyocins of which many are iron siderophore receptors, including FpvAI, FpvAII and FptA (Baysse *et al.*, 1999, Elfarash *et al.*, 2014, Elfarash *et al.*, 2012), yet little is known about these pyocin-receptor complexes. Moreover, no specific translocator proteins have been identified for pyocins. Like colicins, pyocins are co-expressed with an immunity protein to protect the producing cell from its lethal activity (Duport *et al.*, 1995, Ling *et al.*, 2010, Elfarash *et al.*, 2012).

As highly potent and specific antibacterials, bacteriocins are being investigated as novel candidates for antibiotics (Cotter *et al.*, 2013). In particular, the potential of pyocins as

protein antibiotics for *P. aeruginosa*, the primary cause of mortality in cystic fibrosis patients, is of great therapeutic interest. Several pyocins have been shown to be active in a murine lung infection model, with pyocin S5 (pyoS5) exhibiting greater efficacy than the most commonly used antibiotic, tobramycin (McCaughey *et al.*, 2016b). Pyocins have also been shown to combat biofilms (Smith *et al.*, 2012), whereas cell lysis induced by the phage-like R-and F-type pyocins has been shown to promote biofilm formation by releasing matrix components (Turnbull *et al.*, 2016).

1.7. Aims of this study

As outlined in this introduction, the Gram-negative cell envelope forms a robust barrier, protecting cells from harmful external agents, whilst permitting the transport of proteins and nutrients. Although there are well characterised mechanisms of protein secretion, there is a limited understanding of protein import systems. The vast majority of proteins in mitochondria and plastids are imported through dedicated systems, namely the TOM and TOC systems, respectively. By contrast, bacteria, from which these organelles evolved, have no known protein import systems. Here, the bacteriocin pyoS2 is used as a model protein to study import across the OM of *P. aeruginosa*. It has been known for some time that the primary cell-surface receptor for pyoS2 is the iron transporter FpvAI, yet there is no evidence of an interaction between these proteins *in vitro*. Moreover, there are no structures of S-type pyocin receptor-binding domains either in isolation or in complex with their receptor. There are also no definitive import mechanisms for bacteriocins in either *E. coli* or *P. aeruginosa*. This study uses a multidisciplinary approach involving a combination of structural biology, biophysics, cell biology and protein engineering to address these questions.

The principal aims were to first demonstrate an interaction between recombinant FpvAI and pyoS2, to identify the minimal receptor-binding domain and to solve the crystal structure of the complex. Secondly, to determine the import requirements of pyoS2 into living *P. aeruginosa*, and finally to use site-specific photo-activated crosslinking in conjunction with advanced proteomics to map the translocation pathway. This work would culminate in the most complete understanding of the cell entry mechanism for any bacteriocin despite bacteriocin biology being almost 100 years old. This new understanding could have profound implications in the development of protein antibiotics to subvert antibacterial resistance and its ongoing threat to modern medicine.

Chapter 2. Materials and Methods

2.1. Bacterial strains, media and growth conditions

Bacterial strains used throughout this study are described in Table 2-1. Bacterial strains were typically cultured in Miller lysogeny broth (LB) medium (10 g/L tryptone, 10 g/L NaCl, 5 g/L yeast extract, pH 7.2) at 37 °C unless otherwise stated. Bacteria were maintained short-term at 4 °C on LB-agar plates (LB+1.5% (w/v) agar) and long-term in LB+50% (v/v) glycerol at -80 °C.

Table 2-1. Bacterial strains used in this study.

Name	Relevant characteristic/s	Source
E. coli		
NEB5α	*fhuA2 Δ(argF-lacZ)U169 phoA glnV44 Φ80 Δ(lacZ)M15 gyrA96 recA1 relA1 endA1 thi-1 hsdR17*	New England Biolabs
BL21(DE3)	*fhuA2 [lon] ompT gal (λ DE3) [dcm] ΔhsdS λ DE3 = λ sBamHIo ΔEcoRI-B int::(lacI::PlacUV5::T7 gene1) i21 Δnin5*	New England Biolabs
TNE012	*ompA*$^{-}$, *ompB*$^{-}$, *tsx*$^{-}$	Cramer lab (Taylor *et al.*, 1998)
P. aeruginosa		
PAO1	Parent strain	Washington library
PA17	Clinical isolate	Walker lab
PW5036	*fpvA*-H02::ISlacZ/hah	Washington two-allele library
PAO6609	*met-9011 amiE200 strA pvd-9*	Lamont lab
K1407	*PAO6609 tonB1*$^{-}$	Lamont lab
K1408	*PAO6609 tonB2*$^{-}$	Lamont lab
MS231	*PAO6609 tonB3*$^{-}$	Lamont lab

2.2. Plasmids

Plasmids used throughout this study are described in Table 2-2.

Table 2-2. Plasmids used in this study.
See Appendix for pET21-a(+), pETM11, pBAD-Myc-HisB and pEVOL vector maps.

Name	Description	Source
pNGH183	FpvAI with OmpF signal sequence cloned into pBAD-Myc-HisB at *Nco*I/*Sac*I sites	Nicholas Housden
pPW06	PyoS2-ImS2-His6 cloned into pET21-a(+) at *Nde*I/*Xho*I sites	Walker lab
pPW11	PyoS2(1-209)-His6 cloned into pET21-a(+) at *Nde*I/*Xho*I sites	This study
pPW12	PyoS2(1-209)-Cys-His6 cloned into pET21-a(+) at *Nde*I/*Xho*I sites	This study
pPW14	Δ1-21PyoS2-ImS2-His6 cloned into pET21-a(+) at *Nde*I/*Xho*I sites	This study
pPW15	PyoS2(22-209)-His6 cloned into pET21-a(+) at *Nde*I/*Xho*I sites	This study
pPW16	PyoS2(22-209)-Cys-His6 cloned into pET21-a(+) at *Nde*I/*Xho*I sites	This study
pPW17	*P. aeruginosa* TonB1(109-342) with TEV-cleavage N-terminal His-tag cloned into pETM11 at *Nco*I/*Sac*I sites	This study
pPW27	PyoS2-ImS2-His6 S10A,M11A,V12A,I13A mutation cloned into pET21-a(+) at *Nde*I/*Xho*I sites	This study
pPW28	PyoS2(1-209)-Cys-His6 S10A,M11A,V12A,I13A mutation cloned into pET21-a(+) at *Nde*I/*Xho*I sites	This study
pPW29	PyoS2(1-209)-His6 S10A,M11A,V12A,I13A mutation cloned into pET21-a(+) at *Nde*I/*Xho*I sites	This study
pPW42	PyoS2(1-209)-DHFR cloned into pET21-a(+) at *Nde*I/*Xho*I sites – synthetic gene	GenScript Ltd
pPW43	PyoS2(1-209)-gp36c cloned into pET21-a(+) at *Nde*I/*Xho*I sites – synthetic gene	GenScript Ltd
pPW44	PyoS2(1-209)-eGFP-His6 cloned into pET21-a(+) at *Nde*I/*Xho*I sites	This study
pPW46	PyoS2(1-209)-eGFP-His6 M11 Amber mutant cloned into pET21-a(+) at *Nde*I/*Xho*I sites	This study
pPW48	PyoS2(1-209)-eGFP-His6 K70 Amber mutant cloned into pET21-a(+) at *Nde*I/*Xho*I sites	This study
pPW49	PyoS2(1-209)-eGFP-His6 A87 Amber mutant cloned into pET21-a(+) at *Nde*I/*Xho*I sites	This study
pPW50	PyoS2(1-209)-eGFP-His6 A96 Amber mutant cloned into pET21-a(+) at *Nde*I/*Xho*I sites	This study
pPW51	PyoS2(1-209)-eGFP-His6 A119 Amber mutant cloned into pET21-a(+) at *Nde*I/*Xho*I sites	This study
pPW52	PyoS2(1-209)-eGFP-His6 Q135 Amber mutant cloned into pET21-a(+) at *Nde*I/*Xho*I sites	This study
pPW53	PyoS2(1-209)-eGFP-His6 Q184 Amber mutant cloned into pET21-a(+) at *Nde*I/*Xho*I sites	This study

pPW54	PyoS2(1-209)-eGFP-His6 V204 Amber mutant cloned into pET21-a(+) at *Nde*I/*Xho*I sites	This study
pPW55	PyoS2(1-209)-eGFP-His6 Q17 Amber mutant cloned into pET21-a(+) at *Nde*I/*Xho*I sites	This study
pPW56	PyoS2(1-209)-eGFP-His6 I23 Amber mutant cloned into pET21-a(+) at *Nde*I/*Xho*I sites	This study
pPW57	PyoS2(1-209)-eGFP-His6 A29 Amber mutant cloned into pET21-a(+) at *Nde*I/*Xho*I sites	This study
pPW58	PyoS2(1-209)-eGFP-His6 Y46 Amber mutant cloned into pET21-a(+) at *Nde*I/*Xho*I sites	This study
pPW59	PyoS2(1-209)-eGFP-His6 K92 Amber mutant cloned into pET21-a(+) at *Nde*I/*Xho*I sites	This study
pPW60	PyoS2(1-209)-pyoS5(301-498)-His6 chimera cloned into pET21-a(+) at *Nde*I/*Xho*I sites	This study
pREN79	PyoS2(1-209)-ColE2(449-581)-Im2-His6 chimera cloned into pET21-a(+) at *Nde*I/*Xho*I sites	Renata Kaminska
pREN82	Δ1-30PyoS2-ImS2-His6 cloned into pET21-a(+) at *Nde*I/*Xho*I sites	Renata Kaminska
pREN84	PyoS2(31-209)-His6 cloned into pET21-a(+) at *Nde*I/*Xho*I sites	Renata Kaminska
pREN90	PyoS2(46-209)-His6 cloned into pET21-a(+) at *Nde*I/*Xho*I sites	Renata Kaminska
pEVOL	*p*-benzoyl-L-phenylalanine tRNA synthetase/tRNA pair	Chin JW et al, 2002

2.3. Molecular biology techniques

2.3.1. Polymerase chain reaction (PCR)

Primers used for all DNA manipulations are listed in Table 2-3. Standard 50 µl PCR conditions are described in Table 2-4. PCR was carried out in an Eppendorf Mastercycler thermal cycler programmed as described in Table 2-5 and Table 2-6 for amplification PCR and whole-plasmid mutagenesis PCR, respectively. When necessary, the dimethylsulphoxide (DMSO) concentration was varied between 0-4% (v/v) to optimise the reaction. Methylated parental DNA was digested by incubating 40 µl of the PCR mix with 1 µl *Dpn*I restriction enzyme for 1 hour at 37 °C. PCR products were analysed by agarose gel electrophoresis.

Table 2-3. Primers used in this study

Name	Sequence 5'→3'	Use
PyoS2_Nterm_F	GGAGGCGGACTACAAGCTCGA GGCAAATGTCGAG	Cloning of pyoS2^{NTD}, forward
PyoS2_Nterm_R	CTCGACATTTGCCTCGAGCTTG TAGTCCGCCTCC	Cloning of pyoS2^{NTD}, reverse
S2_NdeI_22_F	CACATGTGCAGGGTGGTCATAT GGACATAATCCAGTATATTC	Removal of pyoS2 residues 1-21, forward
S2_NdeI_22_R	GAATATACTGGATTATGTCCAT ATGACCACCCTGCACATGTG	Removal of pyoS2 residues 1-21, reverse
PyoS2N_Cys_F	GCGGACTACAAGCTCTGCCAC CACCACCACCAC	Introduction of Cys into pyoS2^{NTD}, forward
PyoS2N_Cys_R	GTGGTGGTGGTGGTGGCAGAG CTTGTAGTCCGC	Introduction of Cys into pyoS2^{NTD}, reverse
tonB_NcoI_F	CTATAACCATGGCGACCCCGG CCGAACTCAAC	Amplification of the *tonB1* gene from genomic DNA, forward
tonB_NcoIdel_F	CGAAGTGCGCCAGGCAATGGC CAAGTGGCGTTTC	Removal of internal *Nco*I site, forward
tonB_NcoIdel_R	GAAACGCCACTTGGCCATTGCC TGGCGCACTTCG	Removal of internal *Nco*I site, reverse
tonB_SacI_R	GTCTCTGAGCTCAGCGGCGCTT CTCGATCTTGAAGAAGAACAT CTTG	Amplification of the *tonB1* gene from genomic DNA, reverse
S2_TBBmut_F	GATTACGAACCTGGTGCGGCT GCTGCTACACATGTGCAGGGT G	PyoS2 TonB box mutation to Ala, forward
S2_TBBmut_R	CACCCTGCACATGTGTAGCAGC AGCCGCACCAGGTTCGTAATC	PyoS2 TonB box mutation to Ala, reverse
S2_EcoRI_F	GGAGGCGGACTACAAGGAATT CAAGGCAAATGTCGAGAAAAA AG	Introduction of *Eco*RI site at the end of *pyoS2^{NTD}* gene for *gfp* insertion, forward
S2_EcoRI_R	CTTTTTTCTCGACATTTGCCTTG AATTCCTTGTAGTCCGCCTCC	Introduction of *Eco*RI site at the end of the pyo*S2^{NTD}* gene for *gfp* insertion, reverse
S2_BamHI_F	CTGGCTTTAAGGCCGGTGGATC CCACCACCACCACCACC	Introduction of *Bam*HI site at the 3' end of the pyo*S2* gene for *gfp* insertion, forward
S2_BamHI_R	GGTGGTGGTGGTGGTGGGATC CACCGGCCTTAAAGCCAG	Introduction of *Bam*HI site at the 3' end of the pyo*S2* gene for *gfp* insertion, reverse
S2_amber11_F	GATTACGAACCTGGTGCGTAG GCTGCTACACATGTGC	Mutation at position 11 to amber (TAG) stop codon, forward

S2_amber11_R	GCACATGTGTAGCAGCCTACG CACCAGGTTCGTAATC	Mutation at position 11 to amber (TAG) stop codon, reverse
S2_amber17_F	CTGCTGCTACACATGTGTAGGG TGGTGGGCGTGAC	Mutation at position 17 to amber (TAG) stop codon, forward
S2_amber17_R	GTCACGCCCACCACCCTACACA TGTGTAGCAGCAG	Mutation at position 17 to amber (TAG) stop codon, reverse
S2_amber23_F	GGGTGGTGGGCGTGACTAGAT CCAGTATATTCCTG	Mutation at position 23 to amber (TAG) stop codon, forward
S2_amber23_R	CAGGAATATACTGGATCTAGTC ACGCCCACCACCC	Mutation at position 23 to amber (TAG) stop codon, reverse
S2_amber29_F	CGTGACATAATCCAGTATATTC CTTAGCGATCAAGCTACGGTAC TCCACC	Mutation at position 29 to amber (TAG) stop codon, forward
S2_amber29_R	GGTGGAGTACCGTAGCTTGATC GCTAAGGAATATACTGGATTAT GTCACG	Mutation at position 29 to amber (TAG) stop codon, reverse
S2_amber46_F	CAGGACCAAGTCCGTAGGTCG GTACTGGAATGC	Mutation at position 46 to amber (TAG) stop codon, forward
S2_amber46_R	GCATTCCAGTACCGACCTACGG ACTTGGTCCTG	Mutation at position 46 to amber (TAG) stop codon, reverse
S2_amber92_F	GAAGCGGGGTTGCCAGGTTAG GCGGTCAGTGCCAATG	Mutation at position 92 to amber (TAG) stop codon, forward
S2_amber92_R	CATTGGCACTGACCGCCTAACC TGGCAACCCCGCTTC	Mutation at position 92 to amber (TAG) stop codon, reverse
S2_amber70_F	CCCATTCAGAACTCAAGTAGA ACCTGAAAAATGAAACCCTG	Mutation at position 70 to amber (TAG) stop codon, forward
S2_amber70_R	CAGGGTTTCATTTTTCAGGTTC TACTTGAGTTCTGAATGGG	Mutation at position 70 to amber (TAG) stop codon, reverse
S2_amber87_F	GATGAACTCAAGAGTGAATAG GGGTTGCCAGGTAAAG	Mutation at position 87 to amber (TAG) stop codon, forward
S2_amber87_R	CTTTACCTGGCAACCCCTATTC ACTCTTGAGTTCATC	Mutation at position 87 to amber (TAG) stop codon, reverse
S2_amber96_F	CAGGTAAAGCGGTCAGTTAGA ATGACATCCGCGATG	Mutation at position 96 to amber (TAG) stop codon, forward

S2_amber96_R	CATCGCGGATGTCATTCTAACT GACCGCTTTACCTG	Mutation at position 96 to amber (TAG) stop codon, reverse
S2_amber119_F	CAAAGCAAAATCGCTAAAGTA GATTGAGGATCGCCCGGCC	Mutation at position 119 to amber (TAG) stop codon, forward
S2_amber119_R	GGCCGGGCGATCCTCAATCTAC TTTAGCGATTTTGCTTTG	Mutation at position 119 to amber (TAG) stop codon, reverse
S2_amber135_F	GGCTTCAGACTTTCCTTAGAAG TCAGAGTCGATG	Mutation at position 135 to amber (TAG) stop codon, forward
S2_amber135_R	CATCGACTCTGACTTCTAAGGA AAGTCTGAAGCC	Mutation at position 135 to amber (TAG) stop codon, reverse
S2_amber184_F	CTTGAAACAAACGTCTTAGGA GCTGGAGAATAAAGCCC	Mutation at position 184 to amber (TAG) stop codon, forward
S2_amber184_R	GGGCTTTATTCTCCAGCTCCTA AGACGTTTGTTTCAAG	Mutation at position 184 to amber (TAG) stop codon, reverse
S2_amber204_F	GAGCCGCTGCTGAGTAGGAGG CGGACTACAAG	Mutation at position 204 to amber (TAG) stop codon, forward
S2_amber204_R	CTTGTAGTCCGCCTCCTACTCA GCAGCGGCTC	Mutation at position 204 to amber (TAG) stop codon, reverse
S2S5_F	GAAGGAGATATACATATGGCT GTCAATGATTACGAACCTGGTT C	Amplification of *pyoS2^{NTD}* gene for fusion with *pyoS5^{CTD}* gene, forward
S2S5_int_R	CCTGCGTCGTGTCGTTTCGGCC TTGTAGTCCGCCTCCACCTC	Amplification of *pyoS2^{NTD}* gene for fusion with *pyoS5^{CTD}* gene, internal
S2S5_int_F	GAGGTGGAGGCGGACTACAAG GCCGAAACGACACGACGCAGG	Amplification of *pyoS5^{CTD}* gene for fusion with *pyoS2^{NTD}* gene, internal
S2S5_R	GTGGTGGTGGTGCTCGAGAAT GGATATTACAAGATTG	Amplification of *pyoS5^{CTD}* gene for fusion with *pyoS2^{NTD}* gene, reverse

Table 2-4. Standard PCR reaction conditions.
Total volume 50 µl. Reagents purchased from NEB.

Component	Amount	Volume
5x Reaction buffer	1x	10 µl
Template DNA	100 ng	1 µl
Primers	10 pmol	2 µl
dNTP mix	200 µM	1 µl
DMSO	0-4%	0-2 µl
Phusion HF DNA polymerase	2 units	1 µl

Table 2-5. Thermal cycler programme for amplification PCR

Step	Temperature	Duration
Initial denaturation	98 °C	2 minutes
Denaturation*	98 °C	1 minute
Annealing*	55-58 °C	30 seconds
Extension*	72 °C	2 minutes
Final extension	72 °C	5 minutes
Hold	14 °C	Indefinite

* repeat steps for 30 cycles

Table 2-6. Thermal cycler programme for mutagenesis PCR

Step	Temperature	Duration
Initial denaturation	98 °C	2 minutes
Denaturation*	98 °C	1 minute
Annealing*	55-58 °C	30 seconds
Extension*	72 °C	5 minutes
Final extension	72 °C	5 minutes
Hold	14 °C	Indefinite

* repeat steps for 16 cycles

2.3.2. Extraction of genomic DNA

Bacterial culture was grown overnight at 37 °C in LB and a maximum of $2x10^9$ cells, as calculated from optical density ($OD_{600\ nm}$), were pelleted at 5000 ×*g* for 10 minutes. Genomic DNA purification was performed using a DNeasy Blood & Tissue Kit (Qiagen) following the instructions (including instructions for pre-treatment of Gram-negative bacteria).

2.3.3. Restriction enzyme digests

Restriction enzyme digests were performed in 50 µl reactions using recommended protocols from New England Biolabs (NEB). Typically, for double digests, up to 1 µg DNA was digested with 2.5 µl of each restriction enzyme in the recommended buffer in a total volume of 50 µl overnight at 37 °C.

2.3.4. DNA ligation

Ligation reactions were performed using T4 DNA ligase following a recommended protocol from NEB. Briefly, 10 µl ligation reactions took place for 30 minutes at room temperature at vector/insert ratios of 1:3, 1:1 or 3:1.

2.3.5. Preparation of chemical transformation competent cells

NEB5α, BL21(DE3) or TNE012 *E. coli* were grown to an $OD_{600\ nm}$ of 0.3 in LB at 37 °C. Cultures were pelleted at 3000 ×*g* for 15 minutes at 4 °C and were re-suspended in 20 ml ice-cold 20 mM Tris-HCl pH 8.0, 50 mM $CaCl_2$. Cells were incubated on ice for 2 hours. Cells were then pelleted as described before and were re-suspended in ice-cold 20 mM Tris-HCl pH 8.0, 50 mM $CaCl_2$, 20% (v/v) glycerol. Competent cells were stored at -80 °C in 100 µl aliquots.

2.3.6. Bacterial chemical transformation

Transformation competent NEB5α, BL21(DE3) or TNE012 *E. coli* were thawed on ice for 30 minutes. Cells were incubated with 100 ng plasmid DNA for 30 minutes on ice and were then heat shocked at 42 °C for 60 seconds. After 2-3 minutes recovery on ice, cells were outgrown in SOC medium (2% (w/v) tryptone, 0.5% (w/v) yeast extract, 10 mM NaCl, 2.5 mM KCl, 10 mM $MgCl_2$, 10 mM $MgSO_4$, 0.2% (w/v) glucose) for 1 hour at 37 °C. Cells were plated onto LB-agar plates containing the appropriate

antibiotic/s for selection (see Table 2-7 for typical antibiotic concentrations used). Plates were incubated overnight at 37 °C.

Table 2-7. Antibiotics used in this study and working concentration

Antibiotic	Working concentration
Ampicillin (Amp)	100 µg/ml
Kanamycin (Kan)	50 µg/ml
Chloramphenicol (Cm)	37 µg/ml

2.3.7. DNA gel electrophoresis

DNA gel electrophoresis apparatus was assembled as described in the manufacturer's instructions. A 1% (w/v) agarose gel in Tris-borate-EDTA (TBE) buffer with 1x SybrSafe dye was made up and left to set. Samples were made up in a 5:1 ratio with 6x DNA loading buffer (30% (v/v) glycerol, 6 mM EDTA, 0.4% (w/v) bromophenol blue). Samples were loaded in 12 µl aliquots with a 1 kb DNA ladder. Electrophoresis was carried out at a constant voltage of 80 V.

2.3.8. Purification of plasmid DNA

After growing at 37 °C in LB overnight, cells were harvested through centrifugation at 6800 ×*g* for 5 minutes at 18 °C. Miniprep plasmid purification was performed using a QIAprep Spin Miniprep Kit (Qiagen) following the instructions. The kit produced 50 µl plasmid DNA with concentrations ranging between 100-300 ng/µl and $A_{260\ nm}/A_{280\ nm}$ values between 1.9 and 2.0. Plasmid DNA was sequenced by SourceBioscience or GENEWIZ using appropriate primers. Larger stocks of plasmid DNA were produced using a QIAGEN Plasmid Plus Midi Kit (Qiagen) with typical yields of 200 µl at 300-500 ng/µl and $A_{260\ nm}/A_{280\ nm}$ values between 1.9 and 2.0. Plasmids were stored at -20 °C.

2.4. Sodium dodecyl sulphate polyacrylamide gel electrophoresis (SDS-PAGE)

SDS-PAGE apparatus was assembled as described in the manufacturer's handbook. Tris-buffered gels ranging from 7.5-15% (w/v) acrylamide were made up and left to set (7.5-15% (w/v) acrylamide (37.5:1 acrylamide/bis-acrylamide), 250 mM Tris-HCl pH 8.8, 0.1% (w/v) SDS, 0.08% (w/v) APS, 0.1% (v/v) TEMED). Precast Novex™ 4-20% Tris-Glycine Mini Gels (ThermoFisher Scientific) were used for electrophoretic separation of crosslinked adducts. All gels were run in Tris-glycine buffer (25 mM Tris, 192 mM glycine, 0.1% SDS). Samples for SDS-PAGE were made up in a 3:1 ratio with 4x loading buffer (200 mM Tris-HCl pH 6.8, 8% (w/v) SDS, 0.4% (w/v) bromophenol blue, 40% (w/v) glycerol, 10% (v/v) β-mercaptoethanol) and were boiled for 5 minutes. Samples were loaded in appropriate volumes along with protein size markers. Electrophoresis was typically carried out at constant current of 30 mA per gel, except for precast gels which were run at constant 225 V. Gels were stained with 10% (w/v) acetic acid, 50% (v/v) ethanol, 0.2% (w/v) Coomassie Blue R-250 for 20 minutes and de-stained in 10% (w/v) acetic acid, 10% (v/v) ethanol.

2.5. Protein expression and purification

2.5.1. Expression and purification of pyoS2 and derivatives

PyoS2 complexed with His-tagged immunity protein S2 (ImS2) was expressed in BL21(DE3) cells grown in sterile LB media at 37 °C. Expression was induced at an $OD_{600\ nm}$ of 0.75 with the addition of 1 mM isopropyl-β-D-1-thiogalactopyranoside (IPTG) for 3 hours. Cells were re-suspended in binding buffer (20 mM Tris-HCl pH 7.5, 500 mM NaCl, 5 mM imidazole) and 1 mM phenylmethylsulphonyl fluoride (PMSF) was added. Cells were lysed through sonication on ice at 70% maximum amplitude, 3 seconds on, 7 seconds off and for a total process time of 90 seconds using a MISONIX S-4000

ultrasonic liquid processor fitted with a 3/8 inch stud probe. Cell debris was removed by centrifugation at 12,500 ×*g* for 20 minutes at 4 °C followed by filtration through a 0.45 µm syringe driven filter unit (Millipore). The cleared lysate was loaded onto a 5 ml HisTrap FF column (GE Healthcare) pre-equilibrated in binding buffer and protein was eluted in a linear gradient of 5-250 mM imidazole. Fractions containing protein as judged by SDS-PAGE were pooled and 1 mM EDTA was added to chelate any Ni^{2+} leached off the column. Protein was dialysed against 25 mM Tris-HCl pH 8.0, 150 mM NaCl at 4 °C and was further purified by size exclusion chromatography (SEC) using a HiLoad Superdex 200 26/600 column (GE Healthcare) equilibrated in the dialysis buffer.

2.5.2. Expression and purification of FpvAI

E. coli TNE012 cells (*ompA*$^{-}$, *ompB*$^{-}$, *tsx*$^{-}$) originally provided by the Cramer lab (Taylor *et al.*, 1998) were transformed with the pNGH183 plasmid carrying the *fpvAI* gene from *P. aeruginosa* with an *E. coli ompF* signal sequence cloned into *Nco*I/*Sac*I sites. Cultures were grown at 37 °C to an $OD_{600\ nm}$ of 1.0 and expression was induced by addition of 0.15% (w/v) L-arabinose. Protein was expressed at 20 °C overnight (~16 hours). Cells were lysed by sonication, as described previously, in 10 mM Tris-HCl pH 8.0, 0.25% (w/v) lithium diiodosalicyclic acid (LIS), 1 mM PMSF and debris was removed by centrifugation at 10,000 ×*g* for 15 minutes at 4 °C. The total membrane fraction was isolated by ultracentrifugation of the cleared lysate at 200,000 ×*g* for 45 minutes at 4 °C. IM proteins were extracted in 10 mM Tris-HCl pH 8.0, 0.25% (w/v) LIS, 2% (v/v) Triton X-100. The remaining OM pellet was washed in 10 mM Tris-HCl pH 8.0 to reduce Triton X-100 carryover. OMPs were extracted in 10 mM Tris-HCl pH 8.0, 5 mM EDTA, 2% (w/v) n-octyl-β-D-glucopyranoside (β-OG). Solubilised OMPs were isolated from remaining insoluble material by ultracentrifugation at 200,000 ×*g*.

FpvAI was purified from the heterogeneous OM fraction by three chromatographic steps. First, the OM fraction was loaded onto a column containing diethylaminoethane (DEAE) Sepharose CL-6B resin (GE Healthcare) equilibrated in 50 mM Tris-HCl pH 7.5, 5 mM EDTA, 0.56% (w/v) β-OG and proteins were eluted on a linear gradient of 0-500 mM LiCl. Next, fractions containing FpvAI were pooled and purified on a HiPrep Sephacryl S-300 16/60 SEC column (GE Healthcare) equilibrated in 50 mM Tris-HCl pH 7.5, 5 mM EDTA, 1% (w/v) β-OG. Finally, relevant fractions were pooled and loaded onto a Mono Q 4.6/100 PE column (GE Healthcare) equilibrated in 50 mM Tris-HCl pH 7.5, 5 mM EDTA, 1% (w/v) β-OG. Protein was eluted over a linear gradient of 0-500 mM LiCl. Purified FpvAI was stored at -20 °C. Prior to use, FpvAI was buffer exchanged into an appropriate buffer on a 5 ml HiTrap desalting column (GE Healthcare).

2.5.3. Purification of FpvAI-pyoS2^{NTD} complex for crystallisation

His-tagged pyoS2^{NTD} was first immobilised onto a 5 ml EDTA-resistant cOmplete™ His-Tag purification column (Roche) equilibrated in 20 mM Tris-HCl pH 7.5, 500 mM NaCl, 5 mM imidazole, 1% (w/v) β-OG. The OM extract containing FpvAI (as described above) was subsequently loaded onto the column where it would bind to immobilised pyoS2^{NTD}. Non-binding proteins were washed away in 10 column volumes of buffer and the complex was eluted in a linear gradient of 5-250 mM imidazole. The complex was further purified on a HiLoad Superdex 200 16/600 column (GE Healthcare) equilibrated in 25 mM Tris-HCl pH 7.5, 150 mM NaCl, 1% (w/v) β-OG. Protein was concentrated to ~20 mg/ml using Vivaspin 4 centrifugal concentrators with a molecular weight cut-off (MWCO) of 50kDa. Finally, the complex was dialysed against 10 mM Tris-HCl pH 7.0, 1% (v/v) n-octylpolyoxyethylene (n-OPOE) overnight at room temperature using MWCO 20kDa microdialysis cartridges (Pierce).

2.5.4. Expression and purification of pyoS2^{NTD}GFP*p*Bpa variants

The non-natural amino acid crosslinker para-Benzoyl-L-phenylalanine (*p*Bpa) was incorporated into pyoS2^{NTD}GFP by Amber suppression. Firstly, Amber (TAG) stop codons were introduced into the desired positions within the pPW44 plasmid by site directed mutagenesis. Each plasmid variant was then co-transformed into BL21(DE3) cells along with the pEVOL plasmid (Chin *et al.*, 2002) carrying the *p*Bpa-tRNA synthetase/tRNA^{pBpa} pair. Transformed cells were cultured in LB containing 0.2 mM *p*Bpa, (purchased from Bachem as H-p-Bz-Phe-OH), to an $OD_{600\ nm}$ of ~0.6 at 37 °C. PyoS2^{NTD}GFP*p*Bpa variants were expressed with 1 mM IPTG and expression of the *p*Bpa-tRNA synthetase/tRNA^{pBpa} pair was induced with 0.15% (w/v) L-arabinose. After 4 hours expression, cells were harvested, lysed by sonication and the lysate was loaded on a 1 ml HisTrap HP column (GE Healthcare) equilibrated in 20 mM Tris-HCl pH 8.0, 500 mM NaCl, 5 mM imidazole. Protein was eluted in a linear gradient of 5-250 mM imidazole and was dialysed against 50 mM Tris-HCl pH 8.0, 300 mM NaCl.

2.5.5. Protein quantification

For most proteins, concentration was determined by absorbance at 280 nm using an Eppendorf Biophotometer with a 10 mm pathlength. The concentration of pyoS2^{NTD}GFP and its *p*Bpa variants was determined by the GFP absorbance maximum at 488 nm and the extinction co-efficient of 55,000 $M^{-1}cm^{-1}$. The molecular weight and molar extinction co-efficient for proteins, determined using the ExPASy ProtParam Tool, are listed in Table 2-8. Denaturing electrospray ionisation mass spectrometry (ESI-MS), used to confirm protein masses, was performed by Dr. David Staunton, Biophysics Facility, Department of Biochemistry, University of Oxford.

Table 2-8. Protein molecular weight and molar extinction coefficients used in this study. Calculated using the ExPASy ProtParam Tool. Masses exclude initiator methionine. See Appendix for protein sequences.

Protein	Molecular weight (Da)	Molar extinction coefficient ($M^{-1}cm^{-1}$)
FpvAI*	86540.5	167540
PyoS2-ImS2‡	84677.9	77240
Δ1-21pyoS2-ImS2‡	82608.6	75750
Δ1-30pyoS2-ImS2‡	81538.4	74260
Δ1-45pyoS2-ImS2‡	80069.7	72770
$PyoS2^{NTD}$‡	24116.0	16390
Δ1-21$pyoS2^{NTD}$‡	22046.8	14900
Δ1-30$pyoS2^{NTD}$‡	20976.5	13410
Δ1-45$pyoS2^{NTD}$‡	19507.9	11920
TonB1(109-342)†	25570.5	6990
PyoS2-E2‡	85697.8	68760
$PyoS2^{NTD}$-S5‡	45658.8	30370
$PyoS2^{NTD}$-Ia‡	43110.0	40340

* Signal sequence cleaved
‡ Plus expression tag LEHHHHHH
† Includes cleaved TEV site artefact and linker GAM

2.6. Pyocin cytotoxicity assays

PyoS2 cytotoxic activity was assayed by plate-based growth inhibition assays. Typically, a 10 ml culture of *P. aeruginosa* was grown at 37 °C to an $OD_{600\ nm}$ of 0.6. Bacterial lawns were prepared by addition of 200 µl culture to 5 ml of molten soft LB-agar (0.75% (w/v) agar in LB) at 42 °C and were poured over LB-agar plates. Once set and dry, 2 µl of 3-fold serially diluted wild-type or variant pyoS2, ranging from 10 µM to ~57 pM, was applied to the lawn. Lawns were allowed to grow overnight at 37 °C and cytotoxicity was determined by observation of clearance zones.

2.7. Native electrospray ionisation mass spectrometry (ESI-MS)

Protein complexes were isolated using a Superdex 200 10/300 GL column (GE Healthcare) equilibrated in 200 mM ammonium acetate, 1% (w/v) β-OG. When necessary, protein was concentrated using Vivaspin 2 centrifugal concentrations with

50 kDa MWCO membranes (Sartorius Stedim Biotech). Samples were further desalted using Bio-Spin 6 columns (BioRad) and loaded into gold-coated nano-spray capillaries for ESI-MS analysis on a hybrid quadrupole time-of-flight mass spectrometer. Native ESI-MS data acquisition and analysis was performed by Dr Jonathan Hopper in the laboratory of Professor Carol V. Robinson, Department of Chemistry, University of Oxford.

2.8. Limited trypsin proteolysis and peptide mass fingerprinting

A total of 1 mg pyoS2-FpvAI complex (1:1 molar ratio) in 25 mM Tris-HCl pH 8.0, 150 mM NaCl, 1% (w/v) β-OG was digested with 1 µg Sequencing Grade Modified Trypsin (Promega) at room temperature overnight. Digestion was stopped with 1 mM PMSF, and fragments were co-purified with FpvAI on a Superdex 200 10/300 GL column (GE Healthcare). Fragments were resolved by SDS-PAGE and bands were excised for in-gel trypsin digestion and peptide mass fingerprinting. Gel slices were dehydrated in acetonitrile and were reduced with Tris(2-carboxyethyl)phosphine (TCEP). Reactive cysteine residues were irreversible alkylated with chloroacetamide. Gel slices were washed in 100% acetonitrile and dried. Protein was digested to completion with 5 µg Sequencing Grade Modified Trypsin (Promega) at 37 °C overnight. Peptides were loaded onto a reverse-phase C18 column and injected into an ESI-TRAP mass spectrometer. MS data acquisition was conducted by Dr Svenja Hester at the Central Proteomics Facility, Department of Biochemistry, University of Oxford. Peptide masses were compared to a *P. aeruginosa* trypsin digest database on the Mascot server.

2.9. Binding assays

2.9.1. Analytical size exclusion chromatography (SEC)

PyoS2^{NTD} was added to a stoichiometric complex of FpvAI and Fe-Pvd (Sigma) in 25 mM Tris-HCl pH 8.0, 150 mM NaCl, 1% (w/v) β-OG and was incubated at room temperature for 6 hours. The mixture was separated on a Superdex 200 10/300 GL column (GE Healthcare) equilibrated in the same reaction buffer monitoring for protein elution at $A_{280\ nm}$ and for Fe-Pvd elution at $A_{400\ nm}$.

2.9.2. Stopped-flow intrinsic tryptophan fluorescence spectroscopy

Fluorescence spectroscopy was performed using a Jobin Yvon Fluoromax 4 (Horiba) fluorimeter. An intrinsic tryptophan fluorescence spectrum was acquired for 1 µM FpvAI in 25 mM Tris-HCl pH 7.5, 150 mM NaCl, 1% (w/v) β-OG and was compared to that of 1 µM FpvAI-pyoS2^{NTD} complex. Excitation wavelength was set to 295 nm and emitted fluorescence was collected between 310-450 nm using 1.6 nm slit widths.

The kinetics of complex association were measured using an Applied Photophysics SX20 stopped-flow spectrofluorimeter in 1:1 mixing mode with the excitation monochromator set to 295 nm. A WG320 long-pass cut-off filter was fitted between the reaction cell and the emission photomultiplier to collect total fluorescence emission >320 nm. Experiments were performed in 25 mM Tris-HCl pH 7.5, 150 mM NaCl, 1% (w/v) β-OG at 25 °C. In pseudo first-order conditions, 0.2 µM FpvAI was present in one syringe with pyoS2^{NTD} in the second syringe spanning a concentration range from 1-40 µM. Kinetic data were fitted to a double exponential rate equation (Equation 1),

$$F_t = \Delta F_1 e^{-k_{obs1}t} + \Delta F_2 e^{-k_{obs2}t} + F_e \qquad \text{(Equation 1)}$$

where F_t is fluorescence at time t, ΔF_1 and ΔF_2 are the fluorescence amplitudes for steps 1 and 2 respectively, k_{obs1} and k_{obs2} are the observed pseudo first-order rate constants for steps 1 and 2 respectively, F_e is the end-point fluorescence and t is time. The concentration dependence of k_{obs1} from Equation 1 was fitted to a hyperbola described in Equation 2. This hyperbolic relationship is indicative of conformational changes occurring after complex formation as in Scheme 1 (Blackburn *et al.*, 1977). The double reciprocal and rearrangement of Equation 2 describes a linear relationship (Equation 3) which was further simplified to determine kinetic parameters K_{d1} and k_2 (Equation 4).

$$[A] + [B] \underset{k_{-1}}{\overset{k_1}{\rightleftharpoons}} [AB] \underset{k_{-2}}{\overset{k_2}{\rightleftharpoons}} [AB^*] \qquad \text{(Scheme 1)}$$

$$k_{obs1} = \frac{k_1[B]k_2}{k_1[B] + k_{-1}} \qquad \text{(Equation 2)}$$

$$\frac{1}{k_{obs1}} = \left(\frac{k_{-1}}{k_1 k_2}\right)\frac{1}{[B]} + \frac{1}{k_2} \qquad \text{(Equation 3)}$$

$$\frac{1}{k_{obs1}} = \left(\frac{K_{d1}}{k_2}\right)\frac{1}{[B]} + \frac{1}{k_2} \qquad \text{(Equation 4)}$$

In second-order experiments, FpvAI and pyoS2^{NTD} were present in individual syringes at 1 µM. Kinetic data were fitted to a second-order rate equation (Equation 5),

$$F_t = F_0 + \frac{\Delta F[E]_0{}^2 kt}{1 + [E]_0 kt} \qquad \text{(Equation 5)}$$

where F_t is fluorescence at time t, F_0 is fluorescence at t=0, ΔF is the fluorescence amplitude divided by the protein concentration, $[E]_0$ is the protein concentration at t=0, k is the bimolecular rate constant ($M^{-1}s^{-1}$) and t is time.

2.9.3. Isothermal titration calorimetry (ITC)

Proteins were prepared in 50 mM potassium phosphate pH 7.0, 1% (w/v) β-OG for FpvAI-pyoS2^{NTD} ITC experiments performed using a MicroCal iTC$_{200}$ thermostated at 25 °C. The cell contained FpvAI at 5 µM and the syringe contained Δ1-45pyoS2^{NTD} at 50 µM. Competition ITC experiments were performed with 10 µM FpvAI and 15 µM Δ1-45pyoS2^{NTD} in the cell, and 70 µM pyoS2^{NTD} in the syringe. TonB1-pyoS2^{NTD} binding experiments were performed using a MicroCal PEAQ-ITC, a more sensitive instrument for measuring binding with a small ΔH. Proteins were prepared in 50 mM potassium phosphate pH 7.0, 150 mM NaCl. The cell contained TonB1 at 15 µM and the syringe contained either pyoS2^{NTD} or Δ1-30pyoS2^{NTD} at 150 µM. In all ITC experiments, the first injection of 0.5 µl was followed by 19 injections of 2 µl with each injection spaced by 180 seconds. ITC data was presented as raw heats per injection in the top panel and integrated injection heats against molar ratio in the bottom panel. Binding isotherms were fitted with a single set of binding sites model or a competitive binding model using the manufacturer's software. ITC data can also be represented as saturable total heat content versus ligand concentration as described by Equation 6.

$$Q = \frac{nM_t\Delta HV_0}{2}\left[1 + \frac{X_t}{nM_t} + \frac{1}{nKM_t} - \sqrt{\left(1 + \frac{X_t}{nM_t} + \frac{1}{nKM_t}\right)^2 - \frac{4X_t}{nM_t}}\right] \quad \text{(Equation 6)}$$

where Q is the total heat content in the cell with volume V_0, M_t is the total protein concentration in the cell, X_t is the total injectant concentration, n is the number of binding sites, ΔH is the enthalpy change and K is the binding constant.

In competitive binding, proteins A and B both bind the same site on protein P (Scheme 2 and 3). The heat change upon injection of the competitor protein B is therefore proportional to the change in concentration of the two competing complexes PA and PB (Sigurskjold, 2000) (Equation 7).

$$[P] + [A] \rightleftharpoons [PA] \quad \text{(Scheme 2)}$$

$$[P] + [B] \rightleftharpoons [PB] \quad \text{(Scheme 3)}$$

$$\Delta Q = V_0(\Delta H_A \Delta[PA] + \Delta H_B \Delta[PB]) \quad \text{(Equation 7)}$$

Entropy change (ΔS) for competition ITC was calculated using Equations 8 and 9,

$$\Delta G = -RT \ln K_a \quad \text{(Equation 8)}$$

$$\Delta G = \Delta H - T\Delta S \quad \text{(Equation 9)}$$

where ΔG is the change in Gibbs free energy, R is the ideal gas constant (1.987 cal/mol/K), K_a is the bimolecular association constant, ΔH is the enthalpy change, ΔS is the entropy change and T is temperature.

2.10. Circular dichroism (CD) spectroscopy

Proteins were dialysed into 10 mM potassium phosphate pH 7.5 and were diluted to 0.1 mg/ml concentration. CD spectra were obtained using a Jasco J-815 Spectropolarimeter over a wavelength range of 260-190 nm, a digital integration time of 1 second and a 1 nm bandwidth. Protein melting temperatures (T_m) were determined by monitoring ellipticity at 222 nm as a function of temperature from 20 °C to 86 °C. CD data in millidegrees were converted to mean residue ellipticity by dividing by molar concentration and number of peptide bonds.

2.11. X-ray crystallography

2.11.1. Crystallisation

FpvAI-pyoS2^{NTD} complex at 8 mg/ml was crystallised by the sitting drop vapour diffusion method in 96-well MRC 2-drop plates (SWISSCI) at 18 °C. Drops consisted of 100 nl protein and 100 nl crystallisation solution dispensed using a Mosquito robot (TTP Labtech). Crystals of the complex were grown in 0.350 M ammonium sulphate, 13.5% (w/v) PEG3350, 0.050 M sodium acetate pH 4.0 and were harvested after 30 days. Crystals were cryo-protected in the crystallisation solution supplemented with 1% (v/v) n-OPOE and 25% (v/v) ethylene glycol before flash-cooling into liquid nitrogen.

2.11.2. X-ray diffraction data collection

X-ray data were collected at the European Synchrotron Radiation Facility (ESRF) on the microfocus (8x6 µm) beamline ID23-2 from a single cryo-cooled crystal (100 K) using a Si-111 monochromator and 225 mm MarMOSAIC CCD detector. X-ray wavelength was fixed at 0.873 Å. Diffraction data were collected for a total of 180° up to a resolution of

2.5 Å with a 0.1° oscillation using an exposure time of 0.02 seconds at 100% transmission.

2.11.3. Data processing, refinement and validation

X-ray diffraction data were indexed and integrated using XDS v0.52 (Kabsch, 2010) and scaled to 2.8 Å in Aimless (Evans and Murshudov, 2013) from the CCP4 v7.0 suite (Winn *et al.*, 2011). The structure was solved by molecular replacement using Phaser (McCoy *et al.*, 2007) and FpvAI as the search model (PDB ID 2W16, chain A (Greenwald *et al.*, 2009)). Crystallographic refinement was performed using Phenix v1.9 (Adams *et al.*, 2010) and Buster v2.10.2 (Bricogne G, 2010) and model building was carried out in Coot v0.8.7 (Emsley and Cowtan, 2004). MolProbity (Chen *et al.*, 2010) was used for structure validation and quality assessment. The atomic coordinates and structure factors for the pyoS2^{NTD}-FpvAI complex (PDB ID 5ODW) have been deposited in the Protein Data Bank

2.11.4. Structure analysis

Buried surface area and interface analysis was calculated using PISA v1.52 (Krissinel and Henrick, 2007). Molecular graphics programs Coot, PyMOL v1.3 (Delano, 2002) and UCSF Chimera (Pettersen *et al.*, 2004) were used for analysis of protein structures. Protein structure figures were made with PyMOL and UCSF Chimera.

2.12. Fluorescence microscopy

2.12.1. Conjugation of maleimide fluorophores to proteins

A C-terminal cysteine residue was introduced into the pyoS2^{NTD} and Δ1-21pyoS2^{NTD} constructs by site-directed mutagenesis. Disulphide bonded homodimeric species were first reduced for 2 hours at room temperature in the presence of 5 mM dithiothreitol (DTT). Protein was buffer exchanged into 20 mM potassium phosphate pH 7.0, 500 mM

NaCl to remove the DTT using a 5 ml HiTrap desalting column (GE Healthcare). Maleimide fluorophores made up as a 10 mM stock in DMSO were added to the reduced protein in a 5-fold molar excess. The labelling reaction was incubated at room temperature for 90 minutes in the dark and was mixed by gentle inversion. The reaction was quenched with 2 mM DTT and protein-fluorophore conjugates were dialysed against 2 litres of 20 mM potassium phosphate pH 7.0, 500 mM NaCl overnight at 4 °C using dialysis tubing of appropriate molecular weight cut off. Remaining fluorophore was removed using a HiLoad Superdex 200 16/600 prep grade column (GE Healthcare). The labelling efficiency (typically >90%) was estimated spectrophotometrically using fluorophore and protein extinction co-efficients (Alexa Fluor 488, ε_{max} = 71,000 $M^{-1}cm^{-1}$, and pyoS2^{NTD} $\varepsilon_{280\ nm}$ = 16,390 cm^{-1} M^{-1}), and correction factors for absorption at 280 nm by the fluorophore (Alexa Fluor 488, $A_{280\ nm} = 0.11 \times A_{488\ nm}$).

2.12.2. Fluorescence recovery after photobleaching (FRAP)

P. aeruginosa PAO1 cells were grown in M9-glucose media (6.78 g/L Na_2HPO_4, 3g/L KH_2PO_4, 0.5g/L NaCl, 10 mM D-glucose, 1 mg/ml NH_4Cl, 2 mM $MgSO_4$) at 37 °C. At an $OD_{600\ nm}$ of 0.6, 600 µl culture was pelleted through centrifugation at 7000 ×*g* for 3 minutes. Cells were re-suspended in 1 µM fluorophore-conjugated pyoS2 construct in M9-glucose and were incubated in the dark at room temperature for 15 minutes. Cells were washed extensively to remove free label by pelleting and re-suspending 3 times in M9-glucose. For CCCP experiments, cells were pre-treated with 100 µM CCCP for 10 minutes and remained present throughout the washes and in the agarose pad. For proteolysis experiments, labelled cells were incubated with 1:100 trypsin/protein at 30 °C for 1 hour, followed by extensive washing. After re-suspension into an appropriate volume typically 10-100 µl, 10 µl of the cell suspension was dispensed onto 1% (w/v) agarose pads in M9-glucose on a microscopy slide before sealing with a clean glass cover

slip. FRAP experiments were performed using a spinning disk confocal microscope (Ultra- VIEW VoX; PerkinElmer; mounted on an IX81 microscope [Olympus]) with a 100x oil-immersion objective (numerical aperture (NA) 1.4) and an electron-multiplying charge-coupled device camera (ImagEM; Hamamatsu Photonics). Images were acquired using the 488 nm laser at 10% power and bleaching was performed at 50% laser power at maximum speed. Recovery images were acquired over a time course up to 2 minutes. Brightfield images were recorded for each FRAP experiment.

2.13. Photo-activated crosslinking

2.13.1. *In vitro* crosslinking

Detergent-solubilised FpvAI was mixed with stoichiometric amounts of pyoS2^{NTD}GFP*p*Bpa variants in 25 mM Tris-HCl pH 7.5, 150 mM NaCl, 1% (w/v) β-OG in 100 µl 96-well plates. Samples were placed on ice and were UV-irradiated at 365 nm for 30 minutes in a CL-1000 Ultraviolet Crosslinker and were analysed by SDS-PAGE.

2.13.2. *In vivo* crosslinking

A 500 ml culture of *P. aeruginosa* PAO1 was grown for 24 hours at 30 °C in iron-free succinate medium (6.1 g/l K_2HPO_4, 3 g/l KH_2PO_4, 4.1 g/l succinic acid) supplemented with 7.5 mM $(NH_4)_2SO_4$, 1 mM $MgSO_4$ and 1x trace metal solution (Prepared as PTM4(Fe^-) described elsewhere (Greenwald *et al.*, 2008)). Cells were washed and re-suspended in 35 ml fresh medium, were incubated for 60 minutes in the presence of 100 nM pyoS2^{NTD}GFP*p*Bpa variants, and were UV irradiated at 365 nm for 30 minutes in a CL-1000 Ultraviolet Crosslinker. Cells were then re-suspended in 10 mM Tris-HCl pH 8.0, 0.25% (w/v) LIS, 2% (v/v) Triton X-100 and were lysed through sonication. The lysate was cleared by centrifugation at 5000 ×*g* for 10 minutes at 4 °C, and the OM

fraction was isolated by ultracentrifugation at 200,000 ×*g* for 45 minutes. The OM fraction was then solubilised in 10 mM Tris-HCl pH 8.0, 5 mM EDTA, 2% (w/v) β-OG. Extracted crosslinked complexes were incubated for 1 hour with EDTA-resistant cOmplete His-Tag purification resin (Roche). The resin was washed in 20 mM Tris-HCl pH 7.5, 500 mM NaCl, 5 mM imidazole, 1% (w/v) β-OG and crosslinks were eluted in 20 mM Tris-HCl pH 7.5, 500 mM NaCl, 500 mM imidazole, 1% (w/v) β-OG in spin columns (Pierce). Purified crosslinks were resolved by electrophoresis on 4-20% precast SDS-PAGE gels.

2.13.3. LC-MS/MS identification of crosslinks

Coomassie-stained crosslink bands were excised from the gel and were submitted to the Advanced Proteomics Facility, Department of Biochemistry at the University of Oxford, directed by Professor Shabaz Mohammed. The following section describes the LC-MS/MS pipeline. Gel slices containing crosslinked protein were prepared for LC-MS/MS by Svenja Hester and MS/MS data was acquired and analysed by Prof Shabaz Mohammed. Briefly, the gel slices were diced into 1 mm^3 cubes and dehydrated with acetonitrile. Thiols were reduced with TCEP and alkylated with chloroacetamide before overnight digestion with Sequencing Grade Modified Trypsin (Promega) at 37 °C. Peptides were separated using a C18 PepMap100 pre-column on an EASY-nLC (Marino *et al.*, 2014) 1000 UHPLC system (Proxeon) and were electrosprayed directly into a Q Exactive mass spectrometer (Thermo Fisher Scientific). Full scan MS spectra were acquired in the Orbitrap over a scan range of 350-2000 m/z and the 10 most intense peaks were selected for HCD fragmentation. HCD spectra were also acquired in the Orbitrap. MS data were converted into mgf format using pParse and searched using the pLink software (Yang *et al.*, 2012). The database contained the target proteins only (pyoS2^{NTD} and FpvAI) using search parameters as follows: maximum number of missed cleavages

= 2, fixed modification = carbamidomethyl-Cys, variable modification 1 = Oxidation-Met, variable modification 2 = Glu to pyro-Glu, mass shift of *p*Bpa = 0.00, mass accuracy filter = 20 ppm for precursor ions with consideration of the first 5 isotopic peaks, MS2 tolerance = 20 ppm. Data were initially filtered by *E*-value (E<1.0e-8). Crosslinks were further filtered/inspected with specific emphasis on fragmentation patterns.

Chapter 3. Biophysical characterisation of the FpvAI-pyoS2 complex

3.1. Introduction

Receptors for bacteriocins are the primary point of contact with the target cell and the first stage of their subsequent import. These cell surface complexes are in most cases high affinity, with dissociation constants in the nanomolar to picomolar range. For example, colicin E9 binds to BtuB with a K_d of 153 nM although this can be increased to 2.4 nM in the presence of calcium ions (Housden *et al.*, 2005). In *E. coli*, colicins are known to exploit OMPs, including the porins OmpF, OmpA and OmpW, the vitamin B_{12} receptor BtuB, and iron siderophore transporters FhuA, FepA and Cir (Papadakos *et al.*, 2012). By contrast, only a few of the S-type pyocins have known receptors; pyocins S2 and S4 both use FpvAI (Elfarash *et al.*, 2012), pyocin S3 uses FpvAII (Baysse *et al.*, 1999) and pyoS5 uses the ferripyochelin receptor FptA (Elfarash *et al.*, 2014). Many of these receptors function as nutrient transporters which bind and transport metal-chelating ligands such as iron-siderophore complexes. Bacteriocins must therefore compete with these ligands for binding. In *E. coli*, ferric enterobactin (Fe-Ent) bound to FepA cannot be displaced by colicin B and therefore protects against colicin B killing, although slow dissociation kinetics prevent Fe-Ent from displacing colicin B that is already in complex (Payne *et al.*, 1997). Competition with nutrient acquisition is also implicated with pyocin resistance in *P. aeruginosa*. Specifically, resistance to pyoS2 is enhanced by increased iron availability (Inglis *et al.*, 2016).

Research into the molecular mechanisms of pyocin function is still in its infancy. In particular, the processes of receptor-binding and cell entry, and the precise roles of individual domains are not fully defined. The first evidence that pyoS2 uses an iron

transporter was reported in 1980 after observing that killing sensitivity was highly dependent on iron concentration in the growth medium (Ohkawa *et al.*, 1980). The authors also identified a receptor candidate through the screening of resistance mutants, though the function of this protein was not known at the time. The link with FpvAI was not made until 1992 when Smith *et al* (1992) noticed that a resistant receptor-knockout strain exhibited a deficiency in Pvd biosynthesis and uptake. However, these observations were initially made with pyocin Sa which was eventually found to be identical to pyoS2 and that FpvAI was indeed the receptor for pyoS2 (Sa). More recently, FpvAI was found also to be the receptor for pyocin S4, a tRNase pyocin with an almost identical N-terminal domain to that of pyoS2 (Elfarash *et al.*, 2012), which supports the previous suggestion that the N-terminal domain is the receptor-binding domain (Michel-Briand and Baysse, 2002). Although the receptor is known, there have been no studies demonstrating an interaction between these proteins *in vitro*.

Bacteriocins are modular proteins with individual domains having distinct roles in the killing mechanism (Cascales *et al.*, 2007). As well as the receptor-binding domain, bacteriocins possess a translocation domain which facilitates import into the cell, and the cytotoxic domain which ultimately kills the cell by nuclease, pore-forming or PG hydrolase activity (Braun *et al.*, 2002). In contrast to colicins which have central receptor-binding domains, pyocins have an N-terminal receptor-binding domain and a central translocator domain, though the precise boundaries of these domains is not well understood (Figure 3-1). The role of the central domain in translocation was suggested due to sequence homology with the N-terminal translocation domain of colicins, although there is no experimental evidence to support this hypothesis (Michel-Briand and Baysse, 2002). For this reason, the central domain (domain III) of pyoS2 has been referred to as the translocation domain. A recent study identified a conserved DPY motif (D-X_4-FP-

X_8-Y) found solely in nuclease bacteriocins (Sharp *et al.*, 2017). This motif is present in pyoS2 at the C-terminal end of the translocation domain suggesting it may be responsible for directing translocation of the nuclease domain across the IM. The N-terminal domain of pyoS2 was shown to be the receptor-binding domain through competitive inhibition of the killing activity of pyocin S4, and like Fe-Pvd, the N-terminal domain of pyoS2 can activate the expression of Pvd biosynthesis genes via FpvAI-mediated signalling (Elfarash *et al.*, 2012). Domain II located between the receptor-binding and translocation domains is not present in all pyocins, though has been shown to bind the *P. aeruginosa* CPA as a means of cell surface targeting (McCaughey *et al.*, 2016a).

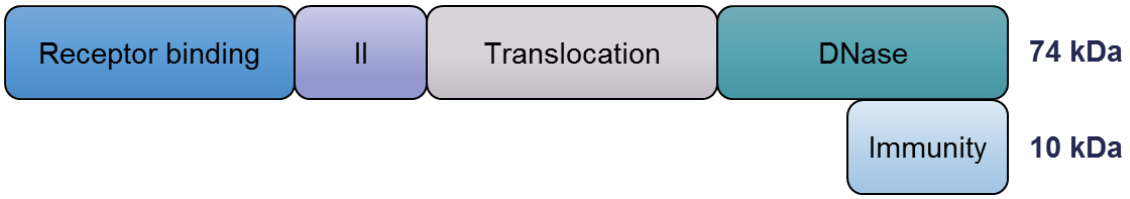

Figure 3-1. Domain architecture of pyoS2.
The N-terminal receptor-binding domain is followed by CPA-binding domain II and the disputed central translocation domain. The C-terminal DNase domain is bound by the pyoS2 immunity protein, ImS2. Approximate molecular weights for pyoS2 and ImS2 are shown.

The aims of this chapter were to produce recombinant pyoS2 and FpvAI and show for the first time that they form a complex *in vitro*. Next, to use limited proteolysis to define the precise domain boundary of the receptor binding domain for further structural and biophysical characterisation. This chapter also aimed to study competition between pyoS2 and Fe-Pvd for binding to FpvAI, specifically, whether both ligands bind at the same site and if so their relative affinities. The final aim was to determine the binding affinity (K_d) of the FpvAI-pyoS2 interaction and compare this with other bacteriocin-receptor complexes.

3.2. Results

3.2.1. Expression and purification of FpvAI and pyoS2

The *P. aeruginosa* iron transporter FpvAI was expressed in *E. coli* TNE012 cells from a pBAD-Myc-HisB vector under an arabinose-inducible promoter. To ensure FpvAI was recognised as an OMP and correctly directed to the OM, the wild-type signal sequence was replaced with that of *ompF* from *E. coli*. The optimal expression conditions were determined by varying the arabinose concentration, expression temperature and duration, and comparing protein levels in the OM fraction by SDS-PAGE (Figure 3-2). Overnight (16 hour) expression at 20 °C using 0.15% (w/v) arabinose was found to be the optimal condition and was used for subsequent large scale FpvAI preparations. FpvAI was purified from the *E. coli* OM fraction which was first isolated by EDTA and β-OG detergent extraction. Using a combination of anion exchange chromatography and SEC (see Materials and Methods 2.5.2), FpvAI was purified to homogeneity with typical yields ranging between 1-1.5 mg per litre of bacterial culture (Figure 3-3). The major contaminant OMPs during FpvAI purification were OmpF and the maltoporin LamB.

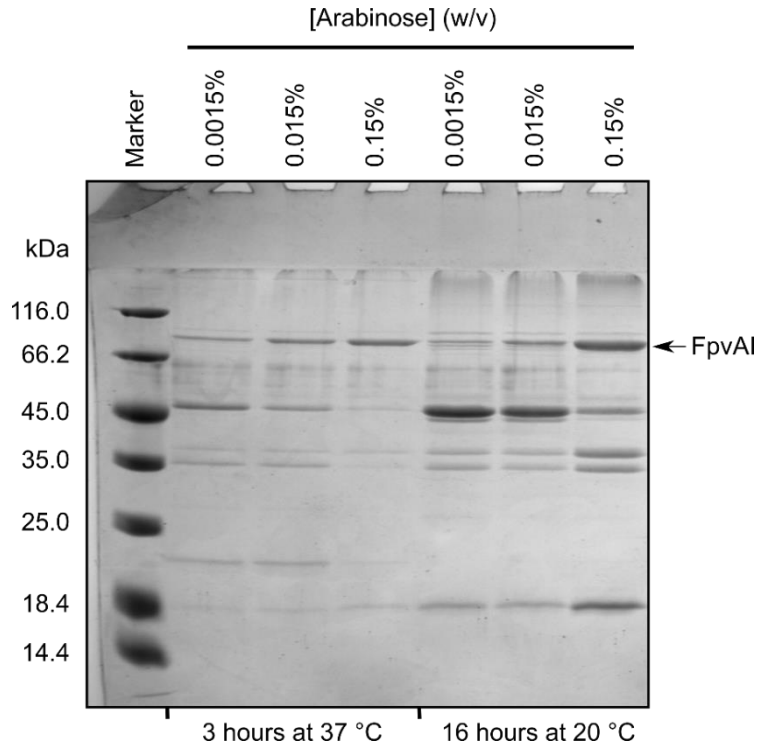

Figure 3-2. Optimisation of FpvAI expression in *E. coli* TNE012 cells.
Coomassie-stained SDS-PAGE gel loaded with 10 µl OM extract from different FpvAI expression conditions. Optimal expression conditions were 0.15% (w/v) L-arabinose induction for 16 hours at 20 °C.

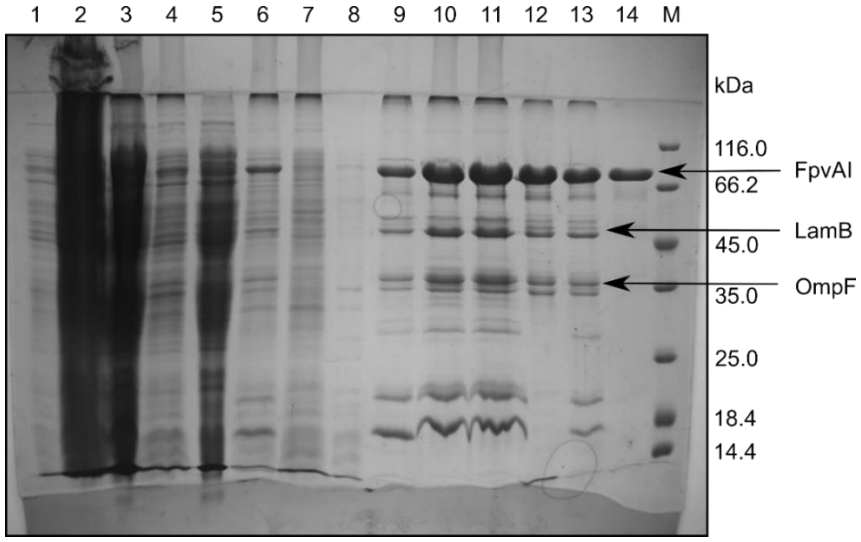

Figure 3-3. Purification of FpvAI from the *E. coli* OM.
Coomassie-stained 12% SDS-PAGE gel loaded with 5 µl sample from each stage of FpvAI purification. 1, Induced bacterial culture. 2, Total cell lysate. 3, First cell lysate supernatant. 4, Second cell lysate supernatant. 5, Soluble fraction. 6, Total membrane fraction. 7, IM extract. 8, Wash. 9, OM extract. 10, DEAE Sepharose eluate. 11, Sephacryl 300 load. 12, Sephacryl 300 eluate. 13, Mono Q load. 14, Mono Q eluate. M = Fermentas unstained protein standard. FpvAI can be clearly seen in the total membrane fraction and the OM extract. Contaminant OMPs, OmpF and LamB, are labelled. After Mono Q anion exchange chromatography FpvAI was highly pure.

PyoS2 was expressed in complex with its high-affinity inhibitor ImS2-His6 to circumvent lethality upon expression. The complex was expressed under IPTG induction from a pET21-a(+) vector in *E. coli* BL21(DE3) cells and was purified by Ni-affinity chromatography and SEC (Figure 3-4). The killing activity of purified pyoS2-ImS2 was assayed by observing clearance zones on plate-based toxicity tests where serial dilutions of toxin were spotted onto lawns of *P. aeruginosa*. The PAO1 strain is resistant to killing due to endogenous expression of ImS2, however, the clinical-isolate strain PA17, which lacks ImS2, is pyoS2-sensitive and was the strain of choice for activity tests (Figure 3-5). ImS2-mediated resistance in the PAO1 strain can be subverted by exchanging the cytotoxic domain with that of another nuclease bacteriocin. In this case, the pyoS2 DNase domain was swapped with the colicin E2 DNase (pyoS2-E2) where there is no cognate immunity protein in PAO1, which effectively sensitises cells to killing (Figure 3-6).

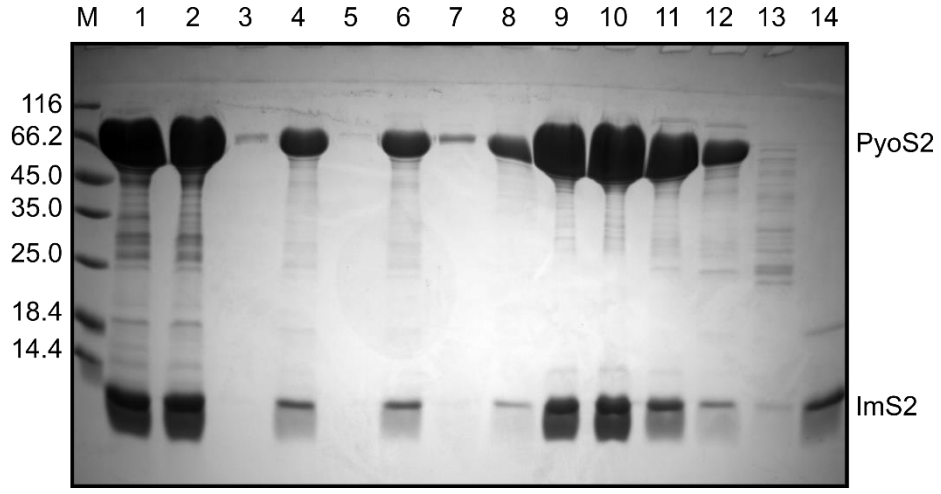

Figure 3-4. SEC purification of pyoS2-ImS2.
Coomassie-stained 15% SDS-PAGE gel loaded with 5 µl samples from Superdex 200 26/60 SEC purification of pyoS2-ImS2. 1, Total *E. coli* cell lysate. 2, Cleared lysate. 3, Flow-through from first protein concentration step. 4, Load 1. 5, Flow through from second protein concentration step. 6, Load 2. 7-14, Elution fractions from load 1. M = Fermentas unstained protein standard.

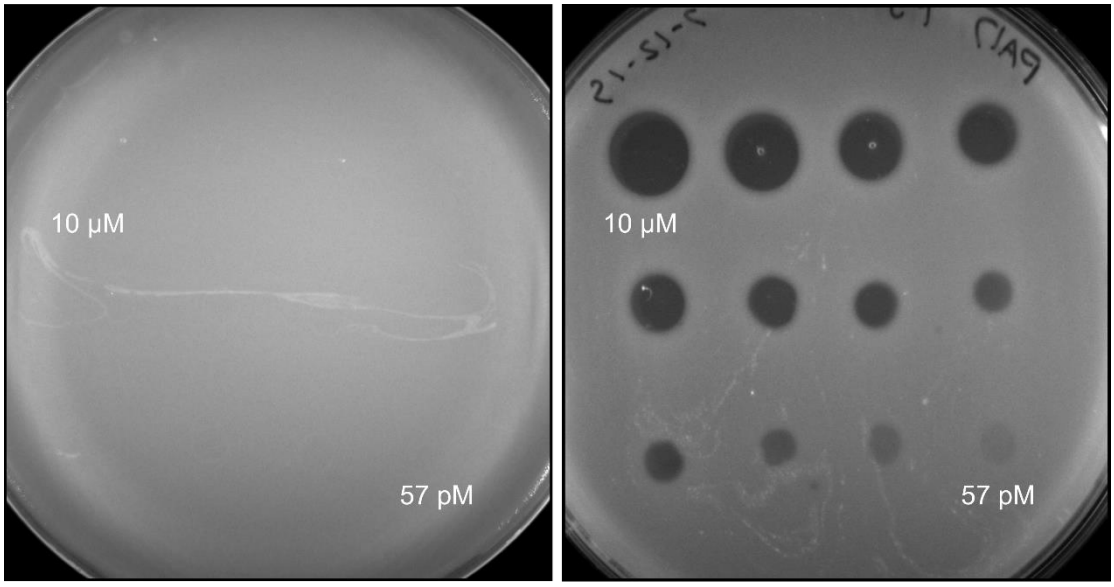

Figure 3-5. Activity of pyoS2 against *P. aeruginosa* PAO1 and PA17.
PyoS2 toxicity tests using *P. aeruginosa* PAO1 and PA17 cells grown in LB showing that PAO1 is resistant. Serial dilutions of pyoS2 were applied onto lawns of *P. aeruginosa* at concentrations ranging from 10 µM *(top left)* to 57 pM *(bottom right).* Zones of clearance indicate cell killing.

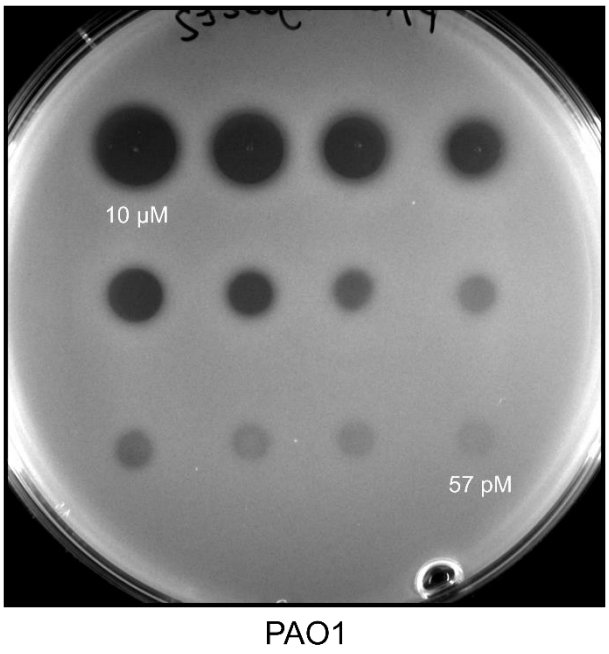

Figure 3-6. Activity of the pyoS2-E2 chimera against *P. aeruginosa* PAO1.
PyoS2-E2 toxicity tests using *P. aeruginosa* PAO1 grown in LB showing that resistance is subverted by replacing the DNase domain with the colicin E2 DNase domain to which there is no cognate immunity protein. Serial dilutions of pyoS2-E2 were applied onto lawns of *P. aeruginosa* PAO1 at concentrations ranging from 10 µM *(top left)* to 57 pM *(bottom right).* Zones of clearance indicate cell killing.

3.2.2. FpvAI and pyoS2 form a complex *in vitro*

Although FpvAI is known to be the receptor for pyoS2, a complex between these two proteins has not been demonstrated *in vitro*. Having purified both FpvAI and pyoS2-ImS2 in sufficient yield and purity, the ability of these proteins to form a complex was first investigated using analytical SEC (Figure 3-7). Individually, FpvAI and pyoS2-ImS2 elute at 1.49 ml and 1.46 ml, respectively, but when run together they elute as a single peak at 1.23 ml. The presence of both proteins in this peak, as seen by SDS-PAGE, demonstrates they form a complex. The shoulder on the complex peak is due to an excess of pyoS2-ImS2.

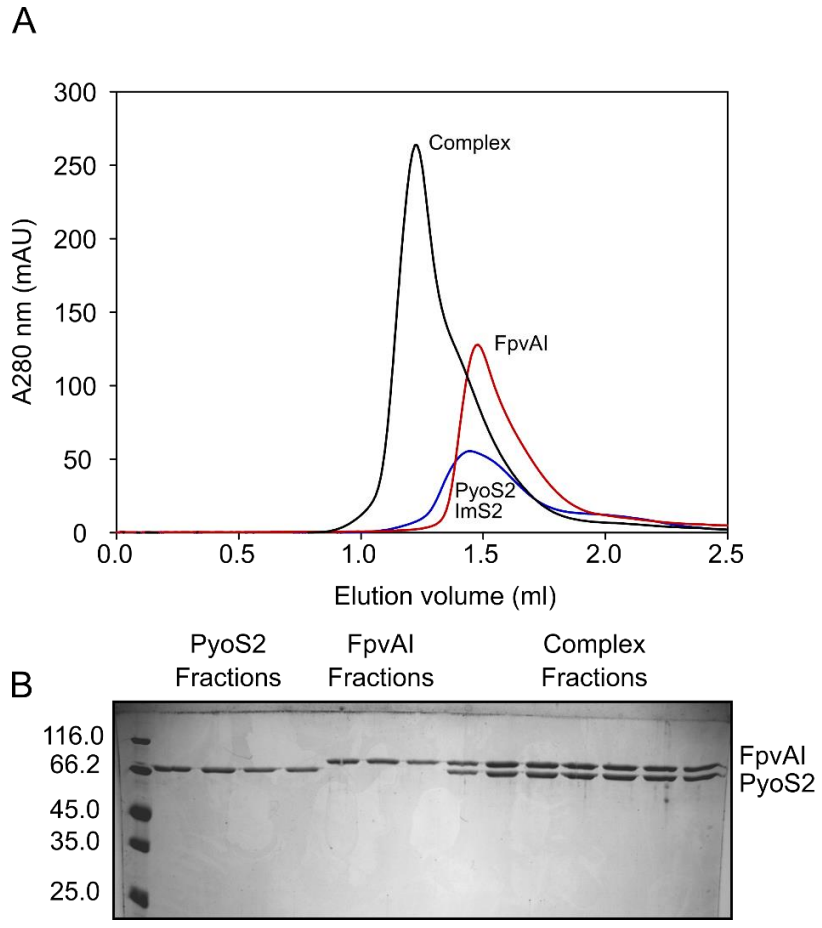

Figure 3-7. FpvAI and pyoS2-ImS2 form a complex *in vitro*.
A, Analytical SEC of FpvAI *(red)*, pyoS2-ImS2 *(blue)* and both *(black)* at 5 µM using a Superdex 200 3.2/30 PC column in 25 mM Tris-HCl pH 8.0, 150 mM NaCl, 1% (w/v) β-OG demonstrate they elute as a single complex. ***B,*** Coomassie-stained 12% SDS-PAGE gel loaded with 5 µl of the peak fractions confirm the presence of both FpvAI and pyoS2. ImS2 (~10 kDa) bands, obscured by the dye front, are not shown. M = Fermentas unstained protein standard.

3.2.3. Identification of the pyoS2 receptor-binding domain

Limited proteolysis of the FpvAI-pyoS2 complex was performed to determine the precise FpvAI-binding domain and to experimentally delineate the domain boundary. The digest pattern of the FpvAI-pyoS2-ImS2 complex was compared to that of pyoS2-ImS2 and FpvAI alone (Figure 3-8) since it was predicted that the FpvAI-binding domain would be partially protected from proteolysis when in complex. FpvAI was largely resistant to the action of trypsin whereas pyoS2 was digested into a number of smaller fragments after 300 minutes. Interestingly, a ~23 kDa proteolysis fragment unique to the complex was detected, highlighted in Figure 3-8, which likely represents the receptor-binding domain. This was later confirmed when this fragment co-eluted with FpvAI in SEC (Figure 3-9). The identity of the ~23kDa fragment was subsequently determined by LC-MS/MS. The sequence coverage of the peptides onto the pyoS2 amino acid sequence identified the receptor-binding domain as residues 2-209 (Figure 3-10) referred to as the pyoS2 N-terminal domain ($pyoS2^{NTD}$).

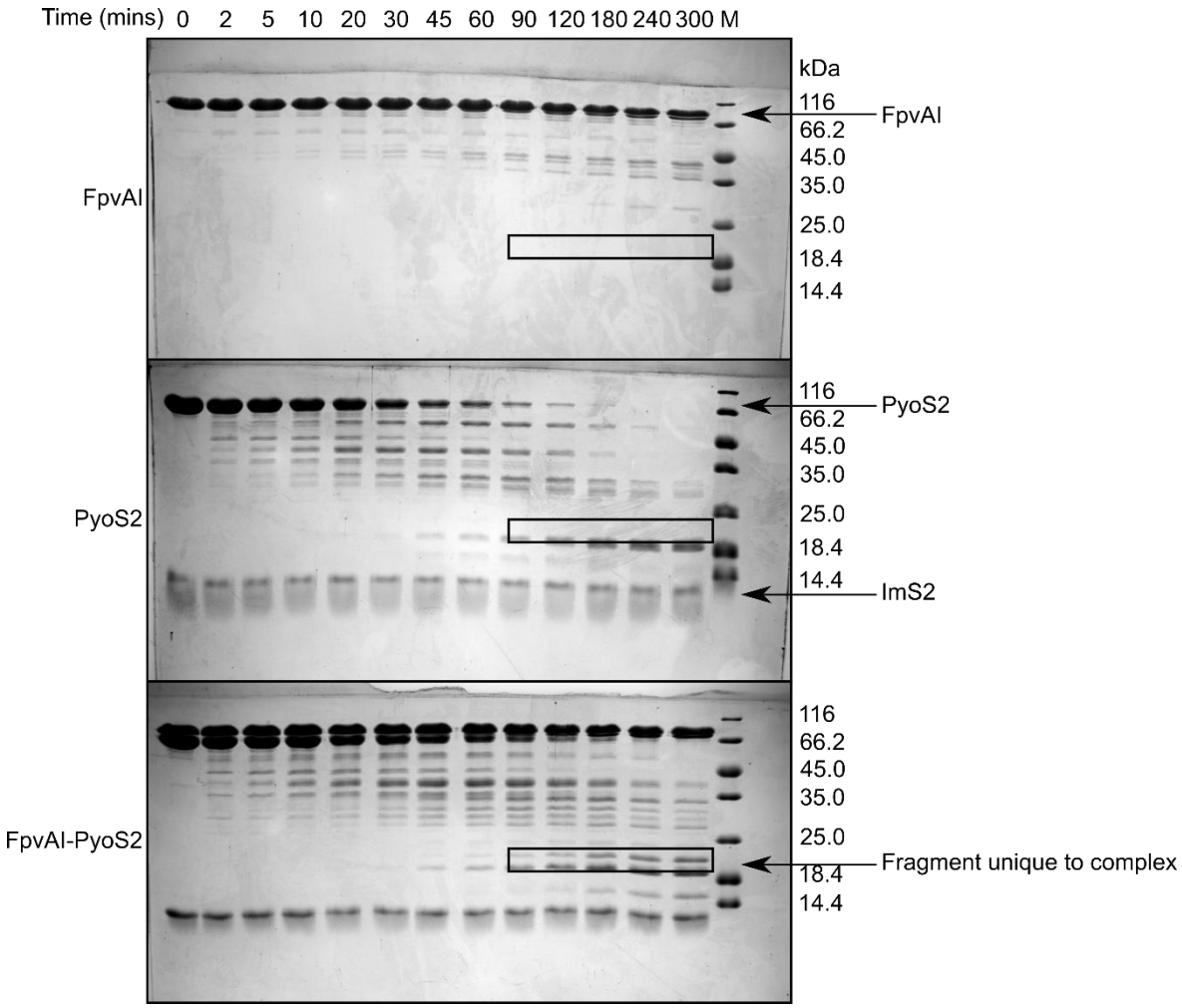

Figure 3-8. Limited trypsin proteolysis to identify the receptor-binding domain.
Digests of 6 µM FpvAI *(upper panel)*, 6 µM pyoS2-ImS2 *(middle panel)* and 6 µM FpvAI-pyoS2-ImS2 *(lower panel)* were monitored on 15% SDS-PAGE gels at time points up to 300 minutes at 30 °C. The reaction contained 1 µg trypsin per 1 mg of protein (1:1000). Wells were loaded with 5 µl sample. The digest fragment unqiue to the complex is highlighted. M = Fermentas unstained protein standard.

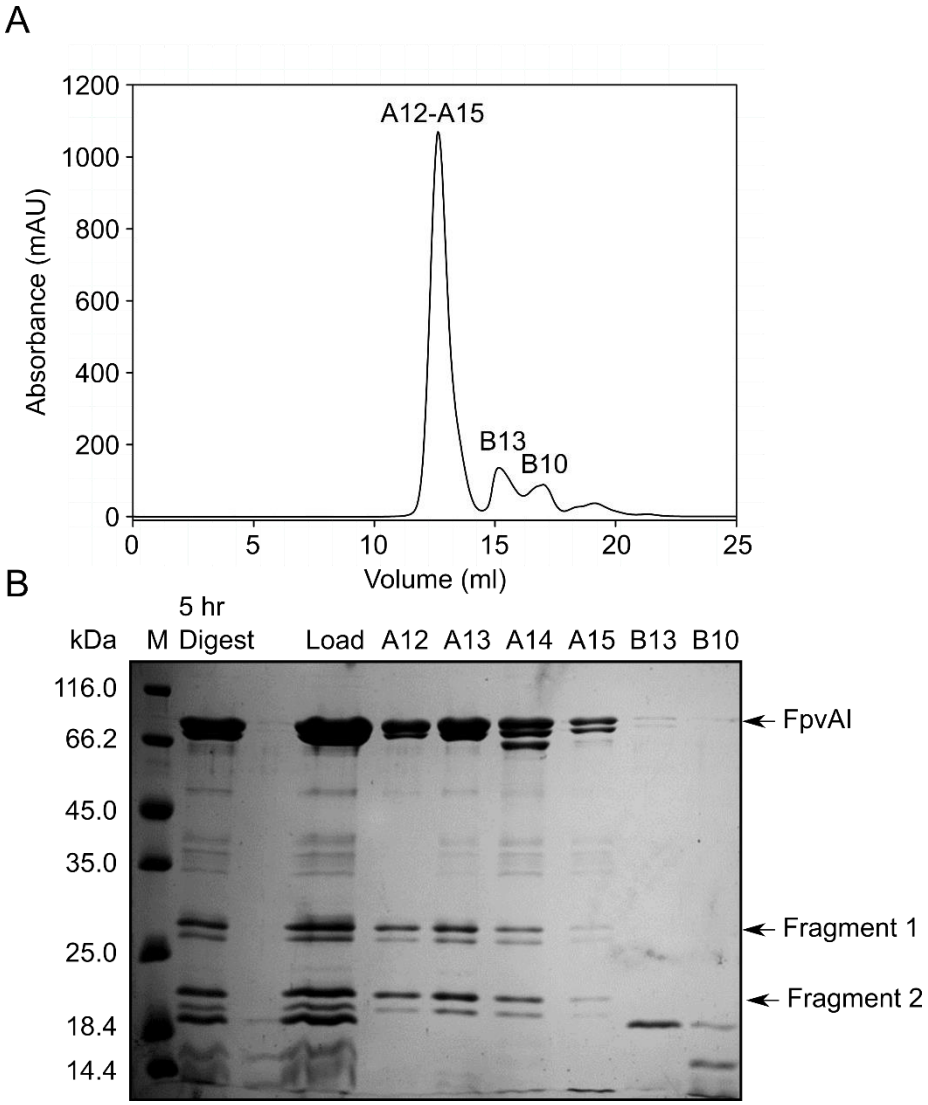

Figure 3-9. Co-elution of a pyoS2 proteolysis fragment with FpvAI.
A, Superdex 200 10/300 GL SEC elution profile of 6 µM FpvAI-pyoS2-ImS2 limited proteolysis stopped after 5 hours by addition of 1 mM PMSF. ***B***, 12% SDS-PAGE analysis of protein in major elution peaks shows fragments which co-elute with FpvAI. Wells were loaded with 10 µl sample. M = Fermentas unstained protein standard.

```
  1 MAVNDYEPGS MVITHVQGGG RDIIQYIPAR SSYGTPPFVP PGPSPYVGTG
 51 MQEYRKLRST LDKSHSELKK NLKNETLKEV DELKSEAGLP GKAVSANDIR
101 DEKSIVDALM DAKAKSLKAI EDRPANLYTA SDFPQKSESM YQSQLLASRK
151 FYGEFLDRHM SELAKAYSAD IYKAQIAILK QTSQELENKA RSLEAEAQRA
201 AAEVEADYKA RKANVEKKVQ SELDQAGNAL PQLTNPTPEQ WLERATQLVT
251 QAIANKKKLQ TANNALIAKA PNALEKQKAT YNADLLVDEI ASLQARLDKL
301 NAETARRKEI ARQAAIRAAN TYAMPANGSV VATAAGRGLI QVAQGAASLA
351 QAISDAIAVL GRVLASAPSV MAVGFASLTY SSRTAEQWQD QTPDSVRYAL
401 GMDAAKLGLP PSVNLNAVAK ASGTVDLPMR LTNEARGNTT TLSVVSTDGV
451 SVPKAVPVRM AAYNATTGLY EVTVPSTTAE APPLILTWTP ASPPGNQNPS
501 STTPVVPKPV PVYEGATLTP VKATPETYPG VITLPEDLII GFPADSGIKP
551 IYVMFRDPRD VPGAATGKGQ PVSGNWLGAA SQGEGAPIPS QIADKLRGKT
601 FKNWRDFREQ FWIAVANDPE LSKQFNPGSL AVMRDGGAPY VRESEQAGGR
651 IKIEIHHKVR IADGGGVYNM GNLVAVTPKR HIEIHKGGK
```

Figure 3-10. Identification of the minimal receptor-binding domain.
Sequence coverage encompassing residues 2-209 of pyoS2 (*red*) determined by LC-MS/MS analysis of the 23 kDa band labelled 'Fragment 2' in Figure 3-9. Tryptic peptides were mapped using the Mascot server. LC-MS/MS data acquisition was performed by Dr. Svenja Hester, Central Proteomics Facility, Department of Biochemistry, University of Oxford.

3.2.4. Characterisation of the pyoS2^{NTD}

His-tagged pyoS2^{NTD} (residues 2-209), expressed and purified in isolation was shown to be folded and α-helical in secondary structure by far-UV CD (Figure 3-11). The FpvAI binding capability of the domain was verified using analytical SEC, which once again demonstrated they form a complex (Figure 3-12). A stoichiometry of 1:1 was confirmed by native ESI-MS revealing two dominant species, the FpvAI-pyoS2^{NTD} complex, and gas-phase dissociated FpvAI (Figure 3-13). The observed masses of the two species were consistent with the calculated masses.

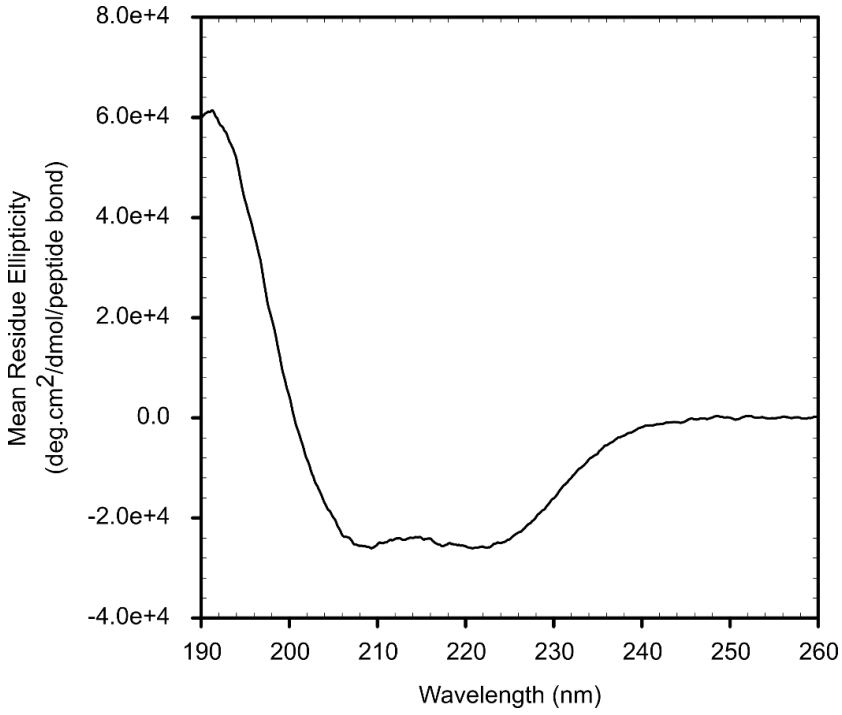

Figure 3-11. PyoS2^{NTD} is folded and α-helical.
Far-UV circular dichroism (CD) spectrum showing double minimal at 208 nm and 222 nm is characteristic of an α-helical secondary structure of pyoS2^{NTD}. CD was performed in 10 mM potassium phosphate pH 7.5 at 20 °C.

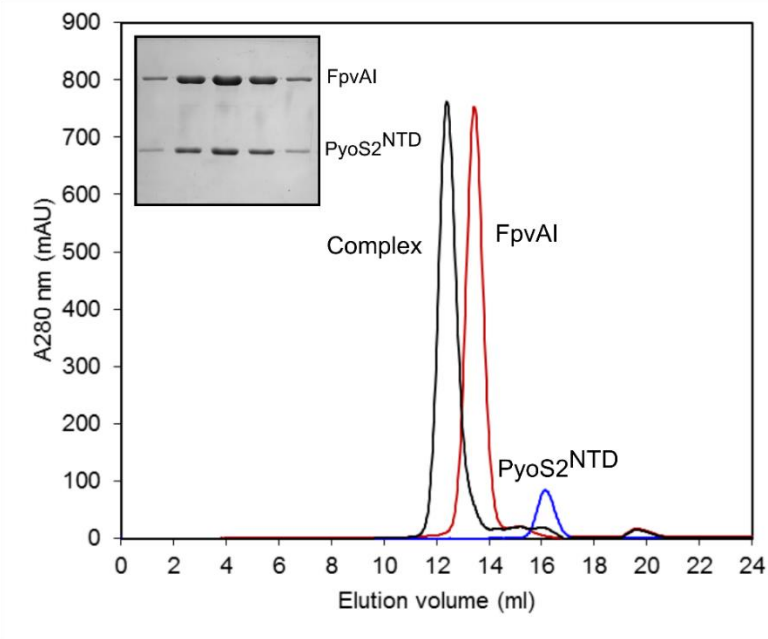

Figure 3-12. PyoS2^{NTD} binds FpvAI *in vitro*.
Analytical SEC of 9 µM FpvAI *(red)*, 9 µM pyoS2^{NTD} *(blue)* and 9 µM both *(black)* using a Superdex 200 10/300 GL column in 25 mM Tris-HCl pH 8.0, 150 mM NaCl, 1% (w/v) β-OG demonstrate that they elute as a single complex. ***Inset,*** coomassie-stained 12% SDS-PAGE gel loaded with 5 µl of the peak fractions confirm the presence of both FpvAI and pyoS2^{NTD}.

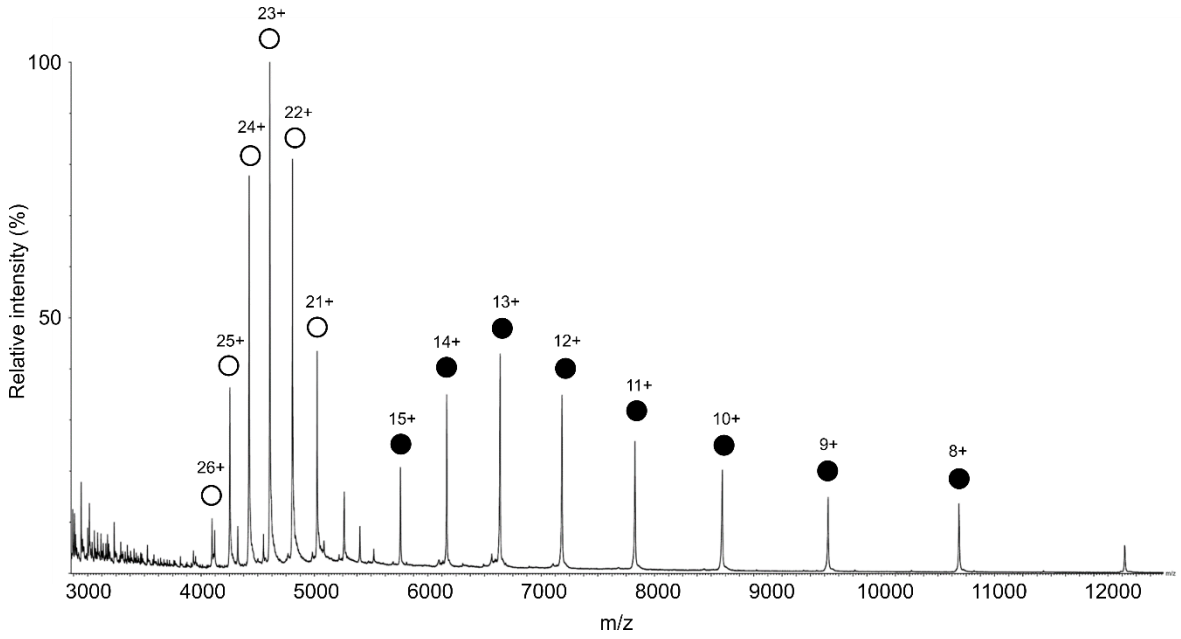

Figure 3-13. FpvAI-pyoS2^{NTD} form a 1:1 complex.
Native ESI-MS spectrum of the FpvAI-pyoS2^{NTD} complex at 8.7 µM in 200 mM ammonium acetate, 1% (w/v) β-OG. The spectrum reveals FpvAI in complex with pyoS2^{NTD} *(open circles)* and gas phase dissociated FpvAI *(solid circles)*. Expected and observed masses for FpvAI-pyoS2^{NTD} were 110,639 Da and 110,580 ± 81 Da, respectively. Native ESI-MS experiments were performed by Dr Jonathan Hopper, Department of Chemistry, University of Oxford.

Binding experiments using analytical SEC were performed to determine if binding of pyoS2^{NTD} competes with that of Fe-Pvd. The Fe-Pvd hydroxamate chromophore has an absorbance maximum (λ_{max}) at 400 nm, which was used to monitor its elution, whilst protein elution was monitored at 280 nm. In the absence of pyoS2^{NTD}, Fe-Pvd binds FpvAI and elutes as a complex (Figure 3-14A). However, after reaching equilibrium in the presence of a stoichiometric amount pyoS2^{NTD}, the majority of Fe-Pvd was competed away from FpvAI and the FpvAI-pyoS2^{NTD} complex was favoured (Figure 3-14B). This not only demonstrates that both pyoS2^{NTD} and Fe-Pvd exploit the same FpvAI binding site, but also pyoS2^{NTD} binds with higher affinity than the endogenous ligand Fe-Pvd.

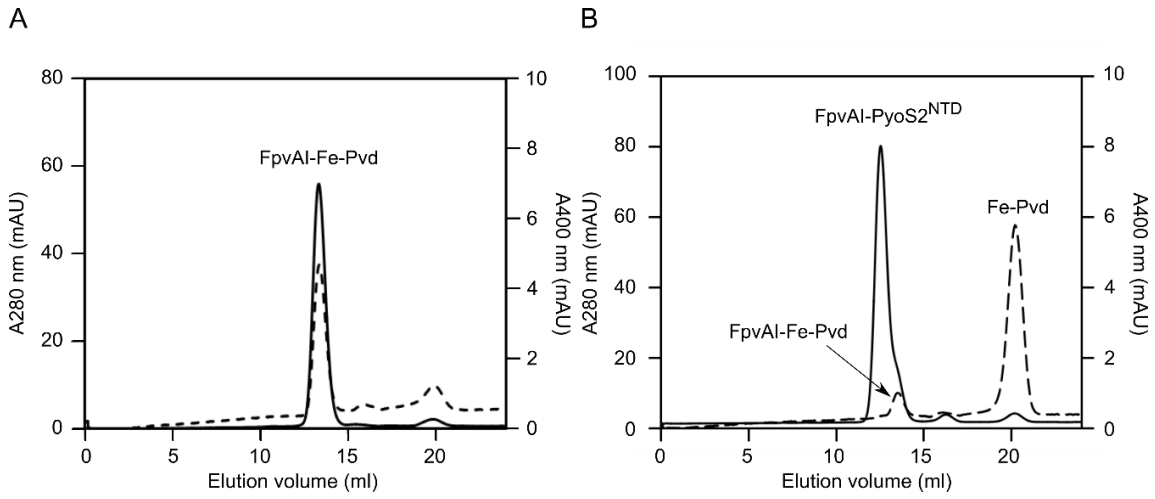

Figure 3-14. PyoS2^{NTD} outcompetes Fe-Pvd for FpvAI binding.
Analytical SEC using a Superdex 200 10/300 GL column in 25 mM Tris-HCl pH 8.0, 150 mM NaCl, 1% (w/v) β-OG monitored for protein elution at $A_{280\ nm}$ (*solid line*) and for Fe-Pvd elution at $A_{400\ nm}$ (*dashed line*). ***A***, 5 µM FpvAI and 5 µM Fe-Pvd co-elute as a complex *in vitro*. ***B,*** PyoS2^{NTD} at 5 µM displaces Fe-Pvd to favour the FpvAI-pyoS2^{NTD} complex.

3.2.5. Determination of the FpvAI-pyoS2^{NTD} dissociation constant (K_d)

Initially, a kinetic approach was used to determine the FpvAI-pyoS2^{NTD} K_d by measuring the bimolecular association (k_{on}) and dissociation (k_{off}) rate constants. Complex formation was monitored by intrinsic tryptophan fluorescence which was blue-shifted and partially quenched in the presence of pyoS2^{NTD} (Figure 3-15). The shift in λ_{max} decreased the total emitted fluorescence >320 nm by ~10% providing a measurable signal change by stopped-flow spectrofluorimetry (see Materials and Methods 2.9.2). The kinetics of complex formation were first investigated under pseudo first-order conditions where pyoS2^{NTD} is in excess of FpvAI (Figure 3-16). The data fitted poorly to a single exponential function but residuals were minimised when fitting to a double exponential. This implies that binding is a two-step process, likely involving formation of an encounter complex followed by structural rearrangements.

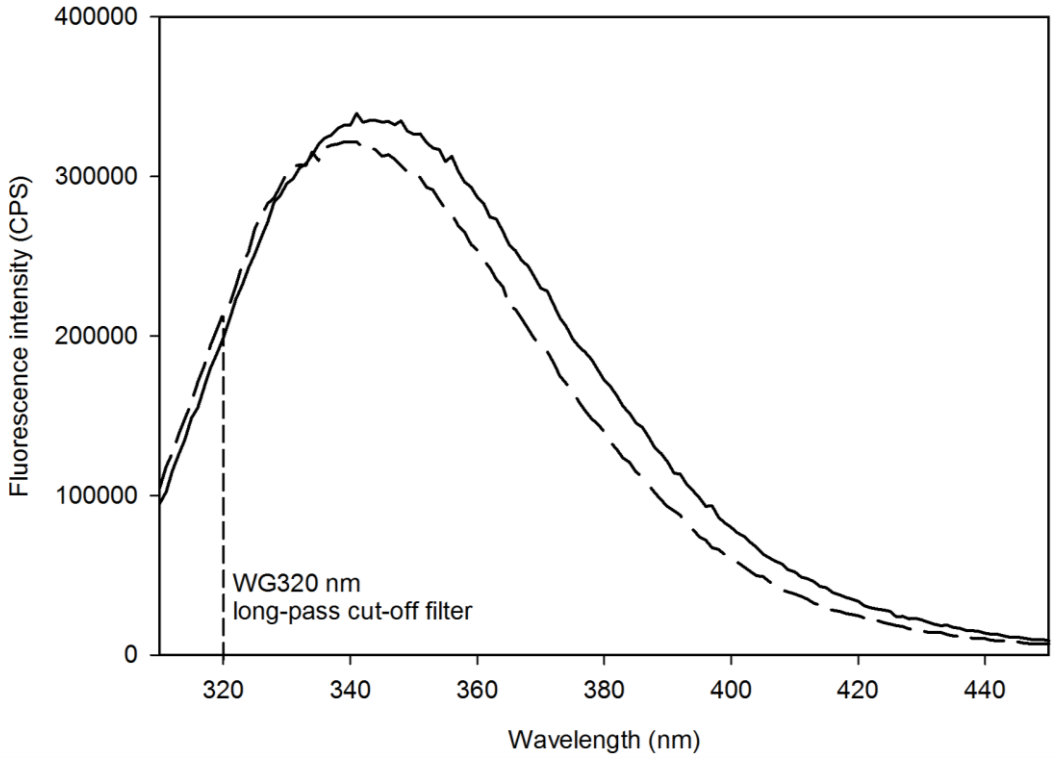

Figure 3-15. Intrinsic tryptophan fluorescence change upon complex formation.
Tryptophan fluorescence emission spectra of 1 µM FpvAI (*solid line*) and 1 µM FpvAI-pyoS2^{NTD} (*dashed line*) upon excitation at 295 nm. The WG320 nm long-pass cut-off filter fitted into the stopped-flow excludes emitted fluorescence <320 nm.

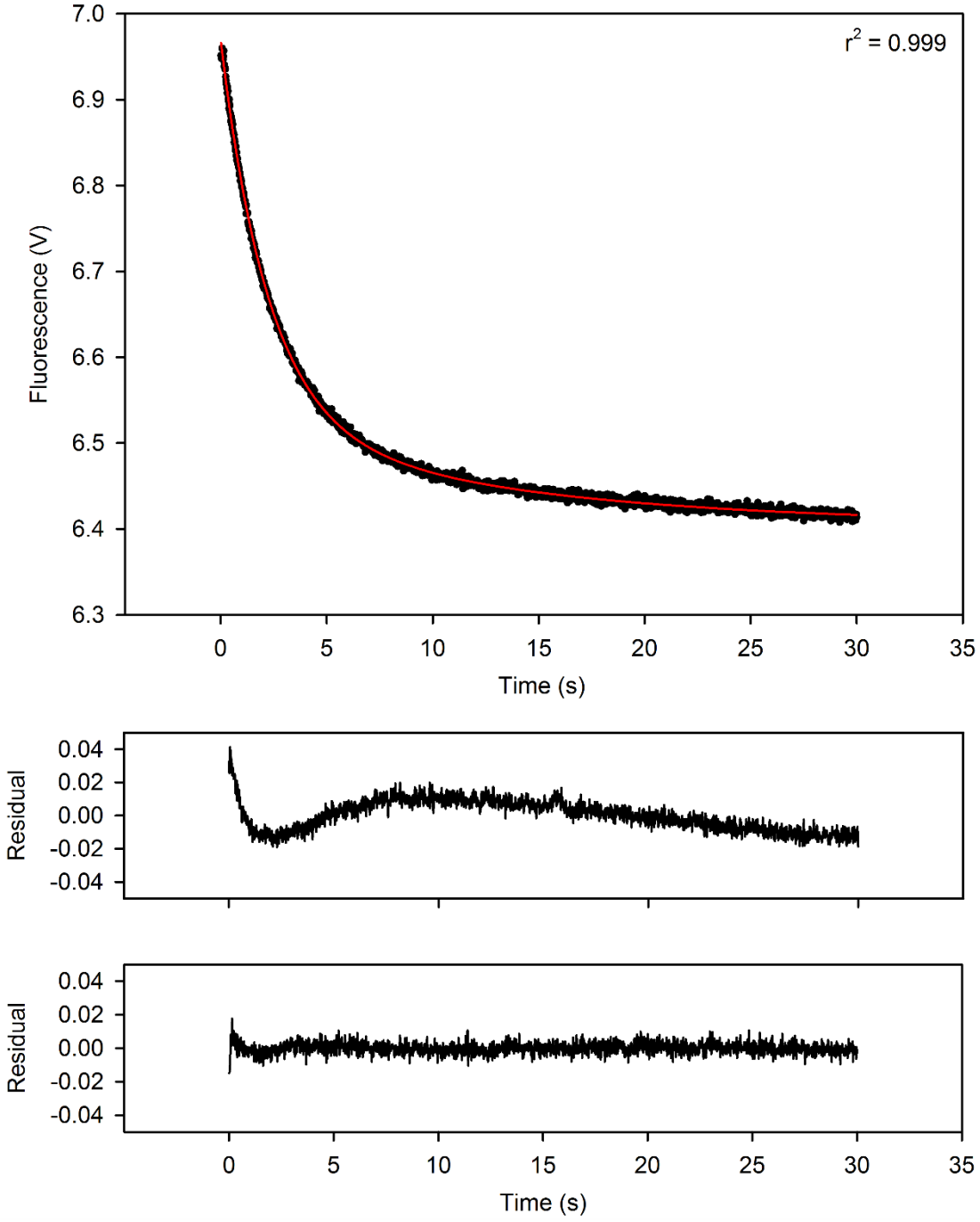

Figure 3-16. Pseudo first-order association kinetics of pyoS2^{NTD} and FpvAI.
Upper panel, stopped-flow tryptophan fluorescence in pseudo first-order conditions. FpvAI and pyoS2^{NTD} were present at 0.1 µM and 1 µM, respectively. Data were fitted to a double exponential function (see Materials and Methods 2.9.2) shown in *red*, to determine values for k_{obs1} and k_{obs2} of 0.4857 s^{-1} and 0.0814 s^{-1}, respectively. Residuals from single (*middle panel*) and double (*lower panel*) exponential fits.

The first observed rate (k_{obs1}), extracted from double exponential fits of stopped-flow data, exhibits a hyperbolic relationship with respect to pyoS2^{NTD} concentration. This implies a two-step reaction mechanism whereby structural rearrangements in the complex occur after the biomolecular association event (Figure 3-17), as described in Scheme 1 (Blackburn *et al.*, 1977).

$$[A] + [B] \underset{k_{-1}}{\overset{k_1}{\rightleftharpoons}} [AB] \underset{k_{-2}}{\overset{k_2}{\rightleftharpoons}} [AB^*] \qquad K_{d1}, K_{d2}$$

Scheme I

The rate constant k_2 and the dissociation constant for the encounter complex (K_{d1}) can be determined by using a double reciprocal plot (Figure 3-17 inset) where the hyperbolic relationship is linearised. Extrapolation of this linear fit to the y-axis where pyoS2^{NTD} concentration is infinite means the observed rate is limited by k_2. The y-intercept is therefore equal to $1/k_2$ and the gradient is K_{d1}/k_2 (see methods 2.9.2 for derivation) determining a k_2 of 1.35 s^{-1} and a K_{d1} of 1.81 µM. The overall K_d, which could not be determined kinetically without additional measurements, is clearly much higher affinity than that of the encounter complex and consequently conformation changes are crucial for kinetic stabilisation of the complex.

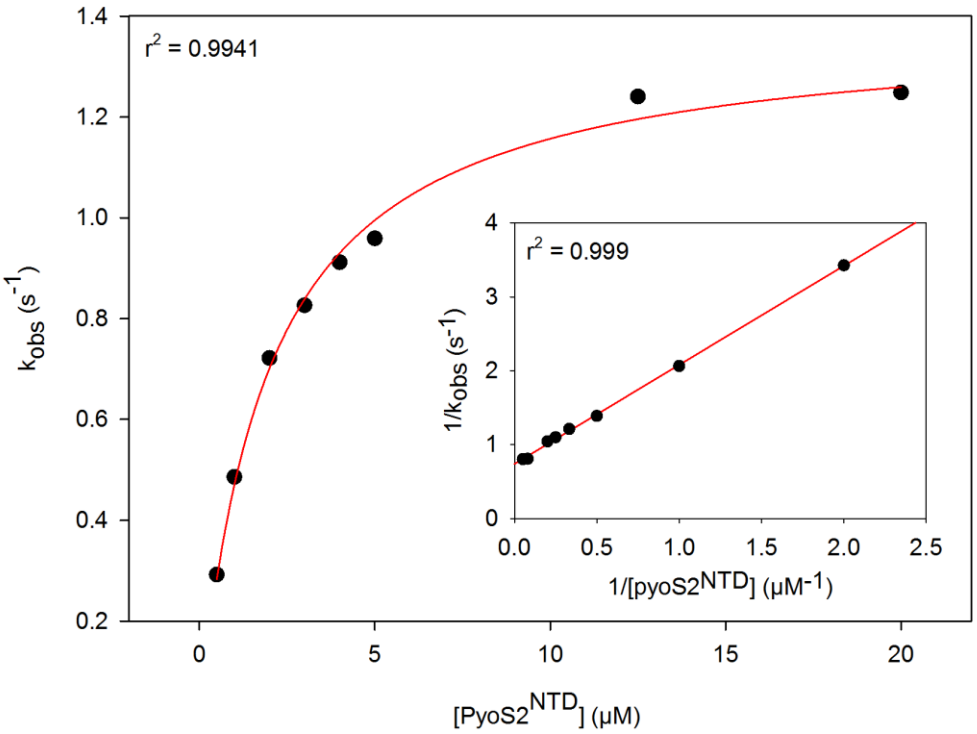

Figure 3-17. Concentration dependence of pseudo first-order rate.
Observed association rates from double exponential fits at pyoS2^{NTD} concentrations of 0.5, 1, 2, 3, 4, 5, 12.5 and 20 μM. Data were fitted to a hyperbolic curve *(red line)*. ***Inset***, the double reciprocal plot of hyperbolic relationship was fitted with a linear regression line *(red line)* to extract kinetic parameters k_2 and K_{d1}.

Association kinetics were also monitored under second-order conditions where both proteins were present in stoichiometric concentrations. Data were fitted to a second-order rate equation (see Materials and Methods 2.9.2) to extract an association rate constant (k_{on}) of 4.16×10^5 $M^{-1}s^{-1}$ (Figure 3-18). At this association rate, K_d values in the pM range ($1\times10^{-9} > K_d > 1\times10^{-12}$) would have dissociation rates ranging from 4×10^{-4} to 4×10^{-7} s^{-1} equivalent to a half-life ($t_{1/2}$) of hours to days.

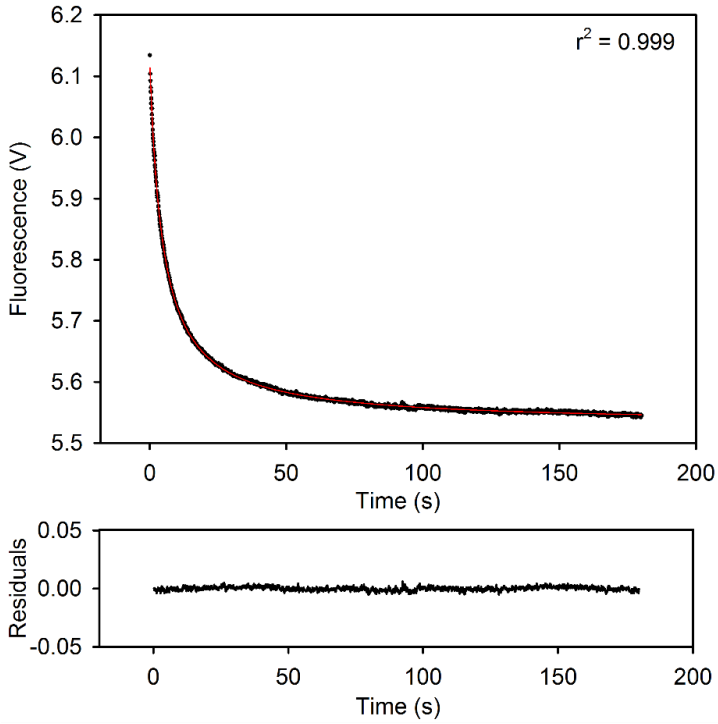

Figure 3-18. Second-order association kinetics of pyoS2^{NTD} and FpvAI.
Tryptophan fluorescence stopped-flow data were fitted to the second-order rate equation (see Materials and Methods 2.9.2) to determine an association rate constant (k_1) of 4.16×10^5 $M^{-1}s^{-1}$. Residuals from the fit are shown *(lower panel)*. Final pyoS2^{NTD} and FpvAI concentrations were 0.5 µM.

Due to the greater than anticipated complexity of the association kinetics, ITC was used to determine the K_d of the FpvAI-pyoS2^{NTD} complex. ITC measures the heat produced or absorbed upon binding and can simultaneously determine the enthalpy and affinity providing full thermodynamic characterisation of the binding event (Cooper, 1999). During the ITC experiment, the heat change on each injection diminishes as the limiting reactant becomes saturated. The total heat per injection is calculated by integration of the injection 'spikes' which together with the protein concentration determines the enthalpy. For high-affinity complexes, the K_d is much lower than the protein concentration required to produce measurable heats upon binding. This causes immediate saturation and a single-step transition which cannot be accurately fit to determine the K_d. The high-affinity FpvAI-pyoS2^{NTD} interaction was therefore investigated by competition ITC

whereby, a weaker-binding competitor lowers the apparent K_d into the measurable range of the instrument. This approach is suitable for determining the thermodynamic parameters of high-affinity (<1 nM) binding events (Sigurskjold, 2000, Velazquez Campoy, 2006). The thermodynamic parameters of the competitor must first be determined in an independent ITC experiment before titration of the high-affinity protein into a preformed competitor-target protein complex. In this case, the weaker-binding competitor, a truncated pyoS2^{NTD} (Δ1-45pyoS2^{NTD}), was titrated into FpvAI to determine its K_d of 190 nM (Figure 3-19A). Using Δ1-45pyoS2^{NTD} as a competing ligand, a K_d of 240 pM was determined for the FpvAI-pyoS2^{NTD} complex (Figure 3-19B). In this experiment the net enthalpy change was positive because the outcompeted competitor ligand has a larger ΔH than pyoS2^{NTD}. The thermodynamic parameters are listed in Table 3.1.

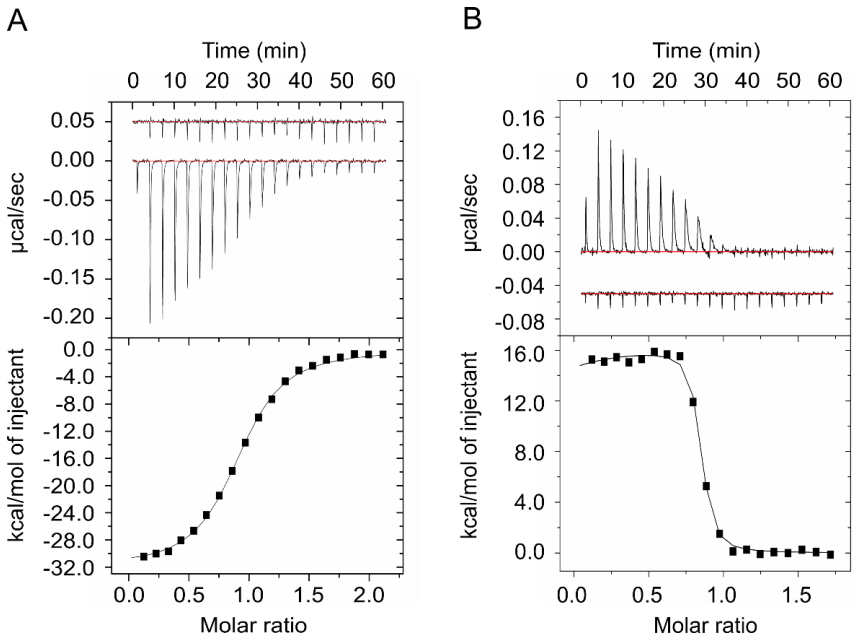

Figure 3-19. High-affinity binding of pyoS2^{NTD} to FpvAI monitored by ITC.
A, ITC data of Δ1-45pyoS2^{NTD} binding to FpvAI. The cell contained FpvAI at 5 µM and the syringe contained Δ1-45pyoS2^{NTD} at 50 µM. Duplicate data were each fitted with a single binding sites model to determine thermodynamic parameters. ***B,*** ITC data for pyoS2^{NTD} binding FpvAI in the presence of a lower affinity competitor, Δ1-45pyoS2^{NTD}. The cell contained FpvAI and Δ1-45pyoS2^{NTD} at 10 µM and 15 µM respectively, and the syringe contained pyoS2^{NTD} at 70 µM. Data from two independent experiments were fitted to a competitive binding model to determine thermodynamic parameters.

Table 3-1. Thermodynamic parameters for pyoS2^{NTD} and Δ1-45pyoS2^{NTD} binding to FpvAI.

Parameter	PyoS2^{NTD}	Δ1-45pyoS2^{NTD}
N (sites)	0.78 ± 0.02	0.88 ± 0.02
ΔH (kcal/mol)	-15.8 ± 1.4	-34.3 ± 2.2
ΔS (cal/mol/K)*	-9.1 ± 4.6	-84.3 ± 7.3
ΔG (kcal/mol)†	-13.1 ± 0.01	-9.2 ± 0.04
K_a (M^{-1})	$4.10 \pm 0.07 \times 10^{9}$	$5.2 \pm 0.03 \times 10^{6}$
K_d (M)	$2.44 \pm 0.04 \times 10^{-10}$	$1.93 \pm 0.12 \times 10^{-7}$

Values are the average of duplicate data along with associated errors
† ΔG was calculated using Equation 8 (See 2.9.3)
* ΔS was calculated using Equation 9 (See 2.9.3)

3.3. Discussion

The results presented in this chapter demonstrate binding between FpvAI and pyoS2-ImS2, with the N-terminal residues 2-209 shown to be sufficient for binding. The pyoS2^{NTD} derived from partial trypsin proteolysis of the complex represents the smallest stable domain able to bind FpvAI, confirming its role as a receptor-binding domain. The natural role of FpvAI is to capture the iron-loaded siderophore Fe-Pvd for its transport across the OM. The binding between Fe-Pvd and FpvAI has been well studied, with K_d values reported in the range of 0.5-1.5 nM (Clément *et al.*, 2004, Hoegy *et al.*, 2005, Schalk *et al.*, 2001). FpvAI expressed and purified from the *E. coli* OM is able to bind Fe-Pvd and pyoS2^{NTD}, but not both simultaneously. Analytical SEC experiments reveal that pyoS2^{NTD} outcompetes Fe-Pvd for binding to FpvAI, though, in a physiological setting, Fe-Pvd would probably be translocated before being displaced by pyoS2. *In vitro* displacement of Fe-Pvd is implicated in the higher binding affinity of pyoS2^{NTD} for FpvAI (240 pM) which lies within the typical picomolar to nanomolar range seen with other bacteriocin-receptor complexes (Housden *et al.*, 2005, Konisky and Cowell, 1972). Removal of the N-terminal 45 residues (Δ1-45pyoS2^{NTD}) decreased the binding affinity almost 1000-fold to 190 nM implying some of this region is located at the complex interface. This will be discussed further in the following chapter. Moreover, the kinetics

of pyoS2^{NTD} binding to FpvAI as monitored by changes in intrinsic tryptophan fluorescence revealed characteristics of biphasic association. The hyperbolic relationship between pyoS2^{NTD} concentration and the observed association rate suggests conformation changes occur after the initial bimolecular association (Blackburn *et al.*, 1977), though complete kinetic characterisation of pyoS2^{NTD} binding was beyond the scope of this work. Also, the binding kinetics are more meaningful in living systems since energy from the PMF during the ligand transport cycle would probably influence ligand binding. Nevertheless, biphasic binding kinetics have also been observed for colicin B-FepA implying that the pyoS2 binding mode exhibits similarities at least with group B colicins (Payne *et al.*, 1997). If localised to the receptor plug domain, conformational changes may be implicated in the translocation mechanism. Subsequent chapters structurally characterise the FpvAI-pyoS2^{NTD} complex providing further insight into the mechanism of translocation.

3.4. Conclusions

The work presented in this chapter shows evidence of binding between FpvAI and pyoS2 *in vitro* and that the interaction is through the N-terminal domain comprising residues 2-209. The pyoS2^{NTD} binds FpvAI with a K_d of 240 pM sufficient to outcompete the endogenous ligand Fe-Pvd. The kinetics of binding reveal a two-step binding mechanism implying structural re-arrangements occur after initial encounter complex formation. PyoS2^{NTD} is folded and α-helical in secondary structure, comparable with the receptor-binding domains of colicins such as colicin E3 and E9.

Chapter 4. Crystal structure of the FpvAI-pyoS2^{NTD} complex

4.1. Introduction

Three dimensional structure determination of proteins and their complexes can provide invaluable and detailed information on biological systems. X-ray crystallography has revolutionised structural biology, from the first ever crystal structure of myoglobin solved by John Kendrew in 1957 (Kendrew and Parrish, 1957), to over 117,000 crystal structures available on the Protein Data Bank (PDB) some 60 years on. Of all the macromolecular structures published, 90% have been determined by X-ray crystallography (http://www.rcsb.org/pdb (Berman *et al.*, 2000)). The basic principle in macromolecular X-ray crystallography involves placing a crystal into a focused X-ray beam, and detecting the X-rays diffracted from atoms within the crystal. As the crystal is rotated on a goniometer, a series of diffraction images are collected which represent reflected X-rays from atomic planes within the crystal lattice, at an angle dictated by the Bragg equation. Diffraction data are then converted to electron density by Fourier methods, to which an atomic model can be built. Iterative rounds of refinement and model building culminates in a 3D atomic model of the macromolecule of interest, which best fits the electron density and satisfies ideal geometry (Rupp, 2010). The following introduction explores how structural biology has advanced our understanding of bacteriocin function.

Structural information is available for a number of full-length bacteriocins, individual domains and bacteriocin-receptor complexes. The first full-length crystal structure of a bacteriocin was published for colicin Ia in 1997 (Figure 4-1), revealing a highly elongated structure with two remarkably long (~160 Å) α-helices (Wiener *et al.*, 1997). The TonB-box can be seen at the N-terminus of the translocation domain, which is essential for colicin Ia activity (Schramm *et al.*, 1987). In the following years, full-length crystal

structures were published for colicins N, E3, B, M, S4 and E9 (Vetter *et al.*, 1998, Soelaiman *et al.*, 2001, Hilsenbeck *et al.*, 2004, Zeth *et al.*, 2008, Arnold *et al.*, 2009, Klein *et al.*, 2016). Interestingly, these structures differ significantly, despite sharing the same domain arrangement. Nuclease bacteriocins form high affinity (fM) complexes with their cognate immunity proteins to protect the producing bacterium from cytotoxic activity. A number of structures have been reported for colicin nuclease-immunity complexes including colicin E9-Im9, colicin E3-Im3, colicin E7-Im7, colicin D-ImD, and colicin E5-Im5 (Kleanthous *et al.*, 1999, Carr *et al.*, 2000, Sui *et al.*, 2002, Graille *et al.*, 2004, Luna-Chavez *et al.*, 2006). Specifically, DNase domains have a mixed α/β fold and their immunity proteins adopt a four α-helical bundle with a characteristic short helix III. These structures have also revealed a common mechanism of inhibition whereby the immunity protein binds at an exosite, inhibiting the nuclease by blocking substrate DNA binding. Moreover, colicin immunity proteins have been used extensively in the study of protein folding landscapes (Morton *et al.*, 2007, Ferguson *et al.*, 2001), and as model systems for the study of protein-protein interaction specificity and binding mechanism (Keeble and Kleanthous, 2005, Kortemme *et al.*, 2004).

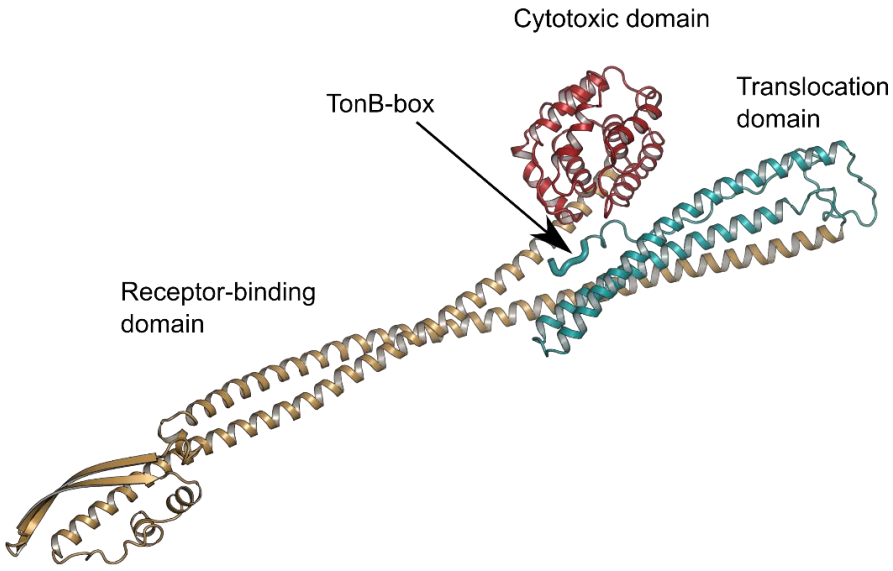

Figure 4-1. Crystal structure of colicin Ia.
Cartoon representation of colicin Ia (PDB ID 1CII (Wiener *et al.*, 1997)) coloured by domain; translocation domain *(blue)*, receptor-binding domain *(light brown)* and cytotoxic domain *(red)*. The TonB-box (residues 23-27) is highlighted.

Structural information on bacteriocin-receptor/translocation complexes can provide useful insights into their mechanism of import. The crystal structure of the colicin E3 receptor-binding domain in complex with BtuB (Figure 4-2) revealed the extended coiled-coil inserts into the barrel at a 45° angle, positioning the translocation domain over OmpF (Kurisu *et al.*, 2003) through which the intrinsically unstructured translocation domain (IUTD) threads (Housden *et al.*, 2013). Moreover, the binding site overlaps with the endogenous ligand, vitamin B_{12}, inducing conformational changes in the extracellular loops. The structures of colicins E2 and Ia bound to BtuB and Cir, respectively, reveal similarities with colicin E3 (Sharma *et al.*, 2007, Buchanan *et al.*, 2007). Instead of direct translocation through the receptor, additional OMPs are recruited as translocators; for colicin E2 and E3 this is OmpF, and for colicin Ia, another copy of Cir is used (Housden *et al.*, 2005, Jakes and Finkelstein, 2010).

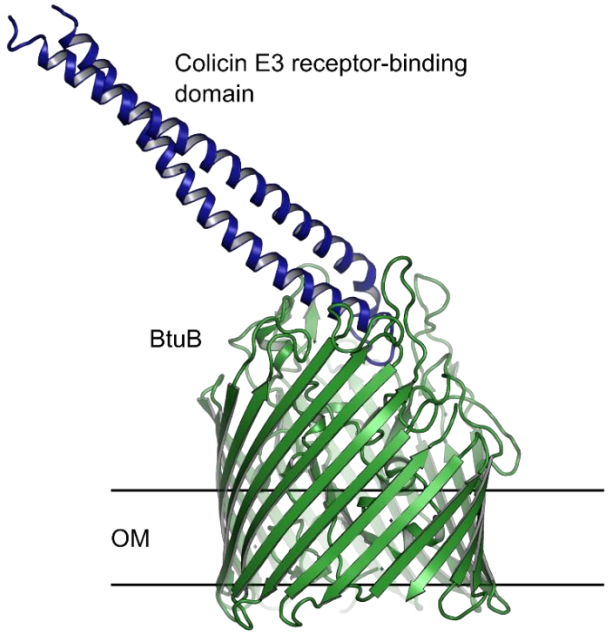

Figure 4-2. Crystal structure of the colicin E3 receptor-binding domain bound to BtuB. Cartoon representation of the colicin E3 receptor-binding domain (*dark blue*) complexed with BtuB (*green*) showing its position in the OM (PDB ID 1UJW (Kurisu *et al.*, 2003)). The receptor-binding domain coiled-coil binds at a 45° angle.

In contrast to colicins, structural information for pyocins is limited, particularly for the S-type pyocins. Currently, only a low resolution small angle X-ray scattering (SAXS) structure exists for full-length pyocins S2 and AP41 revealing an elongated morphology (Klein *et al.*, 2016), consistent with that of some colicins. High-resolution crystal structures of the C-terminal domains of pyoS2 and pyoAP41 complexed with their immunity proteins exhibit similarity with colicins, whereby the mixed α/β nuclease domain is bound by the four α-helical bundle immunity protein (Figure 4-3) (Joshi *et al.*, 2015). The only full-length, high resolution crystal structure for a pyocin is the recently identified lectin-like pyocin, pyocin L1. The structure identified a C-terminal D-rhamnose-binding domain which targets the CPA of *P. aeruginosa*, though the mechanism of killing is still unclear (McCaughey *et al.*, 2014). No structural information

exists for pyocin receptor-binding or translocation domains, either in isolation, or in complex with their receptor.

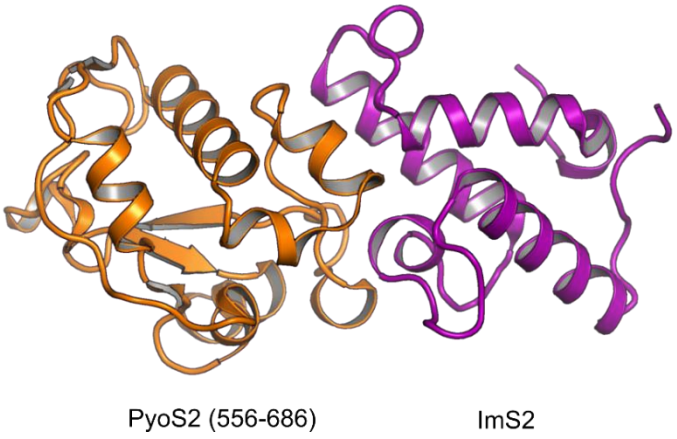

Figure 4-3. Crystal structure of the pyoS2 cytotoxic domain complexed with ImS2.
Cartoon representation of the C-terminal cytotoxic domain of pyoS2 (residues 555-686) *(orange)* in complex with its cognate immunity protein ImS2 (*purple)*. PDB ID 4QKO (Joshi *et al.*, 2015).

Having discussed key structural features of colicins, the overall aim of this chapter was to determine the crystal structure of FpvAI in complex with pyoS2^{NTD} for comparison with other colicins. Structural information on pyoS2^{NTD} would provide new insights into the import mechanism, which could be further explored through manipulations and modifications. To date, this would be the first and only crystal structure of an S-type pyocin receptor-binding domain in complex with its receptor.

4.2. Results

4.2.1. Co-purification of the FpvAI-pyoS2^{NTD} complex

Initial attempts to crystallise pyoS2-ImS2, both alone and in complex with FpvAI, were unsuccessful, possibly due to flexibility between individual domains. It was therefore decided to pursue a crystal structure of FpvAI bound to the pyoS2 minimal binding domain, pyoS2^{NTD}, identified in Chapter 3. To produce sufficient quantities of FpvAI-pyoS2^{NTD} complex for crystallisation, an affinity-based co-purification strategy was used. This involved first immobilising His-tagged pyoS2^{NTD} on an EDTA-compatible Ni-affinity column to act as 'bait' for FpvAI. The OMP extract containing FpvAI was flowed through the Ni-affinity column where it bound to immobilised pyoS2^{NTD}. After washing to remove OMP impurities, the purified complex was eluted in an imidazole gradient, and was further purified by SEC (Figure 4-4).

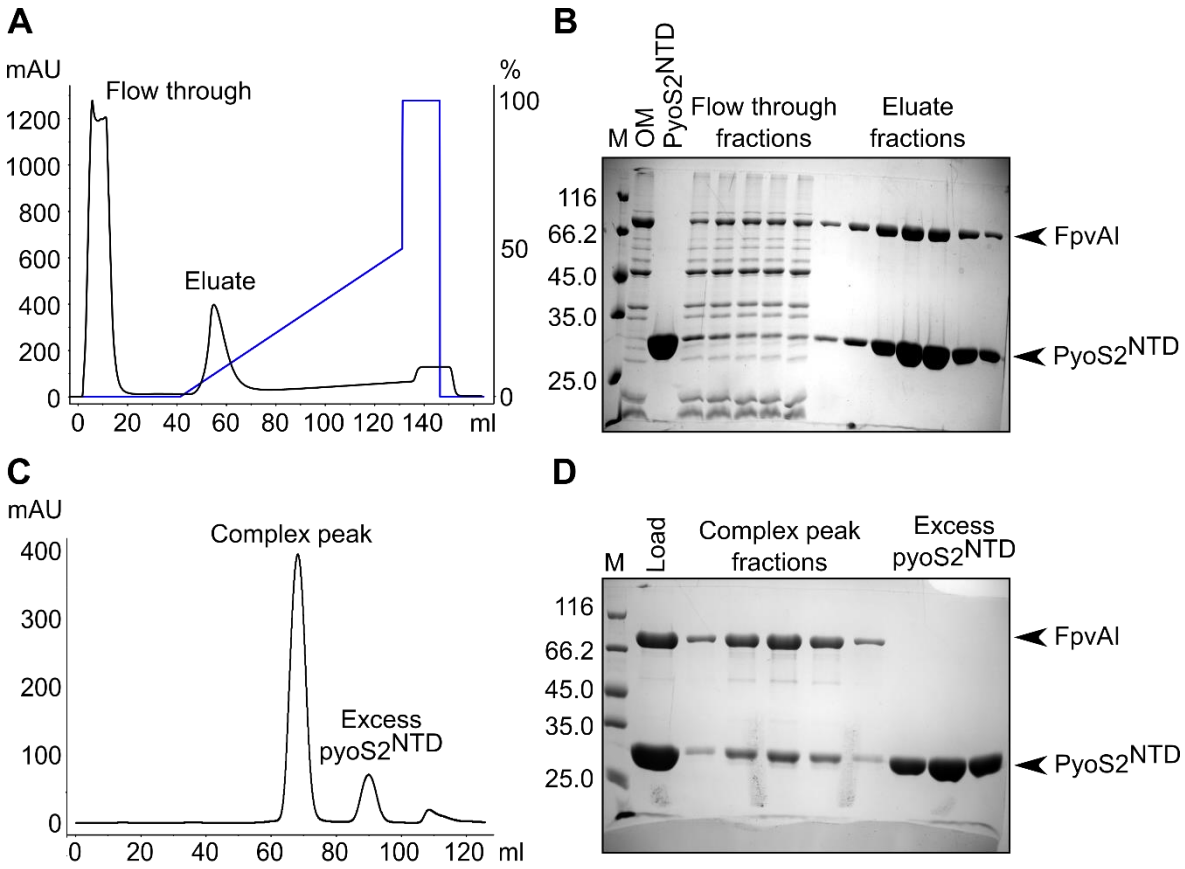

Figure 4-4. Co-purification of the FpvAI-pyoS2^{NTD} complex.
A, Ni-affinity co-purification elution profile using a 5 ml EDTA-resistant cOmplete HisTrap column (Roche). Complex elution was monitored by A280 nm *(black)* using a linear gradient of 0-50% elution buffer *(blue)* (5-250 mM imidazole) (see Materials and Methods). ***B***, Coomassie-stained 10% SDS-PAGE gel loaded with 10 µl of fractions from Ni-affinity co-purification of the FpvAI-pyoS2^{NTD} complex. FpvAI is the major protein in the OM sample. PyoS2^{NTD} was immobilised as 'bait'. A small amount of complex was lost in the flow through along with all the impurities. Elution fractions from an imidazole gradient contain pure FpvAI-pyoS2^{NTD} complex. ***C***, Superdex 200 16/600 SEC purification elution profile monitored by A280 nm *(black)*. ***D***, Coomassie-stained 10% SDS-PAGE gel loaded with 10 µl of fractions from Superdex 200 16/600 SEC purification of the FpvAI-pyoS2^{NTD} complex. Fractions from the major peak contain pure FpvAI-pyoS2^{NTD} complex and the minor peak contains excess pyoS2^{NTD}. M = Fermentas unstained protein standard.

4.2.2. Initial crystallisation screening and optimisation

Crystallisation screening trials for FpvAI-pyoS2^{NTD} were set up using the commercially available screens MemGold, MemGold2, MemPlus and ProPlex. MemGold and MemGold2 screens sample conditions which have been successful for crystallisation of α-helical membrane proteins, whereas MemPlus samples successful conditions for β-sheet proteins (Newstead *et al.*, 2008a, Parker and Newstead, 2012, Newstead *et al.*,

2008b). The ProPlex screen is particularly useful for protein complexes as it maintains protein-protein interactions whilst reducing protein solubility (Radaev *et al.*, 2006). The FpvAI-pyoS2^{NTD} complex crystallised in a number of conditions across the MemGold, MemGold2 and MemPlus screens, and examples of crystals are shown in Figure 4-5. Crystals were cryo-protected in the growth condition supplemented with 1% (w/v) β-OG and typically 25% (v/v) glycerol or ethylene glycol, and were cryo-cooled in liquid nitrogen for X-ray diffraction. Many of the crystals from preliminary screening failed to diffract but crystals from the MemGold2 condition E9 diffracted to <5 Å resolution. In an attempt to improve the internal order of the crystals for higher resolution, a gradient screen was set up for finer variation of polyethylene glycol (PEG) and salt concentration. Crystals were reproducible but resolution was only marginally improved. Further attempts at optimisation involved the screening of other detergents since this may be a critical factor for high-order packing within the crystal. The detergent, β-OG, was exchanged for n-OPOE, a mixture of detergents with different length ethylene chains (C_8E_n, where n=0-7). The highest resolution diffracting crystals were grown in 0.350 M ammonium sulphate, 13.5% (w/v) PEG3350, 0.050 M sodium acetate pH 4.0, and were cryo-cooled in the presence of 25% (v/v) ethylene glycol and 1% (v/v) n-OPOE. It was also apparent that distinct micro-domains within the crystal produced diffraction data of different quality. Grid scans across the crystal were performed prior to X-ray centering to find the best region to obtain high-resolution diffraction data.

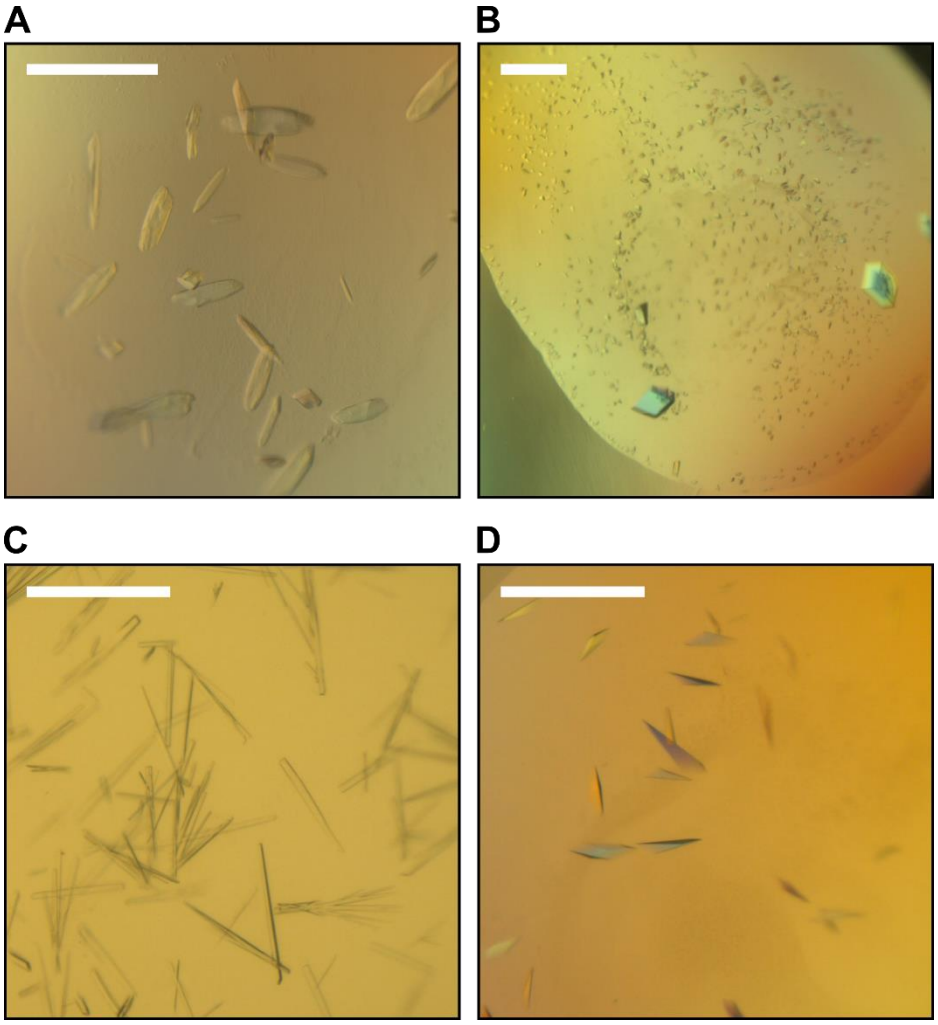

Figure 4-5. Example crystals of FpvAI-pyoS2^{NTD} complex from preliminary screening. ***A***, Crystals grown for 30 days in 0.225 M ammonium sulphate, 0.05 M sodium acetate pH 4.0, 12% (w/v) PEG4000. This condition was selected for further optimisation by varying salt/PEG concentration. ***B***, Crystals after 30 days grown in 0.025 M magnesium chloride hexahydrate, 0.4 M NaCl, 0.02 M Tris pH 7.5, 12.5% PEG2000 MME. ***C***, Crystals after 3 days grown in 0.04 M magnesium sulphate heptahydrate, 0.02 M NaCl, 0.02 M MES pH 6.0, 8% (w/v) PEG1450. ***D***, Crystals after 10 days grown in 0.37 M potassium nitrate, 0.1 M MES pH 6.5, 22% (v/v) PEG400. Scale bars, 0.2 mm. Final protein concentration in the drops was 8 mg/ml.

4.2.3. Crystal structure of the FpvAI-pyoS2^{NTD} complex at 2.8 Å.

Crystals of the FpvAI-pyoS2^{NTD} complex belonged to an orthorhombic space group *I*222 with unit cell parameters a = 115.1 Å, b = 208.6 Å, c = 214.8 Å, α = 90°, β = 90° and γ = 90°. The crystal structure of the FpvAI-pyoS2^{NTD} complex was solved at 2.8 Å resolution by molecular replacement using FpvAI as the search model (see Materials and Methods). The structure revealed two non-crystallographic symmetry (NCS)-related complexes in

the asymmetric unit with continuous density for residues 11-208 of the pyoS2^{NTD} and almost complete density for FpvAI (Figure 4-6A and Table 4-1).

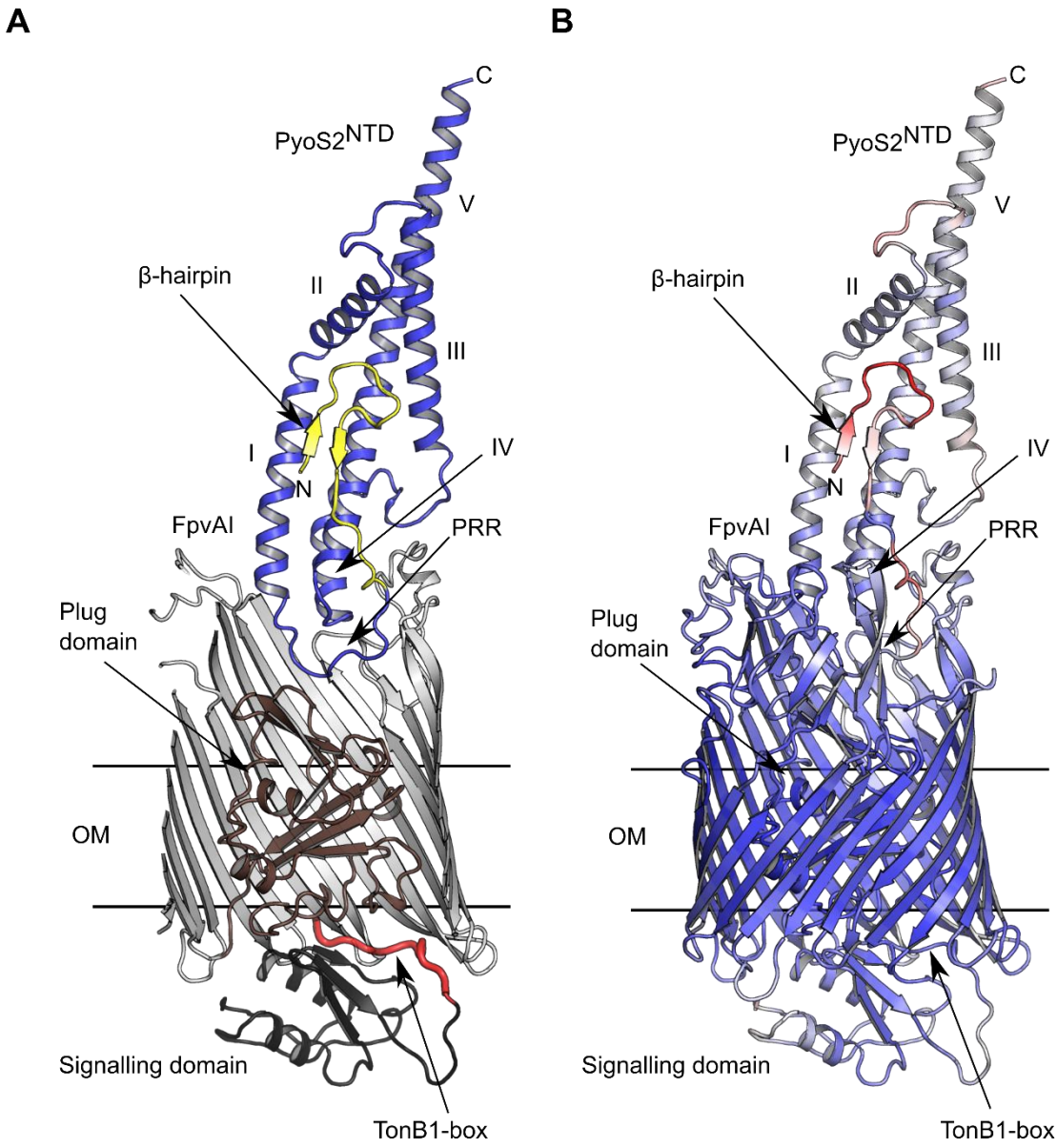

Figure 4-6. The 2.8 Å crystal structure of pyoS2^{NTD} in complex with FpvAI.
A, The structure of pyoS2^{NTD} (*blue*) in complex with FpvAI (*grey*) highlighting the pyoS2^{NTD} β-hairpin *(yellow)*, the FpvAI plug domain (*brown*), the signalling domain (*black*), and the TonB1-box (*red*). Helices I-V are labelled. Several of the β-strands that make up the β-barrel of FpvAI have been removed to highlight the plug domain. ***B***, Structure of the FpvAI-pyoS2^{NTD} complex coloured by B-factor ranging from low B-factor (*blue)* to high B-factor *(red)*. The lowest B-factors, ranging from 5-50 Å^2, were found in the FpvAI barrel and plug. The highest B-factors, ranging from 90-110 Å^2, were found in the pyoS2^{NTD} β-hairpin loop. The high B-factors of the pyoS2^{NTD} β-hairpin suggests this region, which makes no contact with the receptor, may be dynamic.

Table 4-1. X-ray data processing, refinement and validation statistics.

Data processing	
X-ray wavelength (Å)	0.873
Space group	*I*222
Cell dimensions (Å)	a = 115.5 b = 209.4 c = 215.9
Cell angles (°)	α = 90 β = 90 γ = 90
Resolution	47.97-2.80 (2.87-2.80)
Unique reflections	63709
Completeness (%)	98.8 (99.5)
I/σ	5.5 (1.3)
CC (1/2)	0.965 (0.412)
R_{meas}	0.421 (1.898)
Multiplicity	5.7 (6.0)
Refinement	
R_{work}/R_{free}	0.225/0.274
Number of atoms	15094
Average B-factor (Å^2)	37.9
Validation	
RMS bonds	0.012
RMS angles	1.75
Ramachandran favoured (%)	96.5
Ramachandran allowed (%)	3.3
Ramachandran outliers (%)	0.2
MolProbity Clashscore	8.48

Values in parentheses denote high resolution shell.

PyoS2^{NTD} is composed of five α-helices with a long C-terminal helix (Helix V) extending ~80 Å from the interface to the end of the domain. Electron density for the N-terminus (residues 11-34) was weak with high B-factors (90-110 Å^2) suggesting that this region may be more dynamic than the helical domain (Figure 4-6B, and Figure 4-7). Notably, this region appears to form a β-hairpin with residues VIT and IQY forming short antiparallel β-strands which dock against the helical bundle. Prior to helix I, spanning residues 35-45 (TPPFVPPGPSP), is an eleven amino acid proline-rich region (PRR) which mostly contacts the FpvAI plug domain, but only contributes ~12% of the total interface surface area (Figure 4-6,Table 4-2). Electron density for the PRR and its binding site on the FpvAI plug domain was well resolved, particularly for the sidechains of Arg204 and Tyr231 (Figure 4-8). This region of the plug domain required substantial re-

building from the original molecular replacement model, suggesting a large conformational change had occurred relative to unliganded FpvAI.

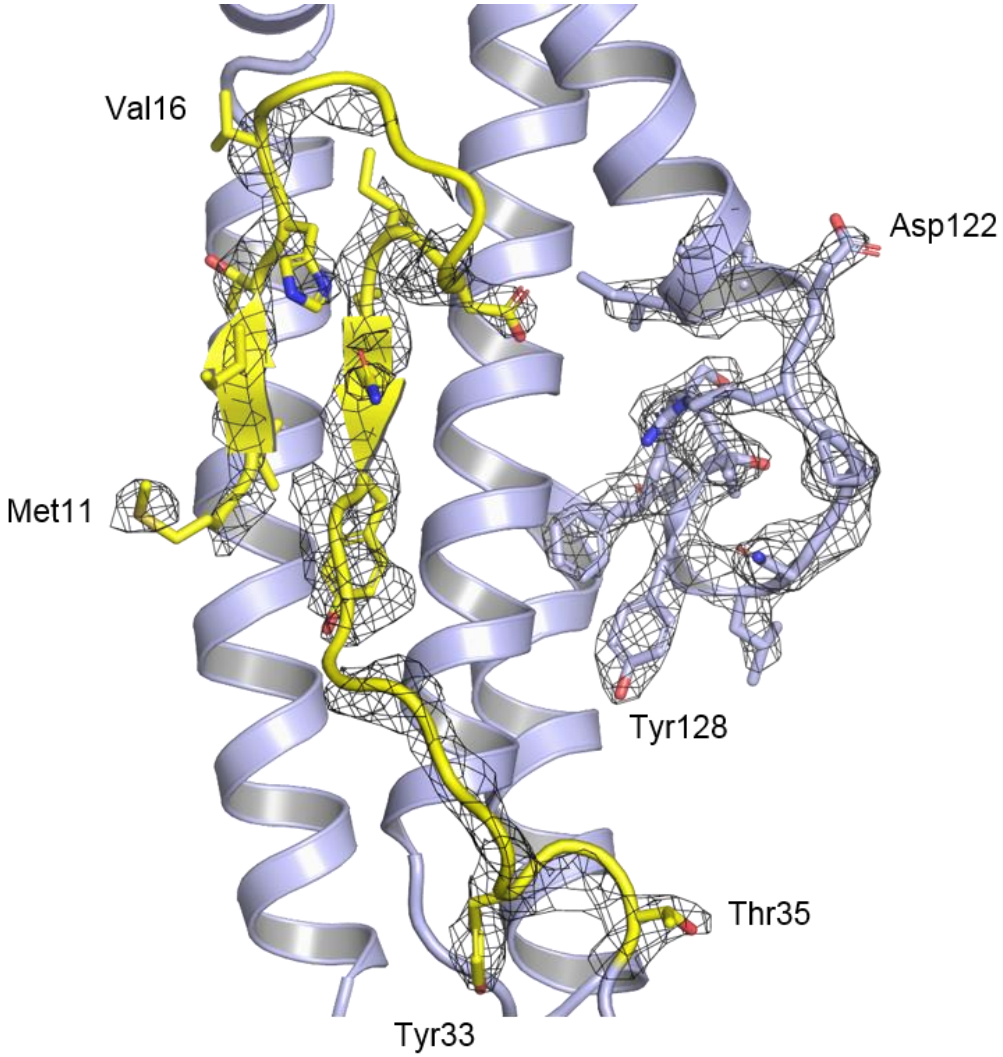

Figure 4-7. Electron density for pyoS2^{NTD} β-hairpin.
2Fo-Fc electron density map for residues 11-35 *(yellow)* and 119-133 (*light-blue*) contoured at 1.0σ with sidechains rendered as sticks. The helical domain is rendered as a cartoon *(light-blue)*. Unlike other regions of pyoS2^{NTD}, density for the β-hairpin is weak due to high B-factors. Specifically, density for the β-strands is better defined but is much weaker for mobile regions such as the β-hairpin loop.

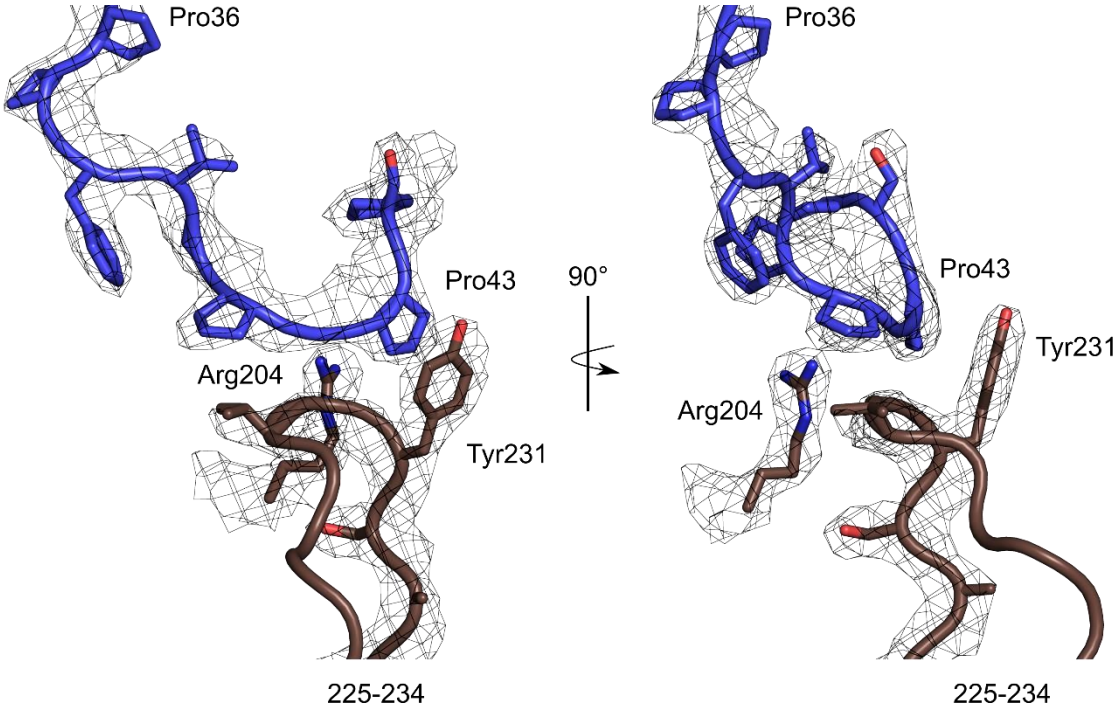

Figure 4-8. Electron density for PRR and FpvAI contact site.
Cartoon and stick representation of pyoS2^{NTD} residues 36-45 *(blue)*, and residues 204 and 225-234 of the FpvAI plug domain with a 2Fo-Fc electron density map contoured at 1.0σ.

As described in Chapter 3, pyoS2^{NTD} binds FpvAI with 240 pM affinity. Analysis of the binding site identified 49 interfacial residues, 14 hydrogen bonds and a salt bridge (Table 4-2). The majority of these interactions involve residues in the extracellular loops of FpvAI (Figure 4-9). Furthermore, 50% of these hydrogen bonds are provided by the PRR and N-terminus, consistent with the ~1000 fold reduction in affinity when truncated (Δ1-45pyoS2^{NTD}) (See Chapter 3.2.5). Tyrosine residues are noticeably abundant at the binding interface, frequently acting as hydrogen bond donors, whilst backbone carbonyls of proline residues within the PRR are common hydrogen bond acceptors. The β-hairpin does not make contact with FpvAI. The most N-terminal hydrogen bonds involve residues Arg30 and Ser32 of pyoS2^{NTD}, contacting Ser750 and Trp752 of FpvAI, respectively.

Table 4-2. PISA analysis of the FpvAI-pyoS2^{NTD} complex interface

Total interface area (Å^2)	1556.0
Plug interface area (Å^2)	190.5 (12.3%)
Barrel interface area (Å^2)	1365.5 (87.7%)
Number of interface residues	49
Number of hydrogen bonds	14
Number of salt bridges	1

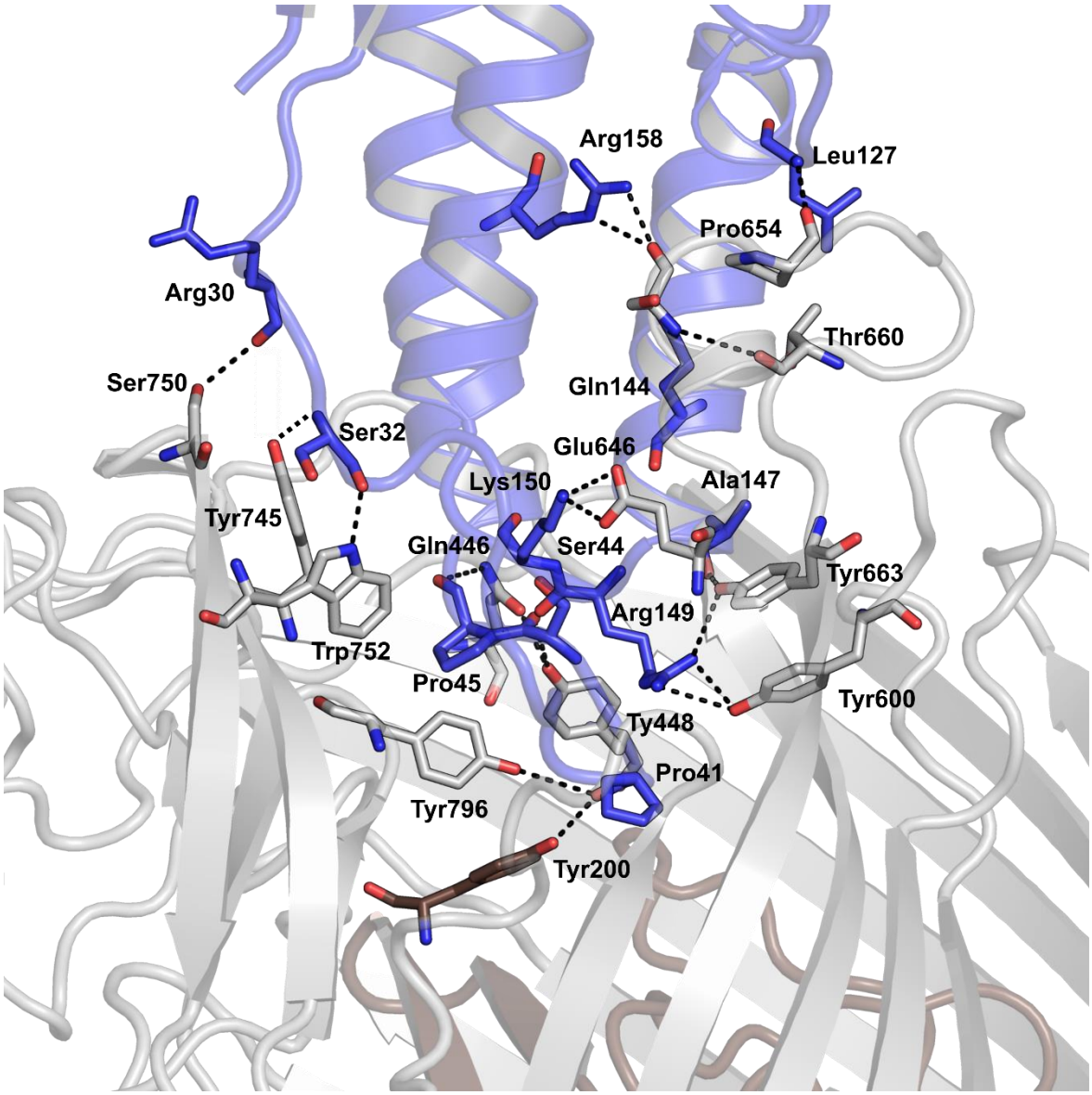

Figure 4-9. Hydrogen bonds at the FpvAI-pyoS2^{NTD} interface.
Cartoon representation of the interface between FpvAI *(grey)* and pyoS2^{NTD} *(blue).* The FpvAI plug domain is coloured *brown.* Residues involved in hydrogen bonding are shown as sticks with the intermolecular bonds highlighted (*black dashed lines*). The majority of hydrogen bonds involve the FpvAI barrel and loops, though a single hydrogen bond exists between Tyr200 of the plug domain and the backbone carbonyl of pyoS2^{NTD} Pro41. A salt bridge also exists between pyoS2^{NTD} Lys150 and FpvAI Glu646.

4.2.4. The FpvAI-pyoS2^{NTD} structure suggests molecular mimicry

On closer inspection of the PRR, it appears to closely resemble the shape of Fe-Pvd, and occupies the same site in FpvAI (Figure 4-10). The proline residues shape the backbone of the PRR such that it mimics that of Fe-Pvd. Backbone root-mean-square deviations (RMSDs), calculated for FpvAI-Fe-Pvd and FpvAI-pyoS2^{NTD} when aligned with unliganded FpvAI, show regions which undergo large conformational changes (Figure 4-11). In the FpvAI-pyoS2^{NTD} structure, the linker region exhibits a shift in backbone RMSD when compared with unliganded FpvAI, though the conformation of the TonB1-boxes are similar. The linker is absent from the FpvAI-Fe-Pvd structure, hence RMSD calculation was not possible. The backbone RMSD shifts across the FpvAI β-barrel represent the large extracellular loop movements required to accommodate pyoS2^{NTD}. As a smaller ligand, loop movements when bound to Fe-Pvd are minimal. Most strikingly, there are large movements localised to region 225-234 within the plug domain, when bound to both ligands. In the absence of a binding partner, residues 225-234 form a mini helix with the Tyr231 hydroxyl making hydrogen bonds with Asp524 and Thr526 within the barrel, and the guanidinium group of Arg204 sits adjacent to this mini helix (Figure 4-12A). When complexed with pyoS2^{NTD} there is a large conformational change within this region of the plug domain. The mini helix becomes an extended loop and notably Tyr231 of FpvAI moves ~11 Å to contact Pro43 of the pyoS2^{NTD}, and Arg204 moves ~8.5 Å to stabilise the new conformation of the binding site. The Trp362 sidechain rotamer changes to accommodate the ligand, rotating ~120° around the Cβ-Cγ bond in order to hydrogen bond with Arg204 (Figure 4-12B). All of these movements are also seen in the Pvd-bound structure (Figure 4-12C). Since conformational changes in the plug are believed to activate the receptor for transport, it is possible that pyoS2 directly mimics Fe-Pvd to initiate translocation.

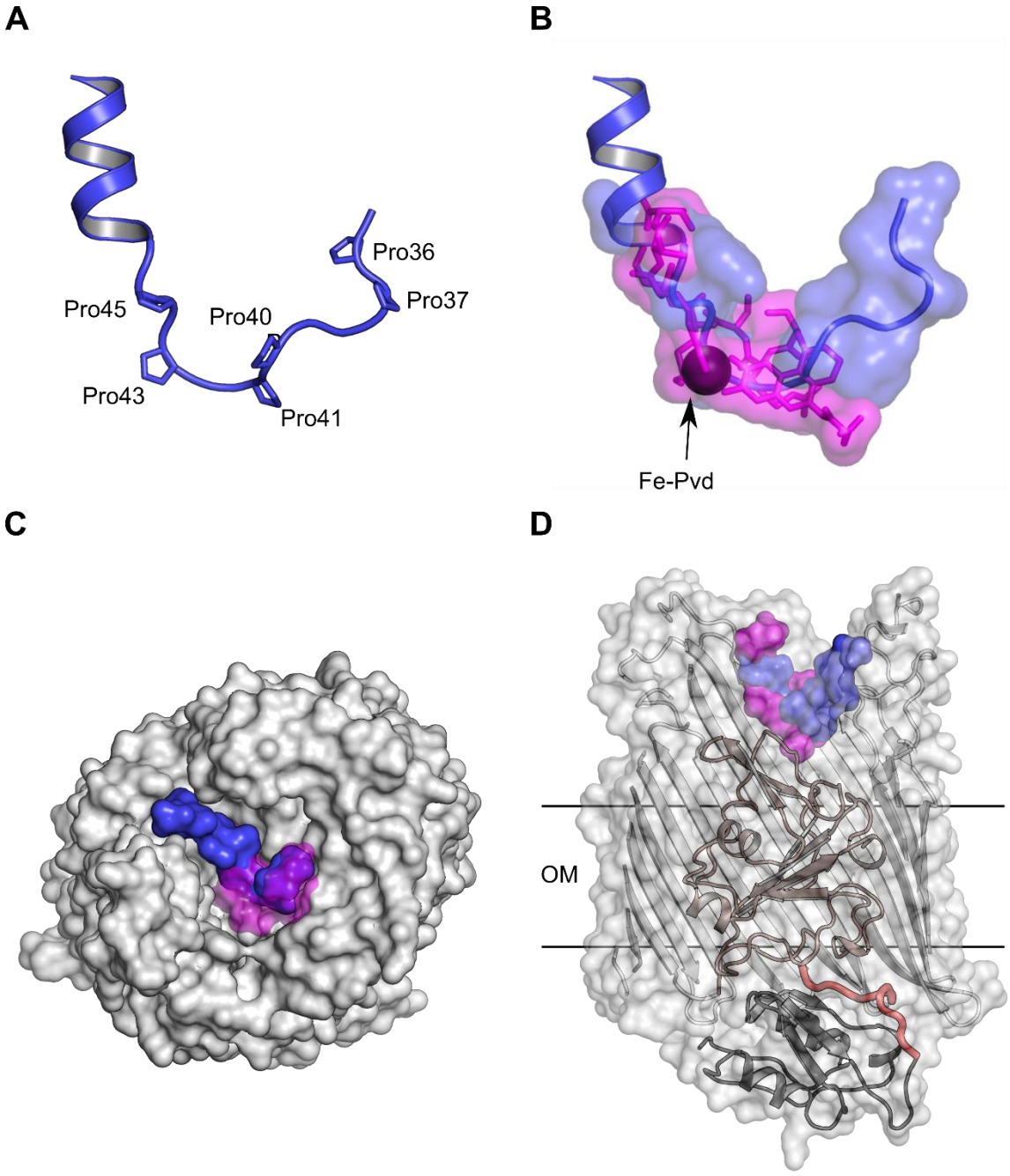

Figure 4-10. PyoS2^{NTD} and Fe-Pvd occupy the same binding site in FpvAI.
A, Cartoon representation of the PRR showing the position of proline residues. ***B***, Overlay of the PRR *(blue)* and Fe-Pvd molecular surfaces *(magenta)*. ***C*** and ***D***, Top and side view molecular surface representations of Fe-Pvd *(magenta)* and pyoS2^{NTD} PRR *(blue)* bound at the same site in FpvAI *(grey)*. The plug domain, signalling domain and TonB1-box region are rendered in *brown, black and red*, respectively. The pyoS2^{NTD} PRR appears to structurally mimic Fe-Pvd.

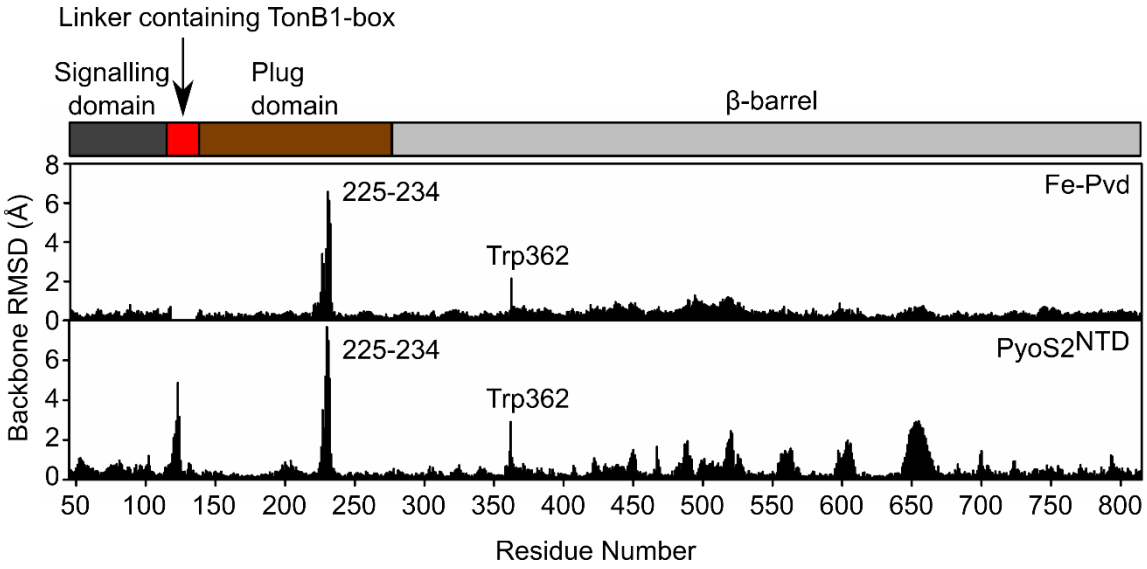

Figure 4-11. PyoS2^{NTD} and Fe-Pvd induce similar conformational changes.
Comparison of backbone RMSDs for complexes of FpvAI bound to Fe-Pvd (*upper panel*) and pyoS2^{NTD} (*lower panel*). Backbone atoms were aligned using Cα atoms for FpvAI in the absence of ligand (PDB ID 2W75 (Greenwald et al., 2009)) and FpvAI complexed with Fe-Pvd (PDB ID 2W16 chain B (Greenwald et al., 2009)) and pyoS2^{NTD}. The largest conformation changes are seen within FpvAI plug residues 225-234 when bound to Fe-Pvd and pyoS2^{NTD}. Missing RMSDs in the *upper panel* is due to the absence of model for the TonB1-box in the FpvAI-Fe-Pvd structure.

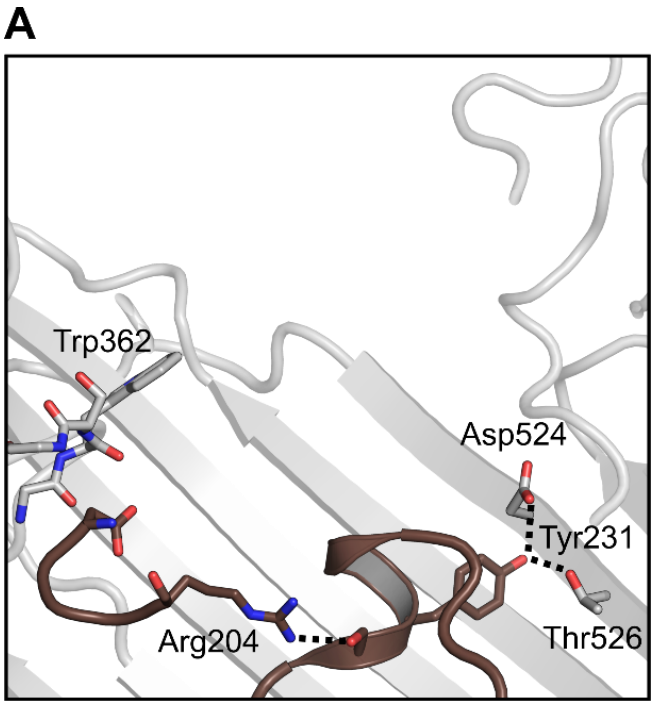

Figure 4-12. Conformational changes within the plug domain. (Legend on next page)

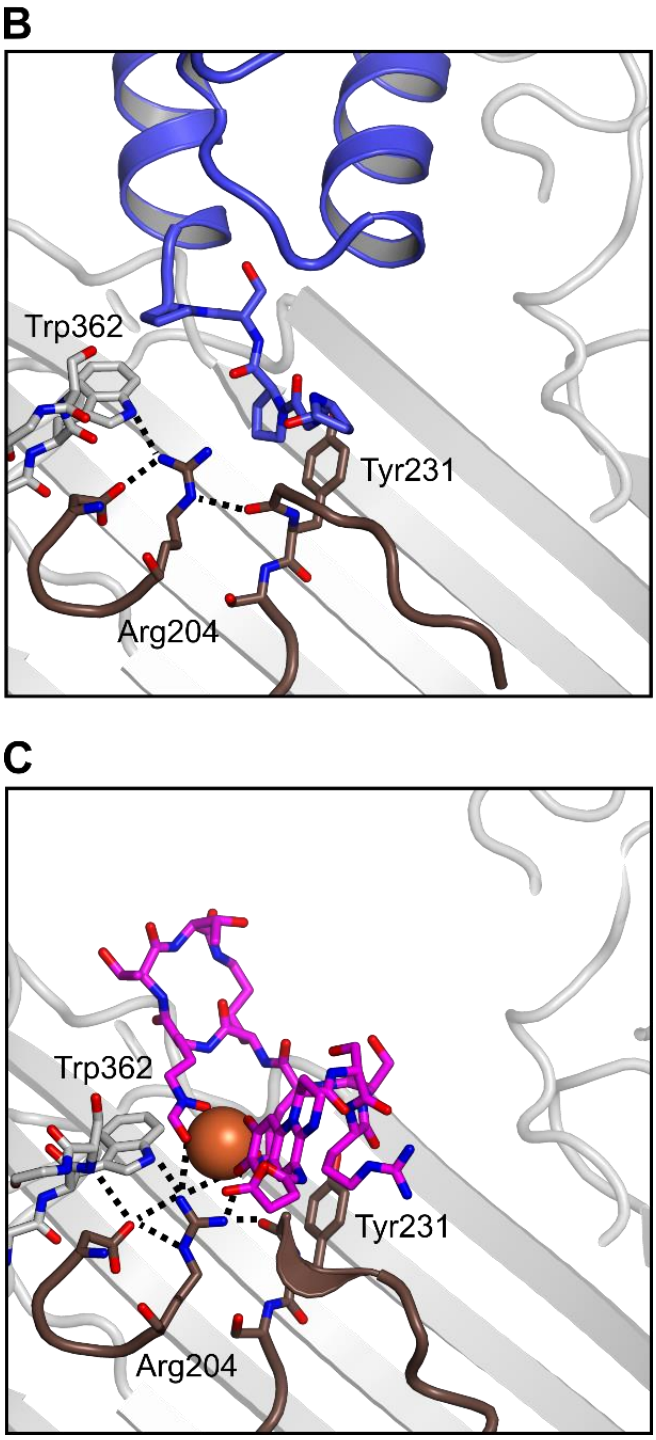

Figure 4-12. Conformational changes within the plug domain.
The FpvAI binding site in the ***A***, unliganded, ***B***, pyoS2^{NTD}-bound, and ***C***, Fe-Pvd-bound states shows comparable sidechain movements involving Arg204, Tyr231 and Trp362. The hydrogen bonding networks are highlighted *(black dashed lines)*.

4.2.5. The N-terminal β-hairpin is required for pyoS2^{NTD} stability

The N-terminal β-hairpin motif appears to shield a hydrophobic surface from the aqueous environment, which may affect the stability of pyoS2^{NTD}. The role of the β-hairpin in the thermal stability of pyoS2^{NTD} was therefore investigated by CD spectroscopy. Removal of the β-hairpin (Δ1-30pyoS2^{NTD}) destabilised the domain as seen by a decrease in T_m from 50 °C to 44 °C (Figure 4-13). Key to this are two isoleucine residues (Ile23 and Ile24) which occupy hydrophobic cavities on the surface of the helical domain, and Tyr26 which stacks against helices I and V (Figure 4-13 inset). The role of the N-terminus in translocation is explored further in subsequent chapters.

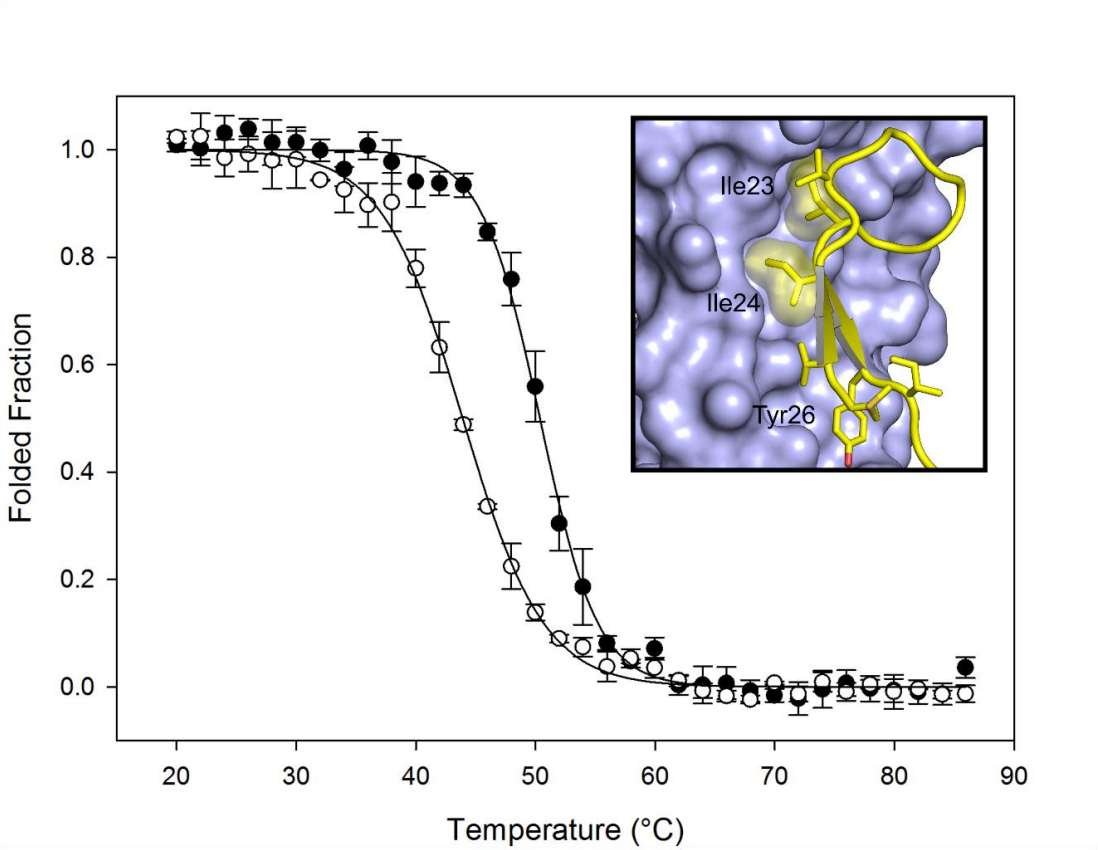

Figure 4-13. The N-terminal β-hairpin stabilises the helices of pyoS2^{NTD}.
Thermal melting curves for isolated pyoS2^{NTD} (*fill circles*) and Δ1-30 pyoS2^{NTD} (*open circles*) obtained by CD spectroscopy in 10 mM potassium phosphate pH 7.5 across a temperature range of 20 to 86 °C. The mid-points of these reversible transitions, the T_m, were 50 and 44 °C, respectively. The normalised average from 3 independent experiments was plotted against temperature along with error bars representing the standard deviation. ***Inset,*** residues 1-30 of pyoS2^{NTD} form the β-hairpin that makes stabilising hydrophobic contacts with the helices of pyoS2^{NTD}.

4.3. Discussion

The crystal structure of pyoS2^{NTD} revealed an N-terminal β-hairpin docked against a bundle of five α-helices. The PRR, located between the N-terminal β-hairpin and the helical domain, mostly contacts the FpvAI plug domain and accounts for ~12% of the total interface surface area. Importantly, the PRR not only mimics the shape of the natural ligand Fe-Pvd, but also induces identical conformational changes within the plug. Mimicry of Fe-Pvd may therefore be implicated in the pyoS2 translocation mechanism.

The asymmetric unit contained two NCS-related complexes differing slightly in terms of model completeness. Incomplete regions of the model, particularly in the FpvAI signalling domain of chain B, were most likely attributed to conformational flexibility from a lack of crystal contacts. No density was seen for residues 2-10, their presence confirmed by N-terminal sequencing of dissolved crystals, and were therefore most likely disordered. The extreme C-terminus, including the His-tag, was also absent from the model, which again, is likely due to conformational flexibility. Indeed, B-factors increased towards the C-terminal end of pyoS2^{NTD} (Figure 4-6B).

The structure of the FpvAI-pyoS2^{NTD} complex is the first structure of an S-type pyocin receptor-binding domain bound to its OM receptor. The five helical structure of pyoS2^{NTD}, with helix V surrounded by four shorter helices, appears to be a novel fold (Fernandez-Fuentes *et al.*, 2010), though bacteriocin receptor-binding domains are mostly α-helical and often in the form of extended coiled-coils (Wiener *et al.*, 1997, Soelaiman *et al.*, 2001, Klein *et al.*, 2016). Helix V was noticeably extended, spanning 57 amino acids and ~80 Å from the FpvAI interface to the end of the domain. The N-terminal β-hairpin may be unique to pyocins as it is not found in other colicins. Instead, colicin translocation domains possess an N-terminal disordered extension required to contact the PMF-linked Ton and Tol systems (Cascales *et al.*, 2007). Compared to other bacteriocin-

receptor complexes, such as BtuB-colicin E3 and Cir-colicin Ia, the pyoS2^{NTD} binding mode appears to be unique (Figure 4-14). The colicin E3 receptor-binding domain is simply a coiled-coil which binds BtuB at a 45° angle, inducing conformational changes in the loops (Kurisu *et al.*, 2003). The colicin Ia receptor-binding domain 'tip', consisting of a pair of antiparallel β-strands and four α-helices, displaces a lid to interact with Cir, also at a 45° angle (Buchanan *et al.*, 2007). A long coiled-coil makes up the rest of the receptor-binding domain, connecting the translocation domain to the cytotoxic pore-forming domain (Wiener *et al.*, 1997). The 45° angle serves to position the translocation domains away from the receptor such that they can interact with translocator porins. The fact that pyoS2^{NTD} binds to FpvAI at a more perpendicular angle to the membrane plane suggests additional translocator OMPs may not be required.

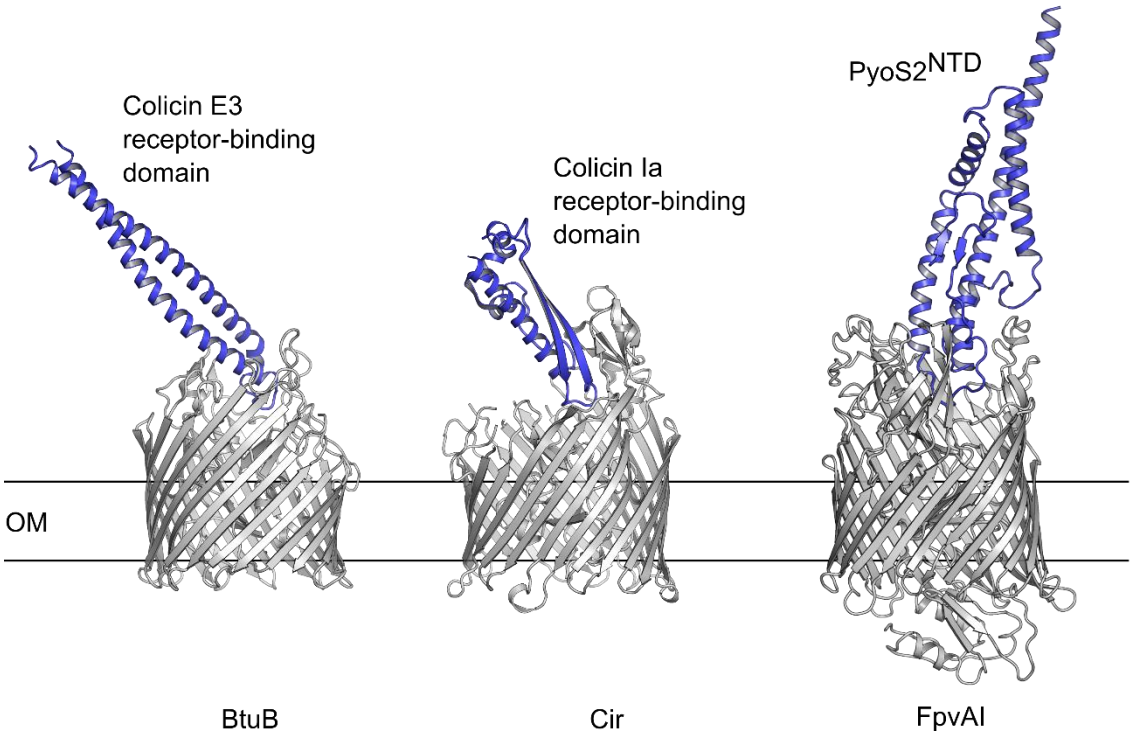

Figure 4-14. Structural comparison of three bacteriocin-receptor complexes.
Crystal structures of BtuB bound to the colicin E3 receptor-binding domain (PDB ID 1UJW (Kurisu *et al.*, 2003)), Cir bound to the colicin Ia receptor-binding domain (PDB ID 2HDI (Buchanan *et al.*, 2007)) and FpvAI bound to pyoS2^{NTD} (this study) illustrate key differences between bacteriocin-receptor complexes.

Analysis of the FpvAI-pyoS2^{NTD} binding surface identified 49 interfacial residues, including 14 hydrogen bonds and a salt bridge. The total buried surface area is 1556 Å^2, greater than the reported values of 1287 Å^2 and 1533 Å^2 for colicins E2 and E3, respectively, bound to BtuB. High affinity complexes (<1 nM) have an average of ten hydrogen bonds and an average buried surface area of 1600 Å, comparable to the FpvAI-pyoS2^{NTD} interface (Lo Conte *et al.*, 1999). The extracellular loops of FpvAI make up the majority (~88%) of the interface surface area, contributing all but one hydrogen bond and also the salt bridge. The high affinity (~240 pM) interaction between FpvAI and pyoS2^{NTD} is implicated in these interface statistics, though, as discussed previously, Δ1-45pyoS2^{NTD} binds ~1000-fold weaker. This truncated construct loses seven hydrogen bonds involving residues Arg30, Ser32, Pro41 and Pro45 of pyoS2, and Tyr200, Gln446, Tyr448, Tyr745, Ser750, Trp752 and Tyr796 of FpvAI (Figure 4-9). Most of the PRR directly contacts the plug domain surface, yet only participates in a single hydrogen bond between the Tyr200 hydroxyl and the backbone carbonyl of Pro41. The remaining hydrogen bonds contact the barrel and loops. In addition to hydrogen bonding, conformational changes in the plug greatly improve packing and therefore van der Waals contacts between the two proteins, likely contribute significantly to binding affinity.

The most significant structural differences between unliganded FpvAI and FpvAI bound to Fe-Pvd or pyoS2 are localised to the plug domain, particularly involving residues 225-234. This is one of the substrate-binding loops common to all TBDTs (Chimento *et al.*, 2005). It was suggested that these conformational changes are propagated to the periplasmic side of the plug to expedite engagement of TonB1 (Greenwald *et al.*, 2009), although there are no obvious movements in the TonB1-box itself, positioned between the plug and signalling domains. However, there are localised movements in the vicinity of the TonB1-box, as seen by comparing backbone RMSDs with the unliganded FpvAI

(Figure 4-11). This linker region, prior to the TonB1-box, connects the signalling and plug domains, allowing movements relative to one another. Consequently, in a bacterial cell, the signalling domain may exhibit a greater degree of conformational freedom, required to expose the TonB1-box. Indeed, the signalling domain must contact FpvR on the IM to upregulate both FpvAI expression and Pvd biosynthesis (Lamont *et al.*, 2002). A second hypothesis for the mechanism of TonB1-dependent transport involves a permanently accessible TonB1-box, but the unplugging event only occurs when a ligand is bound. In this scenario, conformational changes triggered in the plug may affect the stability of the plug domain, facilitating TonB1-dependent remodelling during the transport cycle. Since crystal structures only provide a snapshot of this transient process, the precise mechanism of TonB1 action is still poorly understood. It is clear, however, that structural changes in the plug domain are consistent in the binding of pyoS2^{NTD} and Fe-Pvd, which implies that translocation initiates by a common mechanism. Intriguingly, no conformational changes have been seen within the plug domains of colicin receptors, which has tended to rule out a direct role in translocation.

In our current understanding of translocation, bacteriocins must unfold for their passage through OMPs, then refold to a functionally active state once inside the cell. Reduced mechanical stability is therefore desired for efficient bacteriocin import, where pulling forces, delivered by the Ton/Tol systems, unfold the protein (Hann *et al.*, 2007, Gumbart *et al.*, 2007, Zhang *et al.*, 2008, Farrance *et al.*, 2013). Despite being relatively thermostable due to efficient packing of their hydrophobic cores, α-helical proteins tend to be less mechanically stable than β-sheet proteins (Brockwell *et al.*, 2003), which probably explains why many bacteriocins are mostly α-helical. CD-based thermal denaturation assays showed pyoS2^{NTD} reversibly unfolds with a T_m of 50 °C, similar to the colicin E1 receptor-binding domain at 52 °C (Griko *et al.*, 2000). This stability is

probably driven by a well-packed hydrophobic core, as well as the abundance of lysine and glutamic acid residues creating numerous long range electrostatic interactions. The N-terminal β-hairpin is also implicated in the stability of the pyoS2^{NTD} helical domain. Specifically, the sidechains of Ile23, Ile24 and Tyr26 shield a hydrophobic surface which decreases thermal stability by 6 °C when removed (Δ1-30pyoS2^{NTD}). During import, the removal of the β-hairpin may facilitate translocation by allowing the helices to unfold more readily. The precise role of the β-hairpin will be discussed in subsequent chapters.

4.4. Conclusions

PyoS2^{NTD} is composed of five α-helices with an N-terminal pre-sequence containing an anti-parallel β-hairpin motif. The receptor-binding mode is unique when compared with other bacteriocin-receptor complex structures, and the overall fold appears to be novel. High-affinity binding is mediated by a large buried surface area, numerous hydrogen bonds, and optimal packing through movements in the loops and plug domain. Importantly, the PRR closely mimics the shape of Fe-Pvd, and induces identical conformational changes in the plug domain. This suggests pyoS2^{NTD} and Fe-Pvd may import by a common mechanism, exploiting FpvAI as a translocation channel. The helical fold of the pyoS2^{NTD} suggests it may be force-labile, but is stabilised by an N-terminal β-hairpin which shields a hydrophobic patch on the helices. Removal of the β-hairpin may therefore expedite unfolding during import. Crucially, solving the crystal structure has also enabled the design of further experimental approaches for complete biochemical characterisation of the translocation mechanism, as will be described in subsequent chapters.

Chapter 5. Outer membrane translocation of pyoS2

5.1. Introduction

Our current understanding of the molecular mechanisms of bacteriocin translocation through the cell envelope is poor. In Gram-negative bacteria, the delivery of cytotoxic effector domains to their subcellular target requires breaching the barrier of the OM, and for some bacteriocins, also the IM. To achieve this, bacteriocins exploit cell envelope proteins such as porins, nutrient transporters, and the Ton and Tol systems (Kleanthous, 2010a). In contrast to pyocins, the mechanisms of colicin translocation have been active areas of research so the following introduction will focus on our current understanding of colicin translocation.

High affinity binding to an OM receptor is the first stage in colicin translocation. This is followed by recruitment of additional 'translocator' proteins which direct signalling epitopes into the periplasm where they interact with the Tol and Ton systems. Colicins which exploit the Tol system are classified as group A, and those which use the Ton system are group B colicins (Papadakos *et al.*, 2012). The enzymatic group A colicins, colicins E2-E9, bind their primary receptor BtuB at an acute angle to the membrane surface (Soelaiman *et al.*, 2001, Klein *et al.*, 2016). Next, the IUTD passes through a single OmpF (or OmpC) β-barrel lumen where OmpF-binding site (OBS) 2 stably associates with the barrel wall. At the extreme N-terminus, OBS1 binds within another barrel lumen of the OmpF trimer in reverse orientation from OBS2. This holds the TolB binding epitope found between OBS1 and OBS2 in a fixed orientation presumably to facilitate binding to the periplasmic TolB (Housden *et al.*, 2010). The resulting translocon complex consists of the colicin bound to BtuB, OmpF and TolB, the latter coupling the

colicin to the PMF through its interaction with the TolQRA complex in the IM (Housden *et al.*, 2013).

Group B colicins translocate in a distinct mechanism from group A colicins. Colicin Ia uses Cir as its receptor before recruiting a second copy of Cir as the translocator (Jakes and Finkelstein, 2010). Because Cir is a plugged TBDT, plug displacement through engagement of TonB with the Cir TonB-box, is essential for entry of the colicin Ia IUTD. Furthermore, the colicin Ia IUTD houses its own TonB-box which is essential for import and activity (Buchanan *et al.*, 2007). It is possible that the IUTD mimics the endogenous ligand in order to activate the receptor for translocation (Kleanthous, 2010b), although this has yet to be demonstrated.

As for the S-type pyocins, no specific translocator proteins have been identified and only a few receptors have been discovered. The translocation mechanisms for pyocins have therefore remained elusive. Pyocins are thought to differ from the colicins in their domain organisation with centrally located translocation domains and N-terminal receptor-binding domains. Consequently, the translocation mechanism may be considerably different from that of colicins. Despite this, the TonB-dependence of the known pyocin receptors, FpvAI, FpvAII and FptA may play a role in import analogous to group B colicins. Chemical potential energy from the PMF is transduced to the OM in the form of mechanical energy by the TonB-ExbB-ExbD complex in the IM. It is not clear whether this mechanical force is generated by rotary action, lateral diffusion, or retraction, but nevertheless, this force acts on the TonB-box of TBDTs to induce remodelling of the plug domain (Gumbart *et al.*, 2007, Klebba, 2016). *P. aeruginosa* possesses three TonB proteins; TonB1 is the primary energy transducer for nutrient receptors including FpvAI (Poole *et al.*, 1996, Takase *et al.*, 2000, Adams *et al.*, 2006), TonB2 plays a minor role in nutrient transport (Zhao and Poole, 2000) and TonB3 is required for twitching motility

(Huang *et al.*, 2004). Requirement of the Ton system would therefore suggest a role for the PMF in translocation akin to the import of group B colicins (Cascales *et al.*, 2007).

Excluding cytotoxic domain-immunity protein complexes, limited structural information is available for S-type pyocins (Joshi *et al.*, 2015, Klein *et al.*, 2016). It is therefore difficult to ascertain whether pyocins possess IUTDs similar to colicins which can be up to 83 amino acids in length. Prediction algorithms repudiate the existence of extended IUTDs but suggest that pyocin N-termini may lack substantial secondary structure. The pyoS2^{NTD} crystal structure described in Chapter 4 revealed that the N-terminus is ordered with a β-hairpin docked against the helical bundle. However, high B-factors suggest this region may be dynamic and therefore may play an active role in translocation.

The aims of this chapter were to explore the requirements of pyoS2 translocation by developing a fluorescence assay to monitor pyoS2 translocation *in vivo*. The PMF and TonB-dependence of translocation could then be probed using chemical ionophores and TonB knockout strains, respectively. Furthermore, import assays would also delineate the minimal domains of pyoS2 required for translocation and identify individual motifs that may be important, including the N-terminal β-hairpin.

5.2. Results

5.2.1. Developing a fluorescence assay for pyoS2 translocation

Firstly, the ability to specifically label live *P. aeruginosa* using fluorophore conjugated pyoS2^{NTD} was investigated. A cysteine residue was introduced at the C-terminal end of the pyoS2^{NTD} by site-directed mutagenesis for conjugation to Alexa Fluor maleimide-fluorophores. A labelling efficiency of 95% for Alexa Fluor 488-conjugated pyoS2^{NTD} (pyoS2^{NTD}-AF488) was estimated spectrophotometrically using λ_{max} at 280 nm and 494 nm for protein and label, respectively (Figure 5-1). Fluorophore labelling efficiencies were typically >90% for other constructs used in this study. Because FpvAI is tightly regulated by iron concentration, *P. aeruginosa* cultures were grown in iron-free M9 minimal media supplemented with 10 mM glucose and 2 mM $MgSO_4$. Incubating pyoS2^{NTD}-AF488 with live FpvAI-expressing *P. aeruginosa* localises fluorescence to the cells (Figure 5-2). Specific labelling of FpvAI was confirmed by the lack of fluorescence labelling in the FpvAI-transposon mutant strain PW5036 (Figure 5-2). Next, the diffusion dynamics of the fluorescent pyoS2^{NTD} were probed using fluorescence recovery after photobleaching (FRAP) experiments. FRAP uses a high laser power to bleach fluorescence at a specific location and diffusion of non-bleached fluorophores brings about fluorescence recovery. It was expected that pyoS2^{NTD} bound to FpvAI would be diffusion restricted and no fluorescence recovery would be observed, as seen for other bacteriocins bound to OMP receptors (Rassam *et al.*, 2015). However, this was not the case. FRAP on fast timescales (<1 second) showed that fluorescent pyoS2^{NTD} is in a freely diffusing environment which does not correlate with the diffusion rates for OMPs (Figure 5-3). Contrary to previous suggestions (Michel-Briand and Baysse, 2002), it appears that pyoS2^{NTD} functions not only as a receptor-binding domain but is capable of translocation across the OM independent of the other pyocin domains.

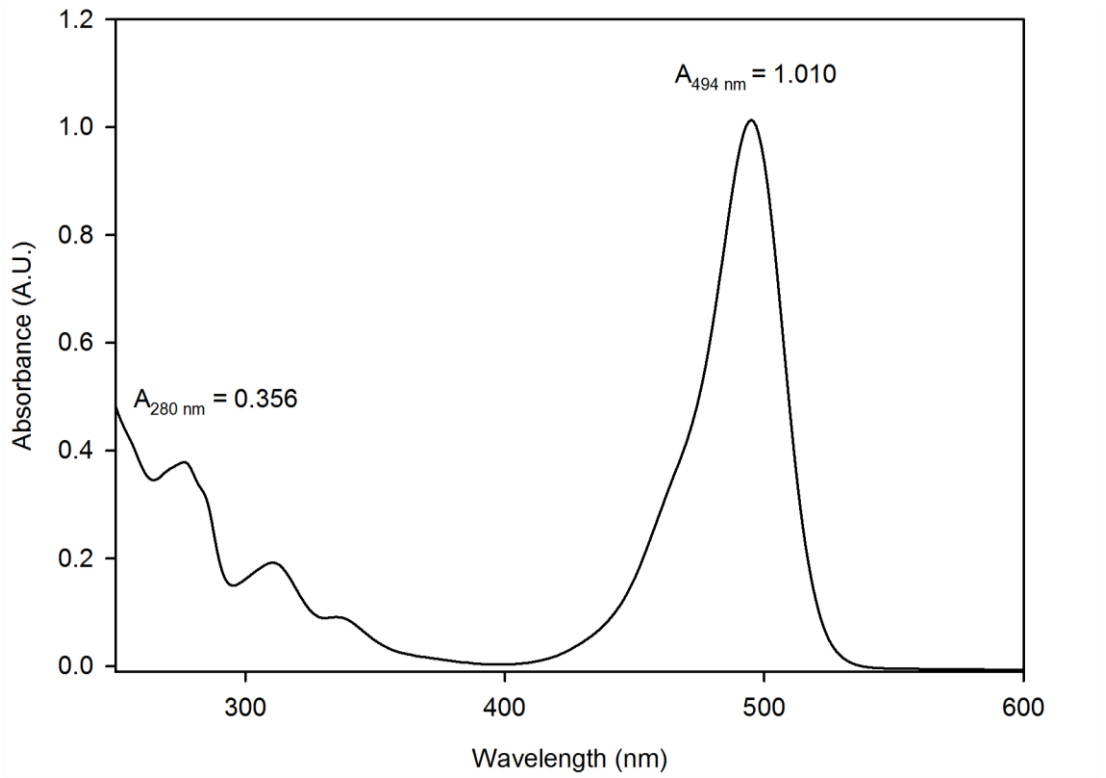

Figure 5-1. Estimation of labelling efficiency of Alexa Fluor 488 conjugates.
UV-visible absorbance spectrum of pyoS2^{NTD}-AF488. Absorbance maxima at 280 nm and 494 nm were used to determine a labelling efficiency of 95% (see Materials and Methods).

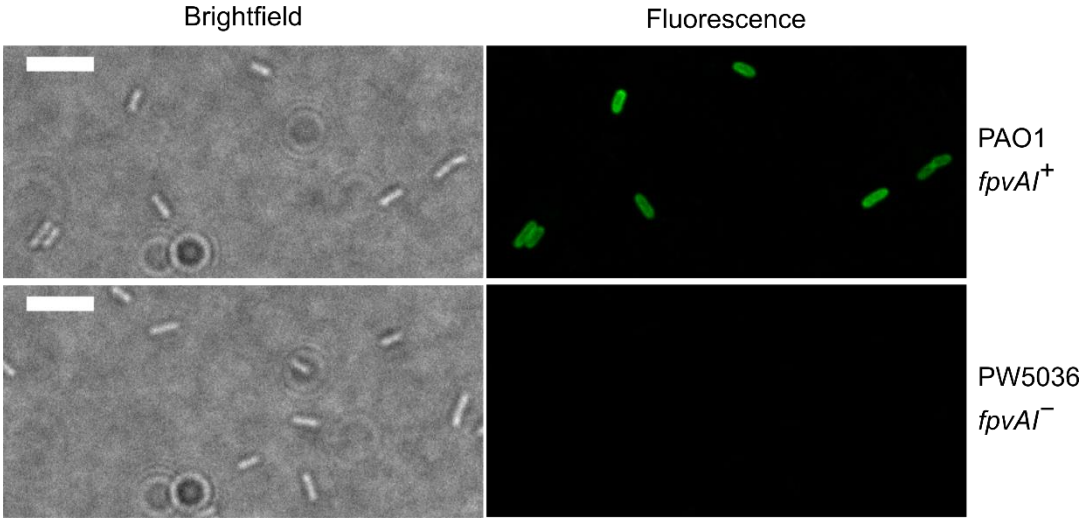

Figure 5-2. FpvAI-specific fluorescence labelling of live *P. aeruginosa*.
Brightfield and confocal fluorescence microscopy images of FpvAI-expressing *P. aeruginosa* PAO1 labelled with pyoS2^{NTD}-AF488. The PAO1 *fpvA*$^{-}$ transposon mutant PW5036 (*fpvA*-H02::ISlacZ/hah) exhibits no labelling. Scale bars, 5 µm.

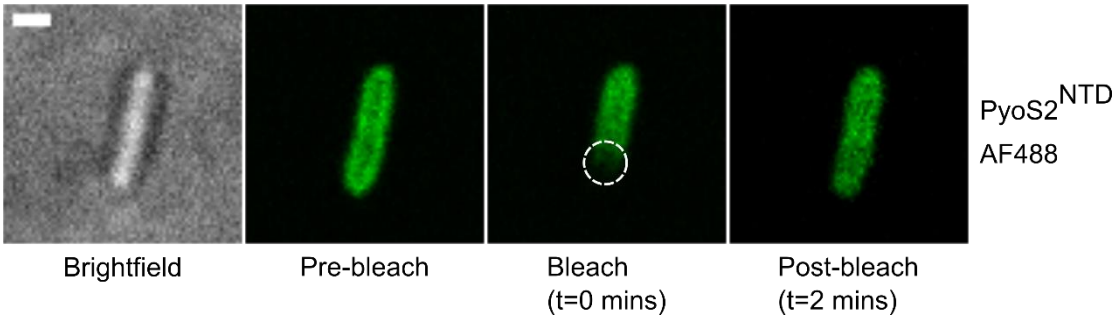

Figure 5-3. PyoS2^{NTD} translocates to the periplasm.
FRAP experiments on PAO1 cells labelled with pyoS2^{NTD}-AF488 highlighting the bleached region *(dashed circle)*. FRAP suggests pyoS2^{NTD}-AF488 has translocated to the periplasm where it can diffuse laterally. Scale bar, 1 µm.

5.2.2. PyoS2 translocation requires the PMF

Next, the import requirements of pyoS2^{NTD} were investigated in greater detail starting with the PMF. To determine whether pyoS2^{NTD} import is dependent on the PMF, cells were pre-treated with the protonophore CCCP. CCCP shuttles protons across the IM to dissipate the PMF, depleting cells of their energy source. Anionic deprotonated CCCP acquires a proton in the periplasm making it electrochemically neutral and more able to permeate the IM, releasing the proton in the cytoplasm. As evident by a lack of fluorescence recovery, CCCP-treated cells did not import pyoS2^{NTD} which demonstrates translocation is an energy-dependent process (Figure 5-4).

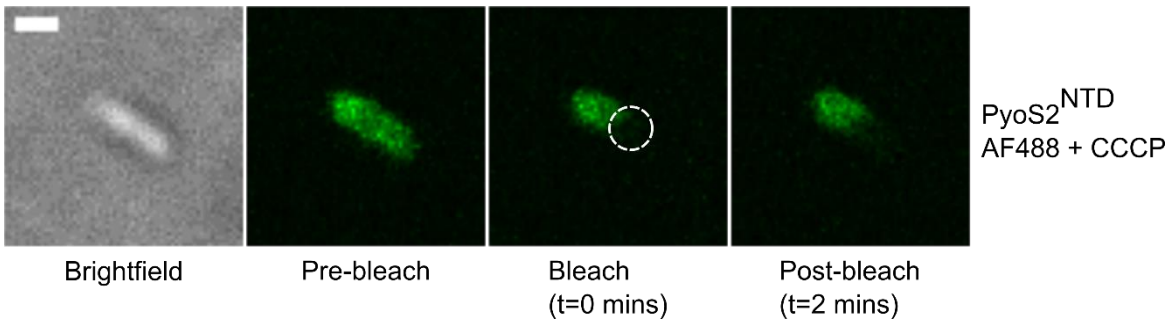

Figure 5-4. Translocation of pyoS2^{NTD} is dependent on the PMF.
FRAP experiments on *P. aeruginosa* PAO1 cells labelled with pyoS2^{NTD}-AF488 pre-treated with 100 µM CCCP which depletes the PMF. The bleached region is highlighted (*dashed circle*). The absence of FRAP in these experiments suggests pyoS2^{NTD} remains bound to FpvAI in the OM where lateral diffusion is restricted. Scale bar, 1 µm.

5.2.3. PyoS2 killing requires TonB1

Because FpvAI is a TBDT, the role of TonB in pyoS2 toxicity was investigated. To determine which of the three TonB proteins is required for pyoS2 toxicity, activity was tested against *tonB* knockout strains of *P. aeruginosa* (kindly provided by Prof Iain Lamont, University of Otago) using plate-based killing assays. The parent strain of these knockouts is PAO6609, a PAO1 derivative which expresses pyoS2 and its immunity protein ImS2. To subvert the endogenous resistance of these strains to pyoS2, the pyoS2-E2 chimera described in Chapter 3 was used. An additional complexity is that the *tonB1* knockout (K1040) is compromised for growth without excess iron supplementation, yet excess iron is known to downregulate FpvAI (Shirley and Lamont, 2009). The difference in killing activity against the wild-type parent strain PAO6609 with and without excess iron supplementation was shown to be minimal but still had a slight effect (Figure 5-5). The *tonB1* knockout was completely resistant to killing but both *tonB2* (K1407) and *tonB3* (MS231) knockouts were sensitive demonstrating that pyoS2 killing is TonB1-dependent (Figure 5-6). This resistant phenotype can be explained by the requirement of TonB1 for transport of FpvAI substrates. Indeed, an interaction between FpvAI and TonB1 was essential for pyoS2 activity (Figure 5-7) as shown by killing assays using a *P. aeruginosa* strain expressing FpvAI mutated in the TonB1-box (PAO *fpvA attP*::*fpvA*$_{TBM}$) (Shirley and Lamont, 2009). In this strain, the FpvAI TonB-box ATMITSN is mutated to ATAAAAN, rendering the cells completely resistant to pyoS2.

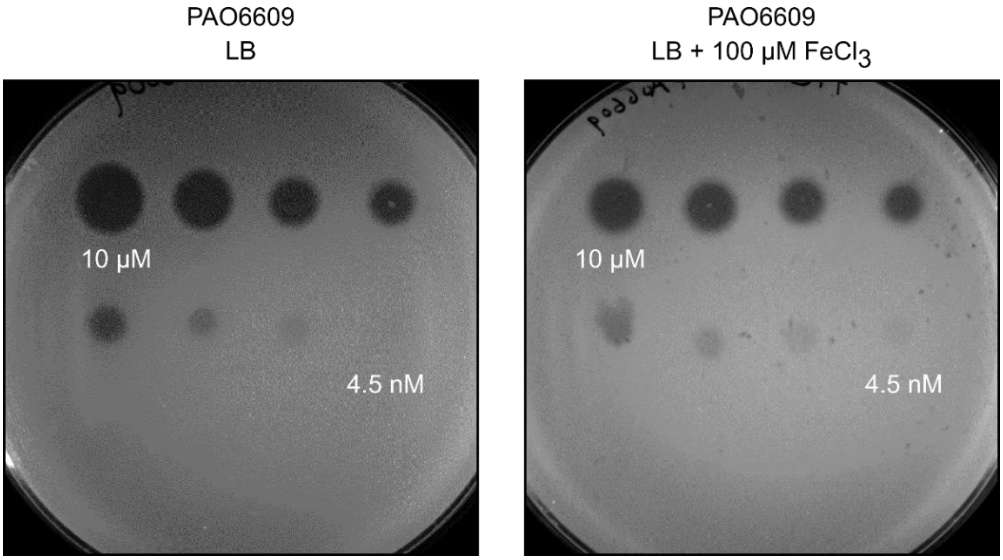

Figure 5-5. Effect of iron on *P. aeruginosa* PAO6609 killing susceptibility by pyoS2-E2.
Plate toxicity assays against PAO6609 grown in LB and LB supplemented with 100 µM $FeCl_3$. Bacterial lawns were spotted with 3-fold serial dilutions of pyoS2-E2 from 10 µM to 4.5 nM. Clearance zones indicate killing. Killing efficiency was marginally impaired with additional iron.

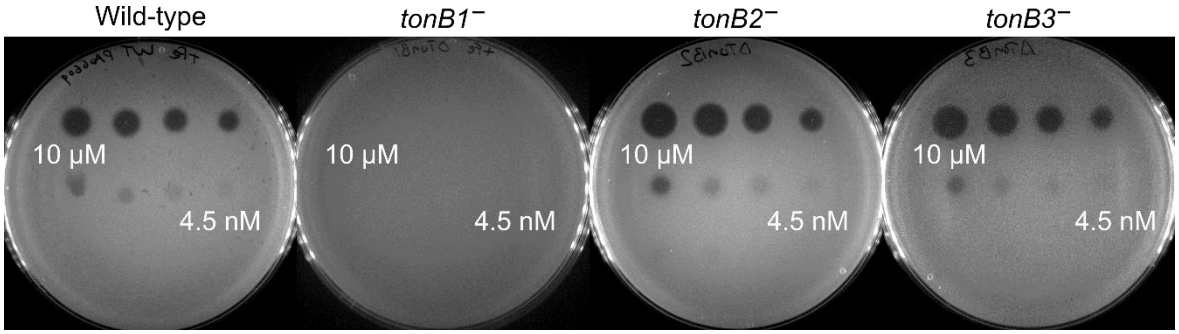

Figure 5-6. PyoS2 killing is TonB1-dependent.
P. aeruginosa toxicity assays using a purified, serially diluted pyoS2-E2 chimera on TonB deletion strains: PAO6609 (Wild-type), K1040 (*tonB1*⁻), K1407 (*tonB2*⁻) and MS231 (*tonB3*⁻). The pyoS2-E2 chimera was used to avoid pyoS2 resistance in PAO6609 cells. Clearance zones indicate cell killing. Only the *tonB1* deletion strain was resistant to pyoS2 killing.

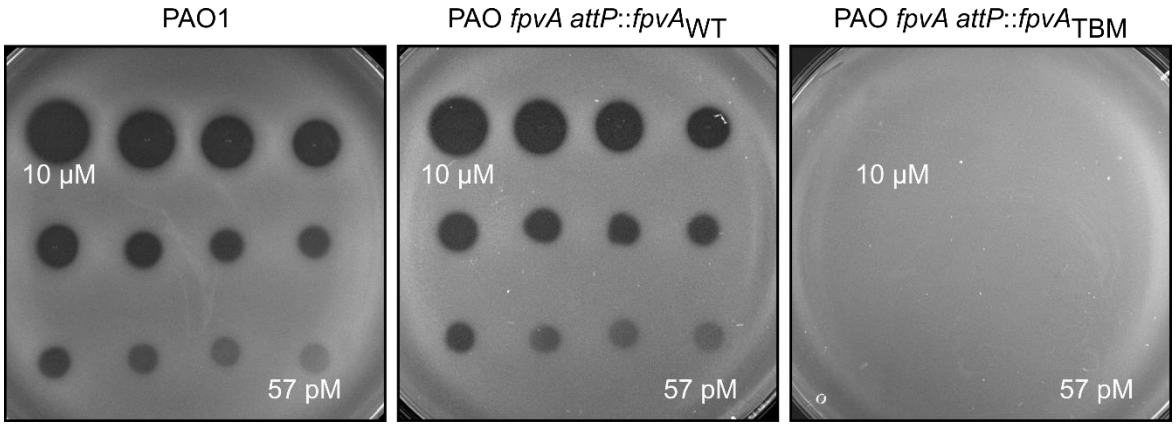

Figure 5-7. PyoS2 killing requires the FpvAI TonB-box.
P. aeruginosa toxicity assays using purified, serially diluted pyoS2-E2 chimera on PAO1, and strains with a functional TonB1-box (PAO *fpvA attP*::*fpvA*$_{WT}$) and a mutant TonB1-box (PAO *fpvA attP*::*fpvA*$_{TBM}$). Clearance zones indicate cell killing. The FpvAI TonB1-box mutant strain is resistant to pyoS2 killing.

5.2.4. The N-terminus of pyoS2 is essential for import

To further explore the role of TonB1 in pyoS2 activity, a potential interaction between the two proteins was investigated by ITC. Titration of pyoS2^{NTD} into TonB1 resulted in saturable endothermic binding with a K_d of 1 µM (Figure 5-8). Next, the TonB1 binding site, (the pyoS2 TonB1-box), was located by testing pyoS2 truncations for killing activity, translocation and *in vitro* binding. Starting with the removal of the first 30 residues (Δ1-30pyoS2^{NTD}), binding to TonB1 was profoundly affected (Figure 5-8) demonstrating that the TonB1-box resides somewhere in the N-terminal β-hairpin region. Moreover, a shorter truncation of the first 21 residues (Δ1-21pyoS2^{NTD}) abolished translocation, as seen in FRAP experiments (Figure 5-9A), and Δ1-21pyoS2 was unable to kill *P. aeruginosa* PA17 (Figure 5-9B). This narrows down the TonB1-box to the first β-strand of the β-hairpin which was further supported by site-specific photo-activated crosslinking experiments. When substituted for the UV-inducible amino acid crosslinker *p*Bpa, the first residue of this β-strand, Met11, effectively crosslinked to TonB1, confirming its position at the binding site (Figure 5-10). The first β-strand also exhibits similarity to

other *P. aeruginosa* TonB1-boxes and inhibited translocation and killing when mutated to alanine (EPGSMVIT→EPGAAAAT) (Figure 5-11A and B). This mutated construct, designated pyoS2^{NTD}TBM, still binds to TonB1 with a similar K_d of 1.7 µM but with exothermic binding enthalpy (Figure 5-11C), suggesting other regions are also involved in binding.

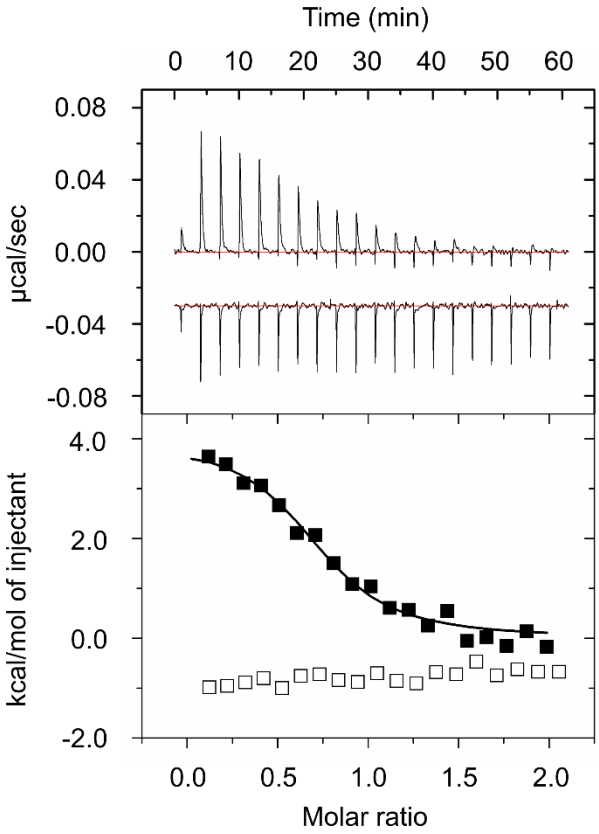

Figure 5-8. PyoS2^{NTD} binds to TonB1 through the N-terminus.
Binding of pyoS2^{NTD} *(filled squares)* and Δ1-30pyoS2^{NTD} *(open squares)* to TonB1 (residues 109-342) observed by ITC. PyoS2^{NTD} binding data from two independent experiments were fitted with a single sites binding model from which the following parameters were obtained: ΔH = 4.4 ± 0.4 kcal/mol, ΔS = 42.3 ± 1.70 cal/mol/K, N = 0.75 ± 0.03 sites, K_d = 0.96 ± 0.09 x 10^{-6} M.

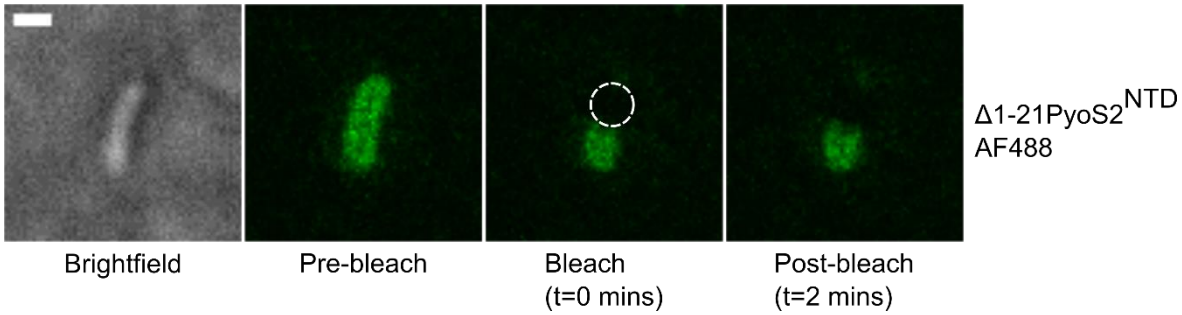

Figure 5-9. The first N-terminal β-strand is required for translocation.
FRAP experiments on PAO1 cells labelled with Δ1-21pyoS2^{NTD}-AF488. Lack of FRAP suggests Δ1-21pyoS2^{NTD}-AF488 remains bound on the OM. Scale bar, 1 µm.

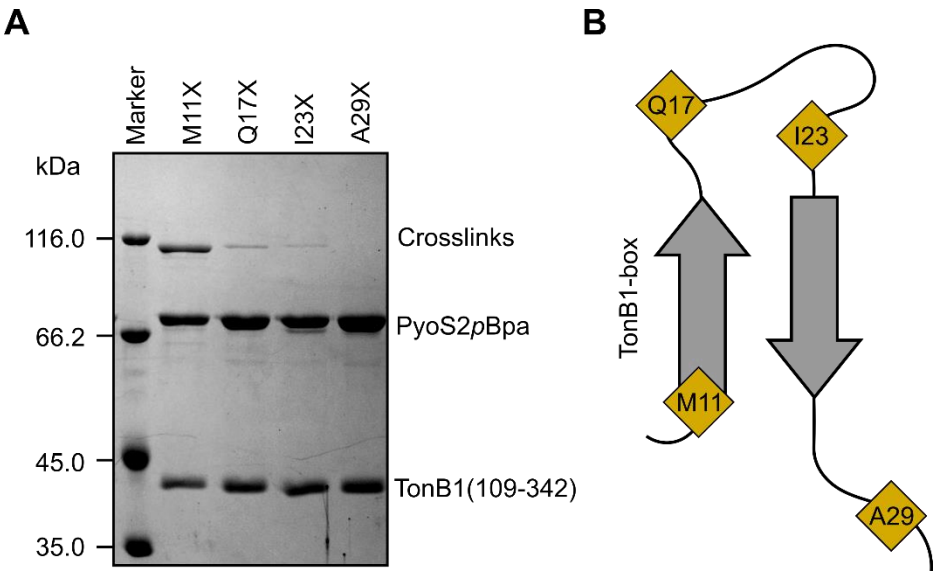

Figure 5-10. Photo-activated crosslinking the pyoS2 TonB1-box to TonB1.
A, Coomassie-stained 10% SDS-PAGE gel loaded with 10 µl samples of photo-activated crosslinking adducts of purified TonB1(109-342) and pyoS2*p*Bpa. Positions M11, Q17, I23 and A29 throughout the N-terminus were substituted with *p*Bpa (X). Met11*p*Bpa efficiently crosslinks to TonB1, confirming the first β-strand ($M^{11}VIT^{14}$) as the TonB1-box. Marker = Fermentas unstained protein standard. ***B***, Positions of the pyoS2*p*Bpa variants throughout the N-terminal β-hairpin.

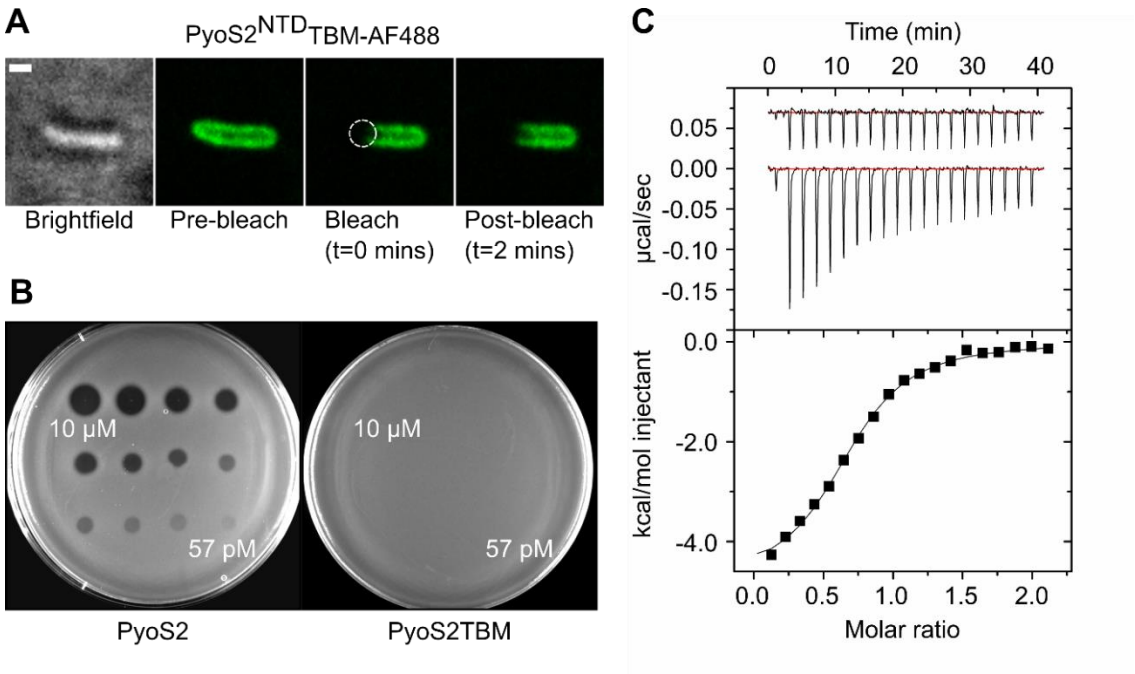

Figure 5-11. The pyoS2 core TonB1-box is located in the first β-strand.
A quadruple alanine mutation in the pyoS2 TonB1-box (EPGAAAAT), designated pyoS2TBM, blocks translocation. ***A***, FRAP experiments on *P. aeruginosa* PAO1 demonstrate pyoS2^{NTD}TBM-AF488 is unable to translocate. ***B***, Plate toxicity assays on *P. aeruginosa* PA17 show pyoS2TBM is inactive compared with wild-type pyoS2. ***C***, ITC data shows pyoS2^{NTD}TBM exhibits residual binding to TonB1(109-342). Heat of dilution control is included in the *upper panel*. Data were fitted with a single sites binding model from which the following parameters were obtained: ΔH = -4.8 ± 0.1 kcal/mol, ΔS = 10.3 cal/mol/K, N = 0.69 ± 0.01 sites, K_d = 1.7 ± 0.13 x 10^{-6} M.

Further support for the internal localisation of the pyoS2^{NTD}, in contrast to Δ1-21pyoS2^{NTD}-AF488, was demonstrated by the loss of fluorescence when exposing cells to trypsin (Figure 5-12). Surface accessible non-translocated pyoS2^{NTD}-AF488 was digested by trypsin resulting in loss of fluorescence whereas internalised pyoS2^{NTD}-AF488 was protected. Taken together, these data establish a role for the pyoS2 N-terminus in binding to TonB1 which couples the PMF for translocation.

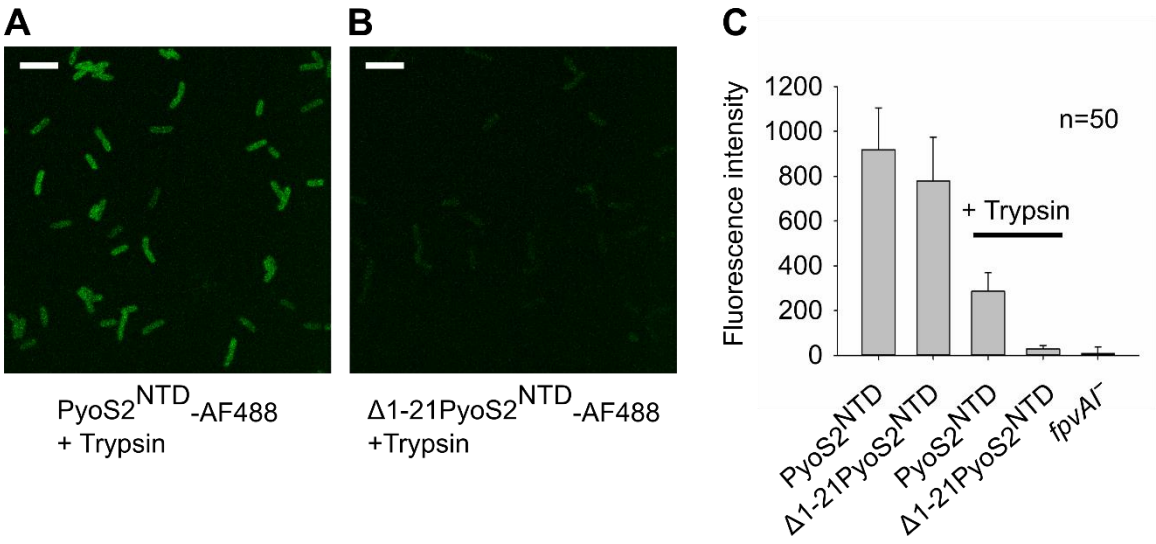

Figure 5-12. Labelling of *P. aeruginosa* PAO1 cells following trypsin treatment.
A, Translocated pyoS2^{NTD}-AF488 is protected from trypsin. ***B***, Surface-accessible Δ1-21pyoS2^{NTD}-AF488 is fully digested, leaving only autofluorescence visible. ***C***, Quantification of fluorescence intensity for *P. aeruginosa* PAO1 cells labelled with pyoS2^{NTD}-AF488 and Δ1-21pyoS2^{NTD}-AF488 with and without trypsin treatment, compared with *fpvA*$^{-}$ cells (PW5036).

5.2.5. Delivery of cytotoxic pore-forming domains into the periplasm

Further evidence of pyoS2^{NTD} translocation across the OM was sought by engineering fusions/chimeras to the domain that could deliver other cytotoxic agents to the periplasm. In this case, the cytotoxic pore-forming domains of pyoS5 (residues 301-498) and colicin Ia (residues 452-626) were fused onto the C-terminal end of pyoS2^{NTD} to generate pyoS2^{NTD}-S5 and pyoS2^{NTD}-Ia chimeras, respectively. Pore-forming domains target the IM from the periplasmic side resulting in membrane depolarisation and cell death. First, the activity of pyoS2^{NTD}-S5 was tested against *P. aeruginosa* PA17 by plate-based cytotoxicity assays resulting in effective cell killing comparable to wild-type pyoS2 or pyoS5 (Figure 5-13). The pyoS5 pore-forming domain of the chimera has very slight activity against PAO1 which can be seen in the pyoS5 control but are mostly resistant due to expression of the pyoS5 immunity protein. As for pyoS2^{NTD}-Ia, killing activity was observed against PAO1 but it was noticed that zones of clearance were more apparent when using a smaller volume of cells to inoculate the soft agar lawn (Figure 5-14). The

results indicate that pyoS2^{NTD} alone is capable of delivering pore-forming cytotoxic domains to the periplasm which result in cell killing. This alludes to the possibility that pyoS2^{NTD} could be used for the targeted delivery of cytotoxic substances across the OM barrier. Attempts to conjugate vancomycin and a phage lysin onto pyoS2^{NTD} are described in the Appendix.

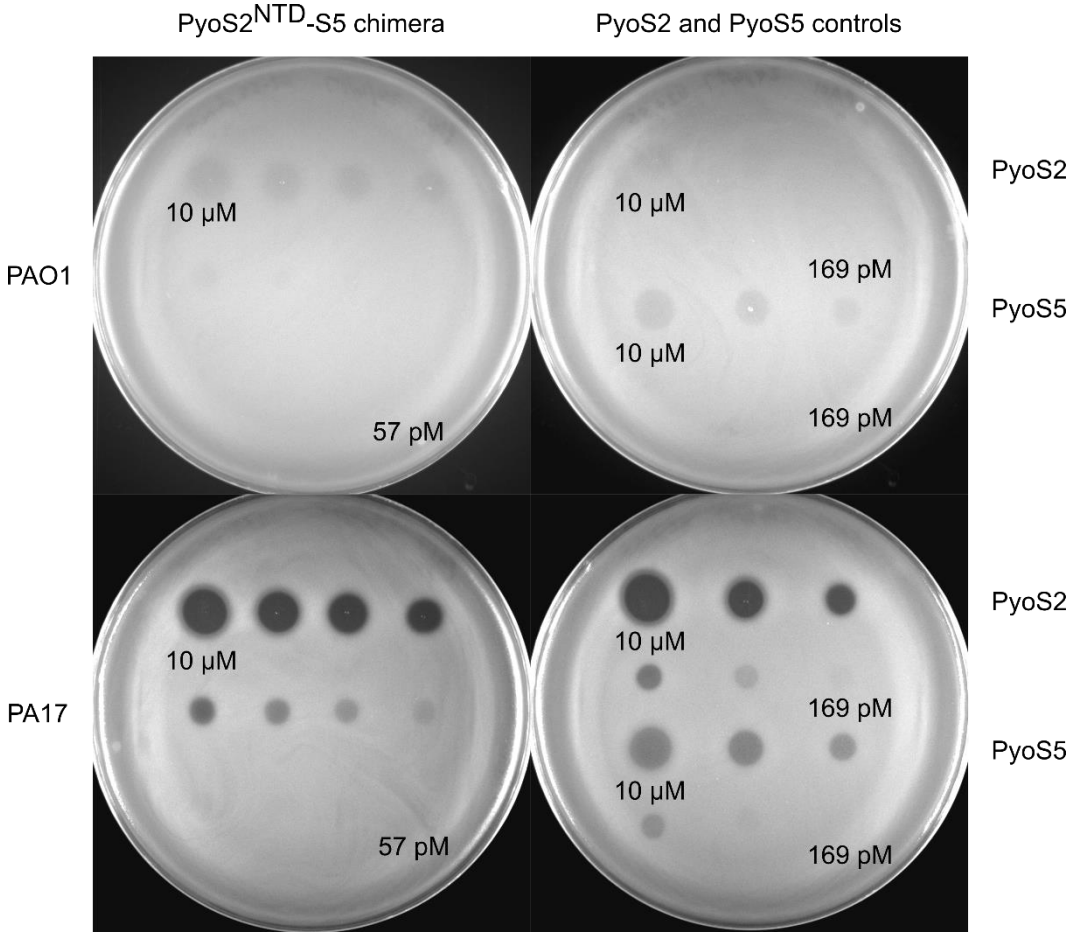

Figure 5-13. Killing activity of pyoS2^{NTD}-S5 chimera against *P. aeruginosa* PAO1 and PA17 strains.
Plate-based toxicity assays against PAO1 (*top*) and PA17 (*bottom*) using 3-fold serially diluted pyoS2^{NTD}-S5 chimera (*left*) and 9-fold serially diluted wild-type pyoS2/pyoS5 controls (*right*). PA17 is effectively killed by pyoS2^{NTD}-S5 at comparable levels to the controls but PAO1 is mostly resistant. PyoS2^{NTD} can therefore deliver a cytotoxic pore-forming domain into the periplasm.

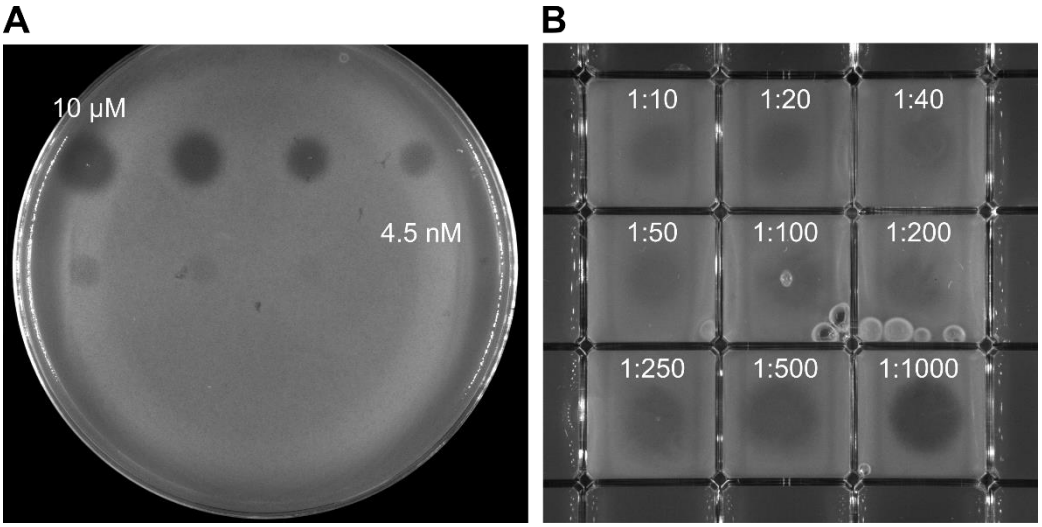

Figure 5-14. Killing activity of pyoS2^{NTD}-Ia chimera against *P. aeruginosa* PAO1.
A, Plate-based toxicity assays against PAO1 using 3-fold serially diluted pyoS2^{NTD}-Ia chimera. 5 ml soft agar was inoculated with 5 µl bacterial culture (1:1000). ***B***, Lawns of PAO1 were produced by inoculating 1 ml soft agar with 100, 50, 25, 20, 10, 5, 4, 2 and 1 µl bacterial culture (1:10, 1:20, 1:40, 1:50, 1:100, 1:200, 1:250, 1:500 and 1:1000, respectively). Lawns were spotted with 2 µl of 10 µM pyoS2^{NTD}-Ia chimera. The most pronounced clearance zones are seen at lower inoculation volumes suggesting killing is relatively slow.

5.3. Discussion

This chapter demonstrated that pyoS2^{NTD} is the minimal translocation domain which is imported to the *P. aeruginosa* periplasm in a PMF- and TonB1-dependent manner. FRAP experiments showed that fluorescent pyoS2^{NTD} is in a freely diffusing environment, which is not consistent with pyoS2^{NTD} remaining bound to its OMP receptor that would have impeded its lateral diffusion. In Gram-negative bacteria, OMPs are sequestered into large macromolecular clusters known as OMP islands, slowing the diffusion of OM complexes in contrast to periplasmic or IM proteins which diffuse freely (Rassam *et al.*, 2015, Gibbs *et al.*, 2004, Oddershede *et al.*, 2002, Spector *et al.*, 2010). Fast fluorescence recovery therefore indicated pyoS2^{NTD} was localised to the periplasm. Additionally, cells retained their fluorescence after trypsin treatment further supporting the internalisation of pyoS2^{NTD}. It is also clear from the quantification of fluorescence intensity following trypsin treatment that two populations exist, a translocated population representing about

a third of the total fluorescence contribution, and a non-translocated population that remained bound to FpvAI on the cell surface. Because translocation is dependent on TonB1, competition with other TBDTs and limited copies of TonB1 may impede the rate of import. This has been observed previously between bacterial nutrient uptake systems (Kadner and Heller, 1995).

The TonB1-dependence of pyoS2^{NTD} import was predicted based on its exploitation of the TonB1-dependent transporter FpvAI, and was confirmed by testing killing activity against TonB1, TonB2 and TonB3 knockout strains. Moreover, the TonB1-box of FpvAI was shown to be essential for pyoS2 killing suggesting the import pathway mirrors that of the ligand Fe-Pvd. These observations indicate that FpvAI plays a direct role in translocation, possibly functioning as the pyoS2 translocation channel. In addition to the TonB-box of the transporter, some bacteriocins possess their own TonB-box. For example, colicins B and Ia that exploit the TBDTs FepA and Cir, respectively, have their own TonB-box motif within their N-termini which is essential for their activity (Mende and Braun, 1990, Jakes and Finkelstein, 2010). There have been no examples of bacteriocins binding to TonB *in vitro*, though direct binding between the Tol-dependent colicins N and E9 to components of the Tol system, has been demonstrated (Isa Gokce, 2000, Sarah L. Hands et al, 2005). In this study, the endothermic binding demonstrated between TonB1 and pyoS2^{NTD} with 1 μM affinity is similar to reported K_d values for TonB1-FpvAI (Adams et al, 2006) although *in vivo* TonB-binding events during transport cycles likely differ. Examples of protein-protein interactions with endothermic binding are relatively rare and are always driven by entropy since positive ΔH values are thermodynamically unfavourable. The large increase in entropy, which compensates for the positive enthalpy change, is often attributed to the displacement of water molecules

at the binding interface, or the localised unfolding of one or both binding partners (Chodera and Mobley, 2013). Indeed, both may be implicated in binding to TonB1.

Identifying the precise pyoS2^{NTD} TonB1-box was unexpectedly challenging and was initially narrowed down to the N-terminal β-hairpin region. The Δ1-30pyoS2^{NTD} construct, lacking the entire hairpin region, did not bind TonB1 *in vitro* and removal of the first β-strand (Δ1-21pyoS2^{NTD}) was sufficient to inhibit translocation and cell killing. In addition, Met11 effectively crosslinked to TonB1 and a quadruple alanine mutation (EPGSMVIT→EPGAAAAT) rendered pyoS2 inactive by inhibiting translocation. From these data, the first β-strand is at least part of the pyoS2 TonB1-box. Binding to TonB proteins often involves β-strand complementation whereby a single β-strand, or a stretch of amino acids with strand propensity forms the fourth β-strand of the TonB β-sheet (Shultis *et al.*, 2006, Pawelek *et al.*, 2006). Furthermore, a strong tendency to bind β-strands explains the frequently observed dimerisation of the TonB CTD by a strand exchange mechanism (Koedding *et al.*, 2004, Chang *et al.*, 2001). The relevance and implications of TonB dimerisation for *in vivo* function is still open to debate (Postle *et al.*, 2010, Klebba, 2016). The TonB1 construct used in this study encompasses the entire periplasmic domain and remained monomeric in solution. The first β-strand also exhibits similarity with other TonB1-boxes in *P. aeruginosa.* These typically begin with an acidic/hydrophobic residue pair closely followed by four residues with β-strand propensity (Figure 5-15). Residues with the greatest β-strand propensity include the β-branched amino acids threonine, isoleucine and valine as well as methionine, tyrosine and phenylalanine (Minor and Kim, 1994). TonB-boxes in *E. coli* also begin with a conserved acidic residue which participates in a salt bridge, followed by a β-strand rich in β-branched amino acids. Asp6 of BtuB and Arg158 of TonB have been suggested to be involved in long range electrostatic association and nucleation of the β-strand (Shultis *et*

al., 2006). Since TonB1-boxes in *P. aeruginosa* also begin with an acidic residue, a similar binding mechanism with both TBDTs and pyocins, may exist. Substituting TonB1-box residues with alanine abolished killing and translocation, but still retained TonB1 binding *in vitro* which implies the TonB1 binding region extends beyond the β-strand. Moreover, the opening of the N-terminal β-hairpin may provide the favourable entropy change which is disrupted by the mutation such that binding proceeds exothermically. Since the role of TonB is to convert chemical potential energy from the PMF to a mechanical force which is applied to the TonB-box of TBDT plug domains (Hickman *et al.*, 2017, Gumbart *et al.*, 2007), the ability of TBDTs to function requires this interaction to be sufficiently strong. It is also heavily dependent on the dissociation rate since mechanical remodelling of the plug domain needs to occur before dissociation of TonB1. Altered binding kinetics may therefore account for translocation inhibition and the resulting loss of pyoS2 activity.

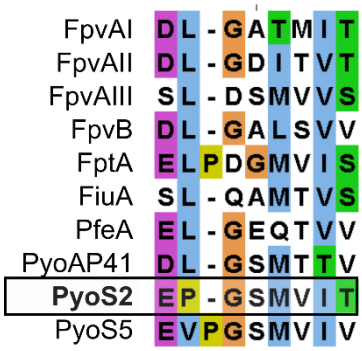

Figure 5-15. MUSCLE alignment of TonB1-boxes in *P. aeruginosa*.
TonB1-boxes for seven TBDTs and three pyocins, aligned using MUSCLE, demonstrates similarity. In most cases, an acidic/hydrophobic pair is closely followed by β-branched residues. The TonB1-box of pyoS2 is highlighted.

Overall, the data presented in the chapter implies that import requires TonB1-dependent remodelling of the FpvAI plug domain, and a TonB1-dependent force on the pyoS2 N-terminus. These two TonB1-dependent steps provide the force required to dissociate the high-affinity complexes between pyoS2 and FpvAI, and the DNase domain and ImS2.

Finally, the ability of pyoS2^{NTD} to transport other cytotoxic payloads across the OM was investigated. Fusions of the pyoS5 and colicin Ia pore-forming domains directly onto the C-terminus of pyoS2^{NTD} exhibited cytotoxicity. The pyoS2^{NTD}-S5 chimera effectively killed *P. aeruginosa* PA17 showing the pyoS2^{NTD} can import the pyoS5 pore-forming domain into the periplasm, where it can insert into the IM. Killing activity against PAO1 was poor due to expression of the pyoS5 immunity protein ImS5, and the residual killing implies ImS5 is not able to offer complete protection against pyoS5 activity. The pyoS2^{NTD}-Ia chimera was able to kill PAO1, showing that pyoS2^{NTD} can deliver an *E. coli* pore-forming domain with a lethal outcome. The clearance zones on the bacterial lawn, indicating cell killing, were more pronounced with lower inoculation volumes, which suggests cell growth outpaces killing. Rate of cell killing may be slower due to inefficient import across the OM, or slower insertion into the IM.

5.4. Conclusions

The data provided in this chapter explore the mechanisms of pyoS2 translocation across the OM of *P. aeruginosa*. It is now evident that pyoS2^{NTD} not only functions as a receptor-binding domain, but also as a translocator, specifically through the actions of the N-terminal β-hairpin. PyoS2^{NTD} is actively transported into the periplasm in a PMF and TonB1-dependent manner and crucially, an interaction between TonB1 and the first β-strand of pyoS2 appears to drive translocation. Additionally, the requirement of an intact FpvAI TonB1-box strongly suggests that FpvAI is exploited as the translocation channel just like Fe-Pvd. This will be further explored in Chapter 6. Finally, pyoS2^{NTD} alone is capable of delivering cytotoxic pore-forming domains into the periplasm resulting in cell killing.

Chapter 6. Mapping pyoS2^{NTD} translocation by photo-activated crosslinking

6.1. Introduction

The mechanism by which proteins are imported into bacteria is poorly understood, yet we know bacteriocins must reach their intracellular target and retain their activity. Protein import into mitochondria requires designated protein translocases (Wiedemann *et al.*, 2004) of which there are no known analogous systems in Gram-negative bacteria. The data presented in this thesis suggest that pyoS2 may follow the same translocation pathway as Fe-Pvd by activation of the receptor FpvAI, and engagement of the energy transducing Ton system. Unlike colicins, which often recruit OM porins, no specific translocators have been identified for pyocins. The majority of group A colicins deliver their disordered N-termini through the lumen of OmpF, with the exception of ColE1 which uses TolC (Housden *et al.*, 2013, Housden *et al.*, 2010, Zakharov *et al.*, 2004). The porin lumen is therefore most likely exploited as a translocation channel for the entire colicin, although this has not been formally shown. The mechanisms by which group B colicins translocate into cells remain elusive, with only colicin Ia known to hijack another copy of its receptor Cir (Jakes and Finkelstein, 2010). Cir is an *E. coli* TBDT that transports iron-siderophore complexes across the OM (Nikaido and Rosenberg, 1990). Whether other TBDTs moonlight as translocation channels for colicins, or indeed pyocins, is not known, but has been previously suggested for FepA and colicin B (Devanathan and Postle, 2007).

Bacteriocin translocation is an active process involving many transient protein-protein interactions that can only be studied in living bacteria. As a result, studies on translocation have been challenging. Chemical crosslinking is a useful method for

stabilising weak or transient protein-protein interactions *in vivo*, and in certain cases, can provide low-resolution structural information where other methods have been unsuccessful (Kluger and Alagic, 2004). Proteins can be non-specifically crosslinked using formaldehyde, which reacts with nucleophiles within macromolecules including the amino-terminus, and the sidechains of lysine, arginine, cysteine, histidine and tryptophan (Metz *et al.*, 2004). Formaldehyde crosslinking requires a moderately alkaline pH since ionisable sidechains only react when deprotonated, forming a methylol intermediate which dehydrates to a Schiff base. The Schiff base then readily reacts with another nucleophile, covalently linking adjacent functional groups (Hoffman *et al.*, 2015). The small size and reactivity makes formaldehyde ideal for quickly determining whether two proteins interact, but the lack of specificity limits its applicability to more detailed structural analysis. Greater specificity can be achieved using amine- or sulfhydryl-reactive crosslinkers containing N-hydroxysuccinimide or maleimide reactive groups, respectively. The reactive functional groups are usually linked with a variable length PEG-based spacer arm, which is particularly useful for probing intermolecular distances as shown for the σ^R-RsrA complex (Rajasekar *et al.*, 2016). Photo-activated crosslinkers are chemically modified amino acids which can be introduced into the primary protein sequence, allowing residue-specific crosslinking. Examples include derivatives of leucine, methionine, phenylalanine and tyrosine where crosslinking is activated by irradiation with light at particular wavelengths (Suchanek *et al.*, 2005, Kauer *et al.*, 1986). Under UV-irradiation at 365 nm, the benzophenone group in *p*Bpa is converted to a ketyl diradical, which readily reacts with C-H bonds within a 3-4 Å distance (Figure 6-1) (Dormán *et al.*, 2016). LC-MS/MS analysis of photo-activated crosslink adducts can then identify transient contact sites between proteins in living systems (Dietsche *et al.*, 2016).

This approach was used to delineate the secretion of the lipoprotein RcsF through the lumen of OmpF and OmpC (Konovalova *et al.*, 2014).

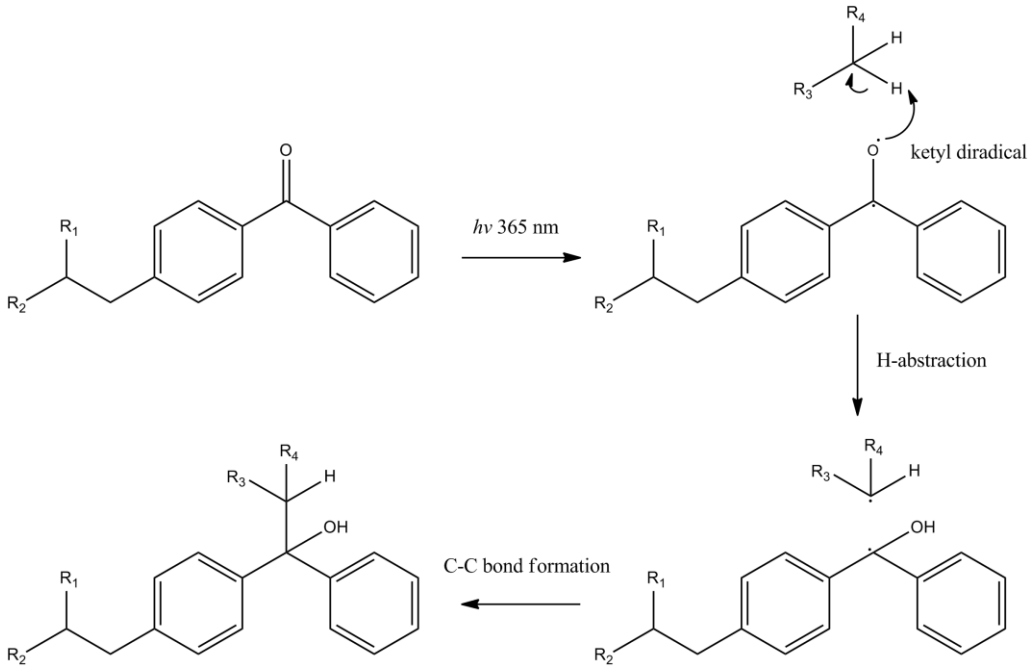

Figure 6-1. Crosslinking reaction mechanism for *p*Bpa.
UV-irradiation converts the benzophenone group to a ketyl diradical which abstracts a proton within 3-4 Å distance. If there is no abstractable proton, the diradical will return to the initial benzophenone within 120 µs. The remaining radicals readily recombine to form a new C-C bond (Dormán *et al.*, 2016).

The aims of this chapter were to use *in vivo* photo-activated crosslinking methods to map the pyoS2^{NTD} translocation pathway across the OM of *P.* aeruginosa. The equilibrium position of intermediate states can be favoured by first devising a strategy to stall import. Then, by substituting specific residues throughout the stalled pyoS2^{NTD} with the UV-inducible amino acid crosslinker *p*Bpa, translocation intermediates could be crosslinked during import into live cells. This chapter describes the development and optimisation of this *in vivo* crosslinking strategy, and the use of LC-MS/MS-based proteomics to map the crosslink sites. Using crosslinking data, along with the developments described in previous chapters, this work would ultimately provide a detailed mechanism of pyoS2 import, and describe the first complete model of bacteriocin translocation, across the OM.

6.2. Results

6.2.1. Stalling pyoS2 translocation using GFP

The crosslinking strategy designed to map the pyoS2 translocation pathway first involved stalling pyoS2^{NTD} during import. The FRAP experiments described in Chapter 5 demonstrated PMF-dependent translocation of pyoS2^{NTD} into the *P. aeruginosa* periplasm. This PMF-dependence was exploited by engineering a C-terminal GFP fusion that can resist unfolding with up to 100 pN of force (Dietz and Rief, 2004), whilst the PMF can only deliver ~20 pN (Farrance *et al.*, 2013). FRAP experiments on *P. aeruginosa* cells labelled with pyoS2^{NTD}GFP did not show fluorescence recovery, consistent with stalled translocation (Figure 6-2).

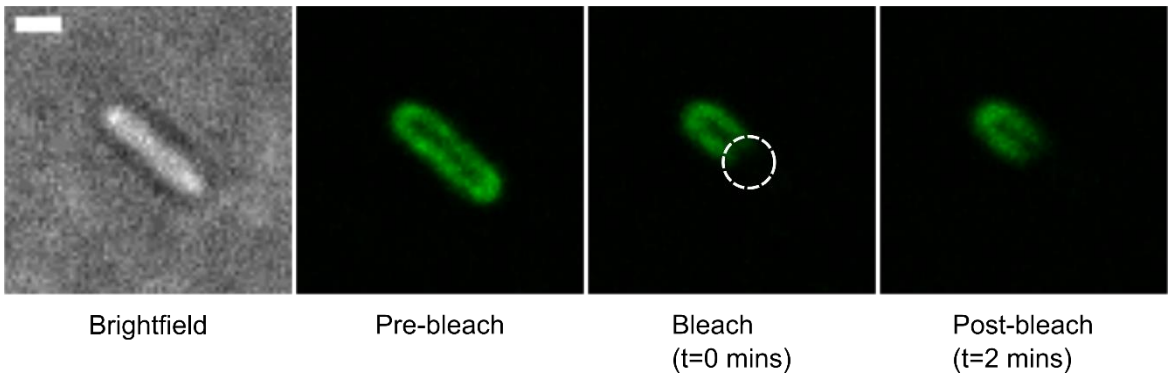

Figure 6-2. A GFP fusion blocks pyoS2^{NTD} translocation.
FRAP experiments on *P. aeruginosa* PAO1 cells labelled with pyoS2^{NTD}GFP highlighting the bleached region (*dashed circle*). No FRAP was observed demonstrating pyoS2^{NTD}GFP is still associated with the OM where lateral diffusion is restricted, consistent with a block in translocation. Scale bar, 1 μm.

6.2.2. Expression and purification *p*Bpa variants

Using Amber suppression, residues throughout the pyoS2^{NTD}GFP construct were substituted for the UV-inducible crosslinker *p*Bpa for covalent crosslinking to the translocation machinery. *p*Bpa was introduced into thirteen positions, including four positions throughout the N-terminus, eight exterior facing sites across the helical domain, and an interfacial site, Tyr46, as a positive control (Figure 6-3). The thirteen variants were expressed in *E. coli* BL21(DE3) cells grown in LB containing the *p*Bpa amino acid (Figure 6-4). Upon encountering the Amber stop (UAG) codon, *p*Bpa is inserted into the nascent polypeptide chain requiring the *p*Bpa-tRNA synthetase/tRNA^{pBpa} pair, encoded on the pEVOL plasmid (Chin *et al.*, 2002). A negative control culture, lacking *p*Bpa, resulted in early translation termination and no mature protein being expressed. After Ni-affinity chromatography, the variants were sufficiently pure for their intended use. Typical yields ranged between 0.5-6.6 mg per 1 litre of bacterial culture (Figure 6-5).

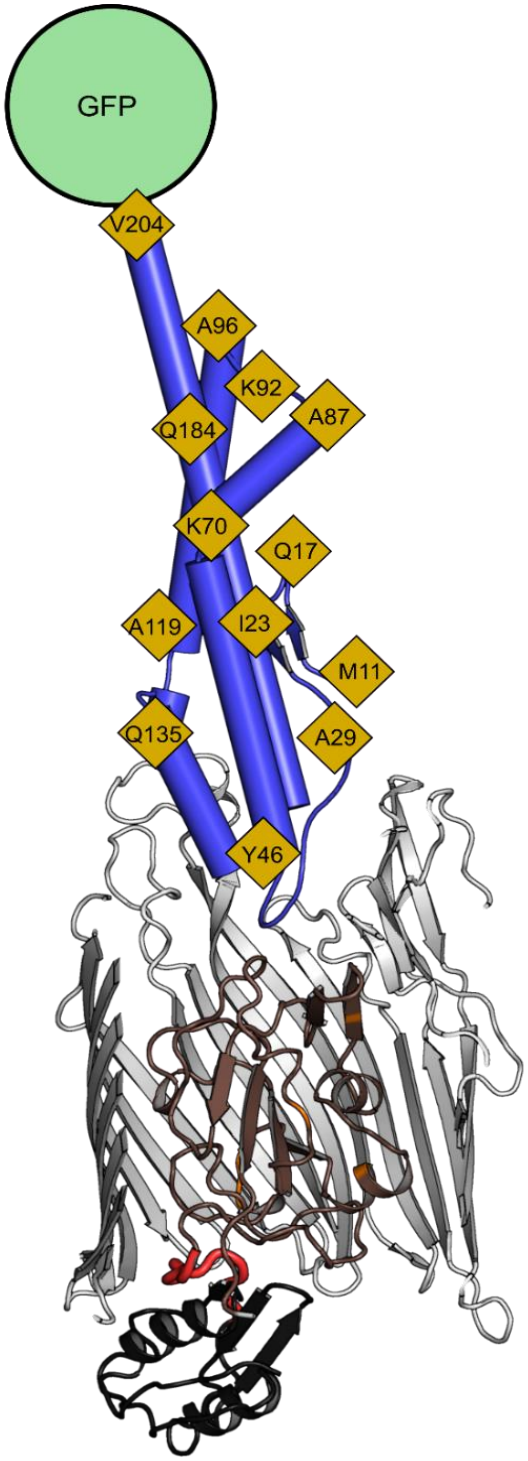

Figure 6-3. Sites of *p*Bpa incorporation in pyoS2^{NTD}GFP. Structure of the FpvAI-pyoS2^{NTD} complex highlighting the position of the GFP fusion (*green circle*) and the residues substituted with *p*Bpa (*yellow diamonds*). The interfacial site at Y46 was included as a positive control. GFP is not drawn to scale.

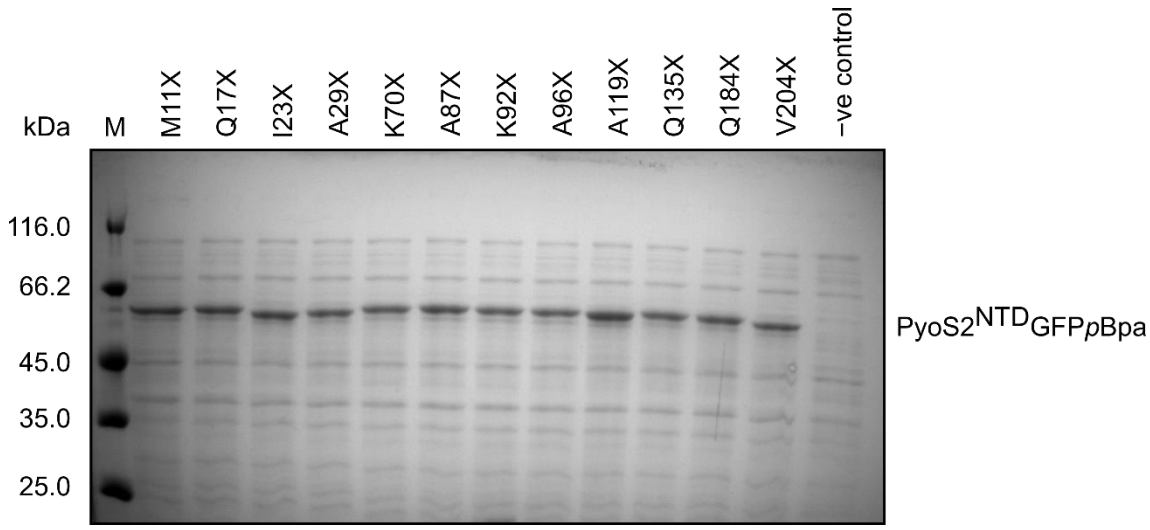

Figure 6-4. Expression of pyoS2^{NTD}GFP*p*Bpa variants.
SDS-PAGE analysis of induced BL21(DE3) cell culture samples expressing pyoS2^{NTD}GFP*p*Bpa variants. No protein was expressed from cultures lacking *p*Bpa (*-ve control*), using the Tyr46*p*Bpa variant in this case. X denotes *p*Bpa. M = Fermentas unstained protein standard.

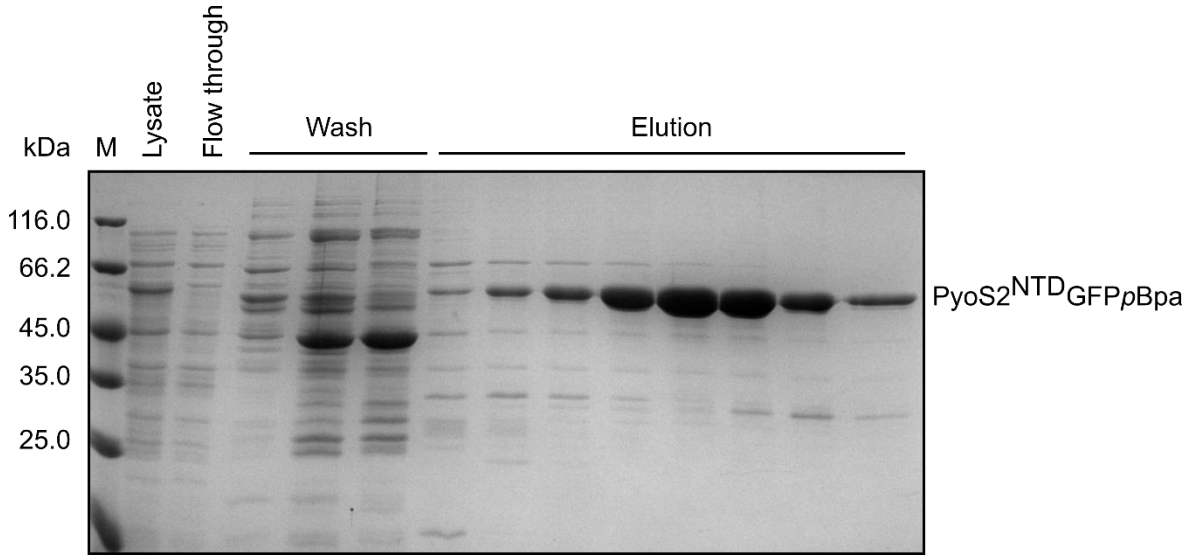

Figure 6-5. Ni-affinity purification of pyoS2^{NTD}GFP*p*Bpa135.
SDS-PAGE analysis of samples from Ni-affinity purification of a single pyoS2^{NTD}GFP*p*Bpa variant using a 1 ml HisTrap HP column. Protein was judged to be of sufficient purity for its application. M = Fermentas unstained protein standard.

6.2.3. *In vitro* photo-activated crosslinking to FpvAI

Photo-activated crosslinking was first tested *in vitro* using detergent-solubilised FpvAI and each of the thirteen pyoS2^{NTD}GFP*p*Bpa variants. Crosslinking was only observed for Tyr46*p*Bpa as evident by a large mobility shift on a Coomassie-stained SDS-PAGE gel (Figure 6-6). Efficient crosslinking was due to the proximity of Tyr46 to FpvAI in the ground-state complex, the other positions being too distant for crosslinking to occur. Moreover, time course experiments showed the amount of crosslink increases with UV exposure time (Figure 6-7).

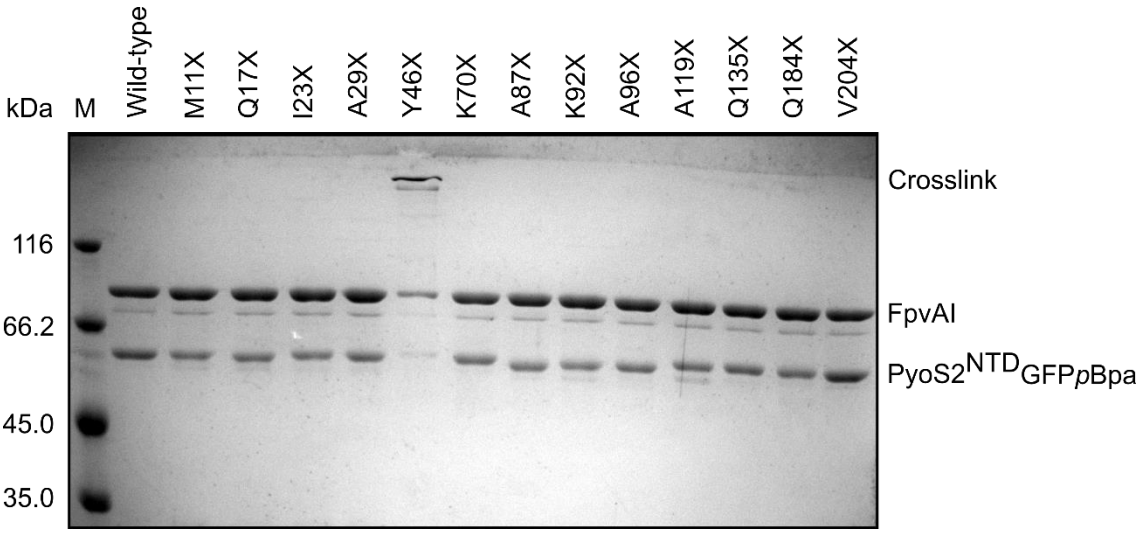

Figure 6-6. *In vitro* crosslinking of purified FpvAI and the pyoS2^{NTD}GFP*p*Bpa variants. Coomassie-stained SDS-PAGE gel loaded with *in vitro* photo-activated crosslinking samples. Detergent-solubilised FpvAI and each of the thirteen pyoS2^{NTD}GFP*p*Bpa variants were UV-irradiated for 30 minutes. Wild-type pyoS2^{NTD}GFP was included as a negative control. Only Tyr46*p*Bpa crosslinks to FpvAI *in vitro*. X denotes *p*Bpa. M = Fermentas unstained protein standard.

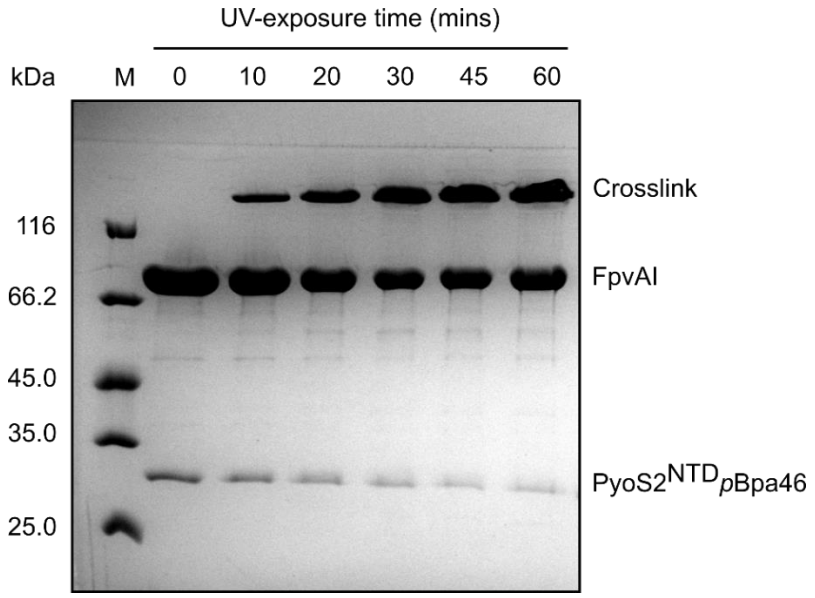

Figure 6-7. Crosslinking efficiency increases with UV exposure time.
Time course of *in vitro* photo-activated crosslinking using detergent-solubilised FpvAI and pyoS2^{NTD}*p*Bpa46 UV-irradiated at 365 nm. Time points from 0 to 60 minutes were analysed by SDS-PAGE showing an increase in crosslinked product over time. M = Fermentas unstained protein standard.

6.2.4. Optimisation of *in vivo* photo-activated crosslinking

Production of a sufficient quantity and purity of crosslinked adducts for downstream LC-MS/MS analysis required optimisation of *P. aeruginosa* growth conditions, incubation time with pyoS2^{NTD}GFP*p*Bpa variants, duration of UV-irradiation, and purification strategy. The *in vivo* crosslinking procedure first involved addition of pyoS2^{NTD}GFP*p*Bpa variants to live *P. aeruginosa* cultures such that they would be actively imported. The cultures were then UV-irradiated to crosslink translocation intermediates, which were subsequently purified from the cells using the C-terminal His-tag on the GFP fusion. Preliminary attempts yielded very low quantities of crosslink, barely visible on Coomassie-stained gels with high levels of background impurities even for the positive control.

Culture growth conditions were first optimised by monitoring growth of PAO1 in LB, M9-glucose and succinate media. As a nutrient-rich medium, LB remains the best medium for growing PAO1 to a high $OD_{600\ nm}$, but is also a possible source of iron contamination which would downregulate FpvAI. It was therefore decided to grow PAO1 in defined media. PAO1 grew poorly in M9-glucose, whilst succinate medium supported *P. aeruginosa* growth resulting in highly fluorescent cultures (Figure 6-8). Fluorescent cultures were a good indication that Pvd was being produced, correlating with high FpvAI expression. Succinate medium was therefore selected as the best defined medium for maximal culture growth and FpvAI expression. In addition, it was noticed that cultures reached a slightly higher $OD_{600\ nm}$ when grown over 24 hours at 30 °C rather than at 37 °C. Optimised growth conditions involved growing PAO1 cells over 24 hours in iron-free succinate medium at 30 °C, resulting in a highly fluorescent green-yellow culture, with an $OD_{600\ nm}$ of ~1.5 (Figure 6-8).

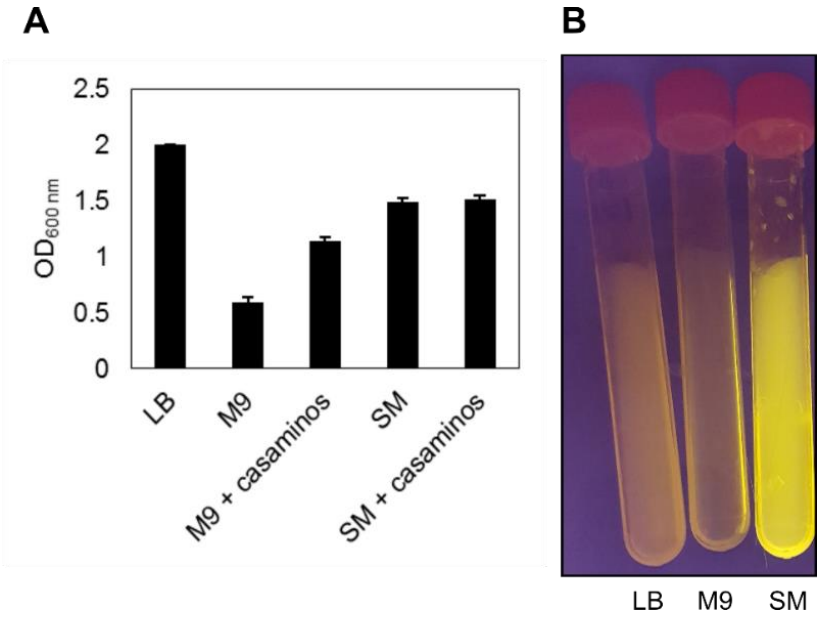

Figure 6-8. Optimisation of growth media for *in vivo* crosslinking.
A, $OD_{600\ nm}$ readings of *P. aeruginosa* PAO1 cultures after 24 hour growth at 30 °C in different media: LB, lysogeny broth; M9, M9-glucose; SM, succinate medium. The effect of casamino acid supplementation was also tested. The average of three readings were taken and error bars represent standard deviation. ***B,*** Culture fluorescence after 24 hour growth at 30 °C in the different media.

The UV-crosslinking protocol was optimised using the positive control Tyr46*p*Bpa variant because this always yielded the most crosslinked adduct both *in vitro* and *in vivo*. Firstly, washing the cells in fresh succinate medium, prior to addition of pyoS2^{NTD}GFP*p*Bpa variants, was shown to be essential for efficient crosslinking (Figure 6-9). Duration of UV exposure was shown to correlate with crosslink yield *in vitro,* but exposure for 1 hour resulted in a poorer crosslinking yield probably due to cell lysis. UV exposure for 30 minutes was found to be sufficient (Figure 6-9). For most variants, introducing a 60 minute incubation step prior to UV-exposure greatly increased the crosslinking efficiency, presumably by allowing more time for translocation and stalling of partially translocated states (Figure 6-10). Finally, the purification protocol was optimised to increase crosslink purity. This involved incubating Ni-affinity beads with a detergent-solubilised OMP extract from which purified crosslink adducts were eluted. The final optimised method is summarised in Figure 6-11 and details are described in Materials and Methods 2.13.

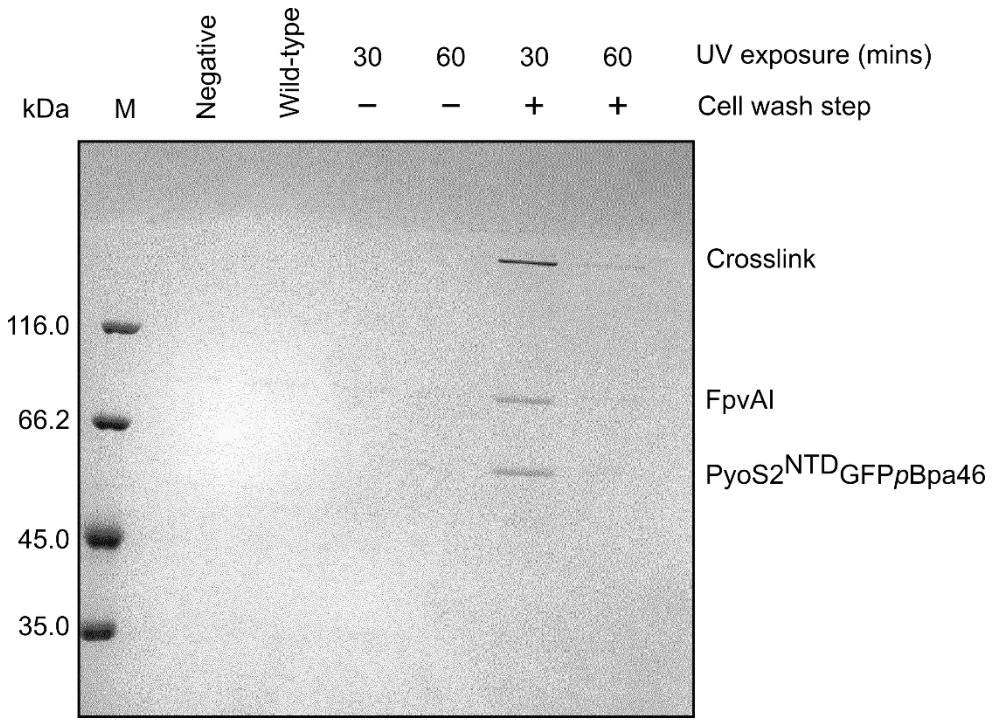

Figure 6-9. Optimisation of *P. aeruginosa in vivo* crosslinking using the positive control variant.
SDS-PAGE analysis of purified *in vivo* crosslink using the pyoS2^{NTD}GFP*p*Bpa46 (positive control) variant. Variables for optimisation included duration of UV exposure and the cell wash step prior to addition of *p*Bpa variant. A negative control sample (*Negative)* where no *p*Bpa variant was added, and the wild-type pyoS2^{NTD}GFP lacking *p*Bpa (*Wild-type*), were also included. Efficient crosslinking required the cell wash step and a UV exposure time of 30 minutes. M = Fermentas unstained protein standard.

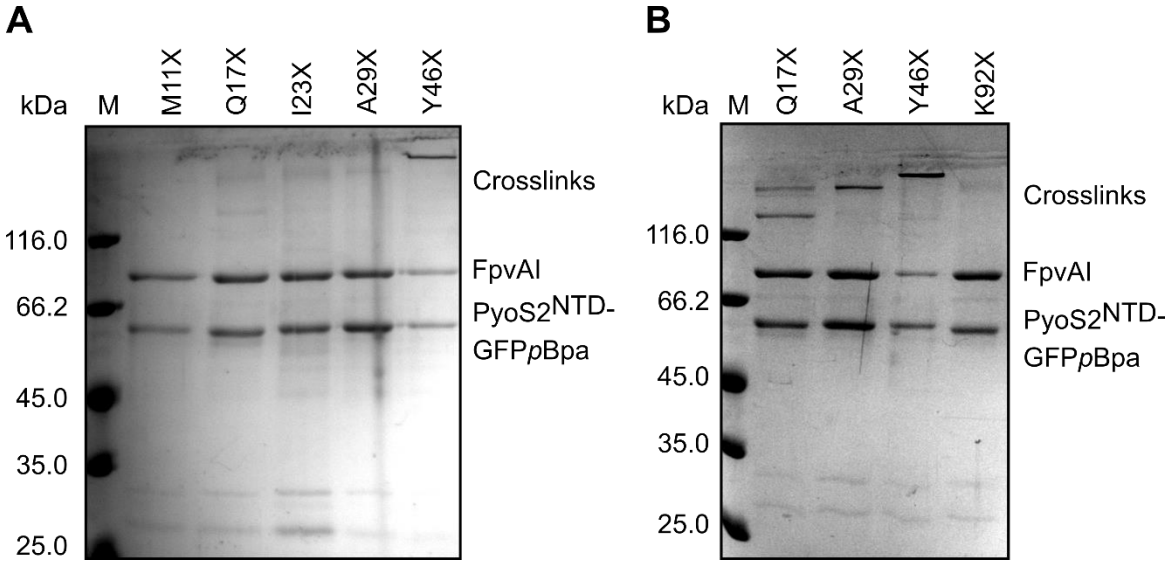

Figure 6-10. Pre-incubation with pyoS2^{NTD}GFP*p*Bpa improves crosslinking efficiency.
SDS-PAGE analysis of *in vivo* crosslinked adducts using selected pyoS2^{NTD}GFP*p*Bpa variants with ***A,*** no pre-incubation, and ***B,*** 1 hour pre-incubation. Incubating pyoS2^{NTD}GFP*p*Bpa variants with cells for 1 hour prior to UV exposure greatly improves crosslinked efficiency. X denotes *p*Bpa. M = Fermentas unstained protein standard.

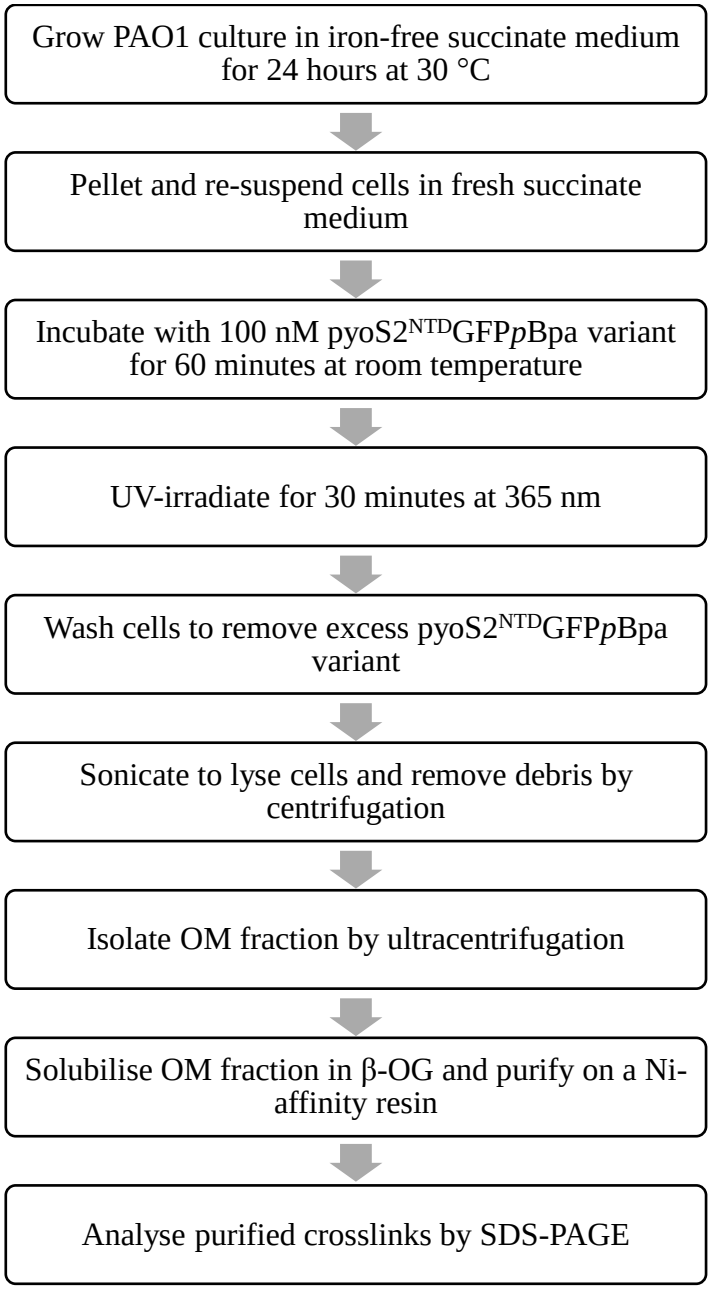

Figure 6-11. Summary of optimised *in vivo* crosslinking protocol.
Flow-chart showing major steps in the *in vivo* crosslinking protocol. See Materials and Methods 2.13 for full details.

Using the optimised *in vivo* crosslinking protocol, crosslinks were seen with almost all pyoS2^{NTD}GFP*p*Bpa variants (Figure 6-12). Tyr46*p*Bpa (positive control) produced the most dominant crosslink species, revealing the ground-state complex as the most populated state. Many variants produced multiple bands with differing electrophoretic

mobility which could represent different sites of crosslinking. LC-MS/MS analysis of crosslink gel bands confirmed both pyoS2 and FpvAI were present. The abundance of crosslinks *in vivo* indicates regions of pyoS2, inaccessible in the ground-state, were brought in close proximity to FpvAI. This demonstrates a considerable conformational change occurs during translocation.

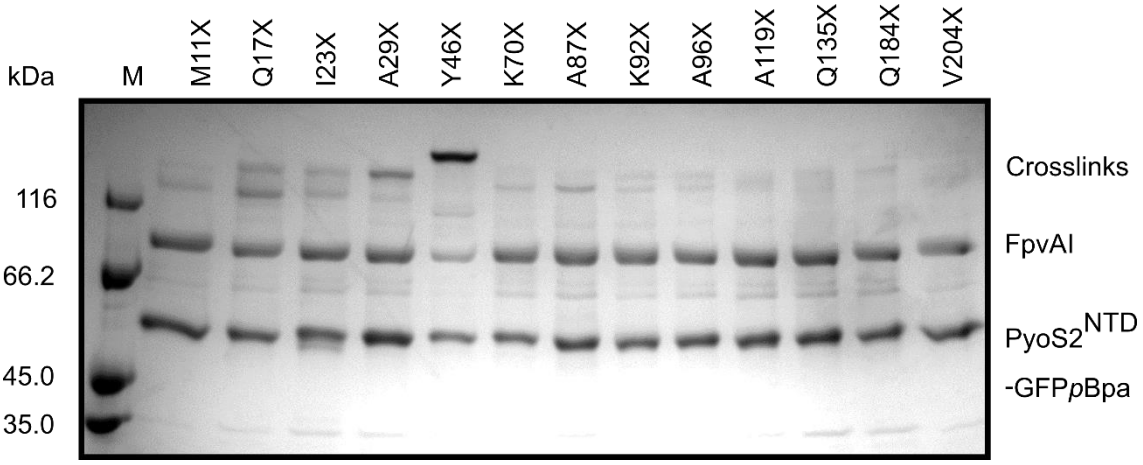

Figure 6-12. *In vivo* crosslinked adducts of translocated pyoS2^{NTD}GFP*p*Bpa variants. Coomassie-stained SDS-PAGE analysis of *in vivo* crosslinked adducts of translocated pyoS2^{NTD}GFP*p*Bpa variants purified from PAO1 OM extracts by Ni-affinity chromatography. X denotes *p*Bpa. M = Fermentas unstained protein standard.

6.2.5. Mapping of photo-activated crosslinked translocation intermediates

Crosslinked adducts selected for LC-MS/MS proteomic mapping were scaled up 6-fold in terms of total culture volume to ensure sufficient quantities of protein. The positive control Tyr46*p*Bpa crosslink was mapped to its neighbouring FpvAI residue (Met431) at the complex interface (Figure 6-13). This is in agreement with its position in the crystal structure, validating the LC-MS/MS data analysis pipeline.

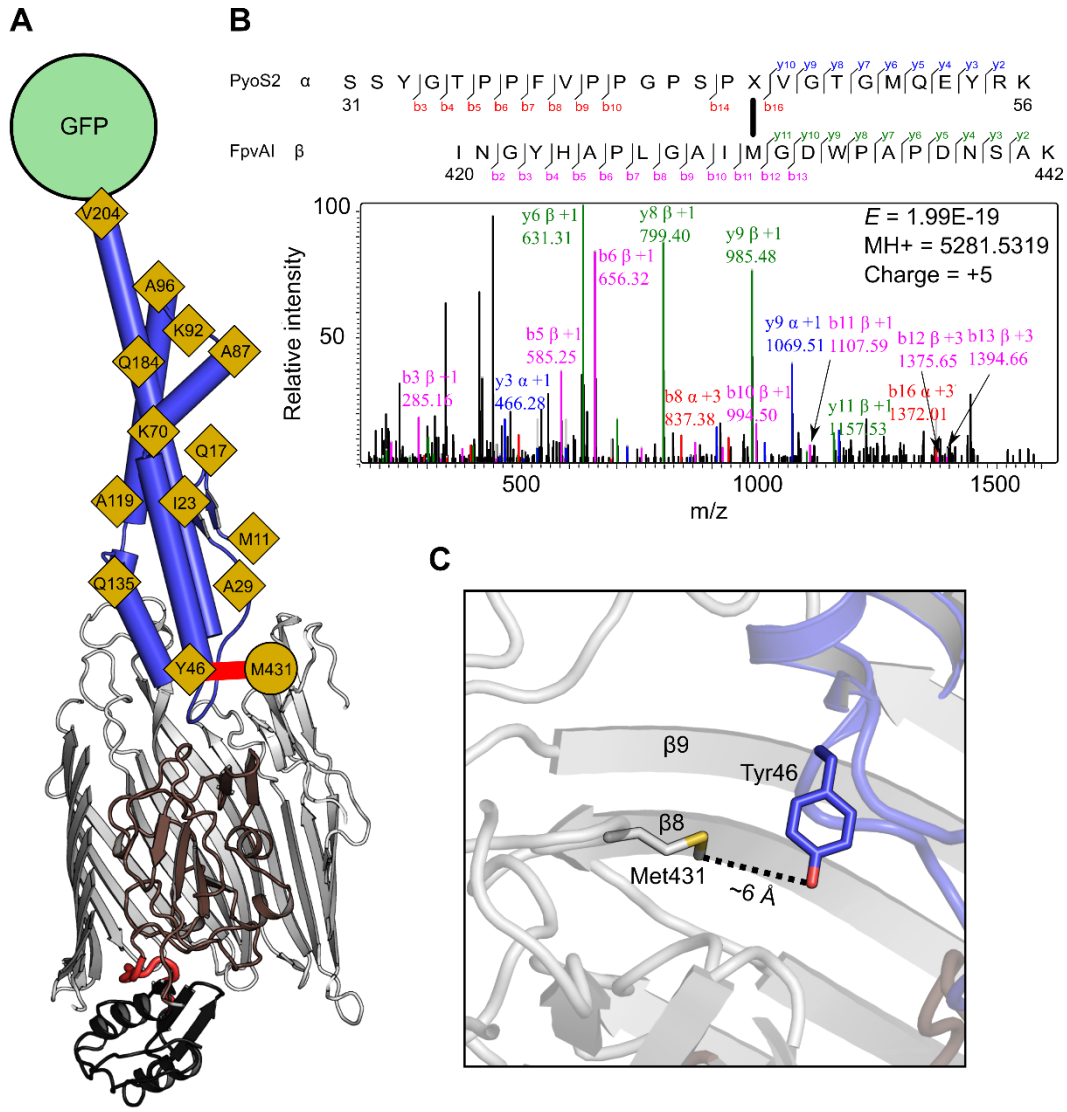

Figure 6-13. Site of Tyr46*p*Bpa crosslinking in FpvAI.
A, Structure of the FpvAI-pyoS2^{NTD} complex highlighting the position of the GFP fusion (*green circle*) and the residues substituted with *p*Bpa (*yellow diamonds*), the crosslink between Tyr46*p*Bpa and Met431 (*yellow circle*) is highlighted (*red line*). GFP is not drawn to scale. ***B,*** LC-MS/MS fragmentation spectrum of *p*Bpa46-Met431 crosslinked peptides (X=*p*Bpa) with b- and y-ions indicated along with the *E*-value, precursor ion mass and precursor ion charge. ***C,*** Inspection of the crystal structure shows the Tyr46*p*Bpa crosslinking partner, Met431 in FpvAI, is located in an extracellular loop between strands β8 and β9 at a distance of ~6 Å. The larger size of the *p*Bpa sidechain, alternative rotamers and localised loop movements could readily bring the two residues within for 3-4 Å distance required for crosslinking. These observations validate the LC-MS/MS pipeline.

Crosslinks for seven *p*Bpa sites substituted into pyoS2^{NTD}GFP in place of Gln17, Ile23, Ala29, Lys70, Ala87, Gln135 and Gln184, were mapped to six principal sites located in transmembrane regions of FpvAI (Figure 6-14). Five of these sites, Pro166, Met177, Leu182, Val197 and Asp239, are within the plug domain that are inaccessible in the ground-state complex. This demonstrates the plug domain has undergone considerable remodelling during import. Gln17*p*Bpa and Ile23*p*Bpa both crosslinked to Met766 of the β-barrel wall, the sidechain projecting into the lumen of FpvAI, showing the N-terminus resides inside the FpvAI lumen. Interestingly, these sites produced a second crosslinked adduct, which mapped to the FpvAI plug domain residue Met177 and adjacent residues. Lys70*p*Bpa, Ala87*p*Bpa and Gln135*p*Bpa also crosslinked to Met177 in FpvAI, suggesting that the entire pyoS2^{NTD} polypeptide chain translocates past this residue during import. Ala29*p*Bpa crosslinks were mapped to a distinct region of the FpvAI plug involving Asp239. All the identified crosslinks demonstrate that pyoS2^{NTD} translocates large distances, including Gln184*p*Bpa that moves 76 Å to crosslink FpvAI Val197. LC-MS/MS fragmentation spectra are shown for the principal crosslink sites (Figure 6-15). After inspection of LC-MS/MS data, it was apparent that residues adjacent to these principal sites are also targeted, but at lower frequency (Figure 6-16). It is evident that the plug domain of FpvAI undergoes a large conformational change, and the N-terminus of pyoS2 resides within the barrel during import. Taken together, the crosslinking data shows that pyoS2^{NTD} imports through the FpvAI β-barrel lumen.

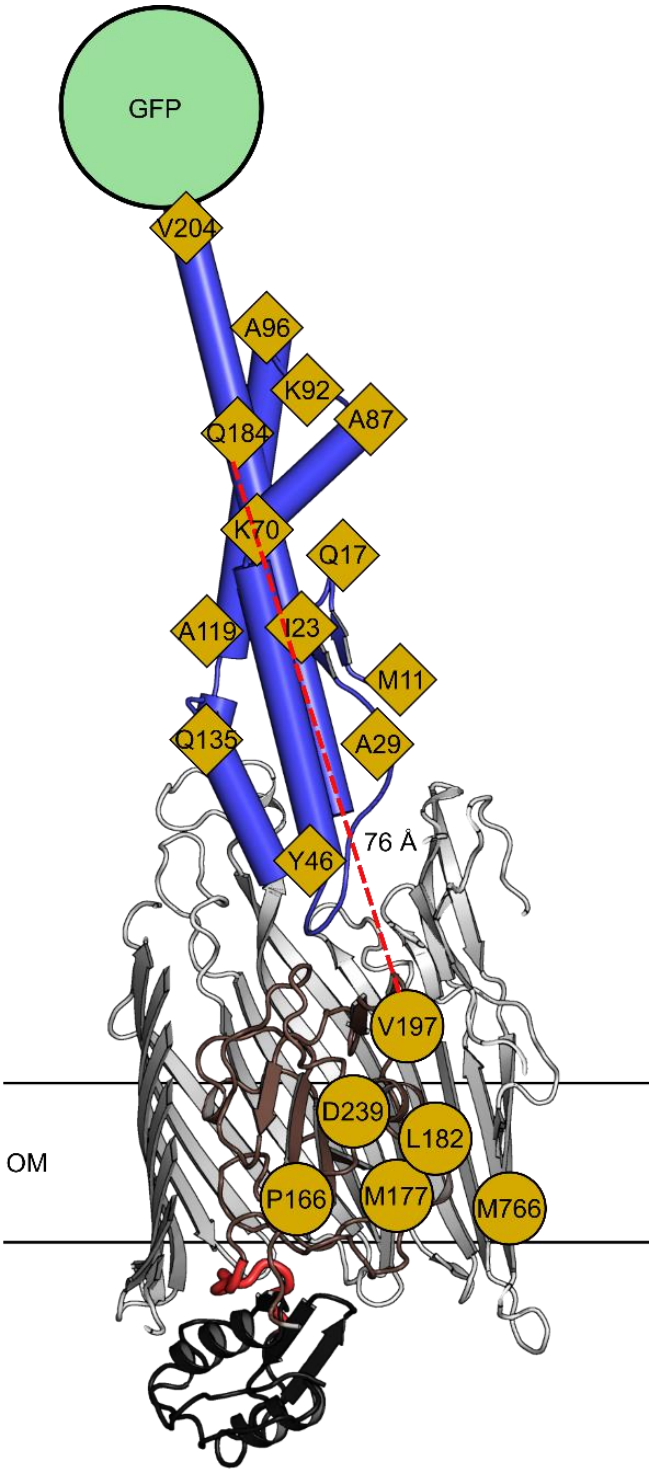

Figure 6-14. Translocation intermediate crosslinking sites in FpvAI.
Structure of the FpvAI-pyoS2^{NTD} complex highlighting the position of the GFP fusion (*green circle*) and the residues substituted with *p*Bpa (*yellow diamonds*). The major crosslink sites in FpvAI (*yellow circles*) are also indicated, most of which are located in the plug domain of the TBDT. The red dotted line indicates the crosslink detected between Gln184*p*Bpa in pyoS2^{NTD} and Val197 in FpvAI, requiring this region of the pyocin to translocate at least 76 Å.

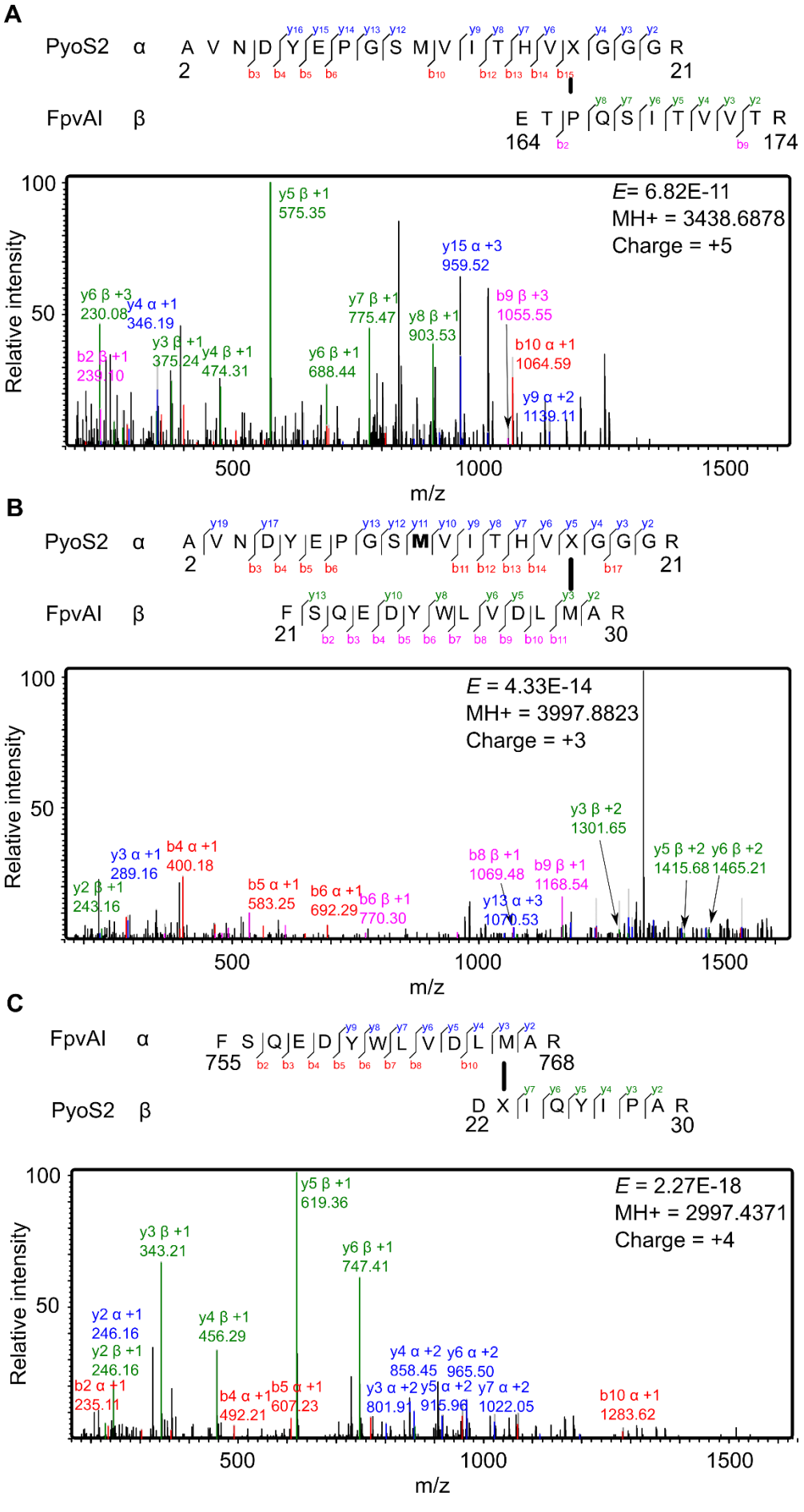
A
PyoS2 α A V N D Y E P G S M V I T H V X G G G R
2 21
FpvAI β E T P Q S I T V V T R
164 174
E= 6.82E-11
MH+ = 3438.6878
Charge = +5
y5 β +1 575.35
y15 α +3 959.52
y6 β +3 230.08
y4 α +1 346.19
y7 β +1 775.47
y8 β +1 903.53
b9 β +3 1055.55
y3 β +1 375.24
y4 β +1 474.31
y6 β +1 688.44
b10 α +1 1064.59
b2 β +1 239.10
y9 α +2 1139.11
Relative intensity
m/z
B
PyoS2 α A V N D Y E P G S M V I T H V X G G G R
2 21
FpvAI β F S Q E D Y W L V D L M A R
21 30
E = 4.33E-14
MH+ = 3997.8823
Charge = +3
y3 β +2 1301.65
y3 α +1 289.16
b4 α +1 400.18
b8 β +1 1069.48
b9 β +1 1168.54
y5 β +2 1415.68
y6 β +2 1465.21
y2 β +1 243.16
b5 α +1 583.25
b6 α +1 692.29
b6 β +1 770.30
y13 α +3 1070.53
Relative intensity
m/z
C
FpvAI α F S Q E D Y W L V D L M A R
755 768
PyoS2 β D X I Q Y I P A R
22 30
E = 2.27E-18
MH+ = 2997.4371
Charge = +4
y5 β +1 619.36
y3 β +1 343.21
y6 β +1 747.41
y2 α +1 246.16
y4 β +1 456.29
y2 β +1 246.16
y4 α +2 858.45
y6 α +2 965.50
b2 α +1 235.11
b4 α +1 492.21
b5 α +1 607.23
y3 α +2 801.91
y5 α +2 915.96
y7 α +2 1022.05
b10 α +1 1283.62
Relative intensity
m/z

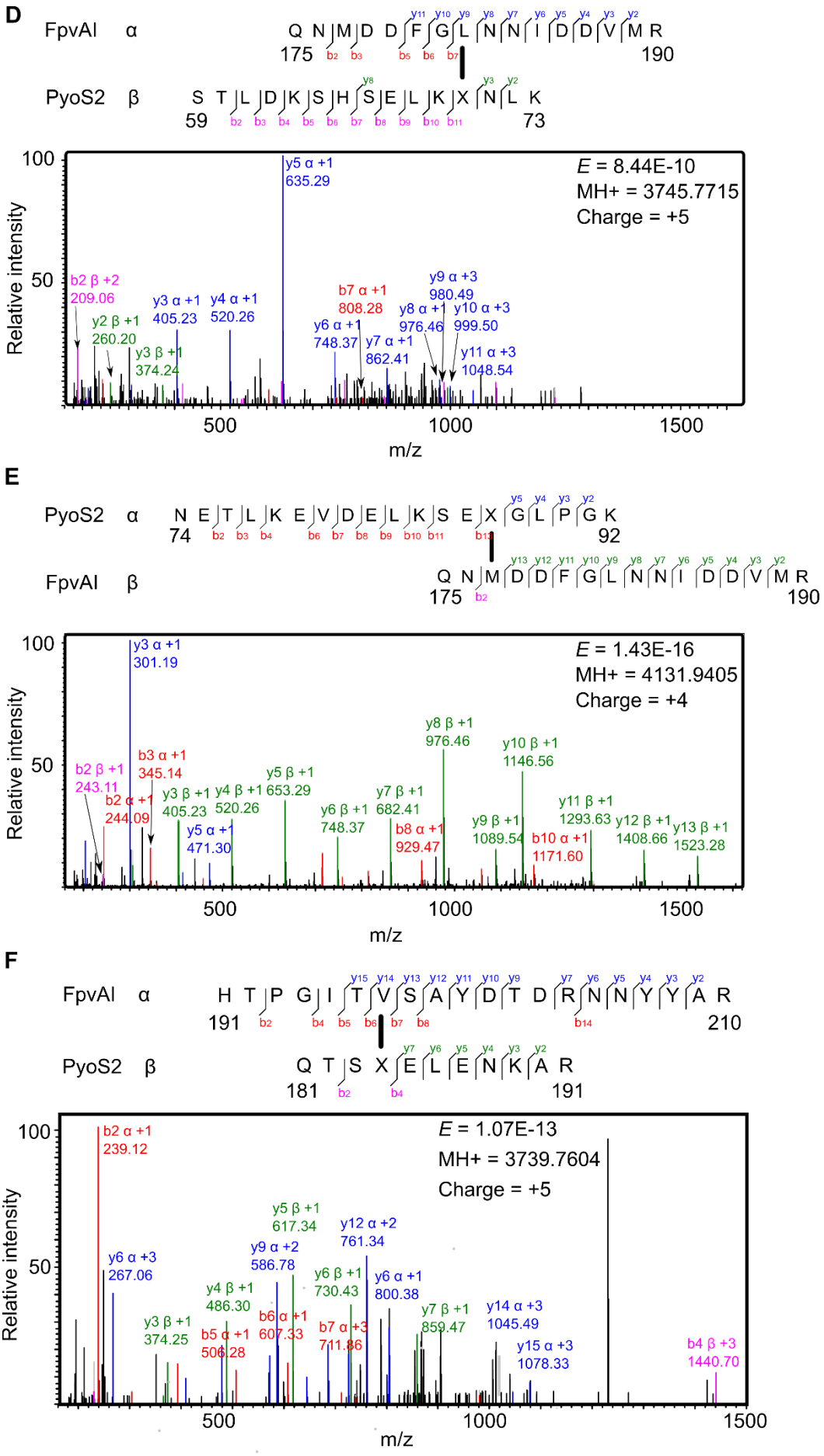
D
FpvAI α
Q N M D D F G L N N I D D V M R
175
190
PyoS2 β
S T L D K S H S E L K X N L K
59
73
Relative intensity
m/z
E = 8.44E-10
MH+ = 3745.7715
Charge = +5
y5 α +1 635.29
b2 β +2 209.06
y2 β +1 260.20
y3 α +1 405.23
y4 α +1 520.26
y3 β +1 374.24
b7 α +1 808.28
y6 α +1 748.37
y7 α +1 862.41
y9 α +3 980.49
y8 α +1 976.46
y10 α +3 999.50
y11 α +3 1048.54
E
PyoS2 α
N E T L K E V D E L K S E X G L P G K
74
92
FpvAI β
Q N M D D F G L N N I D D V M R
175
190
E = 1.43E-16
MH+ = 4131.9405
Charge = +4
y3 α +1 301.19
b2 β +1 243.11
b2 α +1 244.09
b3 α +1 345.14
y3 β +1 405.23
y4 β +1 520.26
y5 α +1 471.30
y5 β +1 653.29
y6 β +1 748.37
y7 β +1 682.41
b8 α +1 929.47
y8 β +1 976.46
y9 β +1 1089.54
y10 β +1 1146.56
b10 α +1 1171.60
y11 β +1 1293.63
y12 β +1 1408.66
y13 β +1 1523.28
F
FpvAI α
H T P G I T V S A Y D T D R N N Y Y A R
191
210
PyoS2 β
Q T S X E L E N K A R
181
191
E = 1.07E-13
MH+ = 3739.7604
Charge = +5
b2 α +1 239.12
y6 α +3 267.06
y3 β +1 374.25
y4 β +1 486.30
b5 α +1 506.28
b6 α +1 607.33
y5 β +1 617.34
y9 α +2 586.78
y12 α +2 761.34
y6 β +1 730.43
y6 α +1 800.38
b7 α +3 711.86
y7 β +1 859.47
y14 α +3 1045.49
y15 α +3 1078.33
b4 β +3 1440.70

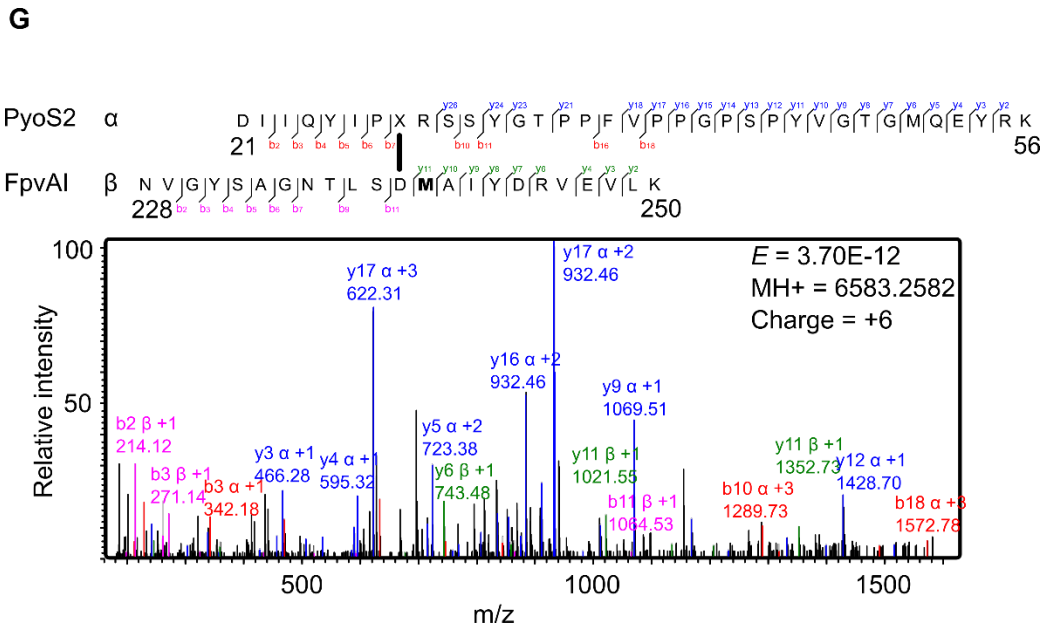

Figure 6-15. LC-MS/MS mapping of pyoS2^{NTD}GFP*p*Bpa crosslinks to FpvAI.
Fragmentation spectra of crosslinked peptides indicating *b*- and *y*-ions along with the *E-value*, precursor ion mass and precursor ion charge. In peptide sequences, X=*p*Bpa and bold typeface denotes oxidised methionine. ***A,*** Gln17*p*Bpa-Pro166. ***B,*** Gln17*p*Bpa-Met766. ***C,*** Ile23*p*Bpa-Met766. ***D,*** Lys70*p*Bpa-Leu182. ***E,*** Ala87*p*Bpa-Met177. ***F,*** Gln184*p*Bpa-Val197 **G,** Ala29*p*Bpa-Asp239.

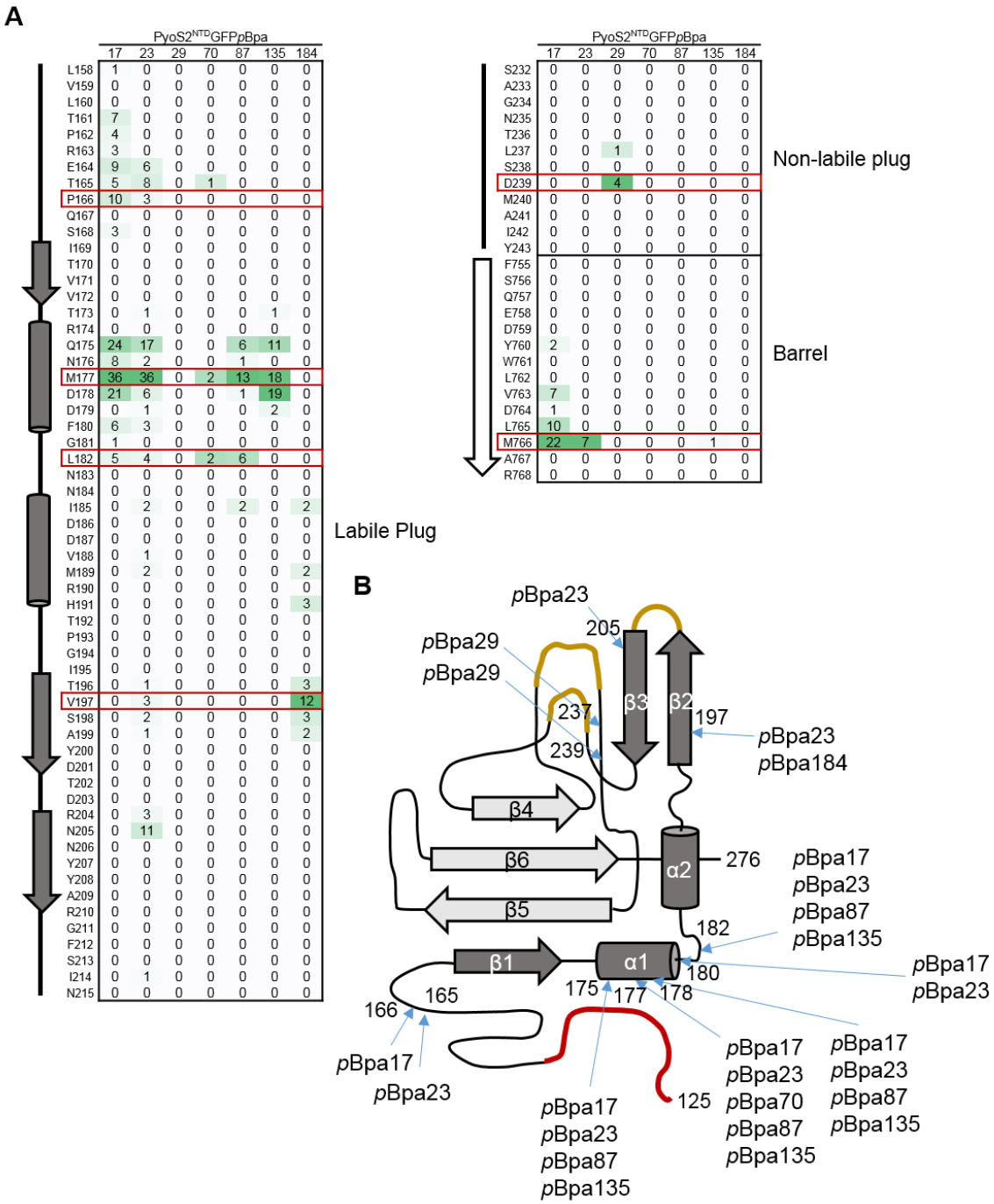

Figure 6-16. Spectral counts for *p*Bpa crosslinking hits across the FpvAI sequence.
A, Hits with an *E*-value $\leq 10^{-8}$ identified by pLink were counted and coloured according to frequency. The sites identified in Figure 6-14 are highlighted in red boxes and the corresponding secondary structure elements are shown adjacent to the sequence. ***B,*** Summary of pyoS2^{NTD}GFP*p*Bpa crosslinking sites across the plug domain of FpvAI (residues 125-276) represented by secondary structure. The labile and non-labile subdomains are coloured in *dark grey* and *light grey*, respectively. The TonB1-box and substrate recognition loops are coloured in *red* and *yellow*, respectively. Figure adapted from Chimento *et al* (2005).

6.3. Discussion

The overall aim of this chapter was to map the translocation pathway of pyoS2 by photo-activated crosslinking. This involved first engineering a mechanically stable C-terminal GFP fusion to populate a partially translocated state, which could then be crosslinked to the translocation machinery using the amino acid *p*Bpa, introduced at specific sites throughout the pyoS2^{NTD}GFP fusion. The success of this approach required substantial optimisation. The efficiency of crosslinking was dependent on a number of factors including *P. aeruginosa* cell count, FpvAI expression level, translocation rate and duration of UV-irradiation, all of which were addressed. Simply increasing cell counts by growing cultures to a higher optical density reduced the amount of UV light penetration such that only the uppermost layer was exposed. It was therefore decided to work with cell cultures at lower optical density, typically at an $OD_{600\ nm}$ around 1.5, and scale-up cell culture volume instead. Succinate medium supported growth of *P. aeruginosa* PAO1 whilst minimising iron contamination, resulting in highly fluorescent cultures. This fluorescence is due to Pvd, known to be upregulated when grown on a succinic acid carbon source (Barbhaiya and Rao, 1985). Since Pvd positively regulates expression of FpvAI, it was assumed that these growth conditions were ideal for high expression of FpvAI. However, the large excess of Pvd would compete with pyoS2^{NTD}GFP*p*Bpa variants for FpvAI binding and translocation. Removing the excess Pvd by washing the cells in fresh medium prior to addition of pyoS2^{NTD}GFP*p*Bpa variants, was shown to be critical for efficient crosslinking. It was also shown that crosslinking efficiency increases with UV exposure time, though excessive irradiation was detrimental, the resulting lysis compromising crosslink yield.

For the majority of pyoS2^{NTD}GFP*p*Bpa variants, no crosslinks were seen *in* vitro using detergent-solubilised FpvAI. This was because the sites of *p*Bpa incorporation were too distant from the FpvAI in the ground-state complex. The positive control variant, Tyr46*p*Bpa, effectively crosslinked to FpvAI, its crosslink partner mapped to nearby Met431 at a distance of ~6 Å in the crystal structure. The larger size of the *p*Bpa sidechain, alternative rotamers and localised loop movements could readily bring the two residues within the 3-4 Å distance required for crosslinking. In contrast to *in vitro* crosslinking, many crosslinks were seen *in vivo,* indicating active translocation had occurred. Import brings many regions of the pyoS2^{NTD}GFP*p*Bpa variants into contact with FpvAI, which were inaccessible in the ground-state. The LC-MS/MS mapping of *in vivo* crosslinking adducts revealed contact between pyoS2^{NTD} and FpvAI residues that are consistent with direct import through the β-barrel lumen, though it was initially difficult to rationalise why the vast majority of crosslink sites were to the plug domain. Clearly though, these sites are inaccessible in the ground-state, demonstrating a large conformational change must take place. Crosslinks between pyoS2 N-terminal *p*Bpa positions (Gln17 and Ile23) and Met766, provides strong evidence that at least this part of pyoS2 resides inside FpvAI barrel lumen. This probably represents the first stable intermediate of pyoS2 import, remaining populated for sufficient time for crosslinking to occur. In this state, the TonB1-box of pyoS2 is accessible from the periplasm where TonB1 induces the next stage of translocation. Next, the mechanical force applied to the TonB1-box drives translocation of the helical domain of pyoS2^{NTD}, stalling once it reaches GFP. In this second state, *p*Bpa sites throughout pyoS2^{NTD}GFP crosslink to the unfolded plug domain.

The distribution of crosslinking sites within the FpvAI plug domain could be readily interpreted in the context of recent atomic force microscopy (AFM) studies on the *E. coli* vitamin B_{12} and ferric hydroxamate TBDTs BtuB and FhuA, respectively (Hickman *et al.*, 2017). Hickman *et al* have shown that the BtuB and FhuA plug domains are composed of two mechanically uncoupled subdomains, and displacement of the force-labile subdomain opens up a ~13 Å wide channel for the transport of substrates. A structural alignment of the plugs of BtuB (PDB ID 1NQH (Chimento *et al.*, 2003)) and FpvAI identified a force-labile subdomain spanning residues from the FpvAI TonB1-box to residue 215 (Figure 6-17). Removal of this labile subdomain opens a translocation channel in the receptor through which the pyoS2 N-terminus can pass. Crosslink sites Met766 and Asp239 are accessible on the barrel wall and non-labile subdomain, respectively (Figure 6-17C).

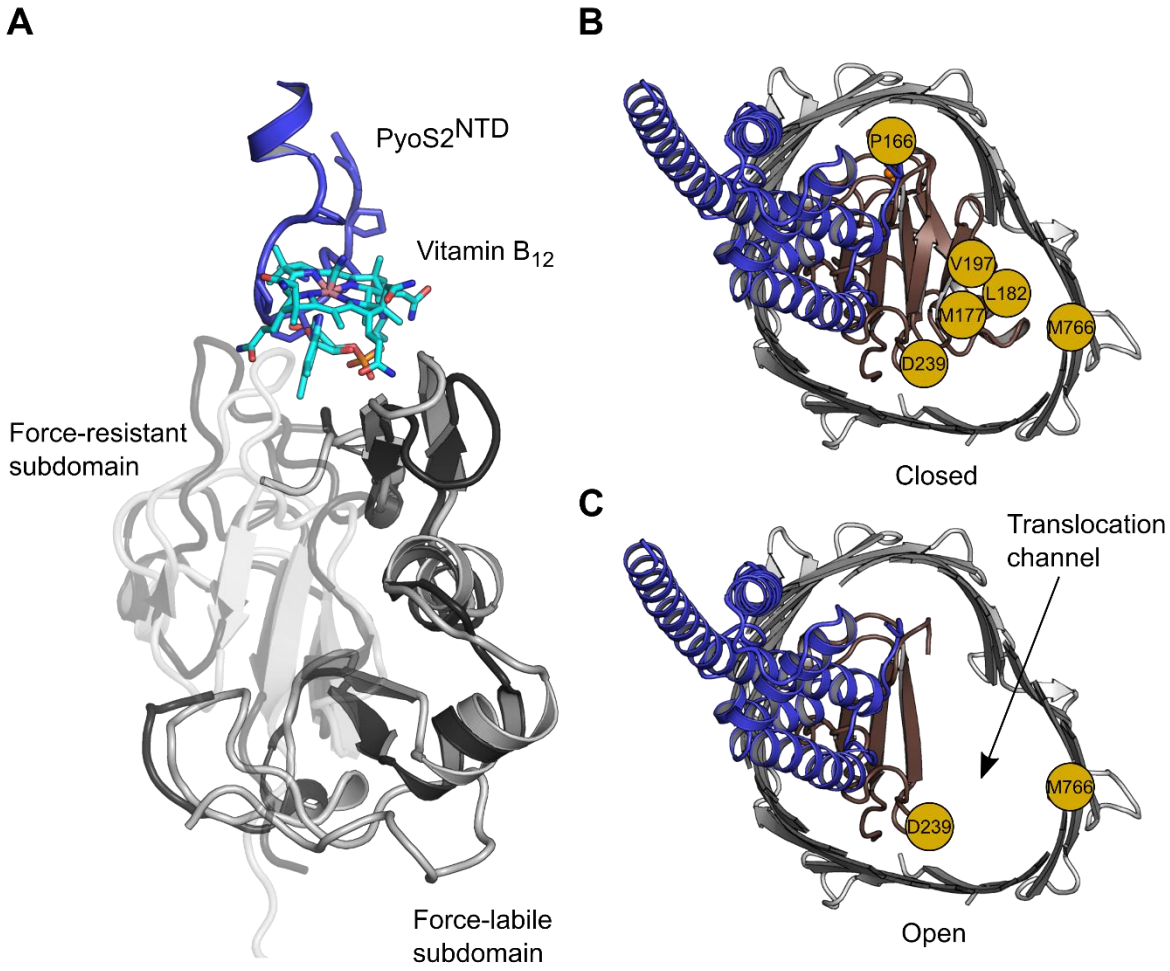

Figure 6-17. Removal of a force-labile plug subdomain opens a translocation path through FpvAI.
A, Structural alignment (RMSD, 1.7 Å) of the plug domains of FpvAI (*light grey*) and BtuB (*dark grey*, PDB ID 1NQH (Chimento *et al.*, 2003)). The labile region of the plug is rendered opaque whereas the non-labile region is rendered transparent. PyoS2^{NTD} PRR (*blue*) and vitamin B_{12} (*cyan*) bound to their respective receptors are also shown. ***B*** and ***C,*** Extracellular views of the pyoS2^{NTD}-FpvAI complex with the labile subdomain of the plug in place (*closed*) and labile subdomain removed (*open*), with the most abundant crosslink sites in FpvAI shown as *yellow circles*. Removal of the labile subdomain opens a 13 Å channel through the transporter.

The majority of crosslinks were mapped to a cluster of residues in the plug domain around Met177, which was frequently targeted. Methionine residues react preferentially with the benzophenone ketyl diradical formed under UV-irradiation (Wittelsberger *et al.*, 2006). It seems feasible that regions of pyoS2 translocate past this hyper-reactive cluster of residues including Met177 but also Pro166, and Leu182. Despite no structural information being available for the conformation of the unfolded plug domain, the hyper-reactive clusters spanning residues 161-166 and 175-182 suggest that at least this region may have some residual structure. Unfolding of the labile subdomain may also play a role in FpvAI-mediated signalling. As well as siderophore transport, FpvAI regulates its own expression through an interaction between the signalling domain and FpvR in the IM (Redly and Poole, 2005). It is possible that the extra length provided by the unfolded labile plug allows the signalling domain to span the periplasm to reach FpvR.

Supported by the findings described in previous chapters and the *p*Bpa crosslinking data, a three-step model of pyoS2^{NTD} translocation through FpvAI is proposed (Figure 6-18). In the first step, binding of pyoS2^{NTD} to FpvAI mimics Fe-Pvd, inducing conformational changes in the plug domain to activate the receptor for substrate transport. Next, a PMF-dependent mechanical force, applied via the ExbB-ExbD-TonB1 complex in the IM, drives unfolding of the labile half of the plug domain allowing the N-terminus of pyoS2^{NTD} to enter the ~13 Å wide cavity. In the third step, the pyoS2 TonB1-box, now presented on the periplasmic side of FpvAI, is bound by another copy of TonB1. This time the mechanical force used to drive translocation of pyoS2^{NTD} through the FpvAI lumen where further translocation is blocked by the force-resistant GFP. Unfolding is facilitated when the N-terminal β-hairpin is no longer stabilising the helical domain. Moreover, helical domains are more force-labile than β-sheets which may explain why bacteriocins are predominantly α-helical (Chen *et al.*, 2015).

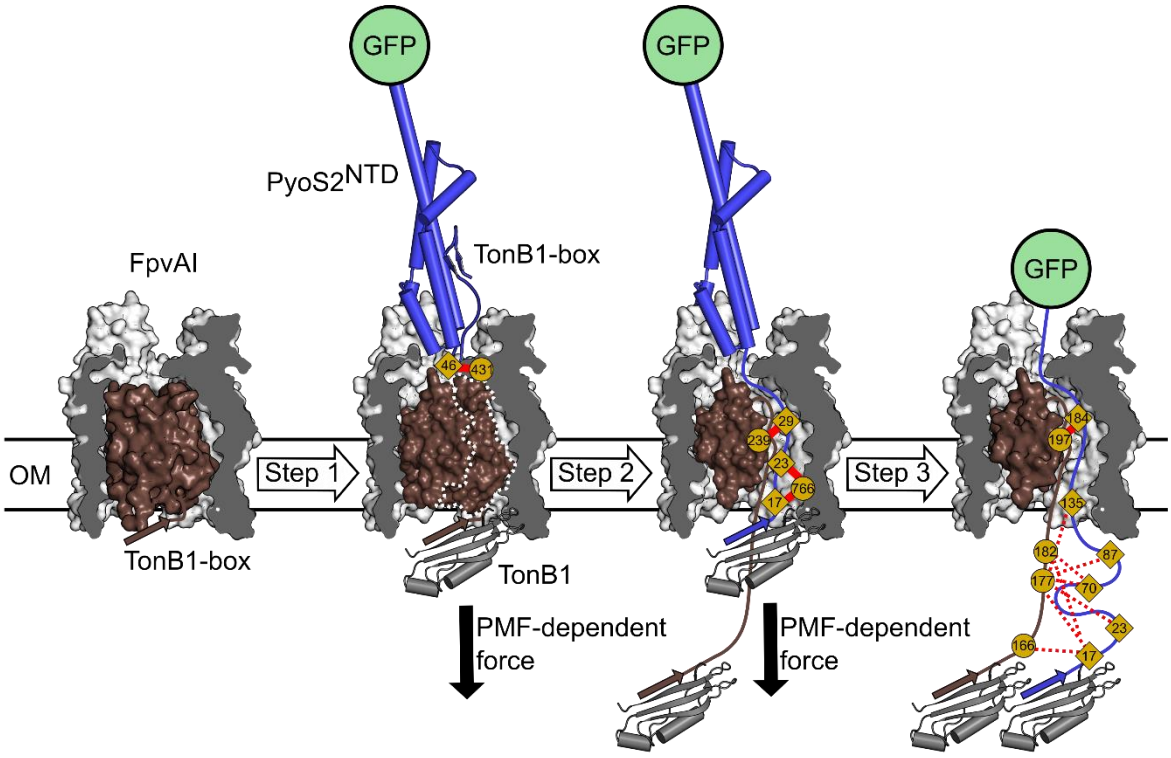

Figure 6-18. Model for pyoS2^{NTD} translocation through FpvAI.
Three-step model of pyoS2^{NTD} translocation through FpvAI supported by *p*Bpa crosslinking data. *Step 1*, Binding of pyoS2^{NTD} to FpvAI mimics Fe-Pvd, activating the receptor for substrate transport and recruiting the CTD of TonB1 in the periplasm. *Step 2*, A PMF-dependent mechanical force, applied via the ExbB-ExbD-TonB1 complex in the IM (not shown), drives unfolding of the labile half of the plug domain. The N-terminus of pyoS2^{NTD} enters the ~13 Å wide cavity that is created allowing it to present its own TonB1-box in the periplasm. *Step 3*, The pyoS2^{NTD} TonB1-box is bound by another copy of TonB1, this time the mechanical force is used to drive translocation of pyoS2^{NTD} through the FpvAI lumen. Further translocation is blocked by the force-resistant GFP (*green circle*). *p*Bpa sites in pyoS2^{NTD}GFP are shown as *yellow diamonds* and crosslinks sites in FpvAI are shown as *yellow circles.* Crosslinks are shows as *red lines*. The multiple crosslinks observed between the labile portion of the FpvAI plug domain and translocated pyoS2^{NTD} residues *(red dashed lines)* are assumed to involve unfolded polypeptide chains in the periplasm.

As with all TBDTs, how substrate binding leads to removal of the labile plug is not yet clear. However, two scenarios seem feasible: 1, remodelling of the plug upon binding propagates conformational changes to the periplasmic side inducing structural changes in the TonB-box, or 2, ligand binding weakens interactions between the labile plug and the rest of the receptor facilitating TonB-dependent unplugging. In scenario 1, structural changes in the TonB-box may increase its affinity for TonB, allowing transport of the ligand before dissociation (Moeck and Letellier, 2001, Moeck *et al.*, 1997). However, the conformation of the TonB-box is often highly variable in crystal structures, and does not correlate with ligand binding (Noinaj *et al.*, 2010). The best evidence for structural changes in the TonB-box used electron paramagnetic resonance spectroscopy to show that the BtuB TonB-box undergoes a structured-to-unstructured transition upon binding of vitamin B_{12} (Fanucci *et al.*, 2003). Scenario 2 assumes TonB binds unliganded and liganded TBDTs with equal affinity, but transport only occurs when a ligand is bound. Which scenario is correct is still an area of debate.

6.4. Conclusions

The work presented in this chapter has shown that pyoS2^{NTD} translocates through the FpvAI barrel lumen, analogous to the pathway taken by Fe-Pvd. Having first stalled import by fusing the force-resistant GFP to the C-terminus of pyoS2^{NTD}, contact sites between pyoS2^{NTD} and FpvAI were revealed by LC-MS/MS analysis of photo-activated crosslink adducts. Sites within the N-terminal β-hairpin crosslinked to two regions of FpvAI, giving rise to two distinct crosslinked adducts, and probably represent two discrete conformational states. Assuming all TBDT plugs are composed of mechanically uncoupled subdomains like BtuB, it seems reasonable to suggest the plug domain of FpvAI is also composed of a force-resistant subdomain and a force-labile subdomain

immediately after the TonB1-box. TonB1-dependent removal of the force-labile subdomain opens up a translocation channel where the N-terminus crosslinked to Met766 of the β-barrel and Asp239 of the remaining plug. Crosslink sites throughout the helical domain were mapped to a cluster of residues around Met177 within the unfolded plug, which may have some residual structure. The three-step mechanism of pyoS2 translocation begins by mimicry of the conformational changes induced by Fe-Pvd, triggering TonB1-dependent unfolding of the labile plug subdomain. The N-terminus occupies the newly created translocation channel, presenting its own TonB1-box in the periplasm. A second TonB1-dependent force applied to the N-terminus of pyoS2 drives complete translocation. This describes the most complete model of bacteriocin import into bacteria to-date.

Chapter 7. General Discussion

7.1. General Discussion

The molecular mechanisms underpinning protein import into bacteria have remained elusive, yet the import of cytotoxic protein bacteriocins is principal to inter-bacterial competition. For bacteriocins to reach their intracellular target, the formidable barrier of the Gram-negative cell envelope must be overcome. Although their eukaryotic descendants, mitochondria and plastids, possess dedicated protein import systems, Gram-negative bacteria have no such systems. Instead, bacteriocins must hijack proteins of the target cell envelope, including OM porins and TBDTs, the Ton and Tol systems, and IM proteins (Papadakos *et al.*, 2012), but the mechanisms by which they do so are not known. In this study, the means by which the nuclease bacteriocin pyoS2 translocates across the OM of *P. aeruginosa* has been uncovered, revealing new insights into the mechanisms by which proteins are imported into bacteria.

In the case of *P. aeruginosa,* an inverse correlation between killing activity and iron concentration identified the iron transporter FpvAI as the cell surface receptor for pyoS2 (Ohkawa *et al.*, 1980). The suggestion that the receptor-binding domain was located at the N-terminus (in contrast to colicins where it is centrally-located), was confirmed when pyocin S4, which has an almost identical N-terminal domain, was also found to be FpvAI-dependent (Michel-Briand and Baysse, 2002, Elfarash *et al.*, 2012). Despite these discoveries, an interaction between FpvAI and pyoS2 had yet to be demonstrated, and no definitive domain boundary had been mapped. The work presented here revealed a high affinity interaction (K_d = ~240 pM) between detergent-solubilised FpvAI and residues 1-209 of pyoS2 (pyoS2^{NTD}), sufficient to outcompete the endogenous ligand, Fe-Pvd. Intrinsic tryptophan fluorescence emission changes upon complex formation were

subsequently used to determine the kinetics of complex association. Biphasic binding kinetics were observed indicative of conformational changes occurring in one or both proteins. The crystal structure of the FpvAI-pyoS2^{NTD} complex later revealed that conformational changes within the receptor do indeed occur and that these are localised to the plug domain. However, as there is no structural information for pyoS2^{NTD} in isolation, it is not clear whether conformational changes also occur in pyoS2^{NTD} upon binding to FpvAI.

The crystal structure of the FpvAI-pyoS2^{NTD} complex, the first for an S-type pyocin-receptor complex, revealed that pyoS2^{NTD} is composed of a bundle of five α-helices, an N-terminal β-hairpin, and an intervening interfacial region rich in proline residues (PRR). The PRR binds at the same site as Fe-Pvd, its proline residues helping to mimic the shape of the ligand, but most intriguingly, the PRR induces conformational changes within the FpvAI plug domain identical to those caused by Fe-Pvd binding. This appears to be the first example of molecular mimicry amongst protein bacteriocins, in contrast to colicin Ia, colicin E2 and colicin E3 (Buchanan *et al.*, 2007, Sharma *et al.*, 2007, Kurisu *et al.*, 2003). However, mimicry amongst the microcins has been documented. Like bacteriocins, microcins are cytotoxic agents produced in times of stress to kill closely related species, but are distinguished by their smaller size (<10 kDa). They are highly resistant to heat, pH and proteases and are implicated in competition amongst commensal species of bacteria, predominantly enterobacteria (Duquesne *et al.*, 2007). Some microcins directly mimic siderophores for uptake by the TonB-dependent iron transporters. The 84-residue microcin MccE492, produced by *Klebsiella pneumoniae*, is post-translationally modified by addition of an enterobactin mimic which coordinates Fe^{3+} ions through a trimeric N-(2,3-dihydroxybenzoyl)-L-serine moiety. The enterobactin mimic is then recognised as a substrate for TonB-dependent import via the

catecholate siderophore receptors FepA, Fiu, IroN or Cir, and the internalised microcin ultimately kills the cell by depolarisation of the IM (Destoumieux-Garzón *et al.*, 2006). Moreover, the peptide itself appears to mimic substrates of iron transporters since post-translationally unmodified MccE492 still possesses killing activity, though with lower efficiency. In addition to MccE492, microcins H47 and M also use catecholate receptors despite having little sequence similarly. They all, however, possess serine-rich C-termini which are thought to be implicated in catecholate siderophore mimicry since receptor substrates are often rich in Ser/Thr residues (Braun *et al.*, 2002). MccJ25 is another siderophore-mimicking microcin that uses FhuA as an OM receptor to kill species of *Escherichia* and *Salmonella* by inhibition of RNA polymerase (Delgado *et al.*, 2001, Salomón and Farías, 1993). Its structure reveals a 21-residue peptide of lasso topology where the C-terminal half is threaded through the N-terminal half, which is cyclised through an isopeptide bond between the amino terminus and the sidechain of Glu8 (Mathavan *et al.*, 2014). Mathavan *et al* (2014) have shown that MccJ25 occupies the same binding site as ferrichrome in FhuA, mimicking the binding mode. Unlike pyoS2, there are no large movements in the plug domain relative to unliganded and ferrichrome-bound FhuA (Locher *et al.*, 1998), suggesting the mechanism of mimicry is more subtle. Despite this, the mimicry of siderophores is clearly important in the import of microcins and bacteriocins alike.

As demonstrated by fluorescence microscopy experiments, pyoS2^{NTD} is actively imported across the OM. Import was dependent on the PMF, TonB1 and an N-terminal TonB1-box motif in both pyoS2^{NTD} and in FpvAI. Indeed, the *in vitro* binding between TonB1 and pyoS2^{NTD} was localised to the N-terminal β-hairpin which suggests the N-terminus is imported first where it contacts TonB1 in the periplasm. This observation is consistent with crosslinking data, where the pyoS2 N-terminus produces two crosslink adducts to

two distinct regions of FpvAI. These N-terminal crosslink sites were mapped to FpvAI residues Met766, projecting inside the lumen, as well as Asp239 of the non-labile plug subdomain. The N-terminus must therefore undergo a large conformation transition, from being abutted against the helical domain to residing within the barrel lumen in the site vacated by the labile plug. How the N-terminus of pyoS2 enters the FpvAI translocation channel in not yet clear. It may be dragged through during the removal of the labile plug but the sole hydrogen bond, between Tyr200 in FpvAI and Pro41 in pyoS2, is probably insufficient. Another possibility is that residues 2-10, not seen in the crystal structure, act as a targeting sequence to guide the N-terminus into the open pore. Moreover, how the remaining domains of pyoS2 translocate is also not yet clear but ultimately the nuclease domain must be delivered to the cytoplasm. The immunity protein at the cell surface is jettisoned by a PMF-dependent force, implying mechanical force is transduced along the length of the protein (Farrance et al., 2013). One possibility is that TonB1 continues to act on the TonB1-box, driving translocation of the entire 689 residue protein. Alternatively, TonB1 provides a mechanical force to overcome the activation barrier, after which translocation proceeds down the energy landscape driven by refolding of successive domains.

The import of siderophores, and indeed peptide microcins, through the lumen of TBDTs seems reasonable due to their small size. Protein bacteriocins, on the other hand, are many times larger. PyoS2 (74 kDa) is ~60 times larger than Fe-Pvd (1.2 kDa), yet they translocate through the same channel in the receptor. The staggering size difference can be seen when comparing the molecular surface Fe-Pvd and the SAXS envelope of pyoS2-ImS2 (Klein *et al.*, 2016) (Figure 7-1). PyoS2-ImS2 extends ~200 Å in length and measures ~35 Å in diameter, whilst Fe-Pvd measures only 23 Å in its longest dimension and 6 Å in its shortest dimension. In the correct orientation, Fe-Pvd could easily pass

through the ~13 Å channel through FpvAI after displacement of the labile half of the plug, whereas a single α-helix would likely be the limit for protein substrates. TonB1-dependent unfolding of pyoS2 therefore seems like the best option for pyoS2 translocation. Although there is limited experimental evidence that this is the case, unfolding is required for the import of several colicins and is generally the accepted mechanism for protein translocation (Vankemmelbeke *et al.*, 2013, Penfold *et al.*, 2004). Moreover, the work presented here shows that pyoS2^{NTD} is destabilised by removal of a β-hairpin from the helical domain, which likely expedites unfolding of the domain during import. The domain can also spontaneously refold as demonstrated by thermal denaturation experiments. Attempts to experimentally verify the unfolding hypothesis are described in the Appendix using disulphide mutants and a fusion with dihydrofolate reductase (DHFR).

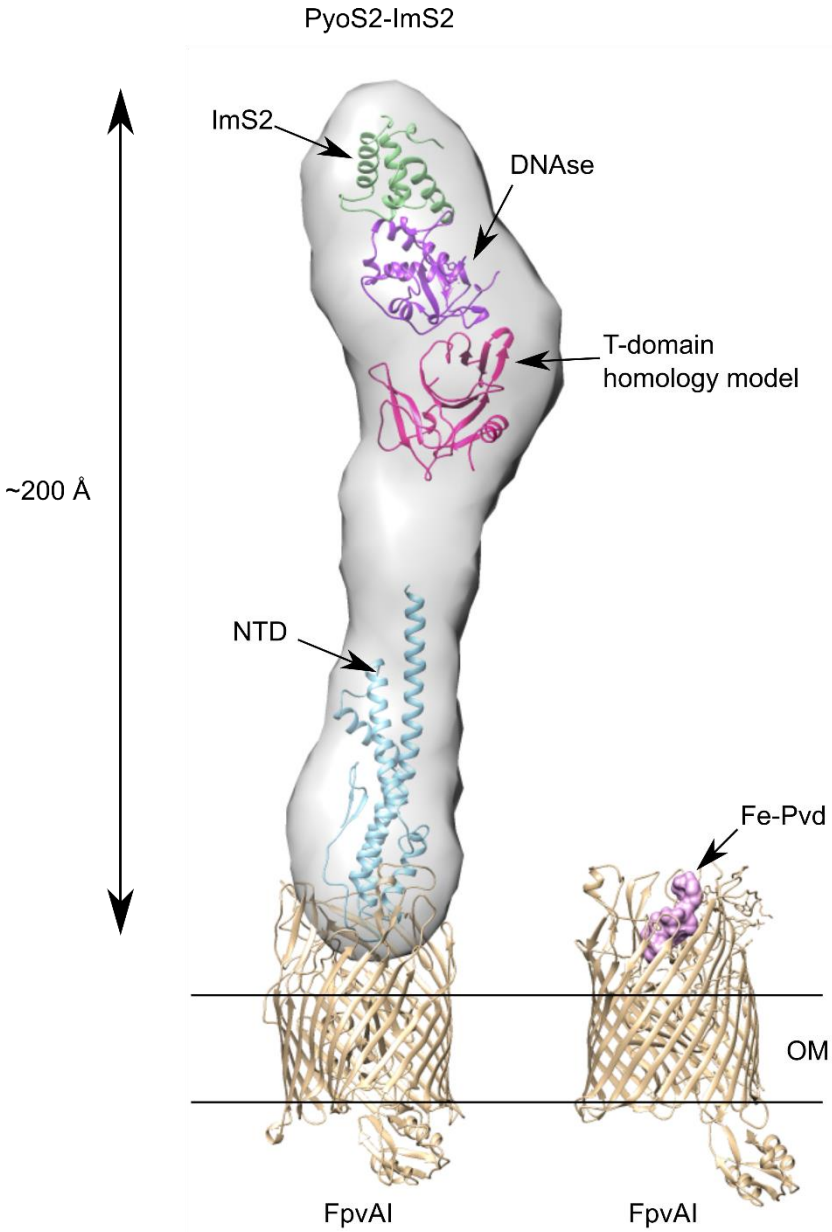

Figure 7-1. A size comparison of the FpvAI translocation substrates pyoS2 and Fe-Pvd. The crystal structures of FpvAI-pyoS2^{NTD} (this study) and the DNase-ImS2 complex (PDB ID 4QKO (Joshi *et al.*, 2015)) were fitted into the SAXS envelope of pyoS2-ImS2 previously determined by Klein *et al* (2016). The approximate location of domain III, often referred to as the translocation domain (*magenta*) was fitted with the structure of an S-type pyocin domain (PDB ID 3MFB, Forouhar *et al*, to be published) with sequence similarity to pyoS2 (415-554) as identified by Sharp *et al* (2017). Remaining density would be occupied by residues including domain II, which has not been structurally defined. The size of pyoS2-ImS2 (~200 Å in length) greatly exceeds that of Fe-Pvd shown as a molecular surface (*pink*).

Not only are protein toxins mediators of competition between species of bacteria, they are also implicated in eukaryotic tissue invasion and pathogenicity. For example, the anthrax, cholera and diphtheria toxins produced by *Bacillus anthracis*, *Vibrio cholerae* and *Corynebacterium diphtheriae*, respectively, result in severe disease. Like bacteriocins, these debilitating toxins are modular, with domains responsible for translocation across biological membranes and domains carrying cytotoxic effector activities. Some toxins carry their own translocation machinery, whilst others parasitise host import systems as do the bacteriocins. Anthrax contains three protein subunits; the protective antigen forms a translocation channel, and the remaining two subunits, lethal factor and edema factor, carry cytotoxic activity (Jiang *et al.*, 2015). After binding to cell surface receptors, the protective antigen is cleaved by furin and forms a pre-pore on the cell membrane. Once the toxin has been endocytosed, acidification of the endosome causes a conformational change in the protective antigen forming a mature translocation pore, through which lethal and edema factors enter the cytosol (Sharma and Collier, 2014). Studies on the anthrax translocation pore have identified a constriction point composed of a ring of phenylalanine residues known as the phi-clamp (Krantz *et al.*, 2005). The phi-clamp catalyses import via a pH-dependent unfolding mechanism known as a Brownian ratchet (Jiang *et al.*, 2015, Feld *et al.*, 2012). Although the pore is cation-selective (Blaustein *et al.*, 1989), acidification of the endosome favours protonation of acidic residues to neutralise their charge, and deprotonation in the cytosol prevents retro-translocation (Feld *et al.*, 2012). This cation-selective property was exploited when a poly-lysine fusion onto the N-terminus of the diphtheria toxin resulted in its import through the anthrax protective antigen (Sharma and Collier, 2014). As shown in this study, a proton gradient (the PMF) is required for pyoS2 import into *P. aeruginosa* through the action of TonB1. It is feasible that a ratcheting mechanism drives the motion

of TonB1 which is mechanically coupled to pyoS2 through an interaction with the TonB1-box. Moreover, the narrow lumen of FpvAI functions as a constriction point requiring pyoS2 to unfold. In the anthrax lethal factor, a force-resistant β-sheet becomes less ordered upon binding to the translocation pores facilitating its import (Feld *et al.*, 2010), whilst in pyoS2, the helical structure is already more force-labile but is further destabilised by removal of the N-terminal β-hairpin. Like anthrax, the diphtheria toxin is composed of multiple domains, one of which forms a translocation channel. The N-terminal domain functions as an enzymatic effector which inhibits protein synthesis by ADP-ribosylation of elongation factor-2, the central domain is the translocation domain and the C-terminal domain binds cell surface receptors (Antignani and Youle, 2008). The diphtheria toxin is also internalised into the endosome where the acidic pH induces partial unfolding that facilitates insertion into the membrane. It then forms a pore through which the enzymatic domain translocates in a pH-dependent manner (Lord *et al.*, 1999, Collier, 2001). Some toxins, such as cholera, rely on host proteins for import. Cholera toxin is composed of an A-subunit with enzymatic activity, and a B-subunit responsible for cell entry. After binding to the cell surface receptor GM1 of intestinal epithelial cells, the toxin is internalised where it eventually reaches the endoplasmic reticulum (ER). The A-subunit is unfolded by protein disulphide isomerase resulting in retrograde translocation into the cytosol via Sec61 by the ER-associated degradation (ERAD) pathway (Schmitz *et al.*, 2000, Wernick *et al.*, 2010). Once in the cytosol, the cholera toxin ADP-ribosylates G-proteins leading to over activity of adenylyl cyclase, overproduction of cyclic AMP and the secretion of chloride ions (Wernick *et al.*, 2010). The massive release of water, driven by osmosis, results in the extreme diarrhoea associated with cholera infection. The ERAD-mediated translocation of the cholera toxin exhibits similarities with the IM translocation of nuclease bacteriocins. The IM AAA^+ ATPase and protease FtsH treats

the IM-associated nuclease as a misfolded protein, translocates it across the IM where it is cleaved by FtsH, and releases it to the cytoplasm (Ito and Akiyama, 2005, Walker *et al.*, 2007). Like bacteriocins, cholera toxin exploits host translocator proteins to deliver its cytotoxic payload.

As effective bactericidal agents with a narrow spectrum of activity, bacteriocins could be exploited as novel treatments for MDR infections (Cotter *et al.*, 2013), and have already shown potent activity in murine lung infection models (McCaughey *et al.*, 2016b). However, bacteriocin immunity proteins serve to protect bacteria against their cytotoxicity (Papadakos *et al.*, 2012). Immunity can be subverted to exchanging cytotoxic domains to generate chimeric bacteriocins. As described in this thesis, replacing the pyoS2 DNase with that of colicin E2 effectively kills the otherwise resistant PAO1 strain. Such a strategy could be used to target specific strains of bacteria that are resistant due to expression of an immunity protein. Not only was it shown that pyoS2^{NTD} is the minimal domain required to permeate the OM barrier of *P. aeruginosa*, but it can also deliver cytotoxic cargo that is active in the periplasm. In particular, the pore-forming domains of pyoS5 and colicin Ia were able to kill *P. aeruginosa* when fused to the C-terminal end of pyoS2^{NTD}. This could be further developed into a delivery platform for antibiotic targets within the cell envelope that would otherwise be unable to cross the OM, or that would be readily excreted. Other potential conjugates include phage lysins, such as T4 lysozyme, which kill bacteria through hydrolysis of the PG cell wall. This strategy proved successful for a pesticin, where a pesticin-T4 lysozyme chimera killed *Yersinia pestis* and *E. coli* via the TBDT FyuA, despite possessing the immunity protein pim (Lukacik *et al.*, 2012, Patzer *et al.*, 2012). Efforts to conjugate the glycopeptide antibiotic vancomycin and the *Pseudomonas*-specific phage lysin gp36c onto pyoS2^{NTD} are discussed in the Appendix.

7.2. Future work

The work presented in this thesis presents a detailed mechanism by which pyoS2 translocates across the OM of *P. aeruginosa*, yet several questions still remain to be answered. Firstly, an internal disulphide bond approach could definitively answer the question of whether pyoS2 unfolds during import, though the model proposed in this study strongly suggests this is the case. An internal disulphide bond between pyoS2^{NTD} helices would prevent complete unfolding thereby blocking import. As discussed in the Appendix, this approach was not successful for pyoS2 but alternative sites for internal disulphide bonds could still be explored. Another strategy could be to engineer rigidity in the DNase domain as this has successfully blocked colicin E9 killing in *E. coli* by preventing immunity protein release (Vankemmelbeke *et al.*, 2013). The disulphide mutant of the colicin E9 DNase domain could directly replace the pyoS2 DNase since inter-species chimeric bacteriocins have shown effective killing activity in this study. Taking this further, immunity protein release could be studied by engineering a fluorophore in the DNase domain and a fluorescence quencher in ImS2. Force-activated immunity protein release should recover fluorescence such that only translocated pyoS2 is fluorescent.

Having developed an assay to monitor pyoS2^{NTD} translocation across the OM of living *P. aeruginosa* both by fluorescence microscopy and crosslinking, the next logical steps would be to perturb the translocation machinery, rather than just the pyocin. As described in this thesis, N-terminal truncations, mutations in the TonB1-box, and a C-terminal GFP fusion all had the effect of blocking import across the OM. Efforts to manipulate the translocation machinery, were limited to mutations in the FpvAI TonB1 box, TonB knockouts and PMF inhibition, but additional mutational studies on FpvAI would further probe the dynamics of translocation. This work would depend on developing a *P.*

aeruginosa plasmid-based expression system where modified FpvAI could be expressed in a knockout strain. Such modifications could include point mutations at key residues involved in Pvd mimicry, specifically Arg204 and Tyr231, which had both undergone significant conformational changes upon binding. Arg204 and Tyr231 do not participate in any obvious intermolecular interactions but may act as 'latches' which provide the signal for initiation of translocation. Mutations which inhibit translocation, whilst maintaining binding could be assayed by FRAP or crosslinking experiments, and would reinforce their role in translocation signalling.

FpvAI modifications could further probe the unplugging mechanism required for pyoS2^{NTD} import. A recent AFM study (Hickman *et al.*, 2017) and a structural comparison with BtuB suggested that the FpvAI plug is composed of force-labile and force-resistant subdomains. Residues at the interface of these subdomains could be substituted for cysteines which when disulphide bonded, tether the two halves of the plug. This should have the effect of blocking unplugging such that pyoS2^{NTD} cannot translocate, validating the subdomain hypothesis. Alternatively, disulphide bonding regions of the plug to the barrel wall should have the same effect. Such approaches could be tricky since it would rely on carefully controlling the transmembrane redox environment. Cysteine residues could also be introduced at sites of photo-activated crosslinking in FpvAI and the corresponding *p*Bpa site in pyoS2^{NTD}GFP. In this strategy, disulphide-bonded partially translocated intermediates could be isolated on a much larger scale, circumventing the need to work at lower optical density and small culture volumes, and potentially providing enough material for downstream structural studies.

Structural information on partially translocated pyoS2 would provide a detailed view of the import mechanism but the limitation has always been the yield. The disulphide-trapping strategy described previously could be one option to address this. During the

writing of this thesis, work has begun on structural characterisation of the ground-state pyoS2-ImS2-FpvAI-TonB1 heterotetrameric complex by electron cryo-microscopy (cryo-EM). The pyoS2 construct was N-terminally truncated to remove its own TonB1-box such that the stoichiometry would be 1:1:1:1, with a total molecular weight of ~193 kDa. Briefly, the complex was co-eluted from a SEC column in a single peak containing all four proteins, and the detergent was exchanged for A8-35 amphipol such that the complex wasn't obscured by the detergent micelle. This work will hopefully culminate in a 3D structure of the tetrameric complex. The same approach could then be applied to partially translocated pyoS2. Obtaining a high-resolution crystal structure of partially translocated pyoS2 would be ambitious due to the heterogeneity between individual complexes and large regions of disorder.

Finally, the process by which pyoS2 is translocated across the IM remains unknown. Nuclease colicins are translocated across the IM by FtsH in *E. coli*, of which there is a *P. aeruginosa* homolog. It is likely that nuclease pyocins, like pyoS2, use the same mechanism, but this has yet to be experimentally verified. IM translocation may be facilitated by domain III of pyoS2 which possesses the same DPY motif seen in other nuclease bacteriocin translocation domains (Sharp *et al.*, 2017). It would be interesting to determine whether fusing the DNase domain directly onto the C-terminus of pyoS2^{NTD} would result in cell killing. This could also be tested with and without the DPY motif. If domains II and III are dispensable for pyoS2 killing, it would raise many questions regarding their function. Indeed, the precise role of domain III has yet to be determined.

7.3. Overall conclusions

In summary, the work described in this thesis used a multidisciplinary approach to unravel the molecular mechanisms involved in pyoS2 translocation across the OM of *P. aeruginosa*. This began by demonstrating an *in vitro* interaction between recombinantly expressed and purified pyoS2-ImS2 and FpvAI for the first time. Proteolysis experiments then narrowed down the binding domain to the N-terminus, referred to as pyoS2^{NTD}, which binds FpvAI with 240 pM affinity, readily outcompeting the binding of the endogenous ligand Fe-Pvd. Biphasic binding kinetics suggested conformational changes occurred during complex formation which were later apparent in the crystal structure. The crystal structure of the FpvAI-pyoS2^{NTD} complex revealed that the pyoS2^{NTD} was composed of five α-helices and an N-terminal β-hairpin, and the intervening PRR interacted with the plug domain to mimic the ligand. Fluorescence microscopy experiments showed that pyoS2^{NTD} was the minimal OM translocation domain and this process was dependent on the PMF, TonB1 and the pyoS2 N-terminal β-hairpin. PyoS2^{NTD} was also able to translocate pore-forming domains from other bacteriocins that are active in the periplasm. The link between the N-terminal β-hairpin and TonB1 was apparent after ITC experiments demonstrated an *in vitro* interaction involving the TonB1-box of pyoS2. Finally, photo-activated crosslinking of a stalled pyoS2^{NTD}GFP fusion mapped the contact sites to FpvAI during translocation. Crosslinking data, along with other observations made throughout this study describe a multi-step mechanism of pyoS2 translocation. In the first stage, binding to FpvAI induces Fe-Pvd-mimicking conformational changes in the plug domain that initiate the TonB1-dependent unplugging of FpvAI. Then, displacement of the labile half of the plug opens a translocation channel through the receptor which is occupied by the pyoS2 N-terminal β-hairpin, presenting the pyoS2 TonB1-box to the periplasmic side. A second TonB1-dependent force is then

applied to the N-terminus of pyoS2 to drive the translocation into the periplasm probably by successive unfolding of the domains.

This work highlights common themes amongst protein import systems that involve the parasitism of the target cell's own translocation machinery, but this is the first example of protein import through an iron transporter. The widely accepted mechanism of protein import is the requirement of dedicated translocation machinery, yet it has been shown here that bacteria possess rudimentary import systems involving energised nutrient transporters. This new understanding has implications in the development of novel antibiotics to combat the ever present threat of antibiotic resistance.

Appendix I

Protein sequences

FpvAI: *E. coli* OmpF signal sequence residues 1-23; FpvAI residues 45-815
MVKRNILAVIVPALLVAGTANAAQEVEFDIPPQALGSALQEFGRQADIQVLYRPEEVRN
KRSSAIKGKLEPNQAITELLRGTGASVDFQGNAITISVAEAADSSVDLGATMITSNQLG
TITEDSGSYTPGTIATATRLVLTPRETPQSITVVTRQNMDDFGLNNIDDVMRHTPGITV
SAYDTDRNNYYARGFSINNFQYDGIPSTARNVGYSAGNTLSDMAIYDRVEVLKGATGLL
TGAGSLGATINLIRKKPTHEFKGHVELGAGSWDNYRSELDVSGPLTESGNVRGRAVAAY
QDKHSFMDHYERKTSVYYGILEFDLNPDTMLTVGADYQDNDPKGSGWSGSFPLFDSQGN
RNDVSRSFNNGAKWSSWEQYTRTVFANLEHNFANGWVGKVQLDHKINGYHAPLGAIMGD
WPAPDNSAKIVAQKYTGETKSNSLDIYLTGPFQFLGREHELVVGTSASFSHWEGKSYWN
LRNYDNTTDDFINWDGDIGKPDWGTPSQYIDDKTRQLGSYMTARFNVTDDLNLFLGGRV
VDYRVTGLNPTIRESGRFIPYVGAVYDLNDTYSVYASYTDIFMPQDSWYRDSSNKLLEP
DEGQNYEIGIKGEYLDGRLNTSLAYFEIHEENRAEEDALYNSKPTNPAITYAYKGIKAK
TKGYEAEISGELAPGWQVQAGYTHKIIRDDSGKKVSTWEPQDQLSLYTSYKFKGALDKL
TVGGGARWQGKSWQMVYNNPRSRWEKFSQEDYWLVDLMARYQITDKLSASVNVNNVFDK
TYYTNIGFYTSASYGDPRNLMFSTRWDF

Pyocin S2
MAVNDYEPGSMVITHVQGGGRDIIQYIPARSSYGTPPFVPPGPSPYVGTGMQEYRKLRS
TLDKSHSELKKNLKNETLKEVDELKSEAGLPGKAVSANDIRDEKSIVDALMDAKAKSLK
AIEDRPANLYTASDFPQKSESMYQSQLLASRKFYGEFLDRHMSELAKAYSADIYKAQIA
ILKQTSQELENKARSLEAEAQRAAAEVEADYKARKANVEKKVQSELDQAGNALPQLTNP
TPEQWLERATQLVTQAIANKKKLQTANNALIAKAPNALEKQKATYNADLLVDEIASLQA
RLDKLNAETARRKEIARQAAIRAANTYAMPANGSVVATAAGRGLIQVAQGAASLAQAIS
DAIAVLGRVLASAPSVMAVGFASLTYSSRTAEQWQDQTPDSVRYALGMDAAKLGLPPSV
NLNAVAKASGTVDLPMRLTNEARGNTTTLSVVSTDGVSVPKAVPVRMAAYNATTGLYEV
TVPSTTAEAPPLILTWTPASPPGNQNPSSTTPVVPKPVPVYEGATLTPVKATPETYPGV
ITLPEDLIIGFPADSGIKPIYVMFRDPRDVPGAATGKGQPVSGNWLGAASQGEGAPIPS
QIADKLRGKTFKNWRDFREQFWIAVANDPELSKQFNPGSLAVMRDGGAPYVRESEQAGG
RIKIEIHHKVRIADGGGVYNMGNLVAVTPKRHIEIHKGGK

Δ1-21pyocin S2: Residues 22-689
MDIIQYIPARSSYGTPPFVPPGPSPYVGTGMQEYRKLRSTLDKSHSELKKNLKNETLKE
VDELKSEAGLPGKAVSANDIRDEKSIVDALMDAKAKSLKAIEDRPANLYTASDFPQKSE
SMYQSQLLASRKFYGEFLDRHMSELAKAYSADIYKAQIAILKQTSQELENKARSLEAEA
QRAAAEVEADYKARKANVEKKVQSELDQAGNALPQLTNPTPEQWLERATQLVTQAIANK
KKLQTANNALIAKAPNALEKQKATYNADLLVDEIASLQARLDKLNAETARRKEIARQAA
IRAANTYAMPANGSVVATAAGRGLIQVAQGAASLAQAISDAIAVLGRVLASAPSVMAVG
FASLTYSSRTAEQWQDQTPDSVRYALGMDAAKLGLPPSVNLNAVAKASGTVDLPMRLTN
EARGNTTTLSVVSTDGVSVPKAVPVRMAAYNATTGLYEVTVPSTTAEAPPLILTWTPAS
PPGNQNPSSTTPVVPKPVPVYEGATLTPVKATPETYPGVITLPEDLIIGFPADSGIKPI
YVMFRDPRDVPGAATGKGQPVSGNWLGAASQGEGAPIPSQIADKLRGKTFKNWRDFREQ
FWIAVANDPELSKQFNPGSLAVMRDGGAPYVRESEQAGGRIKIEIHHKVRIADGGGVYN
MGNLVAVTPKRHIEIHKGGK

Δ1-30pyocin S2: Residues 31-689

MSSYGTPPFVPPGPSPYVGTGMQEYRKLRSTLDKSHSELKKNLKNETLKEVDELKSEAG
LPGKAVSANDIRDEKSIVDALMDAKAKSLKAIEDRPANLYTASDFPQKSESMYQSQLLA
SRKFYGEFLDRHMSELAKAYSADIYKAQIAILKQTSQELENKARSLEAEAQRAAAEVEA
DYKARKANVEKKVQSELDQAGNALPQLTNPTPEQWLERATQLVTQAIANKKKLQTANNA
LIAKAPNALEKQKATYNADLLVDEIASLQARLDKLNAETARRKEIARQAAIRAANTYAM
PANGSVVATAAGRGLIQVAQGAASLAQAISDAIAVLGRVLASAPSVMAVGFASLTYSSR
TAEQWQDQTPDSVRYALGMDAAKLGLPPSVNLNAVAKASGTVDLPMRLTNEARGNTTTL
SVVSTDGVSVPKAVPVRMAAYNATTGLYEVTVPSTTAEAPPLILTWTPASPPGNQNPSS
TTPVVPKPVPVYEGATLTPVKATPETYPGVITLPEDLIIGFPADSGIKPIYVMFRDPRD
VPGAATGKGQPVSGNWLGAASQGEGAPIPSQIADKLRGKTFKNWRDFREQFWIAVANDP
ELSKQFNPGSLAVMRDGGAPYVRESEQAGGRIKIEIHHKVRIADGGGVYNMGNLVAVTP
KRHIEIHKGGK

Δ1-45pyocin S2: Residues 46-689

MYVGTGMQEYRKLRSTLDKSHSELKKNLKNETLKEVDELKSEAGLPGKAVSANDIRDEK
SIVDALMDAKAKSLKAIEDRPANLYTASDFPQKSESMYQSQLLASRKFYGEFLDRHMSE
LAKAYSADIYKAQIAILKQTSQELENKARSLEAEAQRAAAEVEADYKARKANVEKKVQS
ELDQAGNALPQLTNPTPEQWLERATQLVTQAIANKKKLQTANNALIAKAPNALEKQKAT
YNADLLVDEIASLQARLDKLNAETARRKEIARQAAIRAANTYAMPANGSVVATAAGRGL
IQVAQGAASLAQAISDAIAVLGRVLASAPSVMAVGFASLTYSSRTAEQWQDQTPDSVRY
ALGMDAAKLGLPPSVNLNAVAKASGTVDLPMRLTNEARGNTTTLSVVSTDGVSVPKAVP
VRMAAYNATTGLYEVTVPSTTAEAPPLILTWTPASPPGNQNPSSTTPVVPKPVPVYEGA
TLTPVKATPETYPGVITLPEDLIIGFPADSGIKPIYVMFRDPRDVPGAATGKGQPVSGN
WLGAASQGEGAPIPSQIADKLRGKTFKNWRDFREQFWIAVANDPELSKQFNPGSLAVMR
DGGAPYVRESEQAGGRIKIEIHHKVRIADGGGVYNMGNLVAVTPKRHIEIHKGGK

Immunity protein S2

MKSKISEYTEKEFLEFVKDIYTNNKKKFPTEESHIQAVLEFKKLTEHPSGSDLLYYPNE
NREDSPAGVVKEVKEWRASKGLPGFKAGLEHHHHHH

PyoS2^{NTD}: Residues 1-209

MAVNDYEPGSMVITHVQGGGRDIIQYIPARSSYGTPPFVPPGPSPYVGTGMQEYRKLRS
TLDKSHSELKKNLKNETLKEVDELKSEAGLPGKAVSANDIRDEKSIVDALMDAKAKSLK
AIEDRPANLYTASDFPQKSESMYQSQLLASRKFYGEFLDRHMSELAKAYSADIYKAQIA
ILKQTSQELENKARSLEAEAQRAAAEVEADYKLEHHHHHH

Δ1-21pyoS2^{NTD}: Residues 22-209

MDIIQYIPARSSYGTPPFVPPGPSPYVGTGMQEYRKLRSTLDKSHSELKKNLKNETLKE
VDELKSEAGLPGKAVSANDIRDEKSIVDALMDAKAKSLKAIEDRPANLYTASDFPQKSE
SMYQSQLLASRKFYGEFLDRHMSELAKAYSADIYKAQIAILKQTSQELENKARSLEAEA
QRAAAEVEADYKLEHHHHHH

Δ1-30pyoS2^{NTD}: Residues 31-209
MSSYGTPPFVPPGPSPYVGTGMQEYRKLRSTLDKSHSELKKNLKNETLKEVDELKSEAG
LPGKAVSANDIRDEKSIVDALMDAKAKSLKAIEDRPANLYTASDFPQKSESMYQSQLLA
SRKFYGEFLDRHMSELAKAYSADIYKAQIAILKQTSQELENKARSLEAEAQRAAAEVEA
DYKLEHHHHHH

Δ1-45pyoS2^{NTD}: Residues 46-209
MYVGTGMQEYRKLRSTLDKSHSELKKNLKNETLKEVDELKSEAGLPGKAVSANDIRDEK
SIVDALMDAKAKSLKAIEDRPANLYTASDFPQKSESMYQSQLLASRKFYGEFLDRHMSE
LAKAYSADIYKAQIAILKQTSQELENKARSLEAEAQRAAAEVEADYKLEHHHHHH

PyoS2^{NTD}GFP: PyoS2 residues 1-209; GFP residues 1-238
MAVNDYEPGSMVITHVQGGGRDIIQYIPARSSYGTPPFVPPGPSPYVGTGMQEYRKLRS
TLDKSHSELKKNLKNETLKEVDELKSEAGLPGKAVSANDIRDEKSIVDALMDAKAKSLK
AIEDRPANLYTASDFPQKSESMYQSQLLASRKFYGEFLDRHMSELAKAYSADIYKAQIA
ILKQTSQELENKARSLEAEAQRAAAEVEADYKEFMSKGEELFTGVVPILVELDGDVNGH
KFSVSGEGEGDATYGKLTLKFICTTGKLPVPWPTLVTTFSYGVQCFSRYPDHMKQHDFF
KSAMPEGYVQERTIFFKDDGNYKTRAEVKFEGDTLVNRIELKGIDFKEDGNILGHKLEY
NYNSHNVYIMADKQKNGIKVNFKIRHNIEDGSVQLADHYQQNTPIGDGPVLLPDNHYLS
TQSALSKDPNEKRDHMVLLEFVTAAGITHGMDELYKASMTGGQQMGRGSHHHHHH

PyoS2-E2: PyoS2 residues 1-209; colicin E2 residues 449-581
MAVNDYEPGSMVITHVQGGGRDIIQYIPARSSYGTPPFVPPGPSPYVGTGMQEYRKLRS
TLDKSHSELKKNLKNETLKEVDELKSEAGLPGKAVSANDIRDEKSIVDALMDAKAKSLK
AIEDRPANLYTASDFPQKSESMYQSQLLASRKFYGEFLDRHMSELAKAYSADIYKAQIA
ILKQTSQELENKARSLEAEAQRAAAEVEADYKARKANVEKKVQSELDQAGNALPQLTNP
TPEQWLERATQLVTQAIANKKKLQTANNALIAKAPNALEKQKATYNADLLVDEIASLQA
RLDKLNAETARRKEIARQAAIRAANTYAMPANGSVVATAAGRGLIQVAQGAASLAQAIS
DAIAVLGRVLASAPSVMAVGFASLTYSSRTAEQWQDQTPDSVRYALGMDAAKLGLPPSV
NLNAVAKASGTVDLPMRLTNEARGNTTTLSVVSTDGVSVPKAVPVRMAAYNATTGLYEV
TVPSTTAEAPPLILTWTPASPPGNQNPSSTTPVVPKPVPVYEGATLTPVKATPETYPGV
ITLPEDLIIGFPADSGIKPIYVMFRAMESKRNKPGKATGKGKPVGDKWLDDAGKDSGAP
IPDRIADKLRDKEFKNFDDFRKKFWEEVSKDPDLSKQFKGSNKTNIQKGKAPFARKKDQ
VGGRERFELHHDKPISQDGGVYDMNNIRVTTPKRHIDIHRGK

Immunity protein E2
MELKHSISDYTEAEFLEFVKKICRAEGATEEDDNKLVREFERLTEHPDGSDLIYYPRDD
REDSPEGIVKEIKEWRAANGKSGFKQGLEHHHHHH

PyoS2^{NTD}-S5: PyoS2 residues 1-209; pyoS5 residues 301-498
MAVNDYEPGSMVITHVQGGGRDIIQYIPARSSYGTPPFVPPGPSPYVGTGMQEYRKLRS
TLDKSHSELKKNLKNETLKEVDELKSEAGLPGKAVSANDIRDEKSIVDALMDAKAKSLK
AIEDRPANLYTASDFPQKSESMYQSQLLASRKFYGEFLDRHMSELAKAYSADIYKAQIA
ILKQTSQELENKARSLEAEAQRAAAEVEADYKAETTRRRTEAERKAAEEQALQDAIKFT
ADFYKEVTEKFGARTSEMARQLAEGARGKNIRSSAEAIKSFEKHKDALNKKLSLKDRQA
IAKAFDSLDKQMMAKSLEKFSKGFGVVGKAIDAASLYQEFKISTETGDWKPFFVKIETL
AAGAAASWLVGIAFATATATPIGILGFALVMAVTGAMIDEDLLEKANNLVISILEHHHH
HH

PyoS2^{NTD}-Ia: PyoS2 residues 1-209; colicin Ia residues 452-626
MAVNDYEPGSMVITHVQGGGRDIIQYIPARSSYGTPPFVPPGPSPYVGTGMQEYRKLRS
TLDKSHSELKKNLKNETLKEVDELKSEAGLPGKAVSANDIRDEKSIVDALMDAKAKSLK
AIEDRPANLYTASDFPQKSESMYQSQLLASRKFYGEFLDRHMSELAKAYSADIYKAQIA
ILKQTSQELENKARSLEAEAQRAAAEVEADYKAINFTTEFLKSVSEKYGAKAEQLAREM
AGQAKGKKIRNVEEALKTYEKYRADINKKINAKDRAAIAAALESVKLSDISSNLNRFSR
GLGYAGKFTSLADWITEFGKAVRTENWRPLFVKTETIIAGNAATALVALVFSILTGSAL
GIIGYGLLMAVTGALIDESLVEKANKFWGILEHHHHHH

TonB1: Residues 109-342
GAMATPAELNLGHGELPKTMQVNFVQLEKKAEPTPQPPAAAPEPTPPKIEEPKPEPPKP
KPVEKPKPKPKPKPKPVENAIPKAKPKPEPKPKPEPEPSTEASSQPSPSSAAPPPAPTV
GQSTPGAQTAPSGSQGPAGLPSGSLNDSDIKPLRMDPPVYPRMAQARGIEGRVKVLFTI
TSDGRIDDIQVLESVPSRMFDREVRQAMAKWRFEPRVSGGKIVARQATKMFFFKIEKRR

PyoS2^{NTD}DHFR: PyoS2 residues 1-209; murine DHFR residues 2-187
MAVNDYEPGSMVITHVQGGGRDIIQYIPARSSYGTPPFVPPGPSPYVGTGMQEYRKLRS
TLDKSHSELKKNLKNETLKEVDELKSEAGLPGKAVSANDIRDEKSIVDALMDAKAKSLK
AIEDRPANLYTASDFPQKSESMYQSQLLASRKFYGEFLDRHMSELAKAYSADIYKAQIA
ILKQTSQELENKARSLEAEAQRAAAEVEADYKGSGVRPLNCIVAVSQNMGIGKNGDLPW
PPLRNEFKYFQRMTTTSSVEGKQNLVIMGRKTWFSIPEKNRPLKDRINIVLSRELKEPP
RGAHFLAKSLDDALRLIEQPELASKVDMVWIVGGSSVYQEAMNQPGHLRLFVTRIMQEF
ESDTFFPEIDLGKYKLLPEYPGVLSEVQEEKGIKYKFEVYEKKDC

PyoS2^{NTD}gp36c: PyoS2 residues 1-209; gp36c residues 738-898
MAVNDYEPGSMVITHVQGGGRDIIQYIPARSSYGTPPFVPPGPSPYVGTGMQEYRKLRS
TLDKSHSELKKNLKNETLKEVDELKSEAGLPGKAVSANDIRDEKSIVDALMDAKAKSLK
AIEDRPANLYTASDFPQKSESMYQSQLLASRKFYGEFLDRHMSELAKAYSADIYKAQIA
ILKQTSQELENKARSLEAEAQRAAAEVEADYKGSGLKQDVFNWRKELAQFEAYRGEAYK
DADGYSVGLGHYLGSGNAGAGTTVTPEQAAQWFAEDTDRALDQGVRLADELGVTNNASI
LGLAGMAFQMGEGRARQFRNTFQAIKDRNKEAFEAGVRNSKWYTQTPDRAEAFIKRMAP
HFDTPSQIGVDWYSAATAE

Vector maps

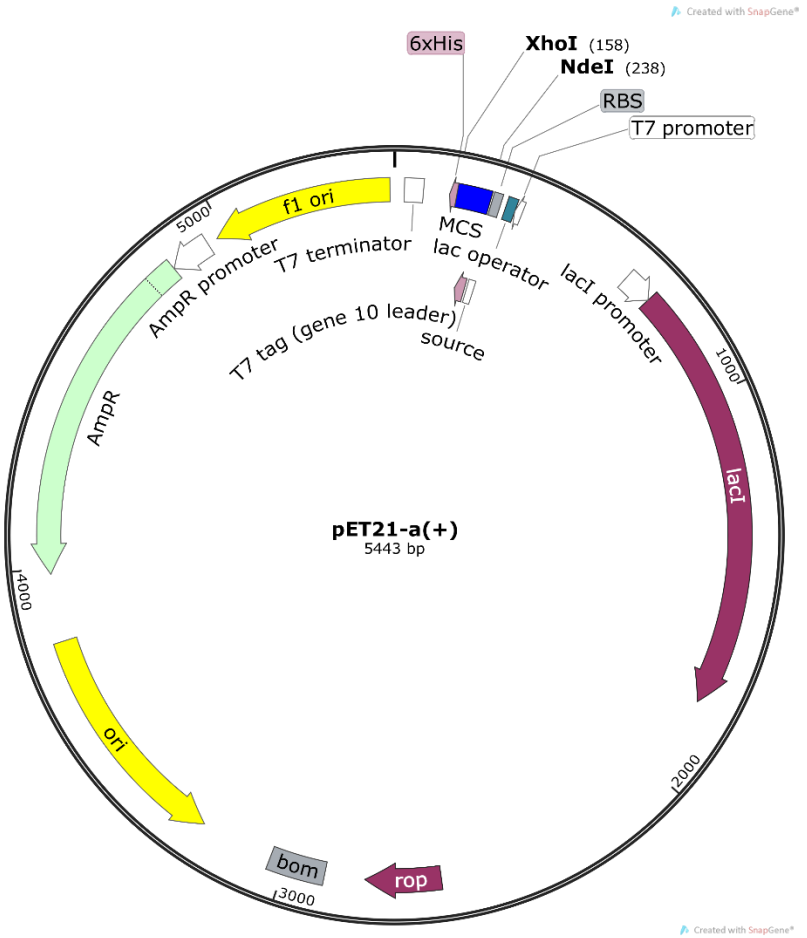
Created with SnapGene®
6xHis
XhoI (158)
NdeI (238)
RBS
T7 promoter
f1 ori
MCS
lac operator
lacI promoter
T7 terminator
AmpR promoter
T7 tag (gene 10 leader)
source
AmpR
lacI
pET21-a(+)
5443 bp
ori
bom
rop
1000
2000
3000
4000
5000

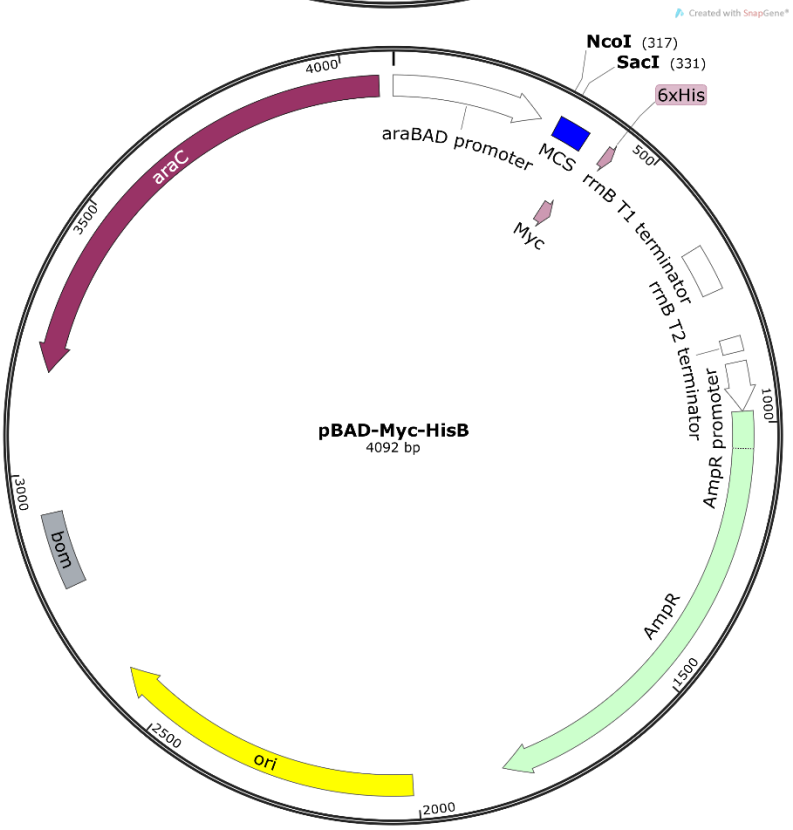
Created with SnapGene®
NcoI (317)
SacI (331)
6xHis
araBAD promoter
MCS
rrnB T1 terminator
rrnB T2 terminator
AmpR promoter
Myc
araC
AmpR
pBAD-Myc-HisB
4092 bp
bom
ori
500
1000
1500
2000
2500
3000
3500
4000

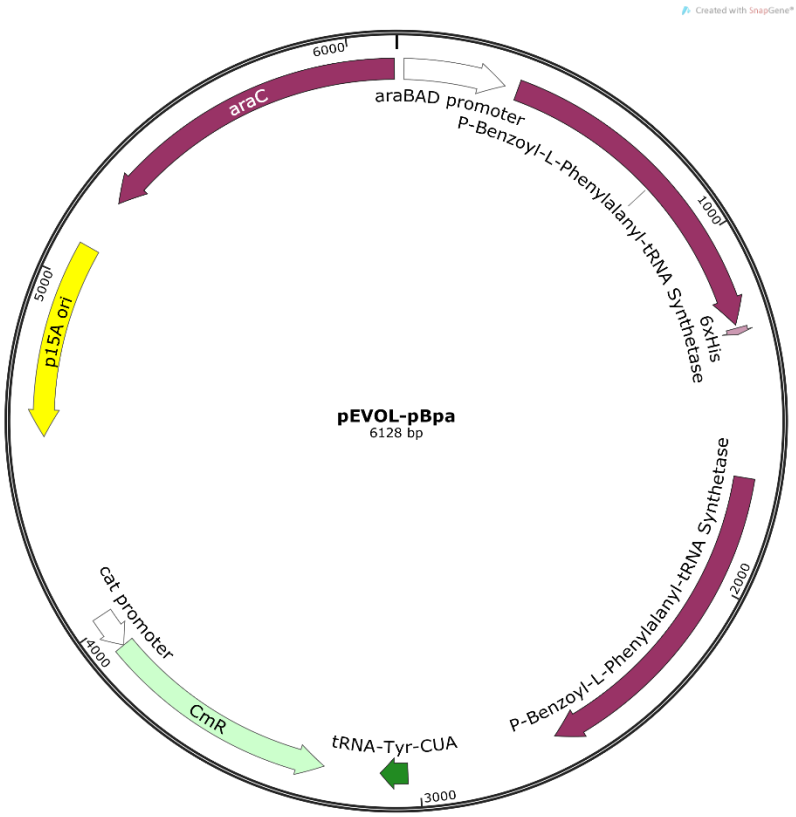
Created with SnapGene®
6000
araC
araBAD promoter
P-Benzoyl-L-Phenylalanyl-tRNA Synthetase
1000
6xHis
5000
p15A ori
pEVOL-pBpa
6128 bp
cat promoter
4000
CmR
tRNA-Tyr-CUA
3000
P-Benzoyl-L-Phenylalanyl-tRNA Synthetase
2000

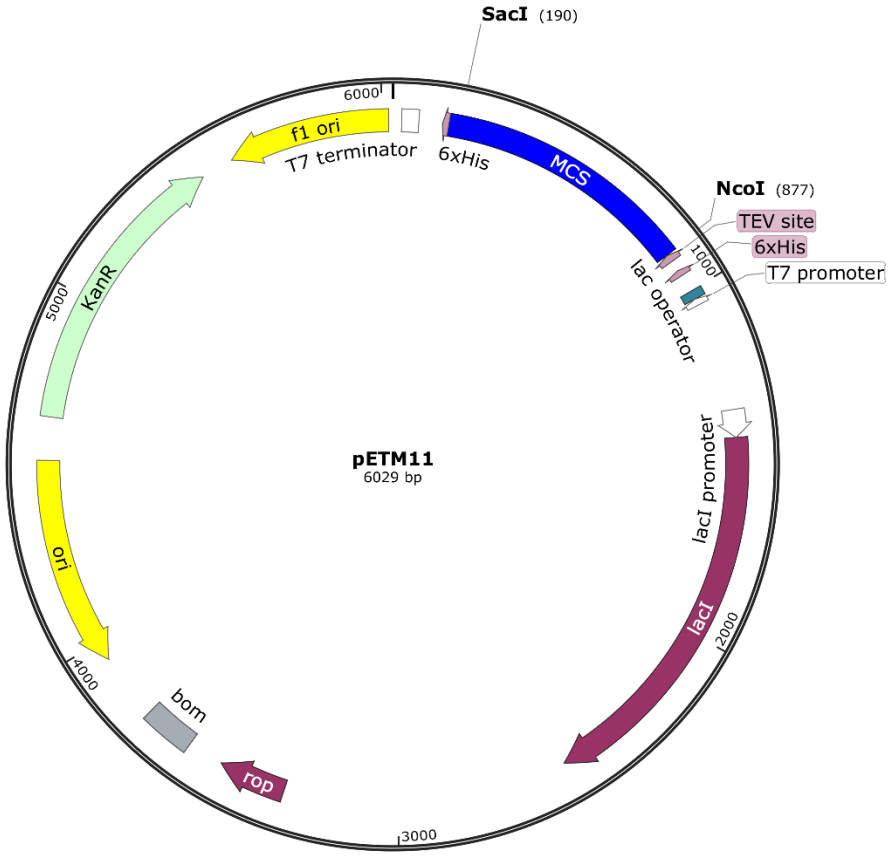
Created with SnapGene®
SacI (190)
6000
f1 ori
T7 terminator
6xHis
MCS
NcoI (877)
TEV site
6xHis
T7 promoter
1000
lac operator
5000
KanR
pETM11
6029 bp
lacI promoter
lacI
2000
ori
4000
bom
rop
3000

Appendix II

This section describes work commenced on further engineering of pyoS2^{NTD}. Firstly, the unfolding hypothesis was investigated by crosslinking adjacent helices in the NTD of pyoS2 using an engineered disulphide bond, and testing the effect on killing activity. A disulphide bond would prevent complete unfolding thereby blocking import and killing. Another strategy involved fusing DHFR onto the C-terminus of pyoS2^{NTD}, which becomes force-resistant when bound to its allosteric inhibitor methotrexate. DHFR fusions have been frequently used in the study of mitochondrial protein import (Voisine *et al.*, 1999, Junker *et al.*, 2005, Wilcox *et al.*, 2005). Methotrexate is a structural analogue of dihydrofolate and is a potent inhibitor of DHFR resulting in a large increase in stability to resist force-dependent unfolding (Ainavarapu *et al.*, 2005, Junker *et al.*, 2005). It was hypothesised that DHFR fused to the C-terminus of pyoS2^{NTD} could be readily unfolded in the absence of methotrexate, whilst addition of methotrexate would block translocation into *P. aeruginosa* by resisting unfolding.

Engineering disulphide bonds to block pyoS2 unfolding

Disulphide by Design software (Craig and Dombkowski, 2013) identified four residue pairs with ideal geometry for disulphide bond formation. His65 and Tyr167 were selected for mutation because the sidechains protrude into the core of helices I and V and have maximum separation in linear sequence. A H65C Y167C double mutant in pyoS2, pyoS2(H65C Y167C), was generated by site directed mutagenesis which should form a disulphide bond as shown in Figure S1.

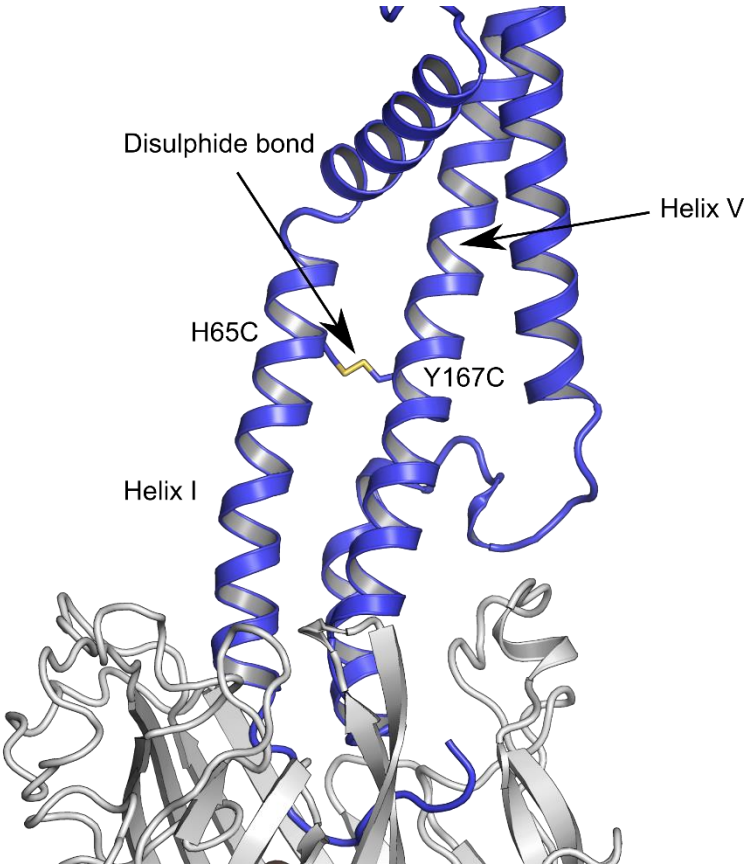

Figure S1. Position of engineered disulphide bond in pyoS2^{NTD}.
Cartoon representation of pyoS2^{NTD} (*blue*) bound to FpvAI (*grey*) showing the position the disulphide bond between H65C of helix I and Y167C of helix V.

Addition of DTT should favour reduction of the disulphide bond allowing the pyoS2^{NTD} to unfold, whilst addition of diamide should favour disulphide bond formation. Unfortunately, there was no difference in killing efficiency when pyoS2(H65C Y167C) was DTT or diamide treated both in plate killing assays (Figure S2) and in liquid culture (Figure S3). The efficiency of disulphide bond formation can be seen on non-reducing SDS-PAGE, which shows a clear distinction between reduced and oxidised protein with the oxidised protein having a slightly greater electrophoretic mobility (Figure S4). DTT treatment ensures the disulphides are fully reduced but diamide treatment is not able to drive disulphide formation to completion. The remaining non-disulphide-bonded population probably accounts for the killing activity. Disulphide-bonded and

non-disulphide-bonded forms will need to be separated in order to obtain useful conclusions from these experiments.

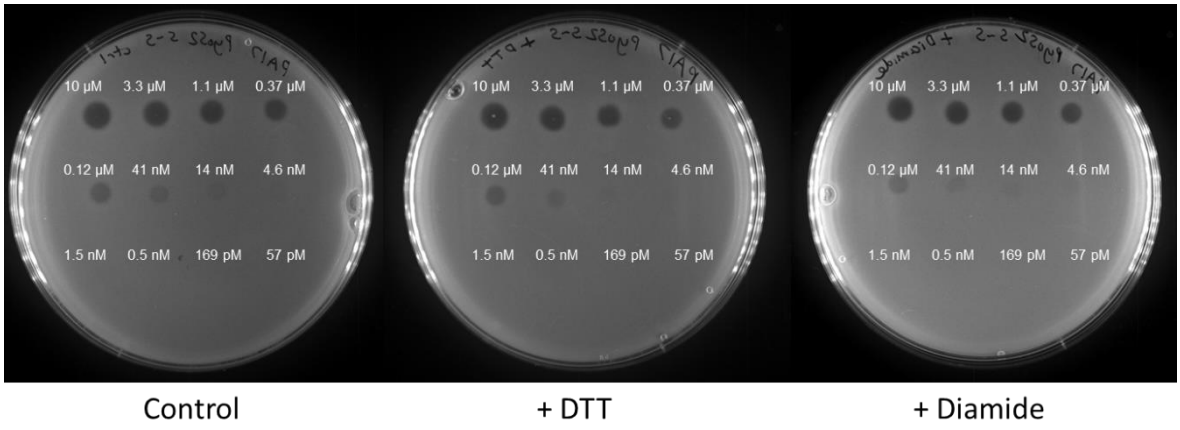

Figure S2. Plate-based killing assays using disulphide crosslinked pyoS2.
PyoS2(H65C Y167C)-ImS2 was spotted onto lawns of *P. aeruginosa* PA17 in 3-fold serial dilutions. Protein was pre-treated with 1 mM DTT to favour the reduced, non-disulphide-bonded form, or with 1 mM diamide to favour disulphide bond formation. Killing activity was comparable across all conditions.

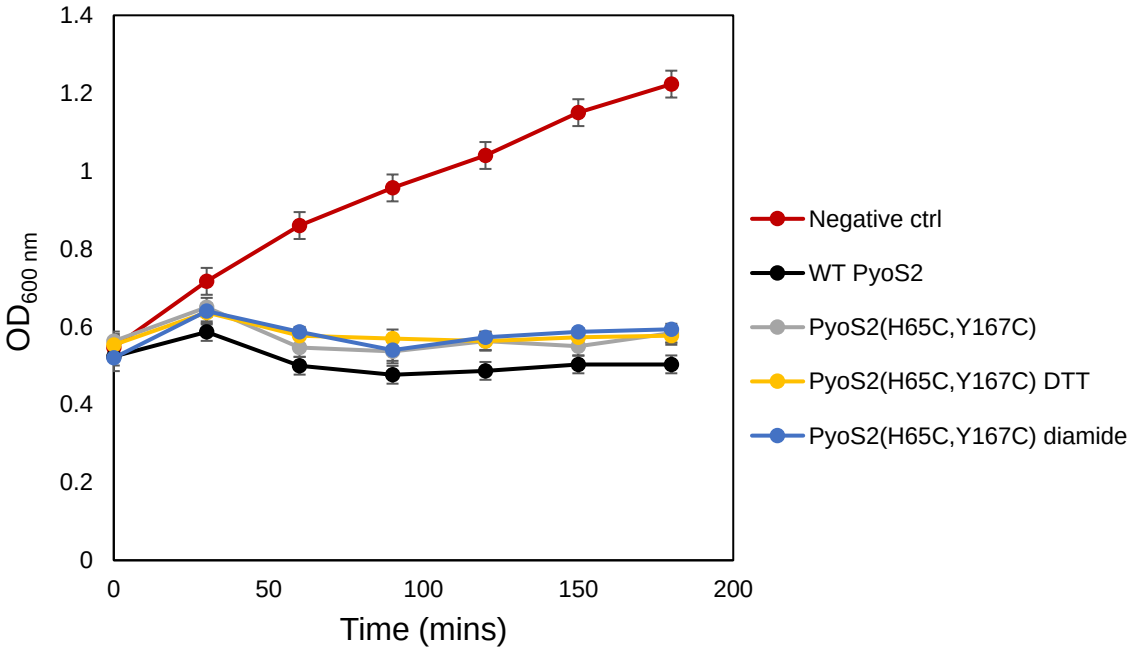

Figure S3. Liquid culture killing assays using disulphide crosslinked pyoS2.
P. aeruginosa PA17 liquid culture killing assays using 100 nM wild-type (WT) pyoS2, 100 nM pyoS2(H65C Y167C) pre-treated with 10 mM DTT or 1 mM diamide, and a no pyoS2 negative control. $OD_{600\ nm}$ measurements from three independent cultures were averaged and error bars represent the standard deviation. The pyoS2(H65C Y167C) mutant kills slightly less effectively than WT pyoS2 but there is no difference upon treatment with DTT or diamide.

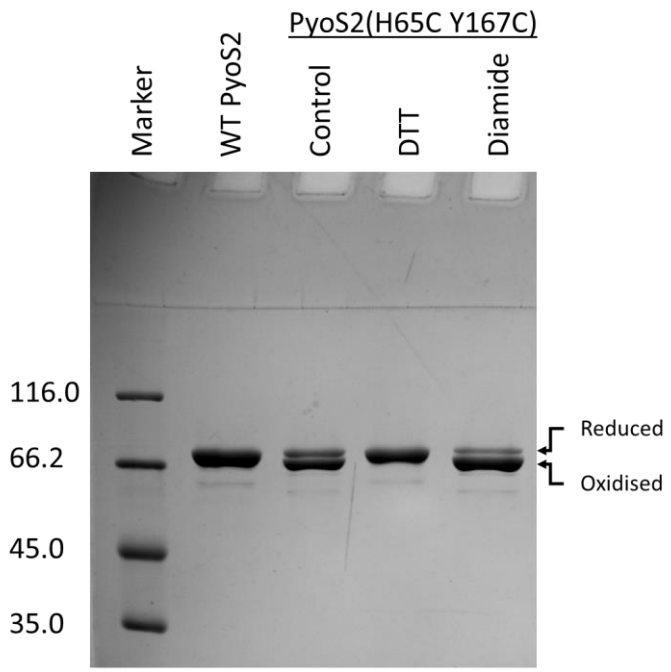

Figure S4. The pyoS2(H65C Y176C) disulphide bond does not fully form.
SDS-PAGE analysis of wild-type (*WT*) pyoS2, pyoS2(H65C,Y167C) treated with 10 mM DTT, 1 mM diamide or nothing (*control*). 10 µl samples in non-reducing SDS-PAGE buffer were loaded onto a 10% polyacrylamide gel. Oxidised (disulphide-bonded) pyoS2(H65C Y167C) migrates slightly faster in non-reducing SDS-PAGE but a reduced population remains despite diamide treatment.

Using a DHFR fusion to block pyoS2^{NTD} import

PyoS2^{NTD} was fused to murine DHFR with Gly-Ser-Gly linker and a C-terminal cysteine for fluorophore conjugation (Figure S5). The biological function of DHFR is to reduce dihydrofolate to tetrahydrofolate using NADPH, which is oxidised to $NADP^+$ (Scheme 4). First, the activity of the DHFR fusion was tested using a spectrophotometric assay, monitoring the oxidation of NADPH by a characteristic decrease in $A_{340\ nm}$. The results showed that the DHFR fusion is catalytically active and is inhibited by methotrexate (Figure S6).

MAVNDYEPGSMVITHVQGGGRDIIQYIPARSSYGTPPFVPPGPSPYVGTGMQEYRKLRS
TLDKSHSELKKNLKNETLKEVDELKSEAGLPGKAVSANDIRDEKSIVDALMDAKAKSLK
AIEDRPANLYTASDFPQKSESMYQSQLLASRKFYGEFLDRHMSELAKAYSADIYKAQIA
ILKQTSQELENKARSLEAEAQRAAAEVEADYKGSGVRPLNCIVAVSQNMGIGKNGDLPW
PPLRNEFKYFQRMTTTSSVEGKQNLVIMGRKTWFSIPEKNRPLKDRINIVLSRELKEPP
RGAHFLAKSLDDALRLIEQPELASKVDMVWIVGGSSVYQEAMNQPGHLRLFVTRIMQEF
ESDTFFPEIDLGKYKLLPEYPGVLSEVQEEKGIKYKFEVYEKKDCLEHHHHHH

Figure S5. Sequence of the pyoS2^{NTD}DHFR fusion protein.
PyoS2^{NTD} (*blue*) was fused to murine DHFR (*green*) with a GSG linker (*black*) and a His6 expression tag (*red*). The C-terminal cysteine is highlighted.

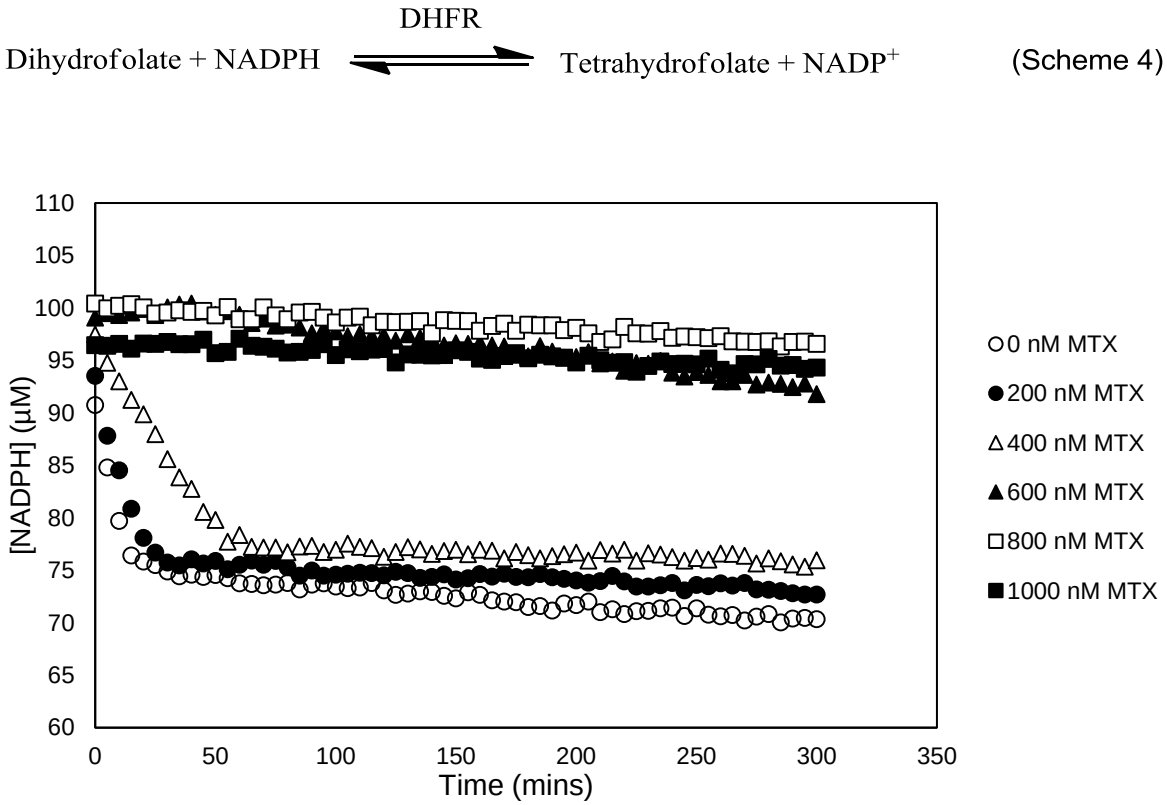

Figure S6. The DHFR fusion is catalytically active and is inhibited by methotrexate.
The oxidation of NADPH during DHFR-mediated catalysis was monitored by $A_{340\ nm}$ measurements which were converted to NADPH concentration using an extinction coefficient ($\varepsilon_{340\ nm}$) of 6200 $M^{-1}cm^{-1}$. NADPH reduction was monitored against time at methotrexate (MTX) concentrations of 0-1000 nM. In the absence methotrexate (*open circles*) NADPH is turned over, but is inhibited with increasing concentrations of methotrexate. Reaction conditions were 1 µM pyoS2^{NTD}DHFR, 100 µM NADPH, 50 mM β-mercaptoethanol, 50 µM dihydrofolate and 0-1000 nM methotrexate in 25 mM Tris-HCl pH 7.5, 150 mM NaCl.

Next, AF488 was conjugated onto the cysteine at C-terminus of DHFR to determine whether methotrexate could block import in fluorescence microscopy experiments. Labelling efficiency was poor possibly due to steric obstruction of the cysteine (Figure S7), yet, *P. aeruginosa* PAO1 cells were suitable fluorescent indicating pyoS2^{NTD}DHFR-AF488 was effectively localising to the cell surface. Unfortunately, FRAP experiments showed pyoS2^{NTD}DHFR-AF488 was not imported even in the absence of methotrexate (Figure S8). Possible explanations for this are: 1, DHFR was binding folate released by lysed cells, inducing a stabilising effect, or 2, the new position of the fluorophore could be sterically blocking translocation.

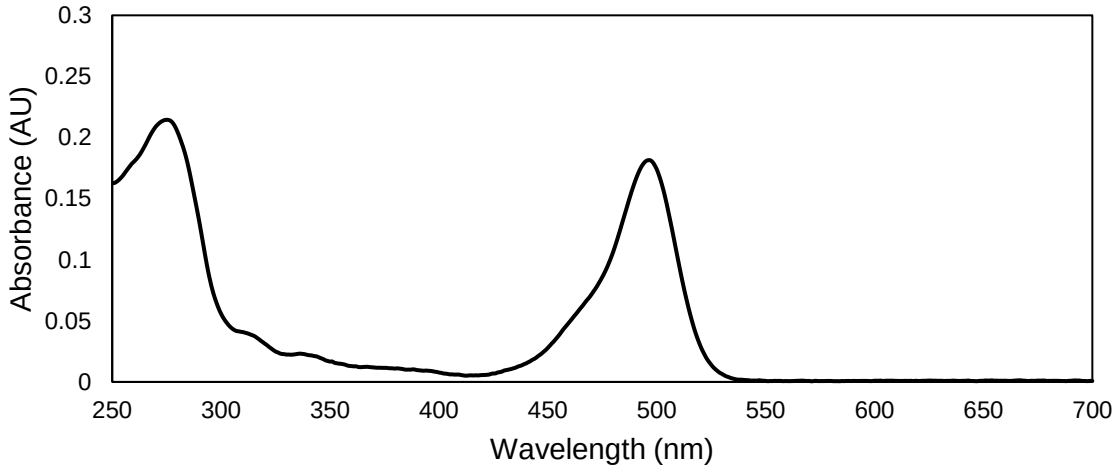

Figure S7. Estimation of pyoS2^{NTD}DHFR-AF488 labelling efficiency.
UV-visible absorbance spectrum of pyoS2^{NTD}DHFR-AF488 conjugate in 20 mM potassium phosphate pH 7.2, 100 mM NaCl determined a labelling efficiency of 56%.

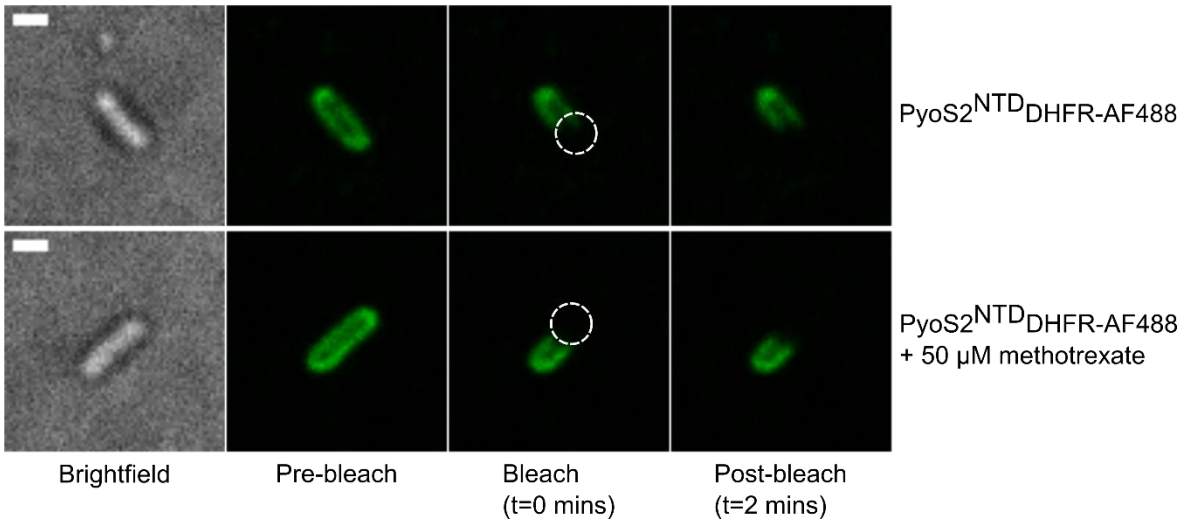

Figure S8. PyoS2^{NTD}DHFR-AF488 is unable to translocate across the OM.
FRAP experiments on PAO1 cells labelled with pyoS2^{NTD}DHFR-AF488 ± 50 µM methotrexate highlighting the bleached region *(dashed circle)*. No FRAP suggests pyoS2^{NTD}DHFR-AF488 cannot translocate to the periplasm even in the absence of methotrexate. Scale bar, 1 µm.

Using pyoS2^{NTD} as a delivery platform for cytotoxic agents

Chimeric bacteriocins described in this thesis were able to effectively kill *P. aeruginosa*, and were even able to subvert PAO1 resistance to pyoS2 in the case of the pyoS2-E2 chimera. Moreover, pyoS2^{NTD} was able to deliver cytotoxic pore-forming domains into the periplasm, as in the case of the pyoS2^{NTD}-S5 and pyoS2^{NTD}-Ia chimeras. It was therefore suggested that pyoS2^{NTD} could become a delivery platform for non-bacteriocin cytotoxic agents such as lysins and small molecule antibiotics, which normally cannot cross the OM barrier. Here describes attempts to fuse a phage lysozyme and the glycopeptide antibiotic vancomycin onto pyoS2^{NTD}.

Fusing a phage lysozyme onto pyoS2^{NTD}

Gp36c is the enzymatic CTD of gp36, a cytotoxic protein produced by the *Pseudomonas* bacteriophage phiKMV that possesses lysozyme activity specific for *Pseudomonas* PG (Lavigne *et al.*, 2003). Here, gp36c has been fused to pyoS2^{NTD} for use in PAO1 killing assays to test whether pyoS2^{NTD} can deliver the phage lysozyme into the *P. aeruginosa* periplasm (Figure S9).

MAVNDYEPGSMVITHVQGGGRDIIQYIPARSSYGTPPFVPPGPSPYVGTGMQEYRKLRS
TLDKSHSELKKNLKNETLKEVDELKSEAGLPGKAVSANDIRDEKSIVDALMDAKAKSLK
AIEDRPANLYTASDFPQKSESMYQSQLLASRKFYGEFLDRHMSELAKAYSADIYKAQIA
ILKQTSQELENKARSLEAEAQRAAAEVEADYKGSGLKQDVFNWRKELAQFEAYRGEAYK
DADGYSVGLGHYLGSGNAGAGTTVTPEQAAQWFAEDTDRALDQGVRLADELGVTNNASI
LGLAGMAFQMGEGRARQFRNTFQAIKDRNKEAFEAGVRNSKWYTQTPDRAEAFIKRMAP
HFDTPSQIGVDWYSAATAELEHHHHHH

Figure S9. Sequence of the pyoS2^{NTD}gp36c fusion protein.
PyoS2^{NTD} (*blue*) was fused to gp36c from bacteriophage phiKMV (*green*) with a GSG linker (*black*) and a His6 expression tag (*red*).

PyoS2^{NTD}gp36c fusion had a very marginal cytotoxic activity against *P. aeruginosa* PAO1 cells (Figure S10). The pyoS2-E2 chimera positive control was effective at killing PAO1 resulting in a large decrease in $OD_{600\ nm}$. Cultures treated with 0.5 mM EDTA did not grow as well as non-treated cultures. More efficient killing in the presence of EDTA may suggest that pyoS2^{NTD}gp36c translocation is inefficient and the OM needs to be compromised in order to see an effect. More experiments required to identify the problem include an *in vitro* lysozyme activity assay and verification of translocation through fluorescence labelling. Moreover, translocation may be inefficient due to the high stability of gp36c (Lavigne *et al.*, 2004) and addition of a chaotrope such as urea may aid translocation.

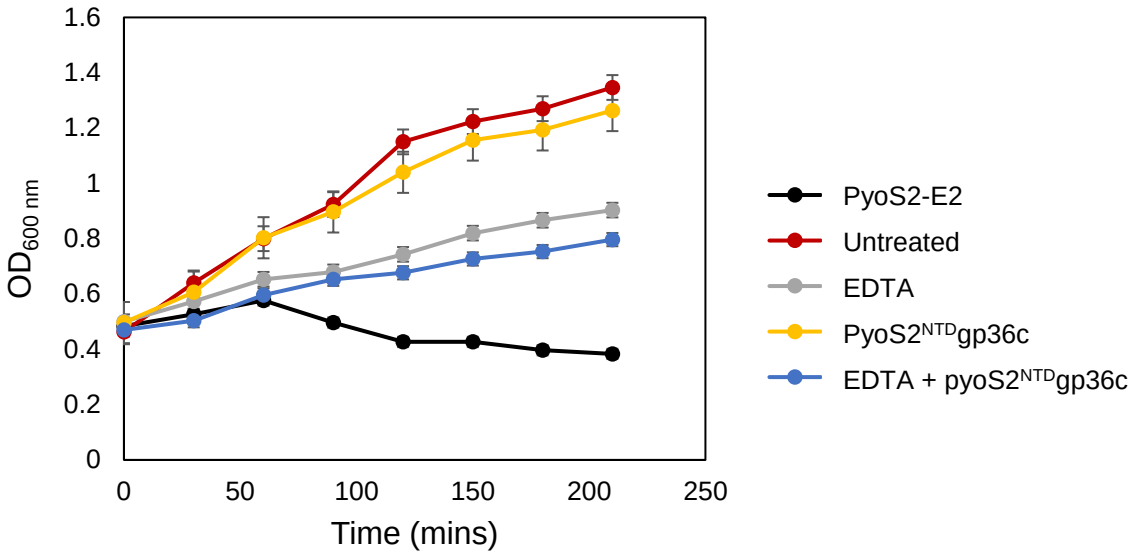

Figure S10. PyoS2^{NTD}gp36c has minimal cytotoxicity against *P. aeruginosa* PAO1.
Liquid culture killing assay on PAO1 cells treated with 1 µM pyoS2^{NTD}gp36c ± 0.5 mM EDTA. The positive control was treated with 100 nM pyoS2-E2 (*black*) and the negative control was left untreated (*red*). PyoS2-E2 exhibits the most cytotoxicity and EDTA treatment impairs growth (*grey*). PyoS2^{NTD}gp36c has a minimal effect on PAO1 growth (*yellow* and *blue*). Data were plotted as the average of three independent measurements and the error bars represent the standard deviation.

Fusing vancomycin onto pyoS2^{NTD}

Vancomycin is a glycopeptide antibiotic commonly used to treat infections of Gram-positive bacteria such as methicillin resistant *Staphylococcus aureus*, and is often the last resort drug used when other antibiotic treatments have failed (William, 1981). Vancomycin hydrogen bonds with D-Ala-D-Ala intermediates of PG synthesis, preventing the assembly of a stable cell wall (Hofmann *et al.*, 2012). In Gram-negative bacteria, the OM prevents vancomycin from reaching its PG target and it is therefore ineffective against these bacteria. Fusing vancomycin to pyoS2^{NTD}, which readily permeates the OM, may sensitise *P. aeruginosa* to killing.

The fusion strategy was based on the methods described in studies by Hoffman *et al* (2012) and Greenwald *et al* (2003). The authors describe using a PEG-based linker containing an amine-reactive succinimidyl ester to react with the primary amine in

vancomycin known as the V_3 position (Figure S11). The linker used in this study was a maleimide-PEG_2-succinimidyl ester; the maleimide reacting with the C-terminal cysteine engineered in pyoS2^{NTD}, whilst the succinimide group reacts with amine groups in vancomycin.

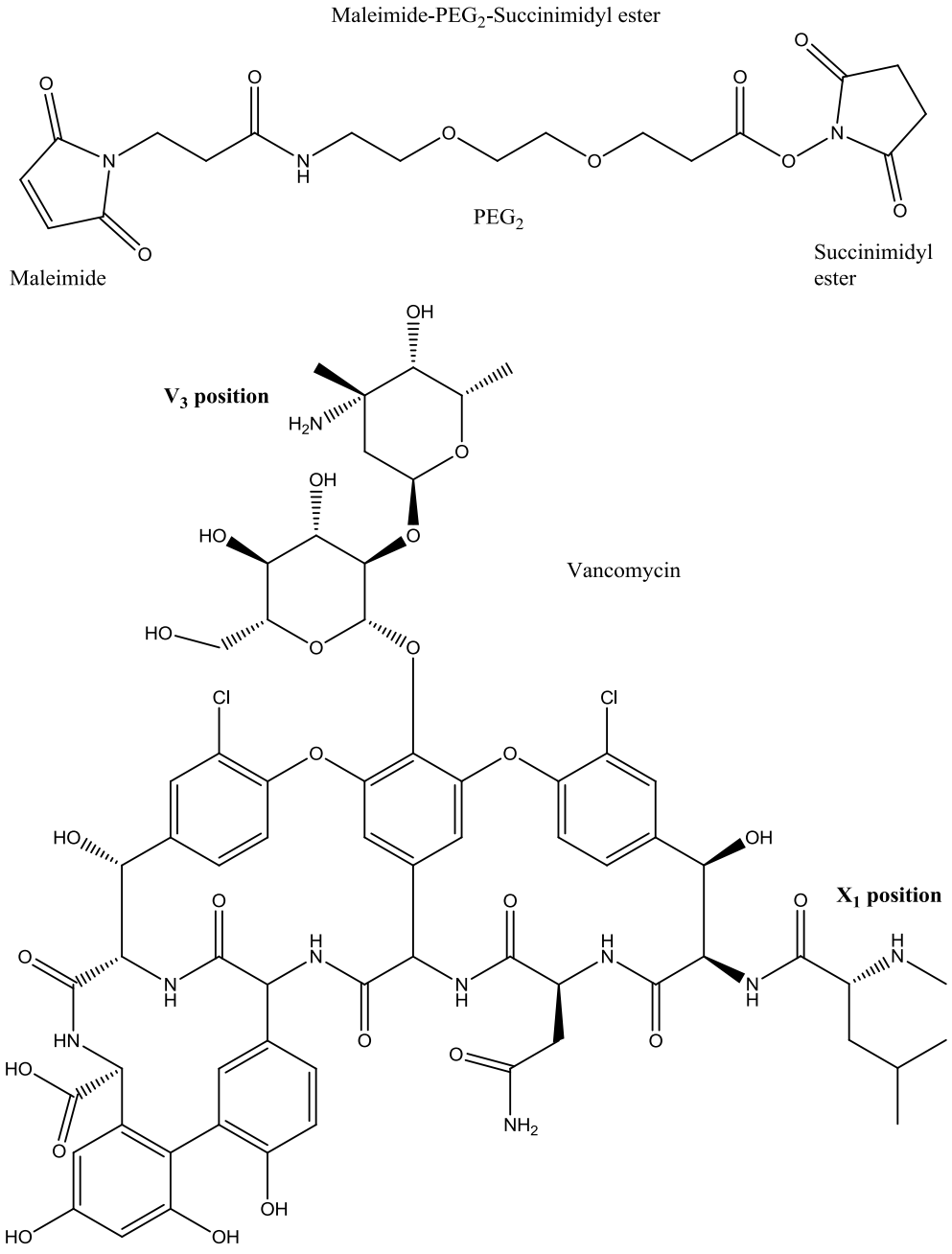

Figure S11. Structures of maleimide-PEG_2-succinimidyl ester and vancomycin.
The maleimide group was used for conjugation to the cysteine residue at the C-terminus of pyoS2^{NTD} and the succinimide group reacts with amines in vancomycin. The primary amine in the V_3 position was the preferred site for conjugation, as opposed to the X_1 secondary amine (Hofmann *et al.*, 2012).

The first step involved using semi-synthetic chemistry methods to conjugate the PEG linker onto the V_3 position on vancomycin. Prior to synthesis, all chemicals (purchased from Sigma Aldrich) were anhydrous and free from impurities as determined by 1D H^1-NMR. To preferentially target the V_3 position over the secondary amine at the X_1 position (Hofmann *et al.*, 2012), a 20-fold molar excess of triethylamine (TEA) is used. The reaction took place in *N*,*N*-dimethylformamide (DMF) to maximise reaction efficiency. Semi-synthesis methods, carried out under supervision and in the laboratory of Dr Sylvia McClain, University of Oxford, are outlined below:

- In a 250 ml Schlenk flask, 80 mg maleimide-PEG_2-succinimidyl ester, 150 ml DMF containing 50 mM TEA and 557 mg vancomycin were added. The final concentrations dissolved in 150 ml DMF were as follows:
- 50 mM TEA (20:1 molar excess to vancomycin)
- 2.5 mM vancomycin (2:1 molar excess to maleimide-PEG_2-succinimidyl ester)
- 1.25 mM maleimide-PEG_2-succinimidyl ester
- Stir under N_2 gas for 15 hours.
- After 15 hours, the reaction mixture (colourless) was transferred dropwise into 300 ml cold diethyl ether by positive pressure from N_2 gas.
- The reaction mixture precipitated in the diethyl ether turning the solution cloudy.
- The product was isolated by pumping off the solvents under vacuum, the volatile diethyl ether evaporating readily under vacuum leaving behind the much less volatile DMF.
- After removing all the solvent, the remaining solid product was collected for the next stage of the conjugation process, covalent attachment to $pyoS2^{NTD}$.

Conjugation of the maleimide-PEG_2-vancomycin product to the C-terminal cysteine of $pyoS2^{NTD}$ used the same protocol as for maleimide-fluorophore conjugation (See Materials and Methods 2.12.1). Unlike fluorophores, there was no distinct absorbance maximum to monitor elution of maleimide-PEG_2-vancomycin, though being a

glycopeptide with several aromatic groups, there was sufficient absorbance at 280 nm. Successful conjugation was judged by a slight peak shift during SEC, indicating an increase in molecular weight (Figure S12). Killing activity of the pyoS2^{NTD}-vancomycin conjugate was tested by liquid culture killing assays (Figure S13). There was no apparent change in growth rate between pyoS2^{NTD} only (negative control) and the pyoS2-vancomycin conjugate (Figure S13 blue and grey traces, respectively). Further growth of the cultures treated with the pyoS2-E2 chimera (positive control) was effectively inhibited (Figure S13, orange trace).

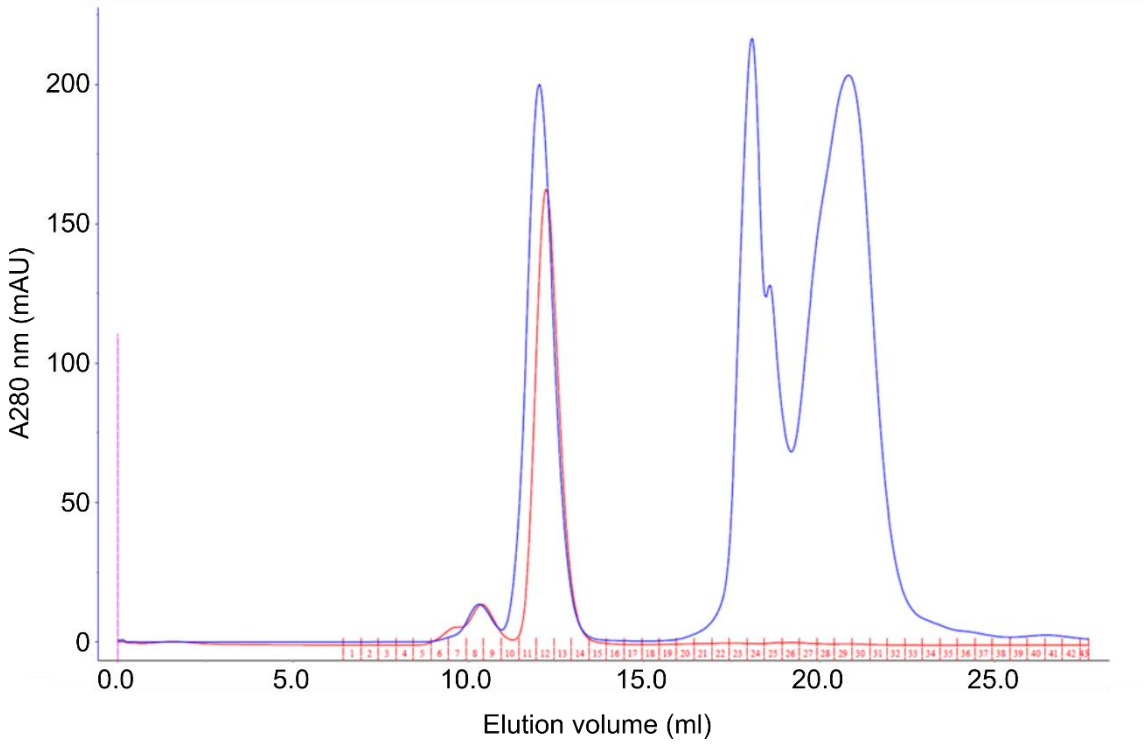

Figure S12. Conjugation of maleimide-PEG$_2$-vancomycin to pyoS2^{NTD}.
SEC elution profile of pyoS2^{NTD} (*red*) and pyoS2^{NTD} coupled to maleimide-PEG$_2$-vancomycin (*blue*) using a S75 10 300 GL column (GE Healthcare). A slight peak shift indicating a higher molecular weight suggests conjugation has been successful.

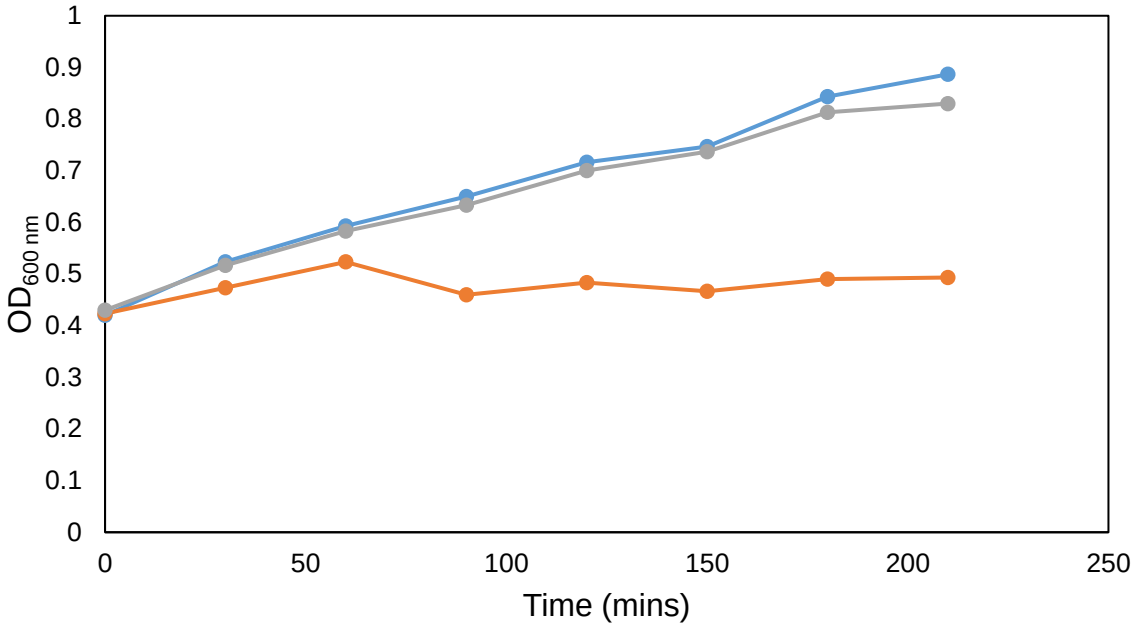

Figure S13. PyoS2^{NTD}-vancomycin is unable to kill *P. aeruginosa* PAO1.
Liquid culture killing assay in M9 minimal media against *P. aeruginosa* PAO1 using 1 µM of pyoS2^{NTD} (*blue*), pyoS2-E2 chimera (*orange*) and pyoS2^{NTD}-vancomycin conjugate (*grey*). PyoS2-E2 exhibits cytotoxicity, whilst pyoS2^{NTD} alone and pyoS2^{NTD}-vancomycin are unable to kill.

Due to time constraints, the reason/s why this strategy failed are not known, but have scope for optimisation in the future. First, the semi-synthesis may have failed requiring full characterisation of the product by mass spectrometry and NMR. The conjugation to pyoS2^{NTD} may also have failed and would require analysis by mass spectrometry to determine whether this has been successful. Finally, the major challenge is the size of vancomycin, which may be too large to pass through the ~13 Å wide channel in FpvAI. Fe-Pvd can be accommodated in the FpvAI translocation channel, whilst vancomycin is probably too large (Figure S14).

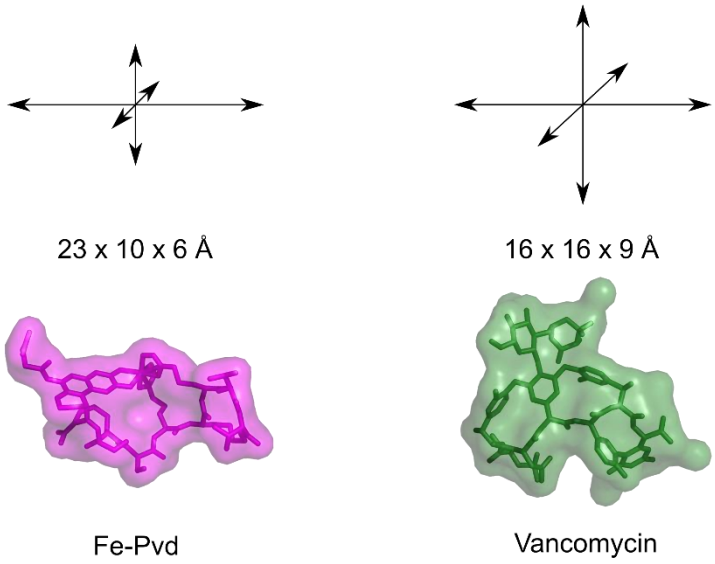

Figure S14. Size comparison of Fe-Pvd and vancomycin.
Surface representation of Fe-Pvd (*magenta*) and vancomycin (*green*) along with dimensions.

Bibliography

Adams, H., Zeder-Lutz, G., Schalk, I., Pattus, F. & Celia, H. 2006. Interaction of TonB with the outer membrane receptor FpvA of *Pseudomonas aeruginosa*. *Journal of Bacteriology,* **188**(16)**,** 5752-5761.

Adams, P. D., Afonine, P. V., Bunkoczi, G., Chen, V. B., Davis, I. W., Echols, N., Headd, J. J., Hung, L. W., Kapral, G. J., Grosse-Kunstleve, R. W., McCoy, A. J., Moriarty, N. W., Oeffner, R., Read, R. J., Richardson, D. C., Richardson, J. S., Terwilliger, T. C. & Zwart, P. H. 2010. PHENIX: a comprehensive Python-based system for macromolecular structure solution. *Acta Crystallographica. Section D, Biological Crystallography,* **66**(Pt 2)**,** 213-21.

Ainavarapu, S. R., Li, L., Badilla, C. L. & Fernandez, J. M. 2005. Ligand binding modulates the mechanical stability of dihydrofolate reductase. *Biophysical Journal,* **89**(5)**,** 3337-44.

Albrecht-Gary, A.-M., Blanc, S., Rochel, N., Ocaktan, A. Z. & Abdallah, M. A. 1994. Bacterial Iron Transport: Coordination Properties of Pyoverdin PaA, a Peptidic Siderophore of *Pseudomonas aeruginosa*. *Inorganic Chemistry,* **33**(26)**,** 6391-6402.

Alteri, C. J. & Mobley, H. L. T. 2016. The Versatile Type VI Secretion System. *Microbiology spectrum,* **4**(2)**,** 10.1128/microbiolspec.VMBF-0026-2015.

Anraku, Y. 1988. Bacterial Electron Transport Chains. *Annual Review of Biochemistry,* **57**(1)**,** 101-132.

Antignani, A. & Youle, R. J. 2008. Endosome fusion induced by diphtheria toxin translocation domain. *Proceedings of the National Academy of Sciences of the United States of America,* **105**(23)**,** 8020-8025.

Arnold, T., Zeth, K. & Linke, D. 2009. Structure and function of colicin S4, a colicin with a duplicated receptor-binding domain. *Journal of Biological Chemistry,* **284**(10)**,** 6403-13.

Bakelar, J., Buchanan, S. K. & Noinaj, N. 2016. The structure of the β-barrel assembly machinery complex. *Science,* **351**(6269)**,** 180-186.

Barbhaiya, H. B. & Rao, K. K. 1985. Production of pyoverdine, the fluorescent pigment of *Pseudomonas aeruginosa* PAO1. *FEMS Microbiology Letters,* **27**(2)**,** 233-235.

Bayer, M. E. 1991. Zones of membrane adhesion in the cryofixed envelope of *Escherichia coli*. *Journal of Structural Biology,* **107**(3)**,** 268-280.

Baysse, C., Meyer, J. M., Plesiat, P., Geoffroy, V., Michel-Briand, Y. & Cornelis, P. 1999. Uptake of pyocin S3 occurs through the outer membrane ferripyoverdine type II receptor of *Pseudomonas aeruginosa*. *Journal of Bacteriology,* **181**(12)**,** 3849-51.

Beck, C. M., Diner, E. J., Kim, J. J., Low, D. A. & Hayes, C. S. 2014. The F pilus mediates a novel pathway of CDI toxin import. *Molecular Microbiology,* **93**(2)**,** 276-290.

Berks, B. C., Sargent, F. & Palmer, T. 2000. The Tat protein export pathway. *Molecular Microbiology,* **35**(2)**,** 260-74.

Berman, H. M., Westbrook, J., Feng, Z., Gilliland, G., Bhat, T. N., Weissig, H., Shindyalov, I. N. & Bourne, P. E. 2000. The Protein Data Bank. *Nucleic Acids Research,* **28**(1)**,** 235-242.

Bernstein, A., Rolfe, B. & Onodera, K. 1972. Pleiotropic properties and genetic organization of the *tolA,B* locus of *Escherichia coli* K-12. *Journal of Bacteriology,* **112**(1)**,** 74-83.

Blackburn, P., Wilson, G. & Moore, S. 1977. Ribonuclease inhibitor from human placenta. Purification and properties. *Journal of Biological Chemistry,* **252**(16)**,** 5904-10.

Blaustein, R. O., Koehler, T. M., Collier, R. J. & Finkelstein, A. 1989. Anthrax toxin: channel-forming activity of protective antigen in planar phospholipid bilayers. *Proceedings of the National Academy of Sciences of the United States of America,* **86**(7)**,** 2209-2213.

Botos, I., Majdalani, N., Mayclin, S. J., McCarthy, J. G., Lundquist, K., Wojtowicz, D., Barnard, T. J., Gumbart, J. C. & Buchanan, S. K. 2016. Structural and Functional Characterization of the LPS Transporter LptDE from Gram-negative Pathogens. *Structure,* **24**(6)**,** 965-976.

Bouveret, E., Rigal, A., Lazdunski, C. & Benedetti, H. 1998. Distinct regions of the colicin A translocation domain are involved in the interaction with TolA and TolB proteins upon import into *Escherichia coli*. *Molecular Microbiology,* **27**(1)**,** 143-157.

Braun, V. 1975. Covalent lipoprotein from the outer membrane of *Escherichia coli*. *Biochimica et Biophysica Acta (BBA) - Reviews on Biomembranes*, **415**(3)**,** 335-377.

Braun, V. 2003. Iron uptake by *Escherichia coli*. *Frontiers in Bioscience,* **8**, s1409-21.

Braun, V. & Herrmann, C. 2004. Point mutations in transmembrane helices 2 and 3 of ExbB and TolQ affect their activities in *Escherichia coli* K-12. *Journal of Bacteriology,* **186**(13)**,** 4402-6.

Braun, V., Patzer, S. I. & Hantke, K. 2002. Ton-dependent colicins and microcins: modular design and evolution. *Biochimie,* **84**(5-6)**,** 365-80.

Bricogne G, B. E., Brandl M, Flensburg C, Keller P, Paciorek P, Roversi P, Sharff a, Smart O, Vonrhein C, Womack T 2010. BUSTER version 2.10.2. Cambridge, United Kingdom: Global Phasing Ltd.

Brillet, K., Journet, L., Célia, H., Paulus, L., Stahl, A., Pattus, F. & Cobessi, D. 2007. A β Strand Lock Exchange for Signal Transduction in TonB-Dependent Transducers on the Basis of a Common Structural Motif. *Structure,* **15**(11)**,** 1383-1391.

Brockwell, D. J., Paci, E., Zinober, R. C., Beddard, G. S., Olmsted, P. D., Smith, D. A., Perham, R. N. & Radford, S. E. 2003. Pulling geometry defines the mechanical resistance of a beta-sheet protein. *Nature Structural Biology,* **10**(9)**,** 731-7.

Brown, D. 2015. Antibiotic resistance breakers: can repurposed drugs fill the antibiotic discovery void? *Nature Reviews Drug Discovery,* **14**(12)**,** 821-832.

Buchanan, S. K., Lukacik, P., Grizot, S., Ghirlando, R., Ali, M. M., Barnard, T. J., Jakes, K. S., Kienker, P. K. & Esser, L. 2007. Structure of colicin I receptor bound to the R-domain of colicin Ia: implications for protein import. *EMBO Journal,* **26**(10)**,** 2594-604.

Carr, S., Walker, D., James, R., Kleanthous, C. & Hemmings, A. M. 2000. Inhibition of a ribosome-inactivating ribonuclease: the crystal structure of the cytotoxic domain of colicin E3 in complex with its immunity protein. *Structure,* **8**(9)**,** 949-60.

Cascales, E., Buchanan, S. K., Duché, D., Kleanthous, C., Lloubès, R., Postle, K., Riley, M., Slatin, S. & Cavard, D. 2007. Colicin Biology. *Microbiology and Molecular Biology Reviews,* **71**(1)**,** 158-229.

Cascales, E. & Christie, P. J. 2003. The versatile bacterial type IV secretion systems. *Nature Reviews Microbiology,* **1**(2)**,** 137-49.

Celia, H., Noinaj, N., Zakharov, S. D., Bordignon, E., Botos, I., Santamaria, M., Barnard, T. J., Cramer, W. A., Lloubes, R. & Buchanan, S. K. 2016. Structural insight into the role of the Ton complex in energy transduction. *Nature,* **538**(7623)**,** 60-65.

Chang, C., Mooser, A., Pluckthun, A. & Wlodawer, A. 2001. Crystal structure of the dimeric C-terminal domain of TonB reveals a novel fold. *Journal of Biological Chemistry,* **276**(29)**,** 27535-40.

Chen, V. B., Arendall, W. B., 3rd, Headd, J. J., Keedy, D. A., Immormino, R. M., Kapral, G. J., Murray, L. W., Richardson, J. S. & Richardson, D. C. 2010. MolProbity: all-atom structure validation for macromolecular crystallography. *Acta Crystallographica. Section D, Biological Crystallography,* **66**(Pt 1)**,** 12-21.

Chen, Y., Radford, S. E. & Brockwell, D. J. 2015. Force-induced remodelling of proteins and their complexes. *Current Opinion in Structural Biology,* **30**, 89-99.

Chimento, D. P., Kadner, R. J. & Wiener, M. C. 2005. Comparative structural analysis of TonB-dependent outer membrane transporters: Implications for the transport cycle. *Proteins: Structure, Function, and Bioinformatics,* **59**(2)**,** 240-251.

Chimento, D. P., Mohanty, A. K., Kadner, R. J. & Wiener, M. C. 2003. Substrate-induced transmembrane signaling in the cobalamin transporter BtuB. *Nature Structural Biology,* **10**(5)**,** 394.

Chin, J. W., Martin, A. B., King, D. S., Wang, L. & Schultz, P. G. 2002. Addition of a photocrosslinking amino acid to the genetic code of *Escherichia coli*. *Proceedings of the National Academy of Sciences of the United States of America,* **99**(17)**,** 11020-11024.

Cho, H., Uehara, T. & Bernhardt, T. G. 2014. Beta-lactam antibiotics induce a lethal malfunctioning of the bacterial cell wall synthesis machinery. *Cell,* **159**(6)**,** 1300-1311.

Chodera, J. D. & Mobley, D. L. 2013. Entropy-enthalpy compensation: Role and ramifications in biomolecular ligand recognition and design. *Annual Review of Biophysics*, **42**, 121-142.

Clavel, T., Germon, P., Vianney, A., Portalier, R. & Lazzaroni, J. C. 1998. TolB protein of *Escherichia coli* K-12 interacts with the outer membrane peptidoglycan-associated proteins Pal, Lpp and OmpA. *Molecular Microbiology,* **29**(1)**,** 359-67.

Clément, E., Mesini, P. J., Pattus, F. & Schalk, I. J. 2004. The Binding Mechanism of Pyoverdin with the Outer Membrane Receptor FpvA in *Pseudomonas aeruginosa* Is Dependent on Its Iron-Loaded Status. *Biochemistry,* **43**(24)**,** 7954-7965.

Cobessi, D., Celia, H. & Pattus, F. 2005. Crystal Structure at High Resolution of Ferric-pyochelin and its Membrane Receptor FptA from *Pseudomonas aeruginosa*. *Journal of Molecular Biology,* **352**(4)**,** 893-904.

Collier, R. J. 2001. Understanding the mode of action of diphtheria toxin: a perspective on progress during the 20th century. *Toxicon,* **39**(11)**,** 1793-1803.

Cooper, A. 1999. Thermodynamic analysis of biomolecular interactions. *Current Opinion in Chemical Biology,* **3**(5)**,** 557-63.

Cotter, P. D., Ross, R. P. & Hill, C. 2013. Bacteriocins - a viable alternative to antibiotics? *Nature Reviews Microbiology,* **11**(2)**,** 95-105.

Craig, D. B. & Dombkowski, A. A. 2013. Disulfide by Design 2.0: a web-based tool for disulfide engineering in proteins. *BMC Bioinformatics,* **14**(1)**,** 346.

Dalbey, R. E., Wang, P. & Kuhn, A. 2011. Assembly of Bacterial Inner Membrane Proteins. *Annual Review of Biochemistry,* **80**(1)**,** 161-187.

De Chial, M., Ghysels, B., Beatson, S. A., Geoffroy, V., Meyer, J. M., Pattery, T., Baysse, C., Chablain, P., Parsons, Y. N., Winstanley, C., Cordwell, S. J. & Cornelis, P. 2003. Identification of type II and type III pyoverdine receptors from *Pseudomonas aeruginosa*. *Microbiology,* **149**(4)**,** 821-831.

Dean, C. R. & Poole, K. 1993. Expression of the ferric enterobactin receptor (PfeA) of *Pseudomonas aeruginosa* - Involvement of a 2-component regulatory system. *Molecular Microbiology,* **8**(6)**,** 1095-1103.

Delano, W. L. 2002. The PyMOL Molecular Graphics System. *DeLano Scientific, Palo Alto, CA, USA.*

Delepelaire, P. 2004. Type I secretion in gram-negative bacteria. *Biochimica et Biophysica Acta (BBA) - Molecular Cell Research,* **1694**(1)**,** 149-161.

Delgado, M. A., Rintoul, M. R., Farías, R. N. & Salomón, R. A. 2001. *Escherichia coli* RNA Polymerase Is the Target of the Cyclopeptide Antibiotic Microcin J25. *Journal of Bacteriology,* **183**(15)**,** 4543-4550.

Delmar, J. A., Su, C. C. & Yu, E. W. 2014. Bacterial multidrug efflux transporters. *Annual Review of Biophysics,* **43**, 93-117.

Destoumieux-Garzón, D., Peduzzi, J., Thomas, X., Djediat, C. & Rebuffat, S. 2006. Parasitism of Iron-siderophore Receptors of *Escherichia coli* by the Siderophore-peptide Microcin E492m and its Unmodified Counterpart. *Biometals,* **19**(2)**,** 181-191.

Devanathan, S. & Postle, K. 2007. Studies on colicin B translocation: FepA is gated by TonB. *Molecular Microbiology,* **65**(2)**,** 441-53.

Diepold, A. & Armitage, J. P. 2015. Type III secretion systems: the bacterial flagellum and the injectisome. *Philosophical Transactions of the Royal Society of London. Series B, Biological Sciences,* **370**(1679).

Dietsche, T., Tesfazgi Mebrhatu, M., Brunner, M. J., Abrusci, P., Yan, J., Franz-Wachtel, M., Schärfe, C., Zilkenat, S., Grin, I., Galán, J. E., Kohlbacher, O., Lea, S., Macek, B., Marlovits, T. C., Robinson, C. V. & Wagner, S. 2016. Structural and Functional Characterization of the Bacterial Type III Secretion Export Apparatus. *PLOS Pathogens,* **12**(12)**,** e1006071.

Dietz, H. & Rief, M. 2004. Exploring the energy landscape of GFP by single-molecule mechanical experiments. *Proceedings of the National Academy of Sciences of the United States of America,* **101**(46)**,** 16192-16197.

Dingemans, J., Ghequire, M. G. K., Craggs, M., De Mot, R. & Cornelis, P. 2016. Identification and functional analysis of a bacteriocin, pyocin S6, with ribonuclease activity from a *Pseudomonas aeruginosa* cystic fibrosis clinical isolate. *MicrobiologyOpen,* **5**(3)**,** 413-423.

Doerrler, W. T., Gibbons, H. S. & Raetz, C. R. H. 2004. MsbA-dependent Translocation of Lipids across the Inner Membrane of *Escherichia coli*. *Journal of Biological Chemistry,* **279**(43)**,** 45102-45109.

Dolezal, P., Likic, V., Tachezy, J. & Lithgow, T. 2006. Evolution of the molecular machines for protein import into mitochondria. *Science,* **313**(5785)**,** 314-8.

Donohue-Rolfe, A. M. & Schaechter, M. 1980. Translocation of phospholipids from the inner to the outer membrane of *Escherichia coli*. *Proceedings of the National Academy of Sciences of the United States of America,* **77**(4)**,** 1867-1871.

Dormán, G., Nakamura, H., Pulsipher, A. & Prestwich, G. D. 2016. The Life of Pi Star: Exploring the Exciting and Forbidden Worlds of the Benzophenone Photophore. *Chemical Reviews,* **116**(24)**,** 15284-15398.

Driessen, A. J. & Nouwen, N. 2008. Protein translocation across the bacterial cytoplasmic membrane. *Annual Review of Biochemistry,* **77,** 643-67.

Duport, C., Baysse, C. & Michelbriand, Y. 1995. Molecular characterization of pyocin S3, a novel S-type pyocin from *Pseudomonas aeruginosa*. *Journal of Biological Chemistry,* **270**(15)**,** 8920-8927.

Duquesne, S., Destoumieux-Garzon, D., Peduzzi, J. & Rebuffat, S. 2007. Microcins, gene-encoded antibacterial peptides from enterobacteria. *Natural Product Reports,* **24**(4)**,** 708-734.

Elfarash, A., Dingemans, J., Ye, L., Hassan, A. A., Craggs, M., Reimmann, C., Thomas, M. S. & Cornelis, P. 2014. Pore-forming pyocin S5 utilizes the FptA ferripyochelin receptor to kill *Pseudomonas aeruginosa*. *Microbiology-Sgm,* **160,** 261-269.

Elfarash, A., Wei, Q. & Cornelis, P. 2012. The soluble pyocins S2 and S4 from *Pseudomonas aeruginosa* bind to the same FpvAI receptor. *MicrobiologyOpen,* **1**(3)**,** 268-275.

Emsley, P. & Cowtan, K. 2004. Coot: model-building tools for molecular graphics. *Acta Crystallographica. Section D, Biological Crystallography,* **60**(Pt 12 Pt 1)**,** 2126-2132.

Evans, P. R. & Murshudov, G. N. 2013. How good are my data and what is the resolution? *Acta Crystallographica. Section D, Biological Crystallography,* **69**(Pt 7)**,** 1204-14.

Fanucci, G. E., Cadieux, N., Kadner, R. J. & Cafiso, D. S. 2003. Competing ligands stabilize alternate conformations of the energy coupling motif of a TonB-dependent outer membrane transporter. *Proceedings of the National Academy of Sciences of the United States of America,* **100**(20)**,** 11382-11387.

Farrance, O. E., Hann, E., Kaminska, R., Housden, N. G., Derrington, S. R., Kleanthous, C., Radford, S. E. & Brockwell, D. J. 2013. A Force-Activated Trip Switch Triggers Rapid Dissociation of a Colicin from Its Immunity Protein. *PLOS Biology,* **11**(2)**,** e1001489.

Feld, G. K., Brown, M. J. & Krantz, B. A. 2012. Ratcheting up protein translocation with anthrax toxin. *Protein Science,* **21**(5)**,** 606-24.

Feld, G. K., Thoren, K. L., Kintzer, A. F., Sterling, H. J., Tang, I. I., Greenberg, S. G., Williams, E. R. & Krantz, B. A. 2010. Structural basis for the unfolding of anthrax lethal factor by protective antigen oligomers. *Nature Structural & Molecular Biology,* **17**(11)**,** 1383-1390.

Ferguson, N., Li, W., Capaldi, A. P., Kleanthous, C. & Radford, S. E. 2001. Using chimeric immunity proteins to explore the energy landscape for alpha-helical protein folding. *Journal of Molecular Biology,* **307**(1)**,** 393-405.

Fernandez-Fuentes, N., Dybas, J. M. & Fiser, A. 2010. Structural Characteristics of Novel Protein Folds. *PLOS Computational Biology,* **6**(4)**,** e1000750.

Freed, D. M., Lukasik, S. M., Sikora, A., Mokdad, A. & Cafiso, D. S. 2013. Monomeric TonB and the Ton box are required for the Formation of a High-Affinity Transporter-TonB Complex. *Biochemistry,* **52**(15)**,** 2638-2648.

Frieden, T. 2013. Antibiotic resistance threats in the United States. U.S. Centers for Disease Control and Prevention.

Germon, P., Ray, M. C., Vianney, A. & Lazzaroni, J. C. 2001. Energy-dependent conformational change in the TolA protein of *Escherichia coli* involves its N-terminal domain, TolQ, and TolR. *Journal of Bacteriology,* **183**(14)**,** 4110-4.

Ghysels, B., Dieu, B. T. M., Beatson, S. A., Pirnay, J.-P., Ochsner, U. A., Vasil, M. L. & Cornelis, P. 2004. FpvB, an alternative type I ferripyoverdine receptor of *Pseudomonas aeruginosa*. *Microbiology,* **150**(6)**,** 1671-1680.

Gibbs, K. A., Isaac, D. D., Xu, J., Hendrix, R. W., Silhavy, T. J. & Theriot, J. A. 2004. Complex spatial distribution and dynamics of an abundant *Escherichia coli* outer membrane protein, LamB. *Molecular Microbiology,* **53**(6)**,** 1771-83.

Gokce, I., Raggett, E. M., Hong, Q., Virden, R., Cooper, A. & Lakey, J. H. 2000. The TolA-recognition site of colicin N. ITC, SPR and stopped-flow fluorescence define a crucial 27-residue segment. *Journal of Molecular Biology,* **304**(4)**,** 621-632.

Gould, S. B., Maier, U. G. & Martin, W. F. 2015. Protein import and the origin of red complex plastids. *Current Biology,* **25**(12)**,** R515-21.

Grabowicz, M. & Silhavy, T. J. 2017. Redefining the essential trafficking pathway for outer membrane lipoproteins. *Proceedings of the National Academy of Sciences of the United States of America,* **114**(18)**,** 4769-4774.

Graille, M., Mora, L., Buckingham, R. H., Van Tilbeurgh, H. & De Zamaroczy, M. 2004. Structural inhibition of the colicin D tRNase by the tRNA-mimicking immunity protein. *EMBO Journal,* **23**(7)**,** 1474-82.

Gram, H. C. 1884. Über die isolierte Färbung der Schizomyceten in Schnitt- und Trockenpräparaten. *Fortschritte der Medizin,* **2,** 185-89.

Gratia, A. 1925. Sur un remarquable exemple d'antagonisme entre deux souches de colibacille. *C.R. Soc.Biol. (Paris),* (**93**)**,** 1040-1041.

Green, E. R. & Mecsas, J. 2016. Bacterial Secretion Systems – An overview. *Microbiology spectrum,* **4**(1)**,** 10.1128/microbiolspec.VMBF-0012-2015.

Greenfield, L. K. & Whitfield, C. 2012. Synthesis of lipopolysaccharide O-antigens by ABC transporter-dependent pathways. *Carbohydrate Research,* **356,** 12-24.

Greenwald, J., Hoegy, F., Nader, M., Journet, L., Mislin, G. L. A., Graumann, P. L. & Schalk, I. J. 2007. Real Time Fluorescent Resonance Energy Transfer Visualization of Ferric Pyoverdine Uptake in *Pseudomonas aeruginosa*: A role for ferrous iron. *The Journal of Biological Chemistry,* **282**(5)**,** 2987-2995.

Greenwald, J., Nader, M., Celia, H., Gruffaz, C., Geoffroy, V., Meyer, J. M., Schalk, I. J. & Pattus, F. 2009. FpvA bound to non-cognate pyoverdines: molecular basis of siderophore recognition by an iron transporter. *Molecular Microbiology,* **72**(5)**,** 1246-59.

Greenwald, J., Zeder-Lutz, G., Hagege, A., Celia, H. & Pattus, F. 2008. The Metal Dependence of Pyoverdine Interactions with Its Outer Membrane Receptor FpvA. *Journal of Bacteriology,* **190**(20)**,** 6548-6558.

Greenwald, R. B., Zhao, H., Xia, J. & Martinez, A. 2003. Poly(ethylene glycol) Transport Forms of Vancomycin: A Long-Lived Continuous Release Delivery System. *Journal of Medicinal Chemistry,* **46**(23)**,** 5021-5030.

Gresock, M. G., Kastead, K. A. & Postle, K. 2015. From Homodimer to Heterodimer and Back: Elucidating the TonB Energy Transduction Cycle. *Journal of Bacteriology,* **197**(21)**,** 3433-3445.

Griko, Y. V., Zakharov, S. D. & Cramer, W. A. 2000. Structural stability and domain organization of colicin E1. *Journal of Molecular Biology,* **302**(4)**,** 941.

Gu, Y., Li, H., Dong, H., Zeng, Y., Zhang, Z., Paterson, N. G., Stansfeld, P. J., Wang, Z., Zhang, Y., Wang, W. & Dong, C. 2016. Structural basis of outer membrane protein insertion by the BAM complex. *Nature,* **531**(7592)**,** 64-9.

Gumbart, J., Wiener, M. C. & Tajkhorshid, E. 2007. Mechanics of Force Propagation in TonB-Dependent Outer Membrane Transport. *Biophysical Journal,* **93**(2)**,** 496-504.

Hann, E., Kirkpatrick, N., Kleanthous, C., Smith, D. A., Radford, S. E. & Brockwell, D. J. 2007. The effect of protein complexation on the mechanical stability of Im9. *Biophysical Journal,* **92**(9)**,** L79-81.

Harmer, C., Alnassafi, K., Hu, H., Elkins, M., Bye, P., Rose, B., Cordwell, S., Triccas, J. A., Harbour, C. & Manos, J. 2013. Modulation of gene expression by *Pseudomonas aeruginosa* during chronic infection in the adult cystic fibrosis lung. *Microbiology-Sgm,* **159,** 2354-2363.

Hickman, S. J., Cooper, R. E. M., Bellucci, L., Paci, E. & Brockwell, D. J. 2017. Gating of TonB-dependent transporters by substrate-specific forced remodelling. *Nature Communications,* **8,** 14804.

Hilsenbeck, J. L., Park, H., Chen, G., Youn, B., Postle, K. & Kang, C. 2004. Crystal structure of the cytotoxic bacterial protein colicin B at 2.5 Å resolution. *Molecular Microbiology,* **51**(3)**,** 711-720.

Hoegy, F., Celia, H., Mislin, G. L., Vincent, M., Gallay, J. & Schalk, I. J. 2005. Binding of Iron-free Siderophore, a Common Feature of Siderophore Outer Membrane Transporters of *Escherichia coli* and *Pseudomonas aeruginosa*. *Journal of Biological Chemistry,* **280**(21)**,** 20222-20230.

Hoffman, E. A., Frey, B. L., Smith, L. M. & Auble, D. T. 2015. Formaldehyde Crosslinking: A Tool for the Study of Chromatin Complexes. *Journal of Biological Chemistry,* **290**(44)**,** 26404-26411.

Hofmann, C. M., Anderson, J. M. & Marchant, R. E. 2012. Targeted Delivery of Vancomycin to Staphylococcus epidermidis Biofilms Using a Fibrinogen-Derived Peptide. *Journal of biomedical materials research. Part A,* **100**(9)**,** 2517-2525.

Housden, N. G., Hopper, J. T., Lukoyanova, N., Rodriguez-Larrea, D., Wojdyla, J. A., Klein, A., Kaminska, R., Bayley, H., Saibil, H. R., Robinson, C. V. & Kleanthous, C. 2013. Intrinsically disordered protein threads through the bacterial outer-membrane porin OmpF. *Science,* **340**(6140)**,** 1570-4.

Housden, N. G., Loftus, S. R., Moore, G. R., James, R. & Kleanthous, C. 2005. Cell entry mechanism of enzymatic bacterial colicins: porin recruitment and the thermodynamics of receptor binding. *Proceedings of the National Academy of Sciences of the United States of America,* **102**(39)**,** 13849-54.

Housden, N. G., Wojdyla, J. A., Korczynska, J., Grishkovskaya, I., Kirkpatrick, N., Brzozowski, A. M. & Kleanthous, C. 2010. Directed epitope delivery across the *Escherichia coli* outer membrane through the porin OmpF. *Proceedings of the National Academy of Sciences of the United States of America,* **107**(50)**,** 21412-7.

Huang, B., Ru, K., Yuan, Z., Whitchurch, C. B. & Mattick, J. S. 2004. TonB3 Is Required for Normal Twitching Motility and Extracellular Assembly of Type IV Pili. *Journal of Bacteriology,* **186**(13)**,** 4387-4389.

Iadanza, M. G., Higgins, A. J., Schiffrin, B., Calabrese, A. N., Brockwell, D. J., Ashcroft, A. E., Radford, S. E. & Ranson, N. A. 2016. Lateral opening in the intact β-barrel assembly machinery captured by cryo-EM. *Nature Communications,* **7,** 12865.

Imperi, F., Tiburzi, F. & Visca, P. 2009. Molecular basis of pyoverdine siderophore recycling in *Pseudomonas aeruginosa*. *Proceedings of the National Academy of Sciences of the United States of America,* **106**(48)**,** 20440-20445.

Inglis, R. F., Scanlan, P. & Buckling, A. 2016. Iron availability shapes the evolution of bacteriocin resistance in *Pseudomonas aeruginosa*. *The ISME Journal,* **10**(8)**,** 2060-2066.

Ito, K. & Akiyama, Y. 2005. Cellular functions, mechanism of action, and regulation of FtsH protease. *Annual Review of Microbiology,* **59,** 211-31.

Jakes, K. S. & Finkelstein, A. 2010. The colicin Ia receptor, Cir, is also the translocator for colicin Ia. *Molecular Microbiology,* **75**(3)**,** 567-78.

Jakob, R. P., Geitner, A.-J., Weininger, U., Balbach, J., Dobbek, H. & Schmid, F. X. 2012. Structural and energetic basis of infection by the filamentous bacteriophage IKe. *Molecular Microbiology,* **84**(6)**,** 1124-1138.

Jiang, J., Pentelute, B. L., Collier, R. J. & Zhou, Z. H. 2015. Atomic structure of anthrax protective antigen pore elucidates toxin translocation. *Nature,* **521**(7553)**,** 545-549.

Jones, N. C. & Osborn, M. J. 1977. Translocation of phospholipids between the outer and inner membranes of Salmonella typhimurium. *Journal of Biological Chemistry,* **252**(20)**,** 7405-7412.

Jordan, L. D., Zhou, Y., Smallwood, C. R., Lill, Y., Ritchie, K., Yip, W. T., Newton, S. M. & Klebba, P. E. 2013. Energy-dependent motion of TonB in the Gram-negative bacterial inner membrane. *Proceedings of the National Academy of Sciences of the United States of America,* **110**(28)**,** 11553-8.

Joshi, A., Grinter, R., Josts, I., Chen, S., Wojdyla, J. A., Lowe, E. D., Kaminska, R., Sharp, C., McCaughey, L., Roszak, A. W., Cogdell, R. J., Byron, O., Walker, D. & Kleanthous, C. 2015. Structures of the Ultra-High-Affinity Protein-Protein Complexes of Pyocins S2 and AP41 and Their Cognate Immunity Proteins from *Pseudomonas aeruginosa*. *Journal of Molecular Biology,* **427**(17)**,** 2852-66.

Junker, J. P., Hell, K., Schlierf, M., Neupert, W. & Rief, M. 2005. Influence of substrate binding on the mechanical stability of mouse dihydrofolate reductase. *Biophysical Journal,* **89**(5)**,** L46-8.

Kabsch, W. 2010. Xds. *Acta Crystallographica. Section D, Biological Crystallography,* **66**(Pt 2)**,** 125-32.

Kadner, R. J. & Heller, K. J. 1995. Mutual inhibition of cobalamin and siderophore uptake systems suggests their competition for TonB function. *Journal of Bacteriology,* **177**(17)**,** 4829-35.

Kauer, J. C., Erickson-Viitanen, S., Wolfe, H. R. & Degrado, W. F. 1986. p-Benzoyl-L-phenylalanine, a new photoreactive amino acid. Photolabeling of calmodulin with a synthetic calmodulin-binding peptide. *Journal of Biological Chemistry,* **261**(23)**,** 10695-700.

Keeble, A. H. & Kleanthous, C. 2005. The kinetic basis for dual recognition in colicin endonuclease-immunity protein complexes. *Journal of Molecular Biology,* **352**(3)**,** 656-71.

Kendrew, J. C. & Parrish, R. G. 1957. The Crystal Structure of Myoglobin. III. Sperm-Whale Myoglobin. *Proceedings of the Royal Society of London. Series A. Mathematical and Physical Sciences,* **238**(1214)**,** 305-324.

Kim, Y. C., Tarr, A. W. & Penfold, C. N. 2014. Colicin import into *E. coli* cells: a model system for insights into the import mechanisms of bacteriocins. *Biochimica et Biophysica Acta (BBA) - Molecular Cell Research,* **1843**(8)**,** 1717-31.

Kirkup, B. C. & Riley, M. A. 2004. Antibiotic-mediated antagonism leads to a bacterial game of rock-paper-scissors *in vivo*. *Nature,* **428**(6981)**,** 412-4.

Kleanthous, C. 2010a. Swimming against the tide: progress and challenges in our understanding of colicin translocation. *Nature Reviews Microbiology,* **8**(12)**,** 843-8.

Kleanthous, C. 2010b. Translocator hunt comes full Cir-Col. *Molecular Microbiology,* **75**(3)**,** 529-33.

Kleanthous, C., Kuhlmann, U. C., Pommer, A. J., Ferguson, N., Radford, S. E., Moore, G. R., James, R. & Hemmings, A. M. 1999. Structural and mechanistic basis of immunity toward endonuclease colicins. *Nature Structural Biology,* **6**(3)**,** 243-52.

Kleanthous, C. & Walker, D. 2001. Immunity proteins: enzyme inhibitors that avoid the active site. *Trends in Biochemical Sciences,* **26**(10)**,** 624-631.

Klebba, P. E. 2016. ROSET Model of TonB Action in Gram-Negative Bacterial Iron Acquisition. *Journal of Bacteriology,* **198**(7)**,** 1013-21.

Klein, A., Wojdyla, J., Joshi, A., Josts, I., McCaughey, L. C., Housden, N., Kaminska, R., Byron, O., Walker, D. & Kleanthous, C. 2016. Structural and biophysical analysis of nuclease protein antibiotics. *Biochemical Journal,* **473**(18)**,** 2799-812.

Kluger, R. & Alagic, A. 2004. Chemical cross-linking and protein–protein interactions—a review with illustrative protocols. *Bioorganic Chemistry,* **32**(6)**,** 451-472.

Koedding, J., Howard, P., Kaufmann, L., Polzer, P., Lustig, A. & Welte, W. 2004. Dimerization of TonB Is Not Essential for Its Binding to the Outer Membrane Siderophore Receptor FhuA of *Escherichia coli*. *Journal of Biological Chemistry,* **279**(11)**,** 9978-9986.

Konings, A. F., Martin, L. W., Sharples, K. J., Roddam, L. F., Latham, R., Reid, D. W. & Lamont, I. L. 2013. *Pseudomonas aeruginosa* Uses Multiple Pathways To Acquire Iron during Chronic Infection in Cystic Fibrosis Lungs. *Infection and Immunity,* **81**(8)**,** 2697-2704.

Konisky, J. & Cowell, B. S. 1972. Interaction of colicin Ia with bacterial cells. Direct measurement of Ia-receptor interaction. *Journal of Biological Chemistry,* **247**(20)**,** 6524-9.

Konovalova, A., Perlman, D. H., Cowles, C. E. & Silhavy, T. J. 2014. Transmembrane domain of surface-exposed outer membrane lipoprotein RcsF is threaded through the lumen of β-barrel proteins. *Proceedings of the National Academy of Sciences of the United States of America,* **111**(41)**,** E4350-E4358.

Korotkov, K. V., Sandkvist, M. & Hol, W. G. J. 2012. The type II secretion system: biogenesis, molecular architecture and mechanism. *Nature Reviews Microbiology,* **10**(5)**,** 336-351.

Kortemme, T., Joachimiak, L. A., Bullock, A. N., Schuler, A. D., Stoddard, B. L. & Baker, D. 2004. Computational redesign of protein-protein interaction specificity. *Nature Structural & Molecular Biology,* **11**(4)**,** 371-9.

Krantz, B. A., Melnyk, R. A., Zhang, S., Juris, S. J., Lacy, D. B., Wu, Z., Finkelstein, A. & Collier, R. J. 2005. A Phenylalanine Clamp Catalyzes Protein Translocation Through the Anthrax Toxin Pore. *Science,* **309**(5735)**,** 777-781.

Krissinel, E. & Henrick, K. 2007. Inference of macromolecular assemblies from crystalline state. *Journal of Molecular Biology,* **372**(3)**,** 774-97.

Kurisu, G., Zakharov, S. D., Zhalnina, M. V., Bano, S., Eroukova, V. Y., Rokitskaya, T. I., Antonenko, Y. N., Wiener, M. C. & Cramer, W. A. 2003. The structure of BtuB with bound colicin E3 R-domain implies a translocon. *Nature Structural Biology,* **10**(11)**,** 948-954.

Lambert, P. A. 2002. Mechanisms of antibiotic resistance in *Pseudomonas aeruginosa*. *Journal of the Royal Society of Medicine,* **95,** 22-26.

Lamont, I. L., Beare, P. A., Ochsner, U., Vasil, A. I. & Vasil, M. L. 2002. Siderophore-mediated signaling regulates virulence factor production in *Pseudomonas aeruginosa*. *Proceedings of the National Academy of Sciences of the United States of America,* **99**(10)**,** 7072-7077.

Lavigne, R., Briers, Y., Hertveldt, K., Robben, J. & Volckaert, G. 2004. Identification and characterization of a highly thermostable bacteriophage lysozyme. *Cellular and Molecular Life Sciences CMLS,* **61**(21)**,** 2753-2759.

Lavigne, R., Burkal'tseva, M. V., Robben, J., Sykilinda, N. N., Kurochkina, L. P., Grymonprez, B., Jonckx, B., Krylov, V. N., Mesyanzhinov, V. V. & Volckaert, G. 2003. The genome of bacteriophage φKMV, a T7-like virus infecting *Pseudomonas aeruginosa*. *Virology,* **312**(1)**,** 49-59.

Ling, H., Saeidi, N., Rasouliha, B. H. & Chang, M. W. 2010. A predicted S-type pyocin shows a bactericidal activity against clinical *Pseudomonas aeruginosa* isolates through membrane damage. *FEBS Letters,* **584**(15)**,** 3354-3358.

Liu, D., Cole, R. A. & Reeves, P. R. 1996. An O-antigen processing function for Wzx (RfbX): a promising candidate for O-unit flippase. *Journal of Bacteriology,* **178**(7)**,** 2102-2107.

Llamas, M. A., Sparrius, M., Kloet, R., Jiménez, C. R., Vandenbroucke-Grauls, C. & Bitter, W. 2006. The Heterologous Siderophores Ferrioxamine B and Ferrichrome Activate Signaling Pathways in *Pseudomonas aeruginosa*. *Journal of Bacteriology,* **188**(5)**,** 1882-1891.

Lo Conte, L., Chothia, C. & Janin, J. 1999. The atomic structure of protein-protein recognition sites. *Journal of Molecular Biology,* **285**(5)**,** 2177-98.

Locher, K. P., Rees, B., Koebnik, R., Mitschler, A., Moulinier, L., Rosenbusch, J. P. & Moras, D. 1998. Transmembrane signaling across the ligand-gated FhuA receptor: crystal structures of free and ferrichrome-bound states reveal allosteric changes. *Cell,* **95**(6)**,** 771-8.

Lord, J. M., Smith, D. C. & Roberts, L. M. 1999. Toxin entry: how bacterial proteins get into mammalian cells. *Cellular Microbiology,* **1**(2)**,** 85-91.

Lukacik, P., Barnard, T. J., Keller, P. W., Chaturvedi, K. S., Seddiki, N., Fairman, J. W., Noinaj, N., Kirby, T. L., Henderson, J. P., Steven, A. C., Hinnebusch, B. J. & Buchanan, S. K. 2012. Structural engineering of a phage lysin that targets gram-negative pathogens. *Proceedings of the National Academy of Sciences of the United States of America,* **109**(25)**,** 9857-62.

Luna-Chavez, C., Lin, Y. L. & Huang, R. H. 2006. Molecular basis of inhibition of the ribonuclease activity in colicin E5 by its cognate immunity protein. *Journal of Molecular Biology,* **358**(2)**,** 571-9.

Mahoney, T. F., Ricci, D. P. & Silhavy, T. J. 2016. Classifying β-Barrel Assembly Substrates by Manipulating Essential Bam Complex Members. *Journal of Bacteriology,* **198**(14)**,** 1984-1992.

Marino, F., Cristobal, A., Binai, N. A., Bache, N., Heck, A. J. R. & Mohammed, S. 2014. Characterization and usage of the EASY-spray technology as part of an online 2D SCX-RP ultra-high pressure system. *Analyst,* **139**(24)**,** 6520-6528.

Mathavan, I., Zirah, S., Mehmood, S., Choudhury, H. G., Goulard, C., Li, Y., Robinson, C. V., Rebuffat, S. & Beis, K. 2014. Structural basis for hijacking siderophore receptors by antimicrobial lasso peptides. *Nature Chemical Biology,* **10**(5)**,** 340-342.

McCaughey, L. C., Grinter, R., Josts, I., Roszak, A. W., Waloen, K. I., Cogdell, R. J., Milner, J., Evans, T., Kelly, S., Tucker, N. P., Byron, O., Smith, B. & Walker, D. 2014. Lectin-like bacteriocins from *Pseudomonas* spp. utilise D-rhamnose containing lipopolysaccharide as a cellular receptor. *PLOS Pathogens,* **10**(2)**,** e1003898.

McCaughey, L. C., Josts, I., Grinter, R., White, P., Byron, O., Tucker, N. P., Matthews, J. M., Kleanthous, C., Whitchurch, C. B. & Walker, D. 2016a. Discovery, characterisation and *in vivo* activity of pyocin SD2, a protein antibiotic from *Pseudomonas aeruginosa*. *Biochemical Journal,* **473**(15), 2345-2358.

McCaughey, L. C., Ritchie, N. D., Douce, G. R., Evans, T. J. & Walker, D. 2016b. Efficacy of species-specific protein antibiotics in a murine model of acute *Pseudomonas aeruginosa* lung infection. *Scientific Reports,* **6,** 30201.

McCoy, A. J., Grosse-Kunstleve, R. W., Adams, P. D., Winn, M. D., Storoni, L. C. & Read, R. J. 2007. Phaser crystallographic software. *Journal of Applied Crystallography,* **40**(Pt 4)**,** 658-674.

Mende, J. & Braun, V. 1990. Import-defective colicin B derivatives mutated in the TonB box. *Molecular Microbiology,* **4**(9)**,** 1523-33.

Metz, B., Kersten, G. F. A., Hoogerhout, P., Brugghe, H. F., Timmermans, H. a. M., De Jong, A., Meiring, H., Hove, J. T., Hennink, W. E., Crommelin, D. J. A. & Jiskoot, W. 2004. Identification of Formaldehyde-induced Modifications in Proteins: REACTIONS WITH MODEL PEPTIDES. *Journal of Biological Chemistry,* **279**(8)**,** 6235-6243.

Micek, S. T., Wunderink, R. G., Kollef, M. H., Chen, C., Rello, J., Chastre, J., Antonelli, M., Welte, T., Clair, B., Ostermann, H., Calbo, E., Torres, A., Menichetti, F., Schramm, G. E. & Menon, V. 2015. An international multicenter retrospective study of *Pseudomonas aeruginosa* nosocomial pneumonia: impact of multidrug resistance. *Critical Care,* **19,** 219.

Michel-Briand, Y. & Baysse, C. 2002. The pyocins of *Pseudomonas aeruginosa*. *Biochimie,* **84**(5-6)**,** 499-510.

Minor, D. L. & Kim, P. S. 1994. Measurement of the beta-sheet-forming propensities of amino acids. *Nature,* **367**(6464)**,** 660-663.

Moeck, G. S., Coulton, J. W. & Postle, K. 1997. Cell Envelope Signaling in *Escherichia coli* : Ligand binding to the ferrichrome-iron receptor FhuA promotes interaction with the energy-transducing protein TonB. *Journal of Biological Chemistry,* **272**(45)**,** 28391-28397.

Moeck, G. S. & Letellier, L. 2001. Characterization of *in vitro* Interactions between a Truncated TonB Protein from *Escherichia coli* and the Outer Membrane Receptors FhuA and FepA. *Journal of Bacteriology,* **183**(9)**,** 2755-2764.

Morton, V. L., Friel, C. T., Allen, L. R., Paci, E. & Radford, S. E. 2007. The Effect of Increasing the Stability of Non-native Interactions on the Folding Landscape of the Bacterial Immunity Protein Im9. *Journal of Molecular Biology,* **371**(2)**,** 554-568.

Murray, T. S., Egan, M. & Kazmierczak, B. I. 2007. *Pseudomonas aeruginosa* chronic colonization in cystic fibrosis patients. *Current Opinion in Pediatrics,* **19**(1)**,** 83-8.

Newstead, S., Ferrandon, S. & Iwata, S. 2008a. Rationalizing α-helical membrane protein crystallization. *Protein Science : A Publication of the Protein Society,* **17**(3)**,** 466-472.

Newstead, S., Hobbs, J., Jordan, D., Carpenter, E. P. & Iwata, S. O. 2008b. Insights into outer membrane protein crystallisation. *Molecular Membrane Biology,* **25**(8)**,** 631-638.

Nikaido, H. 2003. Molecular basis of bacterial outer membrane permeability revisited. *Microbiology and Molecular Biology Reviews,* **67**(4)**,** 593-656.

Nikaido, H. & Rosenberg, E. Y. 1990. Cir and Fiu proteins in the outer membrane of *Escherichia coli* catalyze transport of monomeric catechols: study with beta-lactam antibiotics containing catechol and analogous groups. *Journal of Bacteriology,* **172**(3)**,** 1361-1367.

Noinaj, N., Guillier, M., Barnard, T. J. & Buchanan, S. K. 2010. TonB-dependent transporters: regulation, structure and function. *Annual Review of Microbiology,* **64,** 43-60.

Ochsner, U. A., Johnson, Z. & Vasil, M. L. 2000. Genetics and regulation of two distinct haem-uptake systems, phu and has, in *Pseudomonas aeruginosa*. *Microbiology,* **146**(1)**,** 185-198.

Oddershede, L., Dreyer, J. K., Grego, S., Brown, S. & Berg-Sørensen, K. 2002. The motion of a single molecule, the lambda-receptor, in the bacterial outer membrane. *Biophysical Journal,* **83**(6)**,** 3152-3161.

Ohkawa, I., Shiga, S. & Kageyama, M. 1980. Effect of Iron Concentration in the Growth Medium on the Sensitivity of *Pseudomonas aeruginosa* to Pyocin S2. *Journal of Biochemistry,* **87**(1)**,** 323-331.

Okuda, S., Sherman, D. J., Silhavy, T. J., Ruiz, N. & Kahne, D. 2016. Lipopolysaccharide transport and assembly at the outer membrane: the PEZ model. *Nature Reviews Microbiology,* **14**(6)**,** 337-45.

Orlov, V. N., Antonenko, Y. N., Bulychev, A. A. & Yaguzhinsky, L. S. 1994. Combination of the electrogenic ionophores, valinomycin and CCCP, can lead to non-electrogenic K+/H+ exchange on bilayer lipid membranes. *FEBS Letters,* **345**(2-3)**,** 104-106.

Papadakos, G., Wojdyla, J. A. & Kleanthous, C. 2012. Nuclease colicins and their immunity proteins. *Quarterly Reviews of Biophysics,* **45**(1)**,** 57-103.

Park, J. S., Lee, W. C., Yeo, K. J., Ryu, K.-S., Kumarasiri, M., Hesek, D., Lee, M., Mobashery, S., Song, J. H., Kim, S. I., Lee, J. C., Cheong, C., Jeon, Y. H. & Kim, H.-Y. 2012. Mechanism of anchoring of OmpA protein to the cell wall peptidoglycan of the gram-negative bacterial outer membrane. *FASEB Journal,* **26**(1)**,** 219-228.

Parker, J. L. & Newstead, S. 2012. Current trends in α-helical membrane protein crystallization: An update. *Protein Science : A Publication of the Protein Society,* **21**(9)**,** 1358-1365.

Paterson, G. K., Northen, H., Cone, D. B., Willers, C., Peters, S. E. & Maskell, D. J. 2009. Deletion of tolA in Salmonella Typhimurium generates an attenuated strain with vaccine potential. *Microbiology,* **155**(Pt 1)**,** 220-8.

Patzer, S. I., Albrecht, R., Braun, V. & Zeth, K. 2012. Structural and Mechanistic Studies of Pesticin, a Bacterial Homolog of Phage Lysozymes. *Journal of Biological Chemistry,* **287**(28)**,** 23381-23396.

Pawelek, P. D., Croteau, N., Ng-Thow-Hing, C., Khursigara, C. M., Moiseeva, N., Allaire, M. & Coulton, J. W. 2006. Structure of TonB in complex with FhuA, E. coli outer membrane receptor. *Science,* **312**(5778)**,** 1399-402.

Payne, M. A., Igo, J. D., Cao, Z., Foster, S. B., Newton, S. M. & Klebba, P. E. 1997. Biphasic binding kinetics between FepA and its ligands. *Journal of Biological Chemistry,* **272**(35)**,** 21950-5.

Penfold, C. N., Healy, B., Housden, N. G., Boetzel, R., Vankemmelbeke, M., Moore, G. R., Kleanthous, C. & James, R. 2004. Flexibility in the receptor-binding domain of the enzymatic colicin E9 is required for toxicity against *Escherichia coli* cells. *Journal of Bacteriology,* **186**(14)**,** 4520-4527.

Pettersen, E. F., Goddard, T. D., Huang, C. C., Couch, G. S., Greenblatt, D. M., Meng, E. C. & Ferrin, T. E. 2004. UCSF Chimera--a visualization system for exploratory research and analysis. *Journal of Computational Chemistry,* **25**(13)**,** 1605-12.

Poole, K. & McKay, G. A. 2003. Iron acquisition and its control in *Pseudomonas aeruginosa*: Many roads lead to Rome. *Frontiers in Bioscience,* **8,** D661-D686.

Poole, K., Neshat, S., Krebes, K. & Heinrichs, D. E. 1993. Cloning and nucleotide-sequence analysis of the Ferripyoverdine receptor gene FpvA of *Pseudomonas aeruginosa*. *Journal of Bacteriology,* **175**(15)**,** 4597-4604.

Poole, K., Zhao, Q., Neshat, S., Heinrichs, D. E. & Dean, C. R. 1996. The *Pseudomonas aeruginosa tonB* gene encodes a novel TonB protein. *Microbiology,* **142**(6)**,** 1449-1458.

Postle, K. & Kadner, R. J. 2003. Touch and go: tying TonB to transport. *Molecular Microbiology,* **49**(4)**,** 869-882.

Postle, K., Kastead, K. A., Gresock, M. G., Ghosh, J. & Swayne, C. D. 2010. The TonB dimeric crystal structures do not exist *In vivo*. *mBio,* **1**(5)**,** e00307-10.

Pukatzki, S., Ma, A. T., Revel, A. T., Sturtevant, D. & Mekalanos, J. J. 2007. Type VI secretion system translocates a phage tail spike-like protein into target cells where it cross-links actin. *Proceedings of the National Academy of Sciences of the United States of America,* **104**(39)**,** 15508-15513.

Radaev, S., Li, S. & Sun, P. D. 2006. A survey of protein-protein complex crystallizations. *Acta Crystallographica. Section D, Biological Crystallography,* **62**(6)**,** 605-612.

Radics, J., Königsmaier, L. & Marlovits, T. C. 2014. Structure of a pathogenic type 3 secretion system in action. *Nature Structural & Molecular Biology,* **21**(1)**,** 82-87.

Raetz, C. R. & Dowhan, W. 1990. Biosynthesis and function of phospholipids in *Escherichia coli*. *Journal of Biological Chemistry,* **265**(3)**,** 1235-8.

Raetz, C. R. H. 1978. Enzymology, genetics, and regulation of membrane phospholipid synthesis in *Escherichia coli*. *Microbiological Reviews,* **42**(3)**,** 614-659.

Raetz, C. R. H. & Whitfield, C. 2002. Lipopolysaccharide Endotoxins. *Annual Review of Biochemistry,* **71**(1)**,** 635-700.

Rajasekar, K. V., Zdanowski, K., Yan, J., Hopper, J. T. S., Francis, M.-L. R., Seepersad, C., Sharp, C., Pecqueur, L., Werner, J. M., Robinson, C. V., Mohammed, S., Potts, J. R. & Kleanthous, C. 2016. The anti-sigma factor RsrA responds to oxidative stress by reburying its hydrophobic core. *Nature Communications,* **7,** 12194.

Rassam, P., Copeland, N. A., Birkholz, O., Toth, C., Chavent, M., Duncan, A. L., Cross, S. J., Housden, N. G., Kaminska, R., Seger, U., Quinn, D. M., Garrod, T. J., Sansom, M. S., Piehler, J., Baumann, C. G. & Kleanthous, C. 2015. Supramolecular assemblies underpin turnover of outer membrane proteins in bacteria. *Nature,* **523**(7560)**,** 333-6.

Redly, G. A. & Poole, K. 2005. FpvIR control of fpvA ferric pyoverdine receptor gene expression in *Pseudomonas aeruginosa*: Demonstration of an interaction between FpvI and FpvR and identification of mutations in each compromising this interaction. *Journal of Bacteriology,* **187**(16)**,** 5648-5657.

Roise, D., Horvath, S. J., Tomich, J. M., Richards, J. H. & Schatz, G. 1986. A chemically synthesized pre-sequence of an imported mitochondrial protein can form an amphiphilic helix and perturb natural and artificial phospholipid bilayers. *EMBO Journal,* **5**(6)**,** 1327-1334.

Ruhe, Z. C., Low, D. A. & Hayes, C. S. 2013. Bacterial contact-dependent growth inhibition. *Trends in Microbiology,* **21**(5)**,** 230-7.

Ruiz, N., Gronenberg, L. S., Kahne, D. & Silhavy, T. J. 2008. Identification of two inner-membrane proteins required for the transport of lipopolysaccharide to the outer membrane of *Escherichia coli*. *Proceedings of the National Academy of Sciences of the United States of America,* **105**(14)**,** 5537-5542.

Rupp, B. 2010. *Biomolecular Crystallography: Principles, Practice and Application to Structural Biology*, New York, N.Y., Garland Science.

Salomón, R. A. & Farías, R. N. 1993. The FhuA protein is involved in microcin 25 uptake. *Journal of Bacteriology,* **175**(23)**,** 7741-7742.

Sankaran, K. & Wu, H. C. 1994. Lipid modification of bacterial prolipoprotein. Transfer of diacylglyceryl moiety from phosphatidylglycerol. *Journal of Biological Chemistry,* **269**(31)**,** 19701-6.

Sano, Y., Kobayashi, M. & Kageyama, M. 1993. Functional domains of S-type pyocins deduced from chimeric molecules. *Journal of Bacteriology,* **175**(19)**,** 6179-6185.

Sauter, A., Howard, S. P. & Braun, V. 2003. *In vivo* evidence for TonB dimerization. *Journal of Bacteriology,* **185**(19)**,** 5747-54.

Schalk, I. J., Hennard, C., Dugave, C., Poole, K., Abdallah, M. A. & Pattus, F. 2001. Iron-free pyoverdin binds to its outer membrane receptor FpvA in *Pseudomonas aeruginosa*: a new mechanism for membrane iron transport. *Molecular Microbiology,* **39**(2)**,** 351-361.

Schiffrin, B., Calabrese, A. N., Devine, P. W. A., Harris, S. A., Ashcroft, A. E., Brockwell, D. J. & Radford, S. E. 2016. Skp is a multivalent chaperone of outer-membrane proteins. *Nature Structural & Molecular Biology,* **23**(9)**,** 786-793.

Schmitz, A., Herrgen, H., Winkeler, A. & Herzog, V. 2000. Cholera toxin is exported from microsomes by the Sec61p complex. *Journal of Cell Biology,* **148**(6)**,** 1203-12.

Schramm, E., Mende, J., Braun, V. & Kamp, R. M. 1987. Nucleotide sequence of the colicin B activity gene cba: consensus pentapeptide among TonB-dependent colicins and receptors. *Journal of Bacteriology,* **169**(7)**,** 3350-7.

Sharma, O. & Collier, R. J. 2014. Polylysine-Mediated Translocation of the Diphtheria Toxin Catalytic Domain through the Anthrax Protective Antigen Pore. *Biochemistry,* **53**(44)**,** 6934-6940.

Sharma, O., Yamashita, E., Zhalnina, M. V., Zakharov, S. D., Datsenko, K. A., Wanner, B. L. & Cramer, W. A. 2007. Structure of the complex of the colicin E2 R-domain and its BtuB receptor. The outer membrane colicin translocon. *Journal of Biological Chemistry,* **282**(32)**,** 23163-70.

Sharp, C., Bray, J., Housden, N. G., Maiden, M. C. J. & Kleanthous, C. 2017. Diversity and distribution of nuclease bacteriocins in bacterial genomes revealed using Hidden Markov Models. *PLOS Computational Biology,* **13**(7)**,** e1005652.

Shen, J., Meldrum, A. & Poole, K. 2002. FpvA receptor involvement in pyoverdine biosynthesis in *Pseudomonas aeruginosa*. *Journal of Bacteriology,* **184**(12)**,** 3268-75.

Shi, L.-X. & Theg, S. M. 2013. The chloroplast protein import system: From algae to trees. *Biochimica et Biophysica Acta (BBA) - Molecular Cell Research,* **1833**(2)**,** 314-331.

Shirley, M. & Lamont, I. L. 2009. Role of TonB1 in Pyoverdine-Mediated Signaling in *Pseudomonas aeruginosa*. *Journal of Bacteriology,* **191**(18)**,** 5634-5640.

Shultis, D. D., Purdy, M. D., Banchs, C. N. & Wiener, M. C. 2006. Outer membrane active transport: structure of the BtuB:TonB complex. *Science,* **312**(5778)**,** 1396-9.

Sigurskjold, B. W. 2000. Exact analysis of competition ligand binding by displacement isothermal titration calorimetry. *Analytical Biochemistry,* **277**(2)**,** 260-6.

Silhavy, T. J., Kahne, D. & Walker, S. 2010. The bacterial cell envelope. *Cold Spring Harbour Perspectives in Biology,* **2**(5)**,** a000414.

Sklar, J. G., Wu, T., Kahne, D. & Silhavy, T. J. 2007. Defining the roles of the periplasmic chaperones SurA, Skp, and DegP in *Escherichia coli*. *Genes & Development,* **21**(19)**,** 2473-2484.

Smith, A. W., Hirst, P. H., Hughes, K., Gensberg, K. & Govan, J. R. 1992. The pyocin Sa receptor of *Pseudomonas aeruginosa* is associated with ferripyoverdin uptake. *Journal of Bacteriology,* **174**(14)**,** 4847-9.

Smith, K., Martin, L., Rinaldi, A., Rajendran, R., Ramage, G. & Walker, D. 2012. Activity of pyocin S2 against *Pseudomonas aeruginosa* biofilms. *Antimicrobial Agents and Chemotherapy,* **56**(3)**,** 1599-601.

Soelaiman, S., Jakes, K., Wu, N., Li, C. & Shoham, M. 2001. Crystal structure of colicin E3: implications for cell entry and ribosome inactivation. *Molecular Cell,* **8**(5)**,** 1053-1062.

Spector, J., Zakharov, S., Lill, Y., Sharma, O., Cramer, W. A. & Ritchie, K. 2010. Mobility of BtuB and OmpF in the *Escherichia coli* Outer Membrane: Implications for Dynamic Formation of a Translocon Complex. *Biophysical Journal,* **99**(12)**,** 3880-3886.

Stevenson, G., Neal, B., Liu, D., Hobbs, M., Packer, N. H., Batley, M., Redmond, J. W., Lindquist, L. & Reeves, P. 1994. Structure of the O antigen of *Escherichia coli* K-12 and the sequence of its rfb gene cluster. *Journal of Bacteriology,* **176**(13)**,** 4144-4156.

Suchanek, M., Radzikowska, A. & Thiele, C. 2005. Photo-leucine and photo-methionine allow identification of protein-protein interactions in living cells. *Nature Methods,* **2**(4)**,** 261-268.

Sui, M. J., Tsai, L. C., Hsia, K. C., Doudeva, L. G., Ku, W. Y., Han, G. W. & Yuan, H. S. 2002. Metal ions and phosphate binding in the H-N-H motif: crystal structures of the nuclease domain of ColE7/Im7 in complex with a phosphate ion and different divalent metal ions. *Protein Science,* **11**(12)**,** 2947-57.

Takase, H., Nitanai, H., Hoshino, K. & Otani, T. 2000. Requirement of the *Pseudomonas aeruginosa tonB* Gene for High-Affinity Iron Acquisition and Infection. *Infection and Immunity,* **68**(8)**,** 4498-4504.

Taylor, R., Burgner, J. W., Clifton, J. & Cramer, W. A. 1998. Purification and characterization of monomeric *Escherichia coli* vitamin B12 receptor with high affinity for colicin E3. *Journal of Biological Chemistry,* **273**(47)**,** 31113-8.

Theg, S. M., Bauerle, C., Olsen, L. J., Selman, B. R. & Keegstra, K. 1989. Internal ATP is the only energy requirement for the translocation of precursor proteins across chloroplastic membranes. *Journal of Biological Chemistry,* **264**(12)**,** 6730-6736.

Turnbull, L., Toyofuku, M., Hynen, A. L., Kurosawa, M., Pessi, G., Petty, N. K., Osvath, S. R., Cárcamo-Oyarce, G., Gloag, E. S., Shimoni, R., Omasits, U., Ito, S., Yap, X., Monahan, L. G., Cavaliere, R., Ahrens, C. H., Charles, I. G., Nomura, N., Eberl, L. & Whitchurch, C. B. 2016. Explosive cell lysis as a mechanism for the biogenesis of bacterial membrane vesicles and biofilms. *Nature Communications,* **7,** 11220.

Vankemmelbeke, M., Housden, N. G., James, R., Kleanthous, C. & Penfold, C. N. 2013. Immunity protein release from a cell-bound nuclease colicin complex requires global conformational rearrangement. *MicrobiologyOpen,* **2**(5)**,** 853-61.

Velazquez Campoy, A. 2006. Isothermal titration calorimetry to determine association constants for high-affinity ligands. *Nature Protocols,* **1**(1)**,** 186.

Ventola, C. L. 2015. The Antibiotic Resistance Crisis: Part 1: Causes and Threats. *Pharmacy and Therapeutics,* **40**(4)**,** 277-283.

Vetter, I. R., Parker, M. W., Tucker, A. D., Lakey, J. H., Pattus, F. & Tsernoglou, D. 1998. Crystal structure of a colicin N fragment suggests a model for toxicity. *Structure,* **6**(7)**,** 863-74.

Visca, P., Imperi, F. & Lamont, I. L. 2007. Pyoverdine siderophores: from biogenesis to biosignificance. *Trends in Microbiology,* **15**(1)**,** 22-30.

Voisine, C., Craig, E. A., Zufall, N., Von Ahsen, O., Pfanner, N. & Voos, W. 1999. The Protein Import Motor of Mitochondria: Unfolding and Trapping of Preproteins Are Distinct and Separable Functions of Matrix Hsp70. *Cell,* **97**(5)**,** 565-574.

Vollmer, W. 2008. Structural variation in the glycan strands of bacterial peptidoglycan. *FEMS Microbiology Reviews,* **32**(2)**,** 287-306.

Vollmer, W., Joris, B., Charlier, P. & Foster, S. 2008. Bacterial peptidoglycan (murein) hydrolases. *FEMS Microbiology Reviews,* **32**(2)**,** 259-286.

Vollmer, W. & Seligman, S. J. 2010. Architecture of peptidoglycan: more data and more models. *Trends in Microbiology,* **18**(2)**,** 59-66.

Walker, D., Mosbahi, K., Vankemmelbeke, M., James, R. & Kleanthous, C. 2007. The role of electrostatics in colicin nuclease domain translocation into bacterial cells. *Journal of Biological Chemistry,* **282**(43)**,** 31389-97.

Webster, R. E. 1991. The *tol* gene-products and the import of macromolecules into *Escherichia coli*. *Molecular Microbiology,* **5**(5)**,** 1005-1011.

Wernick, N. L. B., Chinnapen, D. J. F., Cho, J. A. & Lencer, W. I. 2010. Cholera Toxin: An Intracellular Journey into the Cytosol by Way of the Endoplasmic Reticulum. *Toxins,* **2**(3)**,** 310-325.

Whiteley, M., Bangera, M. G., Bumgarner, R. E., Parsek, M. R., Teitzel, G. M., Lory, S. & Greenberg, E. P. 2001. Gene expression in *Pseudomonas aeruginosa* biofilms. *Nature,* **413**(6858)**,** 860-4.

Who. 2014. Antimicrobial resistance: global report on surveillance *In:* CADMAN, H. & MARINEZ, L. (eds.). Geneva: World Health Organization.

Wiedemann, N., Frazier, A. E. & Pfanner, N. 2004. The Protein Import Machinery of Mitochondria. *Journal of Biological Chemistry,* **279**(15)**,** 14473-14476.

Wiedemann, N. & Pfanner, N. 2017. Mitochondrial Machineries for Protein Import and Assembly. *Annual Review of Biochemistry,* **86,** 685-714.

Wiener, M., Freymann, D., Ghosh, P. & Stroud, R. M. 1997. Crystal structure of colicin Ia. *Nature,* **385**(6615)**,** 461-464.

Wilcox, A. J., Choy, J., Bustamante, C. & Matouschek, A. 2005. Effect of protein structure on mitochondrial import. *Proceedings of the National Academy of Sciences of the United States of America,* **102**(43)**,** 15435-15440.

William, M. M. K. 1981. Vancomycin Therapy in Severe Staphylococcal Infections. *Reviews of Infectious Diseases,* **3,** S236-S239.

Winn, M. D., Ballard, C. C., Cowtan, K. D., Dodson, E. J., Emsley, P., Evans, P. R., Keegan, R. M., Krissinel, E. B., Leslie, A. G., McCoy, A., McNicholas, S. J., Murshudov, G. N., Pannu, N. S., Potterton, E. A., Powell, H. R., Read, R. J., Vagin, A. & Wilson, K. S. 2011. Overview of the CCP4 suite and current developments. *Acta Crystallographica. Section D, Biological Crystallography,* **67**(Pt 4)**,** 235-42.

Wittelsberger, A., Thomas, B. E., Mierke, D. F. & Rosenblatt, M. 2006. Methionine acts as a "magnet" in photoaffinity crosslinking experiments. *FEBS Letters,* **580**(7)**,** 1872-1876.

Wu, T., Malinverni, J., Ruiz, N., Kim, S., Silhavy, T. J. & Kahne, D. 2005. Identification of a multicomponent complex required for outer membrane biogenesis in *Escherichia coli*. *Cell,* **121**(2)**,** 235-45.

Yamaguchi, A., Nakashima, R. & Sakurai, K. 2015. Structural basis of RND-type multidrug exporters. *Frontiers in Microbiology,* **6,** 327.

Yamaguchi, K., Yu, F. & Inouye, M. 1988. A single amino acid determinant of the membrane localization of lipoproteins in E. coli. *Cell,* **53**(3)**,** 423-32.

Yang, B., Wu, Y.-J., Zhu, M., Fan, S.-B., Lin, J., Zhang, K., Li, S., Chi, H., Li, Y.-X., Chen, H.-F., Luo, S.-K., Ding, Y.-H., Wang, L.-H., Hao, Z., Xiu, L.-Y., Chen, S., Ye, K., He, S.-M. & Dong, M.-Q. 2012. Identification of cross-linked peptides from complex samples. *Nature Methods,* **9**(9)**,** 904-906.

Zakharov, S. D., Eroukova, V. Y., Rokitskaya, T. I., Zhalnina, M. V., Sharma, O., Loll, P. J., Zgurskaya, H. I., Antonenko, Y. N. & Cramer, W. A. 2004. Colicin occlusion of OmpF and TolC channels: outer membrane translocons for colicin import. *Biophysical Journal,* **87**(6)**,** 3901-3911.

Zeth, K., Romer, C., Patzer, S. I. & Braun, V. 2008. Crystal structure of colicin M, a novel phosphatase specifically imported by *Escherichia coli*. *Journal of Biological Chemistry,* **283**(37)**,** 25324-31.

Zhang, Y., Vankemmelbeke, M. N., Holland, L. E., Walker, D. C., James, R. & Penfold, C. N. 2008. Investigating Early Events in Receptor Binding and Translocation of Colicin E9 Using Synchronized Cell Killing and Proteolytic Cleavage. *Journal of Bacteriology,* **190**(12)**,** 4342-4350.

Zhao, Q. & Poole, K. 2000. A second *tonB* gene in *Pseudomonas aeruginosa* is linked to the *exbB* and *exbD* genes. *FEMS Microbiology Letters,* **184**(1)**,** 127-132.

Zimorski, V., Ku, C., Martin, W. F. & Gould, S. B. 2014. Endosymbiotic theory for organelle origins. *Current Opinion in Microbiology,* **22,** 38-48.